Apport de la modélisation aux procédés d'élaboration de matériaux solides hétérogènes

Claudia Cogné

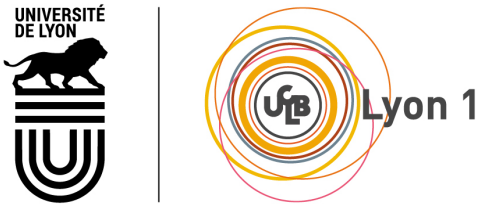

Université Claude Bernard Lyon 1

N° d'ordre : 012-2018

HABILITATION À DIRIGER DES RECHERCHES

Spécialité : Génie des Procédés

par

Claudia COGNÉ

Apport de la modélisation aux procédés d'élaboration de matériaux solides hétérogènes

---

Présentée le 10 Avril 2018 devant le jury composé de :

Jean-Louis LANOISELLE	Professeur (UBS, Pontivy)	Président
Michel HAVET	Professeur (ONIRIS, Nantes)	Rapporteur
Hervé MUHR	Directeur de Recherche (ENSIC, Nancy)	Rapporteur
Khashayar SALEH	Professeur (UTC, Compiègne)	Rapporteur
Jocelyn BONJOUR	Professeur (INSA, Lyon)	Examinateur
Mohamed GUESSASMA	Professeur (UPJV, Saint-Quentin)	Examinateur
Denis MANGIN	Professeur (UCBL, Lyon)	Examinateur
Roman PECZALSKI	Professeur (UCBL, Lyon)	Examinateur

Remerciements

Mes remerciements s'adressent tout d'abord à mes rapporteurs, Michel Havet, Hervé Muhr et Khashayar Saleh, qui m'ont fait l'honneur d'évaluer mon travail et l'ensemble de ma démarche scientifique. Je les remercie pour leur compétence et pour la spontanéité avec laquelle ils ont accepté d'être les rapporteurs de ce manuscrit.

J'exprime toute ma reconnaissance à mes examinateurs, Jocelyn Bonjour, Mohamed Guessasma et Jean-Louis Lanoisellé qui ont eu la gentillesse d'apporter leurs regards pertinents à l'évaluation de mon travail et me prodiguer de judicieux conseils pour la suite de ma carrière. Ce fut également un plaisir pour moi de collaborer avec chacun d'entre eux.

Je remercie également Denis Mangin et Roman Peczalski pour leur expertise scientifique, leurs conseils et leur soutien dans le déroulement de ma carrière d'enseignant-chercheur, ainsi que pour la confiance qu'ils m'ont témoignée depuis ma mutation à Lyon en m'associant spontanément à leurs activités.

Ce travail d'HDR doit beaucoup à tous ceux avec qui j'ai partagé mes idées, mes doutes, mes projets. Depuis 2004, quatorze années riches et bien remplies qui m'ont donné l'occasion de rencontrer et de côtoyer des collègues et des amis que je tiens tout particulièrement à remercier. J'espère que chacun se reconnaîtra à travers ses quelques mots !

Je pense tout d'abord à mes collègues et amis du LTI, qui ont partagé avec moi une riche expérience en modélisation et qui ont favorisé le démarrage de ma carrière d'enseignant chercheur. Et je garde en mémoire, à travers ces 7 années picardes, d'heureux moments et des souvenirs inoubliables.

Mes premiers pas dans la recherche ont été guidés par mes encadrants de thèse et de post-doctorat. Cela induit à vie des liens tout à fait privilégiés, à la fois intellectuels et amicaux. J'ai une pensé toute particulière pour le jeune retraité parti à la conquête des grands espaces pendant ma soutenance. Je ne saurais trop souligner à quel point les moments scientifiques et extra-scientifiques partagés ensemble ont influé durablement sur moi.

J'exprime également toute ma sympathie à mes collègues du LAGEP et de l'IUT Lyon1 avec qui je partage les problèmes et les plaisirs quotidiens. Un remerciement plus particulier à l'ensemble de l'équipe PES pour l'ambiance conviviale qui permet un travail de recherche stimulant et fructueux.

J'adresse un grand merci à l'ensemble des services techniques, administratifs et informatiques du LTI et du LAGEP pour leur aide et leur disponibilité permanente. Je n'aurais pu mener mes travaux dans de bonnes conditions sans le soutien de ces équipes des deux laboratoires.

Au-delà des remerciements, c'est ma très profonde reconnaissance que je souhaite exprimer à celles et ceux et qui ont soutenu ma démarche d'HDR. Sans leur générosité attentive et leurs encouragements bienveillants, je n'aurais certainement jamais commencé ce mémoire.

Enfin, je ne manquerais bien sûr pas de remercier les doctorants et post-doctorants avec qui j'ai ou j'ai eu plaisir à travailler : Viet, Uyen, Thouaïba, Pierre, Nabil et Stéphane. J'associe également à ces remerciements tous les stagiaires que j'ai pu encadrer pour des durées plus ou moins longues, et sans qui ce travail n'aurait pas vu le jour.

Enfin, mes remerciements vont bien sur à ma famille et à mes amis pour leur confiance, leur soutien et leurs encouragements qui m'ont permis de mener à bien tous mes projets.

Table des matières

Liste des figures

Liste des tableaux

Liste des sigles et acronymes

ACL	*Article dans une revue nationale ou internationale avec comité de lecture*
ACLN	*Articles dans des revues avec comité de lecture non répertoriées dans des bases de données internationales*
ACTI	*Communication avec actes dans un congrès international*
ACTN	*Communication avec actes dans un congrès national*
BRE	*Brevet*
CETHIL	*Centre d'Energétique et de Thermique de Lyon (UMR 5008)*
CIFRE	*Convention Industrielle de Formation par la Recherche*
CM	*Cours Magistraux*
CNAM	*Conservatoire National des Arts et Métiers*
CNU	*Conseil National des Universités*
CRBC	*Centre Belge de la Céramique*
CRITT MDTS	*Centre Régional et d'Innovation de Transfert de Technologie en Matériaux, Dépôts et Traitements de Surface*
DEM	*Discrete Element Method*
DTS	*Distribution des Temps de Séjours*
DUT	*Diplôme Universitaire de Technologie*
EGDS	*EthyleneGlycol DiStéarate*
ENSCBP	*École Nationale Supérieure de Chimie, Biologie et Physique*
ENSCL	*École Nationale Supérieure de Chimie de Lille*
ENSIACET	*École Nationale Supérieure des Ingénieurs en Arts Chimiques et Technologiques*
ENSIC	*École Nationale Supérieure des Industries Chimiques*

GDR	*Groupement de Recherche*
GCGP	*Génie chimique - Génie des Procédés*
INERIS	*Institut National de l'Environnemment Industriel et des Risques*
IUT	*Institut Universitaire Technologique*
LAGEP	*Laboratoire d'Automatique et de Génie des Procédés (UMR CNRS 5007)*
LPro	*Licence Professionnelle*
LTI	*Laboratoire des Technologies Innovantes (EA 3899)*
NSCD	*Non Smooth Contact Dynamics*
RAPSODEE	*Centre de Recherche d'Albi en génie des Procédés des Solides Divisés, de l'Énergie et de l'Environnement (UMR CNRS 5302)*
SCD	*Smooth Contact Dynamics*
SIRRIS	*Centre collectif de l'industrie technologique belge*
TMIR	*Transformations Intégrées de la Matière Renouvelable (EA 4297)*
TD	*Travaux Dirigés*
TP	*Travaux Pratiques*
UCBL	*Université Claude Bernard Lyon1*
UNIT	*Université Numérique Ingénierie et Technologie*
UPJV	*Université de Picardie Jules Verne*
UTC	*Université Technologique de Compiègne*
UVHC	*Université de Valenciennes et du Hainaut Cambrésis*

Introduction

Ce manuscrit, présenté en vue de l'obtention d'une Habilitation à Diriger des Recherches, est une synthèse de mes activités de recherche et d'enseignement depuis mon doctorat jusqu'à aujourd'hui. Mon parcours de chercheur a débuté au Laboratoire d'Automatique et de Génie des Procédés (LAGEP - UMR CNRS 5007) de l'Université Claude Bernard Lyon1 où j'y ai effectué ma thèse et mon post-doctorat.

En 2004, j'ai intégré l'Université de Picardie Jules Verne (UPJV) en tant que maître de conférences, à l'IUT de l'Aisne (Département Génie Chimique - Génie des Procédés à Saint-Quentin) pour l'enseignement et au Laboratoire des Technologies Innovantes (LTI - EA 3899) pour la recherche. Ma nomination dans une équipe à forte dominante mécanique m'a permis de renforcer mes connaissances en modélisation tout en restant dans mon domaine de compétences, le génie des procédés. De plus, sur ce site délocalisé, et peut être encore plus qu'ailleurs, la nécessité de rencontres avec d'autres enseignants-chercheurs et le travail d'équipe ont été des éléments fondateurs de mes travaux. J'ai ainsi pu nouer des liens avec l'Université Technologique de Compiègne (UTC) ou encore intégrer un réseau de scientifiques franco-belges dans le cadre d'un projet européen. Ce contexte particulier de travail, où la synergie entre diverses disciplines scientifiques a été privilégiée, a positivement contribué à mes activités de recherche.

Après 7 années passées à l'UPJV, j'ai obtenu ma mutation en septembre 2011 à l'Université Claude Bernard Lyon1 (UCBL), au LAGEP en recherche et à l'IUT Lyon1 (Département Génie Chimique - Génie des Procédés) en enseignement. L'intégration dans un laboratoire UMR CNRS, à forte vocation Génie des Procédes, m'a permis de recentrer mes compétences dans mon domaine de formation, de bénéficier de moyens expérimentaux variés et modernes, ainsi que d'être entourée d'experts reconnus dans la section CNU 62.

Mes activités de recherche se concentrent depuis mon stage de DEA en 2000, sur l'utilisation de la simulation numérique pour l'amélioration des procédés et des produits. Un des fils conducteur de mon travail a toujours été de proposer des outils numériques applicatifs répondant à des problématiques technologiques ou industrielles bien définies. Toutefois, la démarche en simulation numérique doit idéalement se structurer selon une méthodologie associant la théorie, la modélisation, et la vérification expérimentale. Ainsi, mes travaux m'ont aussi conduit à mener des études expérimentales pour alimenter et valider des modèles numériques. Le champ de mes recherches se décline selon deux grands axes : les procédés de congélation et les milieux particulaires. Un aperçu chronologique de mes principaux travaux et de la production scientifique associée est présenté dans le Tableau 1.

Année	Titre de l'étude	Financement	N° de référence de la production scientifique [1]
2000-2003 (Thèse)	Étude expérimentale et modélisation de la congélation des crèmes glacées industrielles	CIFRE (Nestlé)	ACL1, ACL2, ACL3 ACLN1 ACTI1 ACTN1, ACTN2
2004 (Post-Doc)	Étude de la cristallisation d'un principe actif pour soins corporels	Rhodia	ACL4 BRE1
2006-2009	Modélisation par la méthode des éléments discrets des phénomènes thermomécaniques et d'usure associés à des frottements et des impacts	Conseil Régional de Picardie	ACL5, ACL6 ACTI2, ACTI3, ACTI4, ACTI5 ACTN4, ACTN5, ACTN7, ACTN8, ACTN9, ACTN11
2006-2010	Étude de la congélation par évapodétente de purées de légumes (SULTRAPID)	Conseil Régional de Picardie Bonduelle	ACL8 ACLN2 ACTI6, ACTI7 ACTN6, ACTN10
2008	Étude d'un matériau à changement de phase pour chambrer une bouteille	Le Creuset	ACTI8 ACTN14, ACTN15
2008-2012	Étude de nouveaux matériaux à gradients pour la gestion de flux thermiques (PRISTIMAT)	Programme européen INTERREG IV	ACL7 ACTI9, ACTI10 ACTN12, ACTN13, ACTN16
2011-2013	Contrôle par ultrasons de la nucléation de la glace (SONONUCLICE)	ANR blanc	ACL9, ACL10, ACL11 OS1 ACTN17, ACTN21, ACTN24 COM1, COM2, COM3
2012-2016	Traitement d'eaux usées industrielles par congélation sur paroi froide	Thèse MENRT	ACL12, ACLN3 ACTI12, ACTI13 ACTN18, ACTN19, ACTN20, ACTN22, ACTN23, ACTN25, ACTN26
2013-2016	Procédé d'intensification de la récupération des phosphates dans les eaux usées (PHORWater)	Programme européen LIFE+	BRE2 ACTI14 COM4
2017	Création d'un portail Genie-des-Procedes.fr	UNIT	ACTN27
2015-2018	Étude et optimisation de la lyophilisation de probiotiques	Thèse MENRT	ACTN29

Tableau 1 – Liste chronologique des contrats de recherche et production scientifique associée.

1. Pour le détail des références bibliographiques, se référer à la page 69 (partie "Production scientifique")

Le contexte des IUT a aussi fortement influencé mon parcours. En effet, ce fut un investissement de chaque jour pour réussir à concilier les contraintes importantes de charges administratives et pédagogiques avec mon activité de recherche. Cette difficulté a été amplifiée en début de carrière par les spécificités du département GCGP de Saint-Quentin ("double" délocalisation, peu de titulaires, professionnalisation importante, responsabilité administrative, ...). Toutefois, je pense pouvoir dire que ces contraintes ont positivement contribué aux résultats de mes recherches obtenus pendant ces années. En effet, cela m'a permis de prendre plus d'assurance dans la responsabilité de mes fonctions, d'étendre l'éventail de mes missions, ainsi que d'être plus autonome et efficace.

Ainsi, les travaux présentés dans cette synthèse sont fortement influencés par le contexte particulier mais formateur dans lequel j'ai évolué durant ces 13 années. Il m'a semblé qu'après avoir découvert toutes les facettes du métier d'Enseignant-Chercheur, qu'après avoir participé à l'encadrement d'étudiants et ayant réussi à stabiliser ma production scientifique, le temps était venu de demander l'Habilitation à Diriger des Recherches.

Première partie

Activités de recherche

1 Congélation et cristallisation

1.1 Bibliographie

1.1.1 Principes de cristallisation

La cristallisation est un phénomène thermophysique important durant lequel une phase solide dispersée apparaît et se développe dans un milieu liquide sursaturé. Ce phénomène se décompose en deux étapes : la nucléation et la croissance de cristaux. Ce processus est mis en oeuvre dans beaucoup de domaines industriels comme la pharmacie, la chimie de spécialité, la cosmétique ou l'industrie pétrolière. La cristallisation est une étape essentielle, influençant directement les propriétés du produit final comme la distribution de tailles des cristaux ou leur morphologie [2].

L'étape de nucléation est la germination de nouveaux cristaux et se produit, soit dans une solution sans cristaux préexistants (nucléation primaire), soit en présence de cristaux de même nature que le solide qui cristallise (nucléation secondaire). La nucléation primaire peut être soit homogène (la solution ne contient pas de particules étrangères ou de cristaux), soit hétérogène (des particules ou surfaces étrangères sont présentes). La force motrice de la nucléation est la sursaturation, souvent exprimée comme la différence entre la concentration en soluté et la concentration en soluté à l'équilibre à la température et à la pression considérée.

L'étape suivante est la croissance des cristaux, tant que la solution reste sursaturée. Les germes apparus lors de la nucléation fournissent désormais un support stable sur lequel la matière se dépose. Le mécanisme de croissance se décompose en deux étapes : le transfert de matière du liquide vers la surface du cristal solide, puis l'incorporation des unités de croissance dans les faces. Toutefois, la nucléation et la croissance de cristaux peuvent se produire simultanément. En outre, les germes initialement formés peuvent être très nombreux, provoquant la limitation de la croissance de chaque cristal. Par conséquent, la compétition entre ces deux étapes va définir la distribution de taille des cristaux.

1.1.2 Cristallisation de l'eau

Dans le cas de la cristallisation d'un milieu fondu, et plus spécifiquement de l'eau, la solution est sursaturée si la température de la phase liquide est plus faible que celle du point de fusion. Dans ce cas, on parle de sous-refroidissement ou surfusion (différence entre la température de nucléation et la température d'équilibre liquide/solide). Les cinétiques de cristallisation de l'eau, aussi appelée congélation, se décomposent en trois étapes (Figure 1) : pré-refroidissement, changement d'état et refroidissement final.

2. Puel *et al.*, Cristallisation - Aspects théoriques. Techniques de l'Ingénieur, J2 710, 1–18, 2015.

Lors de l'étape de pré-refroidissement (A-B), la température du produit diminue et l'échantillon liquide passe d'un état stable à un état métastable. Au point B, la température de nucléation T_N est inférieure à celle du début de la congélation (ou température de fusion) T_F au point C : c'est la surfusion. Elle est caractérisée par la persistance de la phase liquide dans un domaine qui, à l'équilibre thermodynamique, devrait être solide. A un certain degré de sous refroidissement ΔT, une barrière énergétique est franchie. De petits agrégats transitoires de molécules d'eau se forment et se désagrègent continuellement, jusqu'à la formation d'un germe cristallin de taille critique pour pouvoir entraîner la transformation en glace de l'échantillon. La température augmente alors rapidement à cause du dégagement de chaleur latente (B-C). C'est alors le phénomène de nucléation. La croissance des cristaux se poursuit à température constante pour l'eau pure (plateau C-D). Enfin, la température de l'échantillon s'équilibre avec le système réfrigérant (D-E).

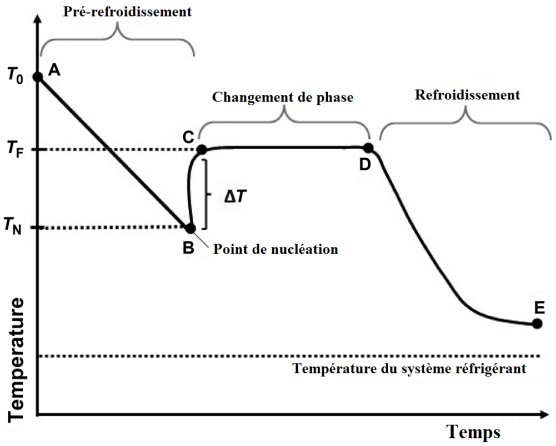

FIGURE *1 – Courbe caractéristique de congélation.*

Ainsi, les deux étapes clés de la congélation sont la nucléation et la croissance des cristaux de glace. Le sous-refroidissement est la force motrice de la nucléation. Selon Burke *et al.* [3], chaque degré de sous-refroidissement multiplie le taux de nucléation par 10. Cependant, la nucléation de la glace se produit de façon spontanée et stochastique dans une vaste gamme de températures. Elle est affectée par plusieurs facteurs comme : les impuretés, les aspérités, les propriétés de surfaces, etc. En général ces facteurs ne peuvent pas être facilement contrôlés.

La vitesse de croissance des cristaux est, quant à elle, liée à la capacité d'évacuer la chaleur au niveau des cristaux de glace en formation. Elle est gouvernée par deux processus physiques bien distincts, la libération de chaleur de la surface du cristal au sein du liquide (transfert de chaleur) et la diffusion des molécules d'eau de la phase liquide vers la surface du cristal (transfert de matière). Les caractéristiques du produit telles que sa composition, ses dimensions ou son emballage, peuvent également affecter les vitesses de croissance [4].

1.1.3 Caractérisation thermophysique

Au cours de la congélation, les propriétés thermophysiques du milieu évoluent. Ces données sont importantes puisqu'elles conditionnent les modèles de simulation et les calculs de dimensionnement. De façon générale, l'enthalpie massique chute brutalement lors de la congélation. A l'effet

3. Burke and Bryant, Water relations of foods, chapter Water in plant tissues and frost hardiness, pages 111–135, New York Academic Press, 1975.

4. Hamdami *et al.*, Simulation of coupled heat and mass transfer during freezing of a porous humid matrix. International Journal of Refrigeration, 27(6), 595–603, 2004.

de refroidissement de l'échantillon (chaleur sensible) s'ajoute la chaleur latente par la formation de la glace. La masse volumique diminue également au cours de la congélation proportionnellement à l'augmentation de volume de la glace. La conductivité thermique du produit augmente car la conductivité thermique de la glace est quatre fois plus élevée que celle de l'eau. Enfin, la proportion d'eau congelée augmente quand la température diminue. Au delà d'une certaine température limite, le pourcentage d'eau congelée n'évolue plus. Il reste une certaine quantité d'eau non congelée en raison de la très forte viscosité de l'adsorbat et des diverses liaisons entre les molécules d'eau et la matière solide non dissoute, on parle d'eau liée à la matrice. Aux températures très basses, il y a soit formation d'un eutectique, soit transition vers un état vitreux.

La plupart de ces propriétés sont fortement discontinues autour de la température de congélation commençante, rendant parfois les mesures expérimentales difficiles autour de ce point. Nombreux sont les travaux qui traitent des mesures de propriétés thermophysiques d'échantillons de part et d'autre du point de congélation. Les techniques les plus couramment utilisées sont sans doute la calorimétrie différentielle et la méthode flash en régime transitoire pour leur simplicité. Les dernières tendances s'orientent vers des méthodes inverses pour identifier simultanément l'ensemble de ces propriétés [5, 6].

1.1.4 Procédés usuels de congélation

Dans le domaine alimentaire, il est généralement admis que plus la congélation est rapide, plus les cristaux sont petits et meilleure est la qualité du produit congelé [7, 8]. Lorsque la vitesse de congélation est lente, on peut considérer que la température de l'échantillon est proche de celle de l'équilibre liquide-solide, il en résulte un nombre réduit de cristaux de grande taille. La formation de gros cristaux peut engendrer un certain nombre de changements indésirables dans la structure du produit congelé, tel qu'un stress mécanique qui peut endommager le tissu cellulaire des aliments [9], la déstabilisation des émulsions [10] ou la synérèse des gels [11].

Cependant dans certains domaines, la formation de cristaux de grande taille est préconisée. C'est le cas pour des applications de cryo-concentration où la pureté du solide sera considérablement améliorée à faible vitesse de refroidissement [12]. C'est également le cas en lyophilisation, procédé de déshydratation où la congélation est la première étape du cycle. Les caractéristiques morphologiques et la distribution de tailles des cristaux de glace ont une influence considérable sur la durée de l'étape de sublimation et sur certaines caractéristiques physiques du lyophilisat [13].

5. Simpson and Cortés, An inverse method to estimate thermophysical properties of foods at freezing temperatures : apparent volumetric specific heat. Journal of Food Engineering, 64(1), 89–96, 2004.

6. Cornejo *et al.*, Inverse method for the simultaneous estimation of the thermophysical properties of foods at freezing temperatures. Journal of Food Engineering, 191, 37–47, 2016.

7. Chevalier *et al.*, Freezing and ice crystals formed in a cylindrical food model : part i. freezing at atmospheric pressure. Journal of Food Engineering, 46, 277–285, 2000.

8. Olivera and Salvadori, Effect of freezing rate in textural and rheological characteristics of frozen cooked organic pasta. Journal of Food Engineering , 90(2), 271–276, 2009.

9. Ngapo *et al.*, Freezing and thawing rate effects on drip loss from samples of pork. Meat Science, 53(3), 149–158, 1999.

10. Degner *et al.*, Influence of freezing rate variation on the microstructure and physicochemical properties of food emulsions. Journal of Food Engineering, 119(2), 244–253, 2013.

11. Freschi *et al.*, Impact of freezing and thawing processes on wheat and potato starch gel syneresis. Starch - Stärke, 66(1-2), 208–215, 2013.

12. Rich *and al.*, Sea water desalination by dynamic layer melt crystallization : Parametric study of the freezing and sweating steps. Journal of Crystal Growth, 342(1), 110–116, 2012.

13. Saclier *et al.*, Effect of ultrasonically induced nucleation on ice crystals' size and shape during freezing in vials. Chemical Engineering Science, 65(10), 3064–3071, 2010.

Ainsi, le choix du procédé conditionne la qualité du produit fini [14]. Les procédés usuels de congélation utilisent des sources frigorifiques mécaniques ou cryogéniques. On peut les classer en fonction de la vitesse de congélation qu'ils permettent d'obtenir [15] :

- congélation ultra-rapide (vitesse > 10 cm.h^{-1}) : ces procédés reposent sur le changement d'état du fluide cryogénique (azote liquide ou dioxyde de carbone solide). Ils permettent d'obtenir des temps de congélation très courts sur des produits de petites tailles. Le coût de fonctionnement du procédé peut constituer un frein en fonction du volume et du prix de revient du produit.

- congélation rapide (vitesse de 1 à 10 cm.h^{-1}) : il s'agit essentiellement des procédés par contact direct avec une surface maintenue à basse température. On peut citer les congélateurs à plaques où le produit est comprimé entre deux parois réfrigérées, les congélateurs à lit fluidisé où le produit est soulevé et agité dans un courant d'air froid, ou encore les échangeurs à surface raclée qui permettent un renouvellement continu de la pellicule de glace formée au contact de la paroi froide.

- congélation normale (vitesse de 0,3 à 1 cm.h^{-1}) : les produits sont immergés dans des saumures. Cette technologie est souple d'utilisation, bien adaptée à des produits de taille modeste et de forme variée. Mais il faut s'assurer de l'innocuité des solutions d'immersion vis-à-vis des produits. La congélation par air pulsé est également une méthode très répandue qui consiste à ventiler les produits à congeler avec de l'air froid.

- congélation lente (vitesse $< 0{,}3$ cm.h^{-1}) : il s'agit essentiellement de chambre froide où l'air est stagnant. Cette technologie, appliquée à la congélation des fruits et légumes, est bien adaptée aux productions de grand tonnage. L'air peut être mis en circulation dans des tunnels pour améliorer l'intensité des transferts thermiques.

1.1.5 Optimisation des procédés de congélation

Depuis plusieurs décennies, les travaux de recherche en congélation se sont focalisés sur l'optimisation des procédés. L'objectif principal des travaux est d'accélérer la congélation à qualité de produits finis identique. Parmi les travaux les plus récents, différentes stratégies d'accélération ont été abordées :

(a) le couplage des technologies, par exemple du froid cryogénique et du froid mécanique. L'étape cryogénique apporte plusieurs avantages. Placée en aval de l'étape de froid mécanique, elle permet d'augmenter les capacités de production. Placée en amont, elle favorise le croûtage des produits fragiles par une pré-congélation rapide superficielle. Par ailleurs, des études ont montré que cette technique mixte est financièrement compétitive vis à vis de la congélation par immersion ou par air pulsé [16].

(b) l'amélioration des coefficients de transferts surfaciques. La technologie des jets d'air consiste à diriger de l'air à haute vélocité directement sur le produit à congeler. Elle a été étudiée comme un moyen efficace pour limiter l'épaisseur de la couche limite au voisinage du produit et donc pour augmenter l'efficacité du transfert de chaleur [17, 18]. Basée sur le même principe, la

14. Hossein and Sun, Water crystallization and its importance to freezing of foods : A review. Trends in Food Science and Technology, 22(8), 407–426, 2011.

15. Chassagne-Berces *et al.*, Congélation de produits végétaux - maîtriser la qualité des fruits congelés. Techniques de l'Ingénieur, F6 277, 2013.

16. Chourot *et al.*, Technical and economical model for the freezing cost comparison of immersion, cryomechanical and air blast freezing processes. Energy Conversion and Management, 44(4), 559–571, 2003.

17. Lanoisellé *et al.*, Application de la technologie des jets d'air à la surgélation des denrées alimentaires. Revue Générale du Froid, 1048, 41–48, 2004.

18. Soto and Bórquez, Impingement jet freezing of biomaterials. Food Control, 12(8), 515–522, 2001.

congélation par hydrofluidisation consiste à fluidiser le produit dans une saumure. Le procédé repose sur une grande turbulence réalisée entre le produit à traiter et le milieu [19]. Pour les deux technologies, les temps de congélation sont considérablement réduits grâce à des coefficients de transferts élevés. Ces deux technologies peuvent fonctionner en continu et les coûts d'investissement sont relativement faibles.

(c) l'étude de nouveaux fluides réfrigérants diphasiques. Il s'agit d'utiliser la chaleur latente du système réfrigérant diphasique pour améliorer l'intensité des transferts. Pour les équilibres liquide/vapeur, des mélanges azéotropiques avec un point d'ébullition compris entre -40 ° C et -80 ° C ont été développés pour des applications de congélation très rapide [20]. Les auteurs ont montré que ces mélanges avaient de bons niveaux de performances, qu'ils étaient compétitifs en terme de coût de fonctionnement et que leur contribution à l'effet serre (déterminée par le calcul du pouvoir de réchauffement global) était très faible. Pour les équilibres liquide/solide, de nombreux travaux ont montré l'efficacité des coulis à changement de phase. Il s'agit de micro-cristaux dispersés dans un fluide porteur qui permettent d'obtenir une puissance frigorifique élevée du fait du changement d'état [21].

(d) l'ajout de composés limitant la croissance des cristaux de glace. A titre d'exemple, il a été récemment montré que l'acétate de zirconium exerçait un contrôle sur la croissance des cristaux de glace et plus particulièrement sur leur morphologie [22]. Les cristaux observés après ajout de cette substance s'avèrent très réguliers. En revanche, sans ajout d'acétate de zirconium, les cristaux de glace ne présentent pas de régularité particulière (Figure 2).

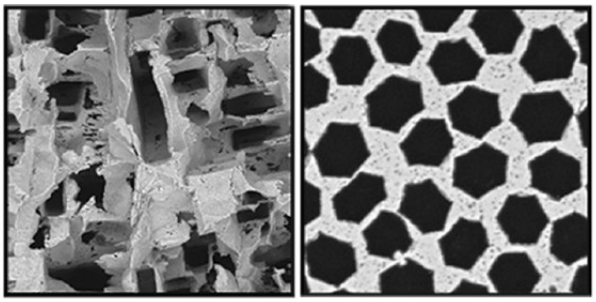

FIGURE *2 – Influence de l'acétate de zirconium sur la morphologie des pores (en noir) après sublimation des cristaux de glace* [22]*. A gauche, sans ajout d'acétate de zirconium ; à droite, avec ajout.*

1.1.6 Contrôle de la nucléation

Depuis une dizaine d'années, les efforts de recherche en congélation se sont portés sur le contrôle de la nucléation en vue d'optimiser les procédés industriels grâce à l'apport de nouvelles technologies. La partie bibliographique qui suit se focalise essentiellement sur l'apport de nouvelles technologies appliquées aux procédés de congélation. L'objectif visé est la maîtrise de la température de surfusion pour s'affranchir de son caractère stochastique difficilement acceptable à l'échelle industrielle.

19. Verboven *et al.*, Surface heat transfer coefficients to stationary spherical particles in an experimental unit for hydrofluidisation freezing of individual foods. International Journal of Refrigeration, 26(3), 328–336, 2003.

20. Cox *et al.*, New high pressure low-gwp azeotropic and near-azeotropic refrigerant blends. International Refrigeration and Air Conditioning Conference, paper 987, 2008.

21. Torres *et al.*, Surface heat transfer coefficients for refrigeration and freezing of foods immersed in an ice slurry. International Journal of Refrigeration, 28(7), 1040–1047, 2005.

22. Deville *et al.*, Ice-structuring mechanism for zirconium acetate. Langmuir, 28 (42), 14892–14898, 2012.

Congélation par champ magnétique

La présence d'un champ magnétique permet d'abaisser la température du produit sans cristalliser l'eau, la vibration transmise aux molécules d'eau les empêche de cristalliser. L'arrêt du champ magnétique entraîne la congélation instantanée du produit, censée induire une congélation flash uniforme.

D'un point de vue technologique, il existe trois méthodes pour appliquer les champs magnétiques : les champs magnétiques statiques, les champs à résonance magnétique et les champs magnétiques pulsés [23]. A titre d'exemple, on peut citer les travaux de Mohanty [24] qui a développé un système de congélation par champ magnétique statique. La figure 3 montre l'influence du traitement par champ magnétique sur l'accélération de la congélation.

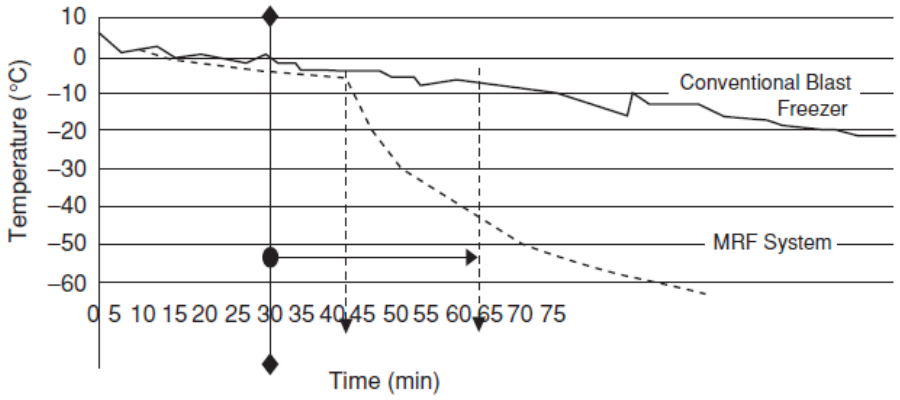

FIGURE *3 – Evolution de la température en fonction du temps lors de la congélation par deux méthodes : air pulsé et champ magnétique* [24].

Il est toutefois important de noter que l'efficacité des champs magnétiques en congélation sur l'amélioration de la qualité du produit n'a pas été clairement démontrée à ce jour. De plus, la littérature fait état de nombreux résultats contradictoires pour expliquer le comportement de l'eau dans un champ magnétique [25].

Congélation par champ électrique

Plusieurs études ont montré les bénéfices apportés par un traitement électrique pendant l'étape de refroidissement. L'application d'un champ électrique permet d'améliorer le niveau d'organisation moléculaire de l'eau, qui se rapprocherait de la structure de la glace. elle permet ainsi de mieux contrôler le degré de surfusion et donc de maîtriser l'apparition des nucléi.

Il existe différentes méthodes d'electro-congélation. Orlowska *et al.* [26] ont appliqué un traitement électrique continu de 10 kV (correspondant à 5000V.cm^{-1}) sur de l'eau distillée. Ils ont pu mettre en évidence que le retard à la cristallisation et le degré de sous-refroidissement pouvaient être réduits avec un champ électrique (Figure 4). De plus, ils ont montré qu'il était possible de contrôler le pourcentage de succès de la nucléation à une température spécifique en faisant varier

23. Dalvi *et al.*, Review on the control of ice nucleation by ultrasound waves, electric and magnetic fields. Journal of Food Engineering, 195, 222–234, 2017.
24. Mohanty, Magnetic resonance freezing system. AIRAH Journal, 55(6), 28–29, 2001.
25. Otero *et al.*, Effects of magnetic fields on freezing : Application to biological products. Comprehensive Reviews in Food Science and Food Safety, 15(3), 646–667, 2016.
26. Orlowska *et al.*, Controlled ice nucleation under high voltage DC electrostatic field conditions. Food Research International, 42(7), 879–884, 2009.

la tension appliquée.

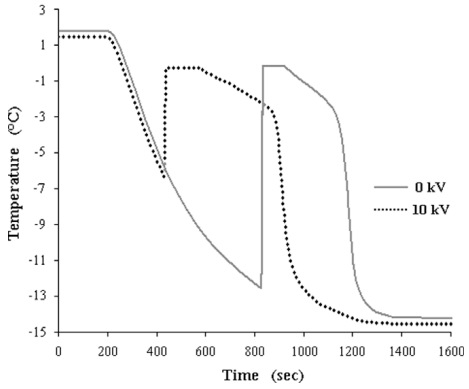

FIGURE *4 – Evolution de la température en fonction du temps de l'eau distillée ; sans traitement électrostatique (trait continu), avec traitement électrostatique (trait discontinu)* [26].

Ben Ammar *et al.* [27] ont réalisé un pré-traitement des tissus végétaux par champ électrique pulsé de faible intensité (400-580 V.cm^{-1}). Un gain significatif de temps de congélation et de lyophilisation ont été obtenus et les produits traités ont un meilleur aspect visuel.

Plus récemment, Xanthakis *et al.* [28] ont étudié la faisabilité d'un procédé de congélation assistée par micro-ondes. Les résultats sont prometteurs, puisqu'une diminution significative de la taille des cristaux et du degré de sous-refroidissement ont été constatés avec la puissance des micro-ondes. Des travaux très récents [29] s'intéressent à la modélisation de ce procédé pour mieux expliquer les phénomènes encore mal compris.

Congélation par détente de pression

D'après le diagramme de phase de l'eau (figure 5), la température de fusion d'eau diminue lorsqu'on augmente la pression, atteignant -21 °C à 210 MPa ; au-dessus de cette pression, la tendance contraire est observée. Le processus de congélation sous pression est indiqué sur le schéma de la figure 5 par le chemin $A \rightarrow B \rightarrow C \rightarrow D \rightarrow E$. Le produit est d'abord maintenu à l'état liquide en dessous de 0 °C à haute pression $A \rightarrow B \rightarrow C$. Le changement de phase se produit lors de la détente rapide $C \rightarrow D$ qui entraîne une surfusion importante [30].

En raison de ce niveau important de surfusion, la formation des cristaux de glace est instantanée et homogène dans tout le volume du produit. Des travaux sur différents produits congelés, in-

27. Ben Ammar *et al.*, Effect of a pulsed electric field and osmotic treatment on freezing of potato tissue. Food Biophysics, 5(3), 247–254, 2010.

28. Xanthakis *et al.*, Development of an innovative microwave assisted food freezing process. Innovative Food Science & Emerging Technologies, 26, 176–181, 2014.

29. Sadot *et al.*, Modélisation d'un procédé de congélation assistée par micro-ondes. Congrès Français de Thermique, Toulouse, Juin 2016.

30. Le Bail *et al.*, High pressure freezing and thawing of foods : a review. International Journal of Refrigeration, 25(5), 504–513, 2002.

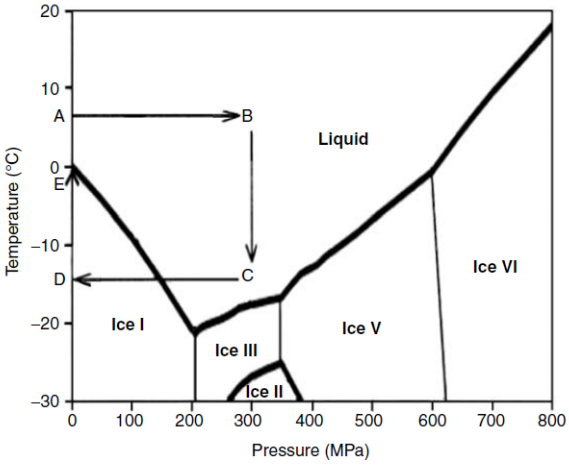

FIGURE *5 – Procédé de congélation haute pression fondé sur le diagramme de phase de l'eau.*

cluant la viande [31], les émulsions [32] et les légumes [33, 34], ont permis de montrer que la congélation haute pression améliorait la qualité de ces produits. Ceci est illustré sur la figure 6 où est représentée la distribution cumulée du diamètre des cristaux de glace dans un gel de gélatine pour différentes conditions de congélation : air convectif (CAF), immersion dans un liquide (LIF), et relâchement de pression de 100, 150 et 200 MPa. La distribution resserrée de la granulométrie aux hautes pressions est attribuée, d'après les auteurs [35], au fort degré de sous refroidissement durant et après le relâchement rapide de pression (3 secondes). Néanmoins, le procédé de congélation par relâchement de pression demeure relativement coûteux et fonctionne uniquement en mode batch, ce qui limite le rendement potentiel.

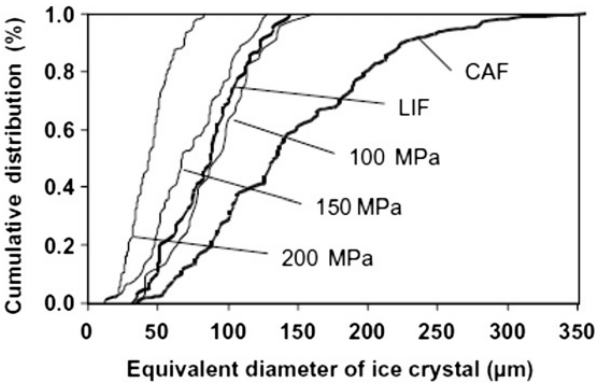

FIGURE *6 – Distribution cumulée de la taille moyenne des cristaux de glace dans un gel de gélatine pour différentes conditions de congélation : air convectif (CAF), immersion dans un liquide (LIF), et relâchement de pression de 100, 150 et 200 MPa* [35].

31. Martino *et al.*, Size and location of ice crystals in pork frozen by high-pressure-assisted freezing as compared to classical methods. Meat Science, 50(3), 303–313, 1998.

32. Lévy *et al.*, Freezing kinetics of a model oil-in-water emulsion under high pressure or by pressure release. Impact on ice crystals and oil droplets. LWT - Food Science and Technology, 32(7), 396–405, 1999.

33. Fuchigami *et al.*, High-pressure-freezing effects on textural quality of carrots. Journal of Food Science, 62(4), 804–808, 1997.

34. Koch *et al.*, Pressure-shift freezing and its influence on texture, colour, microstructure and rehydration behaviour of potato cubes. Food/Nahrung, 40(3), 125–131, 1996.

35. Zhu *et al.*, Ice-crystal formation in gelatin gel during pressure shift versus conventional freezing. Journal of Food Engineering, 66(1), 69–76, 2005.

Concernant la modélisation de la congélation par relâchement de pression, il existe deux grandes approches. Dans la première catégorie de modèles, on s'intéresse aux variations des propriétés de l'eau le long de sa courbe d'équilibre. La glace est supposée se former instantanément après l'expansion adiabatique du liquide. Le calcul de la quantité de glace est alors basé sur la variation du volume spécifique du mélange eau/glace avec la pression [36, 37]. Dans cette approche, l'état métastable n'est donc pas pris en compte, bien que constaté expérimentalement. La deuxième catégorie de modèles développés dans la littérature tient compte du sous-refroidissement et est basée sur un bilan énergétique : la quantité de chaleur, soudainement dégagée lors de la nucléation, ne peut pas être évacuée par le système réfrigérant et est donc absorbée par le milieu sous forme de chaleur sensible [38]. Ces modèles permettent d'estimer la quantité de glace formée et de calculer des temps de congélation. La plus grande difficulté rencontrée consiste à déterminer les propriétés thermophysiques du milieu à haute pression.

1.1.7 Positionnement de mes travaux

C'est dans ce contexte général que j'ai développé mes activités de recherche sur la cristallisation au cours des douze dernières années. La synthèse de mes travaux sera découpée en deux grandes parties :

- les travaux traitant de la mise en oeuvre de la congélation pour différents types de produits. Dans cette catégorie, différents procédés de congélation (congélation convective, congélation sous vide et congélation sur paroi froide) sont optimisés en vue de maîtriser la qualité finale du produit et/ou accélérer les cinétiques de congélation.
- les travaux traitant de la nucléation des cristaux. Les bénéfices apportés par les nouvelles technologies (ultrasons), par l'intensification de procédés (cristallisation/décantation), ou l'optimisation de phases (cristallisation en émulsion) seront abordés. Nucléation et croissance cristalline étant intimement liées, ces deux mécanismes pourront être abordés dans cette partie, même si l'accent a été mis sur la naissance des cristaux.

36. Sanz *et al.*, Freezing processes in high-pressure domains. International Journal of Refrigeration, 20(5), 301–307, 1997.

37. Chevalier *et al.*, Evaluation of the ice ratio formed during quasi-adiabatic pressure shift freezing. High Pressure Research, 21(5), 227–235, 2001.

38. Otero and Sanz. High-pressure shift freezing. Part 1. Amount of ice instantaneously formed in the process. Biotechnology Progress, 16(6), 1030–1036, 2000.

1.2 Etude et optimisation des procédés de congélation

1.2.1 Congélation convective de crèmes glacées industrielles

Ce travail a été réalisé au cours de ma thèse (2000-2003) sous la direction de Pr. Julien Andrieu et Pierre Laurent et a été financé par un contrat CIFRE de Nestlé R&D (Beauvais) avec le LAGEP de l'Université Claude Bernard Lyon1.

Contexte

Comme pour tous les produits surgelés, le procédé de congélation joue un rôle primordial dans la qualité finale du produit. Cette caractéristique est d'autant plus importante pour les crèmes glacées qu'elles sont consommées à l'état congelé.

La congélation est donc au coeur de la technologie des crèmes glacées. Traditionnellement, elle s'effectue en deux étapes :

- Lors de la première étape, le mix est foisonné et précristallisé dans un échangeur thermique à surface raclée (freezer). Il sort de cette étape à une température comprise entre –2 ° C et –8 ° C, avec environ 50% de l'eau totale congelée en glace. Cette température est dictée par la formulation du produit et par la qualité finale désirée.

- Au cours de la seconde étape, le produit est mis en forme et congelé jusqu'au moins –18 ° C à coeur. Cette dernière étape est réalisée soit en tunnel d'air froid pulsé pour des produits emballés, soit dans des solutions de saumure pour des produits moulés. Dépendant du volume et de la forme du produit, la durée de l'étape de durcissement varie de quelques minutes à plus d'une heure.

L'enjeu de ce travail a été d'optimiser l'étape de durcissement en fonction de la qualité finale de la crème glacée. Outre le volume du produit, la vitesse de durcissement dépend typiquement de la température du produit en sortie de freezer donc de son taux de nucléation initial, de sa formulation et en particulier de sa porosité, de ses propriétés thermophysiques et de la qualité de l'échange thermique avec le milieu réfrigérant. Une étude numérique a été développée afin de prédire les temps de congélation et de corréler les cinétiques de congélation aux tailles moyennes de cristaux.

Détermination des propriétés thermophysiques

La modélisation du comportement de la crème glacée au cours de la congélation nécessite la connaissance d'un certain nombre de paramètres physico-chimiques dont les propriétés thermophysiques. L'analyse bibliographique a montré qu'il était difficile de trouver des données sur la crème glacée industrielle. Elles ont donc été mesurées expérimentalement, à partir de dispositifs couramment utilisés dans le domaine agro-alimentaire.

A titre d'exemple, les mesures de conductivité thermique ont été réalisées par la méthode transitoire de la sonde à choc, bien adaptée aux échantillons congelés. Les différents essais (figure 7) ont permis de mettre en évidence l'influence de la température sur la conductivité thermique équivalente des crèmes glacées foisonnées. En effet, de manière générale, la conductivité thermique augmente lorsque la température diminue. Ceci s'explique par l'apparition de la glace lors de la congélation, puisque celle-ci présente une conductivité thermique intrinsèque quatre fois plus grande que celle de l'eau liquide. Par ailleurs, la conductivité diminue avec l'augmentation du taux de foisonnement, en raison des propriétés isolantes de l'air. En parallèle des essais expérimentaux, un modèle prédictif a été développé. Il est le résultat de la combinaison de trois

modèles élémentaires de conductivité thermique (modèle parallèle pour modéliser la phase continue, modèle de De Vries qui caractérise la dispersion des cristaux de glace, modèle de Maxwell pour définir la dispersion des bulles d'air). Étant donné le caractère physique de la modélisation ainsi que la bonne adéquation des valeurs prédites avec les mesures expérimentales (figure 7), le modèle a pu être étendu avec confiance à différentes formulations de crème glacée dès l'instant que la composition et la structure étaient connues.

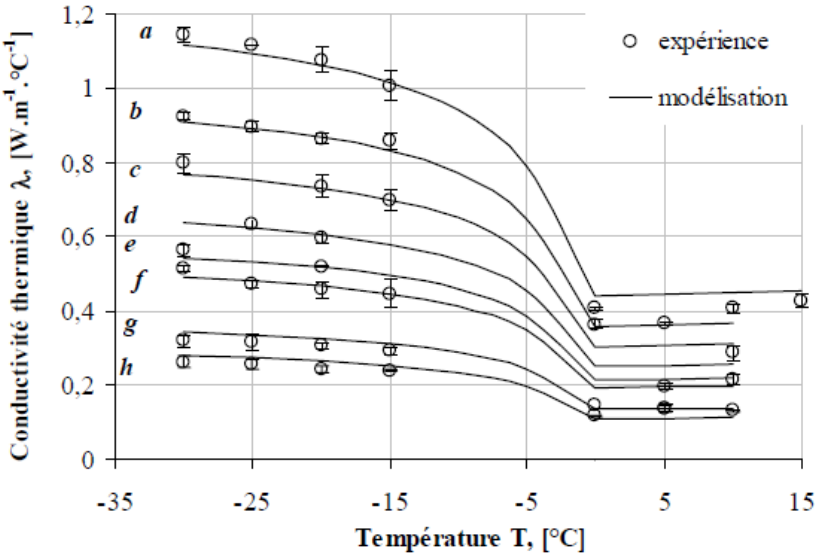

FIGURE 7 – *Influence de la porosité sur la conductivité thermique de la crème glacée. Cercles : valeurs expérimentales – Lignes continues : modélisation. Porosité : (a) 0%, (b) 13%, (c) 23%, (d) 33%, (e) 41%, (f) 46%, (g) 60%, (h) 67%.*

Publication associée : [ACL1] (page 79)

Modélisation des cinétiques de congélation

L'objectif de la modélisation est de déterminer les cinétiques de congélation lors de l'étape de durcissement, afin de prédire les temps de congélation (temps nécessaire pour atteindre -18 °C au coeur du produit). Elle est basée sur la résolution de l'équation de la chaleur, dans laquelle le transfert par conduction et le changement de phase ont été pris en compte. Le modèle tient compte du taux de glace initial par l'intermédiaire des propriétés thermophysiques de la crème glacée, de la géométrie de l'échantillon (bâtonnet, vrac, ...), des conditions de refroidissement (saumure ou air pulsé) grâce à un coefficient d'échange convectif défini aux limites du produit et des conditions initiales de l'échantillon (correspondant aux conditions de fin de glaçage). L'approche que nous avons retenue pour simuler le changement d'état de l'eau liquide en glace est celui du modèle à une zone avec une capacité calorifique apparente. Ainsi, cette grandeur tient compte à la fois de l'augmentation de la chaleur sensible et de la chaleur latente de changement d'état. Le coefficient d'échange convectif a été le paramètre le plus délicat à estimer dans les conditions industrielles (tant d'un point de vue théorique que pratique) et est la principale source d'incertitude du modèle. Les résultats numériques ont d'abord été validés à partir de profils expérimentaux de température obtenus en congélation statique unidirectionnelle, puis à partir des courbes expérimentales de congélation de crème glacée dans des conditions semi-industrielles telles que le durcissement de bâtonnets moulés en saumure ou de vracs en chambres d'air froid pulsé.

La bonne représentativité du modèle a permis de tester l'influence des différents paramètres de

congélation – température initiale de la crème glacée, taux d'air, température du milieu réfrigérant, mode de congélation – sur les cinétiques de congélation. La diminution de la température initiale de la crème glacée ainsi que celle du milieu de réfrigération ambiant ont pour effet d'accélérer de façon significative la congélation de l'échantillon. En revanche, en agissant à la fois sur la densité du produit et sur la conductivité thermique, l'effet du foisonnement sur les cinétiques de congélation est plus difficile à mettre en évidence. De façon générale, en fonction du mode de refroidissement et de la géométrie du produit, l'ajout d'air peut soit freiner, soit accélérer, soit n'avoir aucune incidence sur les temps de congélation.

Publication associée : [ACL2] (page 90)

Caractérisation de la structure

En vue de corréler les conditions opératoires du procédé de fabrication à des critères physiques de qualité du produit (taille des cristaux de glace et des bulles d'air), la caractérisation de la structure de la crème glacée a été effectuée pour différentes conditions de congélation. Trois méthodes d'analyses par microscopie optique ont été étudiées et comparées : la microscopie optique par transmission après dispersion de l'échantillon dans un solvant adapté à la phase que l'on souhaite conserver, la microscopie électronique à balayage après lyophilisation de l'échantillon et la microscopie optique par réflexion en observant directement et in situ la surface d'une coupe de crème glacée. La comparaison de ces trois méthodes conduit aux mêmes tendances.

Un des paramètres les plus importants dans la qualité finale de la crème glacée est la température de sortie de freezer, correspondant à la température initiale de la crème glacée en début de durcissement. Ce critère détermine non seulement la taille mais également la morphologie des cristaux de glace, comme le montre la figure 8. Lorsque la fraction de glace en sortie de freezer est faible, correspondant à une température initiale d'échantillon élevée (-1 $^\circ$ C, très proche du point de congélation commençante), le changement d'état liquide – solide de l'eau se produit principalement au cours de l'étape ultérieure de durcissement. La propagation du front de congélation contraint les cristaux de glace à croître avec une morphologie dendritique dans la même direction que le flux de chaleur. A l'inverse, lorsque la température en sortie de freezer est plus faible (-5 $^\circ$ C), le taux de glace est important puisque environ 50% de l'eau initiale est déjà congelée en glace. Ainsi, lors de l'étape de durcissement, la présence de nombreux germes cristallins limite la quantité d'eau disponible pour leur croissance ultérieure.

La quantité d'air agit à un degré moindre sur la taille des cristaux de glace. Augmenter le taux de foisonnement conduit à une meilleure répartition des cristaux de glace en réduisant les effets de recristallisation. Enfin, l'influence de la vitesse de refroidissement au cours de l'étape de durcissement est très significative sur la taille moyenne des cristaux de glace de la crème glacée « fraîche ». En revanche, l'effet est nettement moins important sur des échantillons ayant subi un vieillissement accéléré par fluctuations thermiques, censées simuler le comportement thermique standard de la crème glacée depuis sa fabrication jusqu'à sa consommation. Ces conclusions ont permis de montrer que la formulation des crèmes glacées doit être modifiée en optimisant également la formulation par ajout de stabilisants, de sucres spécifiques, ou de protéines "antifreeze".

Publication associée : [ACL3] (page 97)

Bilan de l'étude

Ce travail a d'abord permis d'établir une base de données des principales propriétés thermophysiques de crèmes glacées industrielles et de valider des modèles physiques de ces propriétés en fonction de la température, de la densité et de la formulation de la crème glacée. De plus, il

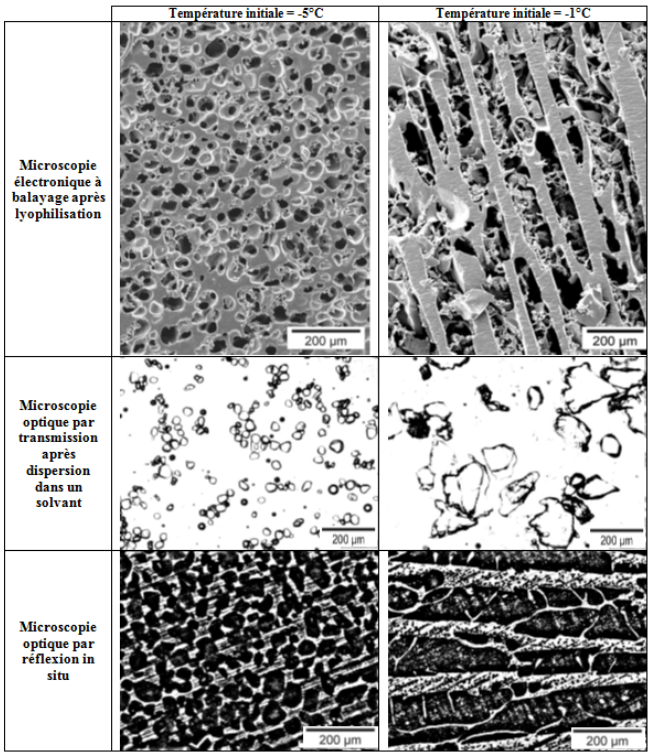

FIGURE *8 – Influence de la température initiale de durcissement sur la taille des cristaux de glace. (Porosité : 5%, T_{air} = -35 ° C).*

a permis d'établir des relations entre la qualité finale du produit et certaines conditions opératoires du procédé de fabrication. Enfin, le développement d'un modèle numérique de congélation a permis de calculer les temps de congélation et d'identifier les paramètres influents.

L'originalité de ce travail a été double :

- travailler avec un matériau complexe (mousse congelée dont la phase continue est une émulsion de matière grasse) fabriqué dans un milieu industriel après les étapes classiques de mélange, de pasteurisation, d'homogénéisation et enfin de maturation.
- convaincre des bénéfices de la modélisation où la connaissance dans ce domaine de l'agro-alimentaire était largement basée sur l'empirisme à l'époque de cette étude.

1.2.2 Congélation par évapo-détente de purées de légumes

Ce travail porte sur la surgélation par le vide de purées de légumes. Ce projet, labellisé par le pôle de compétitivité Industries et Agro-Ressources des régions Picardie et Champagne-Ardennes, a été porté par le laboratoire TMIR de l'UTC (Pr. Jean-Louis Lanoiselle) en collaboration avec le groupe Bonduelle. Ce projet a été financé par le Conseil Régional de Picardie et Bonduelle. Il a fait l'objet de la thèse de Phong-Uyen Nguyen (2006-2010).

Contexte

Le groupe Bonduelle a imaginé dès 2004 un procédé basé sur un tunnel à bande maintenu sous vide pour congeler en quelques minutes des produits divers tels que des légumes en morceaux, en purée ou en sauce [39]. Par la suite, afin d'accélérer encore la surgélation, en particulier pour des

39. Maureaux *et al.* Procédé et installation pour la préparation et conservation de denrées, brevet n° EP1632140 (A1), 2006.

produits semi-liquides ou pâteux, un procédé continu de surgélation ultra-rapide par atomisation sous vide a été envisagé.

Le principe de ce procédé (figure 9) est de pulvériser la matière première dans une enceinte sous vide maintenue à quelques millibars. Sous l'effet de la pression réduite, une partie de l'eau de constitution du produit s'évapore, ce qui entraîne un refroidissement et une congélation rapide du produit. Le contrôle des paramètres du procédé (débit et pression d'entrée du produit, pression dans la tour, teneur en eau initiale du produit) permet d'obtenir la cristallisation d'une fraction de l'eau et de rigidifier la purée. En sortie de la tour, le produit peut ensuite être formé (sous forme de galets par exemple) avant que la surgélation soit terminée dans un tunnel classique. La combinaison des phénomènes d'expansion de la vapeur d'eau et de cristallisation ultra-rapide de la glace permet d'améliorer la texture du produit et de limiter les phénomènes d'exsudation lors de sa décongélation.

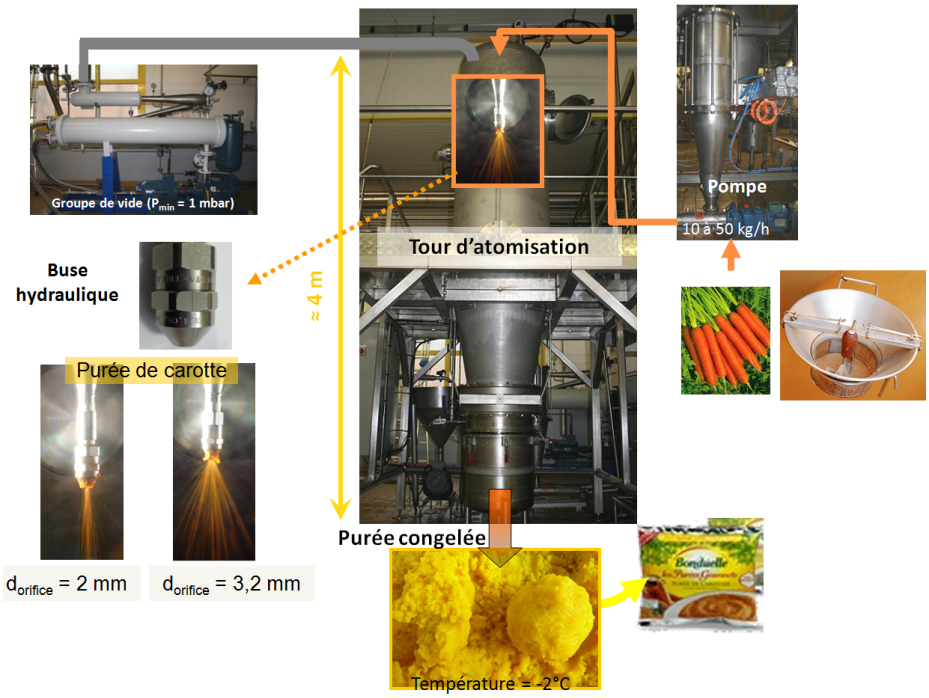

FIGURE *9 – Pilote de surgélation par le vide.*

Les études menées dans le cadre de ce projet ont porté sur la rhéologie, la caractérisation des propriétés thermophysiques, la pulvérisation, la modélisation des transferts de chaleur et de masse ainsi que la mise en oeuvre du procédé de surgélation par le vide. Les parties expérimentales ont été réalisées par l'UTC et par Bonduelle. Pour ma part, ma contribution à ce travail s'est limitée au développement du modèle de congélation, donc seule cette partie sera détaillée dans cette synthèse. L'objectif est de déterminer les cinétiques de congélation des gouttes de purée, ainsi que de connaître les paramètres du procédé influant sur les temps de congélation et les quantités d'eau évaporée. La partie nucléation n'a donc pas été abordée dans cette étude et les phénomènes de surfusion n'ont pas été pris en compte dans la modélisation. La principale difficulté dans le développement du modèle a été la connaissance des propriétés thermophysiques de la purée nécessaires pour alimenter le modèle. Certaines ont pu être mesurées expérimentalement en fonction de la température et/ou de la pression, les autres sont issues de la littérature.

Modélisation des cinétiques de congélation

Au sein de la goutte, les transferts thermiques sont essentiellement conductifs. L'approche retenue pour simuler le changement d'état est identique à celle développée dans les travaux de congélation de crèmes glacées, avec une capacité calorifique apparente. L'avantage principal de cette méthode est sa simplicité de programmation. En revanche, par cette méthode, le phénomène de surfusion expérimentalement constaté lors de la congélation de gouttes de purée n'est pas pris en compte.

En parallèle des transferts thermiques, les molécules d'eau au sein de la goutte de purée subissent la diffusion radiale gouvernée par un gradient de concentration entre le centre et la périphérie de l'échantillon. La résolution de l'équation de la chaleur couplée à l'équation de diffusion de l'eau a été réalisée avec un logiciel commercial de calcul par éléments finis, Comsol. Le développement de ce modèle en régime transitoire est basé sur l'application de différentes hypothèses en vue de simplifier l'écriture mathématique du problème sans s'éloigner des phénomènes physiques réellement mis en jeu. On a supposé notamment que l'évaporation de l'eau était uniquement surfacique et qu'il existe un équilibre entre la surface de la goutte et la vapeur environnante. Par ailleurs, le diamètre de la goutte est supposé constant, le rétrécissement éventuel de l'échantillon n'a pas été pris en compte.

Dans ces conditions, à la fois les transferts conductifs et diffusifs sont contrôlés par le flux d'eau évaporée à la surface d'une goutte de purée. Le flux massique d'évaporation est ainsi proportionnel au gradient de pression entre l'interface de la goutte et le milieu ambiant. Le flux thermique transféré à la paroi se déduit du flux massique d'évaporation connaissant la chaleur latente de vaporisation ou de sublimation, estimées expérimentalement par DSC.

La pression totale dans l'enceinte est un paramètre primordial du procédé puisqu'elle gouverne aussi bien les transferts thermiques que massiques (Figure 10). Sachant que la température de congélation commençante des purées est de -2 ° C (déterminée expérimentalement par DSC), la goutte de purée n'est pas congelée mais seulement refroidie pour une pression supérieure à 500 Pa. On retrouve ces résultats en analysant l'évolution de la quantité d'eau évaporée en fonction de la pression. Au dessous de 400 Pa, plus de 10% de la quantité d'eau initiale est évaporée. Pour des pressions supérieures à 400 Pa, la quantité d'eau évaporée n'est pas suffisante pour absorber la chaleur latente de changement d'état d'eau en glace, l'échantillon n'est donc pas congelé.

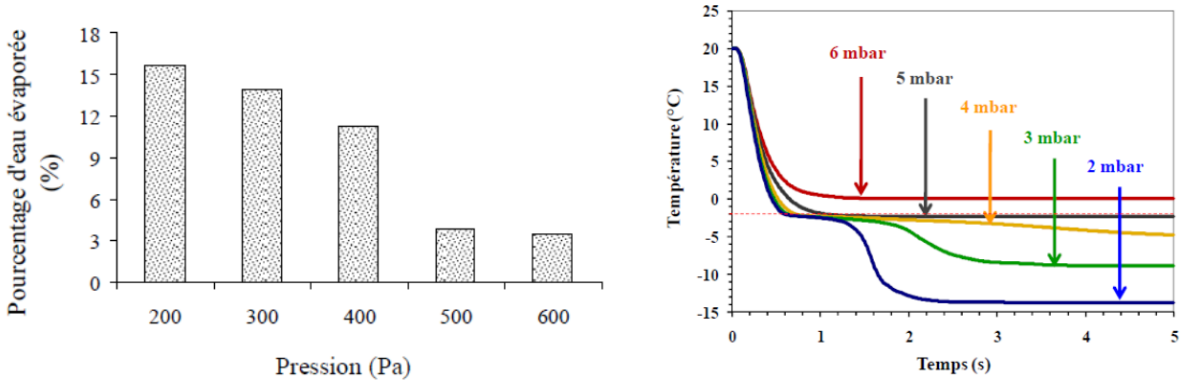

FIGURE *10 – Effet de la pression sur l'évolution de la température et du pourcentage d'eau évaporée. (Diamètre de la goutte 1 mm ; température initiale : 20 ° C).*

Publication associée : [ACL8] (page 146)

Bilan de l'étude

Ce projet a abouti à la conception d'un pilote d'atomisation permettant la surgélation ultra-rapide (2s) de purées de légumes. Des gains qualitatifs sur la perception de la texture et de la saveur du produit ont été constatés, dûs en partie au foisonnement interne du produit et à sa fine cristallisation, ce qui en fait un avantage concurrentiel. Par ailleurs, le procédé est moins gourmand en énergie que la congélation classique. D'un point de vue numérique, le modèle développé est un outil permettant aisément un transfert vers l'échelle industrielle.

1.2.3 Traitement d'eaux usées industrielles par congélation sur paroi froide

Ce travail porte sur la faisabilité d'un procédé de congélation pour le traitement d'effluents industriels. Il s'inscrit dans la continuité de deux thèses effectuées au LAGEP sur le dessalement de l'eau de mer par congélation. Ce projet a fait l'objet de la thèse de Thouaïba Htira (2012-2016), financée par une bourse MENRT et dirigée par Pr. Denis Mangin.

Contexte

Le traitement d'eaux industrielles par congélation permet d'une part d'obtenir un effluent concentré qui peut alors être recyclé dans le procédé, traité par oxydation ou incinéré à moindre coût énergétique. D'autre part, la glace obtenue par cette technique doit toutefois satisfaire les normes de rejets en vigueur. Bien que, selon la thermodynamique, les cristaux formés sont censés être purs, des impuretés peuvent être incorporées dans le réseau cristallin pour des raisons cinétiques. L'incorporation peut s'expliquer par la microstructure de la couche cristalline présentant des espaces interstitiels où le liquide peut être piégé. Les précédentes recherches effectuées au LAGEP sur le dessalement de l'eau de mer par congélation [40] étaient prometteuses et ont montré qu'une conduite optimisée du procédé permettait d'obtenir des puretés de glace satisfaisantes.

Cette technologie de séparation est proposée comme alternative à la distillation ou à la filtration et présente certains avantages [41]. La maintenance de l'ensemble du procédé est plus simple qu'avec les procédés de filtration, très sensibles au colmatage. Le procédé par congélation pose également moins de problèmes de corrosion et d'entartrage que la distillation, compte tenu des niveaux bas des températures de travail. De plus, aucun ajout de produits chimiques n'est nécessaire pour purifier l'eau, la cristallisation en milieu fondu est considérée comme un procédé "vert". Enfin, son coût d'exploitation pourrait même être inférieur à celui de la distillation.

La solution binaire eau/acétone a été choisie comme effluent modèle pour cette étude. En effet, l'acétone est une molécule très largement utilisée à l'échelle industrielle. On la retrouve notamment dans la fabrication de l'aspirine. En général, cette solution est traitée par distillation. Mais à cause des faibles teneurs en soluté, se pose la question de la rentabilité de la distillation par rapport à un procédé de traitement par congélation.

L'enjeu de ce travail a été de montrer la faisabilité technologique du procédé et de comprendre les mécanismes physiques mis en jeu lors des transferts pour limiter les phénomènes d'incorporation d'impuretés dans la glace produite. Pour cela, trois aspects ont été développés : (i) l'étude thermodynamique du mélange eau/acétone, (ii) l'étude paramétrique du procédé par la méthodologie des plans d'expériences et l'analyse microscopique, (iii) la modélisation des transferts. D'un point de vue expérimental, la principale difficulté à surmonter est d'obtenir des conditions

40. Mandri *et al.*, Parametric study of the sweating step in the seawater desalination process by indirect freezing. Desalination, 269(1-3), 142–147, 2011.

41. Jiang *et al.*, Research progress and model development of crystal layer growth and impurity distribution in layer melt crystallization : A review. Industrial & Engineering Chemistry Research, 53(34), 13211–13227, 2014.

opératoires maîtrisées et répétables. D'un point de vue de la simulation numérique, le couplage des phénomènes a nécessité un maillage très fin, des temps de calculs assez longs, et certaines configurations (notamment les simulations à fortes concentrations en soluté) n'ont pas pu être simulées à ce jour.

Élaboration du diagramme d'équilibre liquide/solide

La détermination du diagramme de phase du mélange binaire eau-acétone est nécessaire pour connaître les phases en présence ainsi que les limites en concentration et en température du domaine de travail. Il a été déterminé par calorimétrie différentielle et par méthode synthétique, puis comparé à des données bibliographiques [42]. Le diagramme obtenu (Figure 11) montre que la glace est en équilibre avec la solution à traiter dans un large domaine compris entre 0 et 30% massique en acétone, rendant possible le traitement d'effluents par congélation.

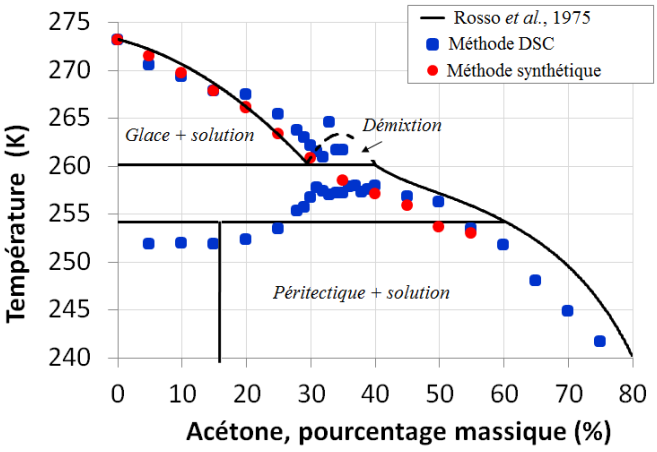

FIGURE *11 – Diagramme d'équilibre liquide/solide eau-acétone. Comparaison entre les valeurs expérimentales et les données bibliographiques (trait continu).*

Publication associée : [ACL12] (page 176)

Étude expérimentale du procédé de congélation

Pour étudier la faisabilité d'un procédé de congélation pour le traitement d'effluents industriels, nous avons choisi un procédé simple de séparation sur paroi froide, qui peut facilement être extrapolé à plus grande échelle.
Le montage expérimental (figure 12) est constitué d'une cuve cylindrique double enveloppée (2) en verre dans laquelle est plongé un doigt de gant (1) en acier inoxydable. Le système peut fonctionner selon deux modes, statique ou dynamique, grâce à une boucle de recirculation externe (7). La croissance de la glace s'effectue dans l'espace annulaire sur le doigt de gant (1), paroi froide du système. Le doigt de gant est initialement ensemencé par une fine couche de glace, ce qui permet de s'affranchir de l'étape de nucléation. Ainsi, on évite d'atteindre de forts degrés de sous refroidissement, qui entraînerait une croissance rapide et la formation de dendrites, favorisant alors l'incorporation d'impuretés dans la glace. Afin de garantir une croissance homogène de la glace, il convient de maîtriser les conditions opératoires.

L'étude systématique de l'influence des paramètres opératoires à travers l'analyse d'un plan d'expériences a mis en évidence le rôle important de la vitesse de refroidissement et surtout de la concentration initiale en acétone sur la pureté de la glace produite. Les impuretés présentes dans

42. Rosso *et al.*, Le système binaire eau-acétone, Comptes rendus hebdomadaires des séances de l'Académie des sciences, 281, 699–702, 1975.

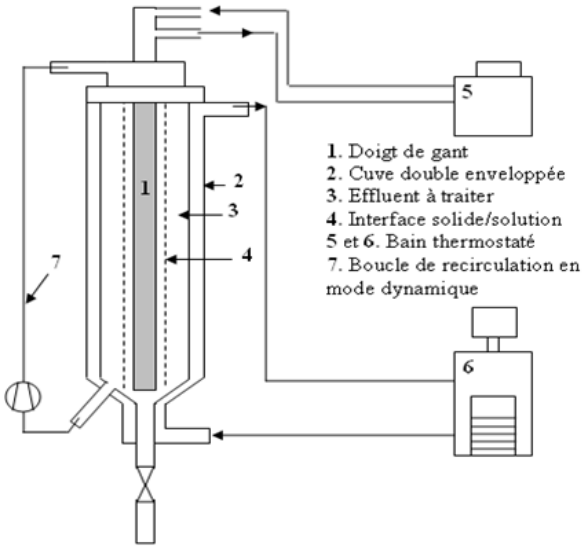

FIGURE *12 – Schéma du dispositif expérimental.*

la glace sont dues à des inclusions de poches de solution. Nous avons pu observer que l'évolution de la concentration en impuretés dans la glace produite n'est pas une fonction linéaire de la concentration initiale en acétone. Il existe donc différents phénomènes pouvant influencer le processus d'inclusion : apparition d'un gradient de concentration lié au rejet du soluté lors de la croissance de la couche de glace, existence de courants de convection dans la solution, effet des impuretés sur le mécanisme de croissance, etc.

Ce point a été confirmé par l'analyse microscopique de la glace produite. La figure 13 compare la structure de la glace pour trois concentrations initiales d'acétone (5%, 10% et 20% massique). La figure 13a montre une structure monocristalline de la glace avec quelques poches de solution très localisées. En revanche, sur les figures 13b et 13c, les impuretés sont essentiellement piégées dans les interstices entre les cristaux de glace, au niveau des joints de grains. On note par ailleurs, qu'au-delà d'une certaine épaisseur de glace formée, le taux d'incorporation des impuretés devient important ; il conviendra que la congélation ne soit pas poursuivie trop loin de manière à ne pas trop concentrer la solution au niveau de l'interface liquide/solide.

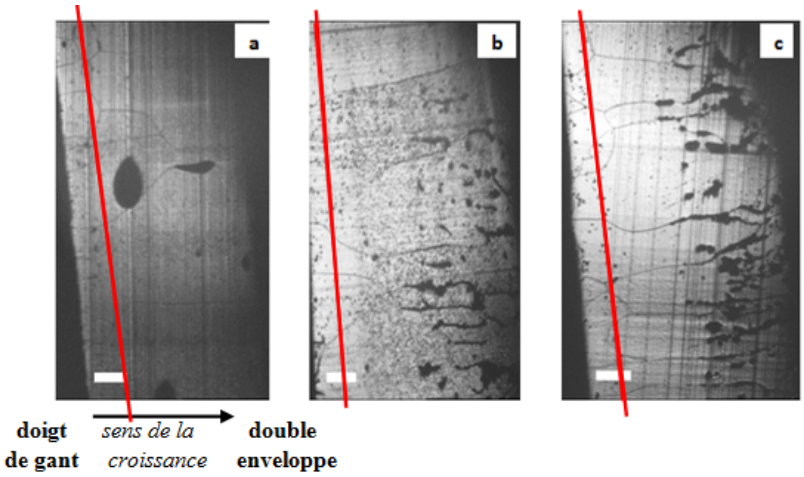

FIGURE *13 – Morphologie de la structure de la glace en fonction de la concentration initiale en acétone (pourcentage massique) ; (a) 5% ; (b) 10% ; (c) 20%. Echelle = 0,5 mm. Trait rouge = épaisseur de la pré-couche à l'étape de l'ensemencement.*

Modélisation et simulation

Afin de comprendre les phénomènes mis en jeu à l'interface glace/solution qui conditionnement la pureté finale de la glace, un modèle 2D axisymétrique du procédé de congélation en régime statique a été développé avec le logiciel COMSOL. Il s'agit d'un problème de changement de phase, couplant transfert de masse et transfert de chaleur avec une frontière mobile entre la zone liquide et la zone solide. Dans sa version la plus complexe, le modèle tient également compte des effets de la convection naturelle induit par les gradients de température et de concentration dans la solution. La résolution du système a néanmoins nécessité les deux approximations suivantes : (a) équilibre thermodynamique à l'interface solide-liquide ; (b) solide pur, rejet total du soluté à l'interface. Le modèle ne prend pas en compte la nucléation, la phase solide étant initialement présente sous forme d'une pré-couche de glace représentant l'ensemencement expérimental du doigt de gant.

La vitesse de croissance calculée avec le modèle est en adéquation avec les valeurs expérimentales. De plus, l'occurrence de mouvements de convection, tels que décrits dans la littérature, a été mise en évidence. Elle induit une déformation conique de glace, le déplacement de la solution permet également un renouvellement du soluté à l'interface liquide/solide. En effet, ces mouvements permettent une refonte locale de la glace tout en diminuant la concentration à l'interface en transportant le soluté loin de celle-ci.

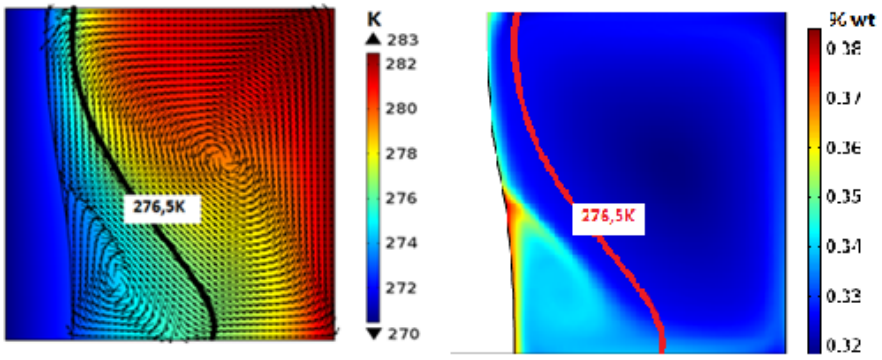

Figure 13b : Modélisation du profil de température (à gauche) et du profil de concentration (à droite).

Des comportements différents sont observés selon la concentration de la solution. L'étude du rapport des forces de volume solutale et thermique permet de montrer qu'il existe différents types d'écoulement en fonction de la nature des boucles de convection générées. L'occurrence de deux boucles de convection est notamment due à des forces thermiques et solutales qui s'opposent. Pour favoriser le renouvellement du soluté à l'interface liquide/solide, il semble préférable d'avoir des vitesses de solution importantes et donc de se placer dans une situation de forces coopérantes, où les effets de la température et de la concentration sur la masse volumique s'ajoutent.

Dans tous les cas, le modèle montre qu'il existe des courants de convection, qui permettent d'éviter d'être en situation d'instabilité de constitution (présence de liquide en surfusion, cas favorable à une croissance dentritique anarchique). L'effet exacerbé de la concentration de la solution sur la pureté de la glace produite ne semble donc pas s'expliquer par le comportement hydrodynamique et thermique de la solution. Il y aurait donc bien un changement de mécanisme d'incorporation lié à la concentration de la solution.

Publication associée : [ACL13]

Bilan de l'étude

Au cours de ce travail, nous avons étudié la faisabilité du traitement de l'eau par congélation sur paroi froide en milieu stagnant. Nous avons choisi pour notre étude, un montage pilote simple constitué d'un tube cylindrique et d'une cuve double enveloppée. Ainsi, les résultats peuvent être exploités en vue de l'application dans une géométrie multitubulaire à plus grande échelle.

D'un point de vue expérimental, les essais préliminaires et les observations de la glace ont confirmé que la couche de glace formée à partir des solutions binaires était polluée par des inclusions de solution. Les glaces les plus pures obtenues jusqu'à présent ont une concentration massique en acétone de 5,63 $g.L^{-1}$ et 4,28 $g.L^{-1}$ pour respectivement le mode statique et le mode dynamique. Par conséquent, il conviendra de purifier la couche cristalline avant sa fusion par une étape de ressuage et/ou d'opérer la congélation en deux cycles afin d'obtenir une couche de glace de concentration respectant les normes de rejet de l'eau (0,30 $g.L^{-1}$ de DCO, soit une concentration en acétone de 0,14 $g.L^{-1}$). D'autre part, si la faisabilité du procédé a été prouvée lors de cette étude, il reste à faire la preuve de sa compétitivité, notamment au niveau de la consommation énergétique.

Concernant les résultats de la simulation, le modèle a permis d'interpréter l'influence des paramètres opératoires sur les transferts de chaleur, de masse et le profil des vitesses au sein de la solution. La modélisation doit néanmoins être complétée par la prise en compte de l'incorporation d'impuretés dans la couche cristalline. Ceci pourrait impliquer la mise en oeuvre d'un modèle de type "mushy zone". On pourra alors favoriser la convergence numérique des simulations qui posent problème à ce jour, puis s'intéresser à la croissance d'une zone solide-liquide (zone pâteuse) représentée comme un milieu poreux, et se rapprocher davantage des résultats expérimentaux.

1.2.4 Étude de la lyophilisation d'une souche modèle de probiotiques

Ce travail porte sur l'étude de cycles de lyophilisation de souche modèle probiotique. Il fait l'objet de la thèse de Pierre Verlhac, démarrée en 2015, financée par une bourse MENRT et co-dirigée par Pr. Séverine Vessot et Ghania Degobert. En raison du caractère interdisciplinaire de cette thèse, le laboratoire AgroSup de Dijon, spécialisé dans la microbiologie alimentaire, est associé à ces travaux.

Contexte

La lyophilisation est l'un des procédés de stabilisation les plus respectueux de la qualité du produit. Pour les produits biologiques tels que les probiotiques, il s'agit de préserver l'activité des bactéries au cours des différentes étapes du procédé de production, notamment lors de l'étape de congélation souvent associée à une perte de viabilité importante. De plus, ce procédé est aussi connu pour ses durées de traitements longues, ses coûts très élevés et les capacités limitées des appareils, ce qui le cantonne aux produits à très haute valeur ajoutée.

Pour diminuer les coûts de la lyophilisation, il apparaît nécessaire de raccourcir les durées de cycle tout en veillant à conserver les qualités du produit. Dans cette optique, la thèse de Pierre Verlhac a pour objectif de mettre au point des formulations cryo-protectrices permettant d'améliorer la stabilité et la conservation de l'activité biologique des probiotiques lyophilisées.

Projet

Lors du procédé complexe de lyophilisation qui engendre 3 changements de phase (congélation, sublimation et désorption), les bactéries subissent de nombreux stress plus ou moins bien connus

(thermique, osmotique, sauts de pH, sous-refroidissement, cristallisation intracellulaire. . .). Ainsi, l'extrapolation au sens large d'une méthode de conservation est très compliquée en raison du caractère unique de chaque souche de bactéries. Les données de la littérature dans ce domaine étant très rares, l'objectif de notre projet est l'optimisation rationnelle d'un procédé de lyophilisation d'une souche probiotique pour réduire les effets des différents stress subis, afin d'obtenir la meilleure survie sur de longues périodes de stockage du lyophilisat final (de 12 à 24 mois).

L'approche développée se base sur l'étude de chaque étape du procédé de lyophilisation (congélation, sublimation, désorption) afin de comprendre l'influence complexe des nombreux facteurs sur le taux de survie d'une souche probiotique modèle (Lactobacillus Casei ATCC 393). Dans un premier temps, nous avons étudié l'immobilisation des cellules par inclusion ou adsorption à l'intérieur de support poreux afin de les protéger contre un environnement hostile. Notre choix s'est porté sur une matrice à base de polyvinylpyrrolidone (PVP), polymère couramment utilisé dans le domaine pharmaceutique et qui pourrait aussi avoir certaines propriétés intéressantes pour la stabilisation des probiotiques.

Diagramme de phase

La transition vitreuse, qui caractérise le passage d'un état liquide à un état solide amorphe, constitue un indicateur fiable des caractéristiques du produit. Au cours d'une opération de déshydratation comme la lyophilisation, la température de transition vitreuse varie fortement entre le début et la fin de l'opération et au sein même du produit à un instant donné. Afin de préserver les qualités du produit, il est important de ne pas la dépasser pour ne pas provoquer la fusion des cristaux de glace engendrant le collapse de l'échantillon.

Notre premier travail a donc consisté à déterminer le diagramme de phase de notre formulation, i.e. les courbes de congélation et la courbe de transition vitreuse par calorimétrie différentielle à balayage modulée, donnée thermodynamique de base qui permet de fixer de manière rationnelle les paramètres de sublimation (pression ; température) puis de désorption.

Étude expérimentale du procédé de lyophilisation

L'étude expérimentale en cours a pour but de mettre en évidence les paramètres clés du procédé. A ce jour, l'étape clé du procédé semble être la phase de congélation. En effet cette période semble être la plus létale pour les micro-organismes en raison de plusieurs phénomènes tels que le sous-refroidissement ou la cristallisation intra-cellulaire. Il est donc de première importance de bien maîtriser chaque paramètre de la congélation (vitesse, annealing, induction de la nucléation, ...) afin d'obtenir un taux de survie conséquent après cet étape, tout en optimisant la forme des cristaux afin de réduire les temps de sublimation en aval.

Les premiers résultats tendent à montrer que l'ajout de polymère dans la formulation ne permet pas d'augmenter le taux de survie des bactéries, hormis lors d'une congélation très lente. Néanmoins, cet ajout devrait permettre de prolonger le temps de conservation du lyophilisat, il sera donc important de voir comment évolue le taux de survie sur une longue période.

Bilan de l'étude et perspectives

A ce jour, les essais expérimentaux sont répétés pour consolider les premières tendances observées. Il faut souligner la difficulté du sujet, pour lequel la lourdeur des cycles de lyophilisation doit se conjuguer à la méticulosité des manipulations de microbiologie. Néanmoins, les essais de faisabilité montrent le potentiel de la démarche.

A plus long terme, la modélisation des transferts de chaleur et de matière lors de la lyophilisation permettrait de mettre au point un outil de pilotage du procédé garantissant, tout au long de l'opération, une température du produit inférieure à la température de transition vitreuse, tout en étant la plus proche possible. Ainsi, il serait envisageable de choisir le protocole le plus avantageux d'un point de vue technico-économique (par exemple, le temps de cycle le plus court) tout en s'assurant que la stabilité du produit sera préservée. Il deviendrait alors possible de moduler la température des étagères ou le niveau de vide pendant le séchage et ainsi de raccourcir de façon significative les cycles du procédé.

1.3 Contrôle de la nucléation

1.3.1 Congélation par ultrasons

Ce travail a porté sur le contrôle par ultrasons de la nucléation de la glace pour l'optimisation des procédés de congélation et de lyophilisation. Il s'inscrit dans le cadre du projet ANR 'blanc' SONONUCLICE (2009-2013), porté par le LAGEP (Pr. Roman Peczalski), en partenariat avec le laboratoire RAPSODEE de l'école des Mines d'Albi. Il a fait l'objet du post-doctorat de Stéphane Labouret au sein du LAGEP (2013).

Contexte

Les ultrasons sont connus pour induire la nucléation de glace dans des solutions sous-refroidies et pour rendre la congélation reproductible à la température souhaitée. Le déclenchement de la nucléation par ultrasons est basé sur le phénomène de la cavitation inertielle au sein du liquide. Ce phénomène est induit par le passage d'une onde acoustique dans un liquide. Il engendre une forte expansion des bulles de gaz, suivie d'une violente implosion qui induit des conditions physiques extrêmes à l'intérieur et à proximité immédiate de la bulle. L'implosion des bulles de gaz en cavitation permet d'atteindre localement des conditions de température et de pression nécessaires au changement de phase liquide-solide de l'eau. Afin de maîtriser la distribution de la taille cristalline, il est nécessaire de connaître parfaitement l'évolution des grandeurs physiques (pression, température, composition) pour le gaz à l'intérieur de la bulle, mais aussi celles du liquide, à l'extérieur de la bulle.

Modélisation de la cavitation d'une bulle unique

Le but de cette partie est d'évaluer, au moment du collapse, la pression et la température à l'interface gaz-liquide et dans le liquide au voisinage immédiat de la bulle. La modélisation de la cavitation acoustique d'une bulle de vapeur a nécessité la mise en équation des phénomènes suivants (Figure 14) :

1. la thermodynamique du gaz dans la bulle basée sur l'hypothèse d'une pression uniforme (P_g) et l'existence d'une couche limite thermique (δ_{tg}) (équation d'état du gaz, équations du bilan thermique du gaz) ;

2. la dynamique de la surface de la bulle et du liquide environnant (résolution de Gilmore des équations de Navier-Stokes à l'intérieur et à l'extérieur de la bulle) ;

3. le transfert de chaleur entre la bulle et le liquide (équation de bilan thermique à la paroi, équation de transfert thermique dans le liquide).

Les résultats discutés par la suite ont été obtenus avec les conditions de simulation suivantes :

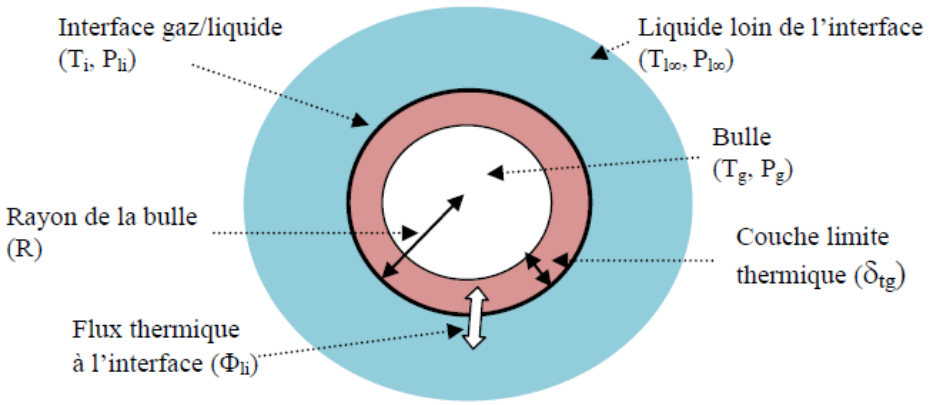

FIGURE *14 – Représentation de la bulle d'air et de son interface gaz (en rouge)/liquide (en bleu).*

1) Rayon initial de la bulle $R_0 = 5\ \mu m$ **2)** Température initiale du liquide $T_{l\infty}$ = -10°C
3) Pression acoustique $P_{ac} = 140\ kHz$ **4)** Fréquence f = 29 kHz

Les résultats conduisent à une élévation modérée de la température d'interface gaz/liquide T_i autour du collapse (610K au maximum). L'amplitude de la variation de température d'interface est très atténuée par rapport à celle dans la bulle T_g estimée à 11000K. Ce résultat est en adéquation avec les résultats des modèles de la littérature les plus élaborés même s'il convient d'être prudent, les conditions n'étant pas rigoureusement comparables (nature du gaz, fréquence acoustique, etc.).

Publication associée : [ACL10] (page 161)

Pression et température dans le liquide

Les distributions spatiales de la pression du liquide (P_l) et de la température du liquide (P_l) autour de la bulle pour différents temps après le collapse sont présentées sur la figure 15 (l'origine des temps correspond à l'instant du collapse).
Ainsi, l'implosion d'une bulle de gaz en cavitation s'accompagne d'une montée très forte de la pression jusqu'à 10 GPa environ, mais d'une élévation plus modérée de la température du liquide autour de la bulle. Cela provoque donc une élévation locale importante du sous-refroidissement (de l'ordre de 350K), favorisant ainsi la nucléation.

La connaissance précise de ces profils de température et de pression dans le liquide permet de vérifier dans le cas de solutions aqueuses sous refroidies, si autour d'une bulle cavitante, les conditions thermodynamiques sont suffisantes pour initier la cristallisation de la glace.

Publication associée : [ACL10] (page 161)

Modélisation du nombre de nuclei formés autour d'une bulle

Le calcul du nombre de nucléi pouvant être générés par l'implosion d'une bulle dans de l'eau sous-refroidie soumise à un champ acoustique est basé sur l'hypothèse la plus répandue dans la littérature[43] : la glace apparaît sous sa forme "haute pression" (VI ou VII) puis induit la formation de glace "normale" (Ih) (mais cette transition reste à prouver).

43. Hickling, Transient, High-Pressure Solidification Associated with Cavitation in Water Phys. Rev. Lett., American Physical Society (APS), 73, 2853-2856, 1994.

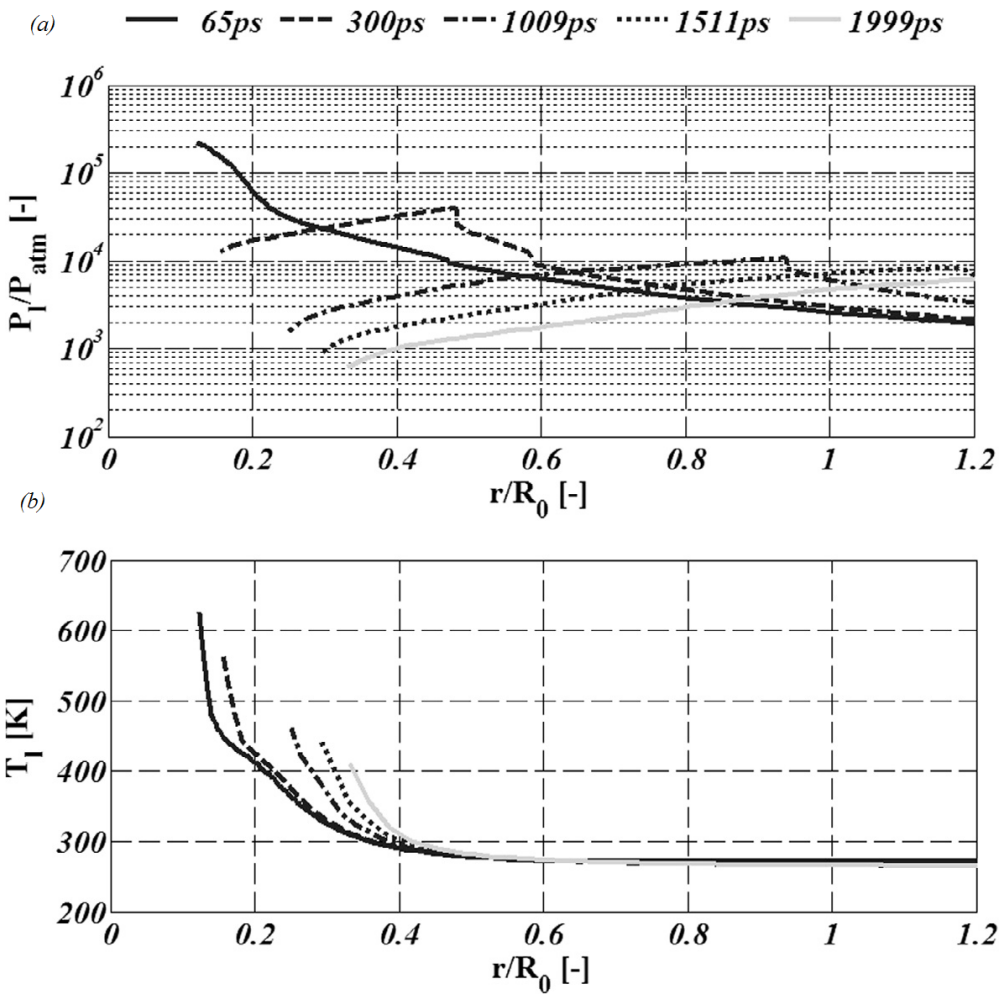

FIGURE *15 – Profil radial de pression (P_l) et de température (T_l) dans le liquide à différents temps après le collapse.*

La connaissance des champs de température et de pression dans le liquide à proximité de la bulle permet de calculer le taux de nucléation en fonction du temps et de la position radiale dans le liquide à partir du centre de la bulle. Ainsi, l'intégration en temps et en volume du taux de nucléation permet d'estimer le nombre de nucléi générés par une bulle.

L'existence d'un domaine optimal d'application des ultrasons pour des pressions modérées centrées sur 220 kPa a été aussi mise en évidence par l'analyse des températures limites d'apparition d'un premier nucleus en fonction de la pression acoustique et du rayon initial de la bulle (figure 16), les zones de nucléation se trouvent entre les branches de chaque isotherme.

D'après nos résultats, il est possible de déclencher la nucléation de la glace à l'aide des ultrasons à partir de sous-refroidissements initiaux aussi faible que 4K à condition d'appliquer une onde de pression acoustique d'amplitude supérieure à 220 kPa à des bulles de plus de 8 µm de rayon. L'existence d'un domaine optimal d'application des ultrasons pour des pressions modérées centrées sur 230 kPa est également mise en évidence sur cette figure. Il y a également un rayon optimal de bulle centré sur 8,5 µm. La nucléation peut facilement être déclenché à -5 ° C. Ainsi, l'hypothèse de déclenchement de la nucléation par l'effet de "haute pression" semble donc être tout à fait plausible.

Publication associée : [ACL11] (page 169)

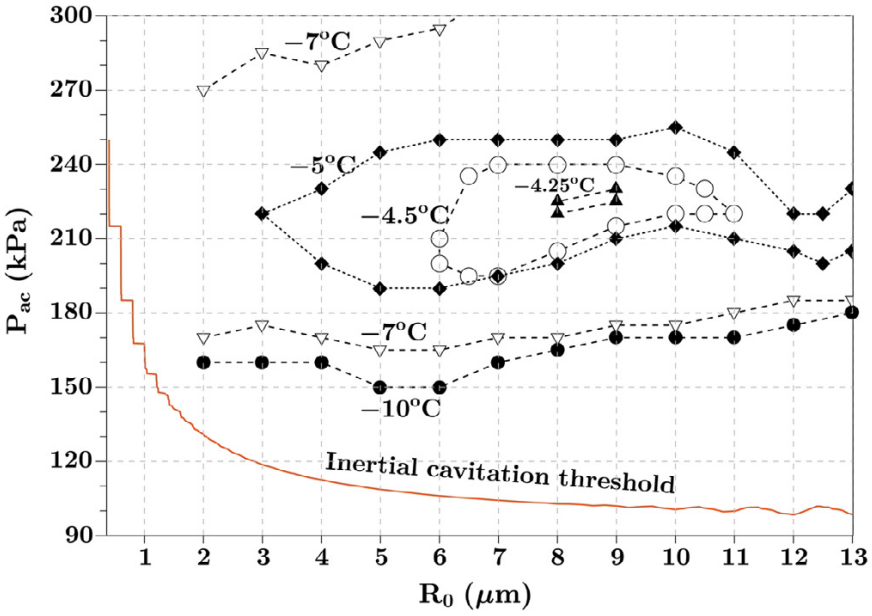

FIGURE *16 – Isothermes de seuil d'apparition des nuclei en fonction de la pression acoustique appliquée et du rayon initial de la bulle.*

Bilan de l'étude

En conclusion, à l'échelle du processus élémentaire, les travaux développés dans ce projet ont notamment permis d'évaluer les effets thermodynamiques de l'implosion d'une bulle unique et de calculer la quantité de nuclei produits. La capacité des ultrasons à agir à des faibles sous-refroidissements et dans un large intervalle de tailles de bulle a pu être quantifiée.

A l'échelle du procédé, d'un point de vue expérimental, l'influence très significative des ultrasons sur la taille des cristaux a été démontrée par des observations microscopiques (Figure 17). L'apport des ultrasons permet de déclencher la nucléation sur commande, de réduire la taille cristalline, et rend homogène la cristallisation sur l'ensemble de l'échantillon. Une analyse plus poussée a également permis de conclure que la température de la solution avait une influence proche de celle de la puissance acoustique et plus importante que celle de la saturation en air sur la taille des cristaux dans les gammes de paramètres considérés.

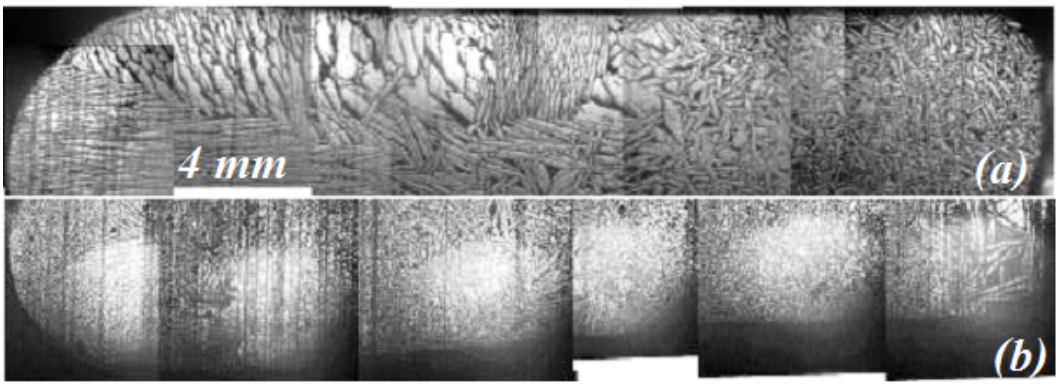

FIGURE *17 – Photographies des cristaux dans la section axiale d'un vial ($T_{initiale}$ = -5 °C) ; (a) sans ultrasons, (b) avec ultrasons.*

Ces résultats offrent des perspectives intéressantes quant au contrôle par ultrasons des tailles cristallines dans les procédés de congélation industriels. Il reste néanmoins quelques pistes d'amé-

lioration en vue d'une extrapolation :

- d'un point de numérique, le code développé, couplé avec le code simulant le champ acoustique réel dans le liquide, pourra servir à prédire les vraies performances des dispositifs de sono-congélation et ensuite à extrapoler les dispositifs de laboratoire vers l'échelle de pilote industriel.
- d'un point de vue expérimental, des études récentes ont été menées pour obtenir une prise en glace plus homogène dans le volume de l'échantillon par rapport à l'application des ultrasons.

1.3.2 Optimisation de la cristallisation en émulsion

Ce travail a concerné l'étude du procédé de cristallisation en émulsion d'un principe actif intervenant dans une formulation pour soins corporels. Il a été réalisé au LAGEP dans le cadre de mon post-doctorat (2004) et s'inscrit dans la continuité des travaux du post-doctorat de L. Lafferrère. Ce travail a été encadré par Pr. François Puel et financé par Rhodia.

Contexte

Pour quantifier les propriétés d'usage d'un shampoing, deux critères visuels sont jugés : la perlescence du produit que l'on peut traduire par l'aspect brillant et irisé et l'opacité qui traduit le pouvoir couvrant de l'échantillon. L'EthyleneGlycol DiStéarate (EGDS) est couramment utilisé sous forme cristalline pour obtenir ces propriétés. Il s'agit d'une cristallisation par refroidissement d'une émulsion huile dans eau. Les cristaux naissent alors dans les gouttes dispersées. Mais la forme et la structure des cristaux sont souvent mal contrôlées, limitant les propriétés visuelles qu'on peut attendre de la formulation cosmétologique.

L'enjeu de ce travail purement expérimental a été d'une part de comprendre l'origine de la perlescence et de l'opacité, d'autre part d'optimiser la formulation et le procédé de cristallisation en émulsion pour avoir des qualités de produit acceptables. Les mécanismes de nucléation et de croissance rencontrés en cristallisation en émulsion sont semblables à ceux intervenant en cristallisation en solution mais rendent l'étude plus complexe pour deux raisons : (i) difficulté accrue de faire un suivi en ligne, en raison d'un milieu triphasique liquide/liquide/solide ; (ii) présence d'émulsifiants qui peuvent modifier l'occurrence et l'intensité des mécanismes de cristallisation.

Résultats

Nous avons élaboré des lots aux propriétés d'usage très différentes dont certains avaient des qualités de perlescence très faibles. La caractérisation de tous ces échantillons a permis de mettre en évidence une relation entre l'aspect perlescent des produits et le faciès des cristaux d'EGDS (Figure 18). Les agglomérats doivent avoir une structure organisée de fines plaquettes pour que le shampoing soit perlescent. Au contraire, des cristaux sphériques et submicroniques conduisent à des échantillons très opaques.

D'un point de vue formulation, la nature de l'EGDS et plus particulièrement le ratio de mono-/diester, est également un facteur déterminant. Nous avons montré que, en accord avec la littérature, l'augmentation de la proportion de diester dans l'EGDS entraîne une amélioration de la perlescence mais engendre des problèmes de blindage de réacteur liés aux fortes valeurs de viscosité du produit.

D'un point de vue procédé, l'augmentation de la vitesse d'agitation lors de la phase de dispersion améliore l'aspect perlescent des shampoings. En terme industriel, ce point est relativement

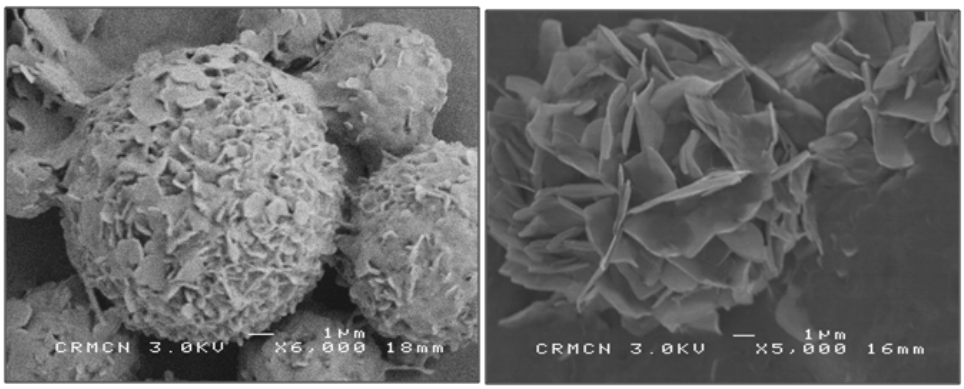

FIGURE *18 – Observation au microscope électronique à balayage de cristaux d'EGDS.*

simple à mettre en œuvre lors de l'émulsification. Le profil du mobile d'agitation a été plus spécifiquement étudié en vue de développer un procédé reproductible et extrapolable qui conduise à un produit aux propriétés d'usage satisfaisantes. Nous avons pu montrer que, en cas de faibles valeurs de viscosité, les turbines Pitch Blades conduisent à des produits perlescents. En revanche, pour des formulations très visqueuses, il est nécessaire de trouver un compromis entre la qualité finale du produit et l'amélioration de la reproductibilité : un système d'agitation de type Trimix (émulsionneur, ancre et pales rotatives) a permis de résoudre les problèmes de blindage mais la perlescence du produit a fortement diminué. Un mobile d'agitation de type ancre n'apporte aucune amélioration pour limiter le blindage du réacteur.

Publication associée : [ACL4] (page 104)

Bilan de l'étude

Cette étude a permis une meilleure compréhension de la cristallisation en goutte de l'EGDS, et a permis de corréler des propriétés d'usage à la morphologie et à la taille des cristaux. Une formulation maitre a été définie et les différentes étapes du procédé ont été optimisées afin d'obtenir d'importantes propriétés de brillance et/ou d'importantes propriétés d'opacité. En maîtrisant les conditions d'agitation et en limitant le blindage du réacteur, nous avons développé un procédé de cristallisation en émulsion assez facilement transposable à l'échelle industrielle.

Ce travail a été poursuivi dans le cadre de la thèse d'A. Khalil [44]. Le réacteur a notamment été instrumenté par deux sondes vidéo pour permettre le suivi vidéo in situ en temps réel de chaque étape du procédé. Cela a permis de montrer que la cristallisation d'une distribution polydisperse diluée est très progressive : elle débute à l'intérieur des gouttes les plus grosses et se termine à l'intérieur des plus petites. Avec le système modèle étudié dans des conditions de faible concentration de gouttes, une goutte a donné naissance à une particule. Aucune nucléation secondaire par collision n'est identifiée.

44. A. Khalil. Étude expérimentale d'un procédé de cristallisation en émulsion huile dans eau : application au distéarate d'éthylène glycol. Thèse de l'Université Lyon 1, 2011.

1.3.3 Intensification du procédé de précipitation de la struvite

Le projet PHORWater (2013-2016) a visé à valider au niveau industriel un procédé d'intensification de la récupération des phosphates dans les eaux usées par précipitation de struvite. Il a été subventionné par le fond LIFE+ de l'Union Européenne. Ce projet a été coordonné par la société DAM (Depuración de Aguas del Mediterráneo) basée à Valence en Espagne. Le laboratoire de recherche CalAgua (Calidad del Agua) de Valence a été également partenaire. Au LAGEP, le projet a été dirigé par Pr. Denis Mangin et a fait l'objet du post-doctorat de Stéphane Labouret.

Contexte

L'étude a visé à valoriser le phosphore contenu dans les eaux usées de stations d'épuration sous forme de struvite cristallisée. Le procédé offre ainsi une réponse aux problématiques environnementales du phosphore tout en apportant une nouvelle source de phosphore qui pourrait réduire son extraction minérale. Il permet également de réduire les dépôts intempestifs de struvite dans les canalisations des stations de traitement d'eaux usées, qui posent d'importants problèmes au niveau de la conduite des stations. Une des étapes clés du projet a été la conception du réacteur de cristallisation. Une intensification de la précipitation est indispensable compte tenu de la faible teneur en phosphate dans les eaux traitées. Le réacteur développé est composé d'une zone de réaction agitée, surmontée d'une zone de décantation. Il permet ainsi de travailler en mode continu avec la phase liquide, tout en conservant la phase solide dans la zone de réaction. Le passage d'un réacteur de laboratoire (15L) à un démonstrateur industriel (5000L) s'est notamment basé sur (i) une modélisation de la dynamique des fluides afin d'optimiser le mélange des flux de réactifs et (ii) un bilan de population pour étudier l'évolution de la taille des particules et définir la fréquence optimale d'extraction de la phase solide.

Modélisation du réacteur

La modélisation de l'hydrodynamique du réacteur (sans particules solides) a été développée avec le logiciel commercial COMSOL. Les résultats numériques (CFD) ont d'abord été validés à partir de données expérimentales tirées de la littérature avec le même type d'hélice que celui utilisé dans le pilote. Les profils d'écoulement dans le réacteur ont ensuite été calculés numériquement pour deux hauteurs verticales d'hélice. Les profils de vitesses obtenus (Figure 19) ont permis de déterminer les positions des tuyaux d'alimentation favorisant un mélange correct des réactifs dans la cuve. Il est important d'éviter des court-circuits qui mettraient les réactifs directement en contact. En effet, ces court-circuits pourraient conduire à des zones de fortes sursaturations engendrant localement de la nucléation primaire ; les fines particules alors produites par ce type de nucléation seraient entraînées avec le surnageant, ce qui induirait une baisse de l'efficacité du procédé. Différentes positions optimales verticales et radiales ont été définies pour les deux positions de l'hélice. Le profil d'écoulement permet également de prédire le risque de dépôt de particules sur le fond du réacteur.

Bilan de l'étude

Le calcul numérique des écoulements a permis de définir la position des injecteurs placés dans un réacteur agité-décanteur destiné à la récupération des phosphates des eaux usées par cristallisation de struvite. Bien que le modèle ne prenne pas en compte les réactions chimiques, il a été possible d'estimer l'influence de la profondeur des injecteurs par rapport à la nécessité de la dilution des réactifs avant leur rencontre. Les sursaturations à proximité des injecteurs ont été évaluées. La prise en compte des réactions et de la consommation des réactifs dans le modèle

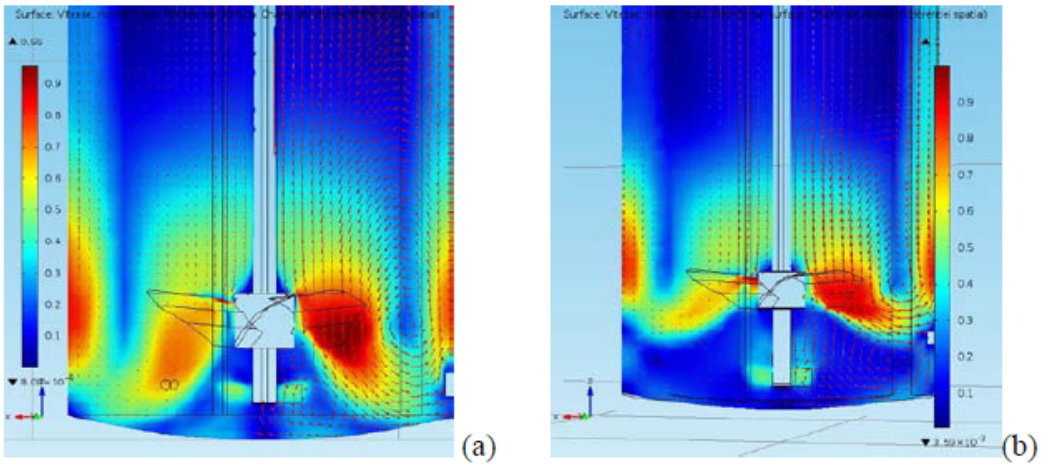

FIGURE *19 – Profil de vitesse en fonction de la position de l'hélice. (a) position basse ; (b) position haute.*

numérique est envisagée pour affiner les résultats. L'optimisation du réacteur durant son exploitation demande d'étudier l'évolution de la population de cristaux sur des durées de plusieurs jours/semaines. Cette étude sera entreprise par la technique de bilan de population et sera un guide utile pour gérer le rythme du prélèvement des cristaux du réacteur.

1.4 Bilan général sur les travaux de cristallisation

Un aperçu des approches théoriques et expérimentales des procédés de congélation développées au cours de mes activités de recherche a été présenté. Une première catégorie de travaux concerne la mise en oeuvre de procédé de congélation, la seconde s'intéresse plus spécifiquement au contrôle de la nucléation des cristaux. Étudier la cristallisation de façon théorique et pratique permet de corréler les paramètres opératoires du procédé à la taille et à la morphologie des cristaux. Cette démarche est utile pour l'intensification des procédés, l'extrapolation des procédés ou la maîtrise des propriétés d'usage des produits formés.

Bien que les problématiques soulevées par ces sujets puissent être différentes, dues à des domaines d'applications divers (agro-alimentaire, génie pharmaceutique, cosmétologique ou environnement), la démarche globale développée est restée la même. Elle consiste en trois étapes :

1. Caractérisation des propriétés du produit à congeler afin de connaître les limites du procédé et d'alimenter au mieux les modèles numériques. Des dispositifs expérimentaux ont été développés afin de déterminer les propriétés thermophysiques du produit étudié et les conditions d'équilibre liquide-solide. La complexité de certaines configurations (notamment les hautes pressions et les hautes températures générés par les ultrasons) n'a pas toujours permis de mesurer expérimentalement ces grandeurs ; le cas échéant, elles sont issues de la bibliographie et utilisées sans validation expérimentale.

2. Modélisation des cinétiques de cristallisation afin de maîtriser finement la conduite du procédé et de sécuriser le changement d'échelle. Cette étape repose sur l'analyse des différents phénomènes mis en jeu, leur mise en équation et la résolution du système. Les modèles développés sont ensuite validés pour certaines configurations à partir de valeurs expérimentales et/ou de données issues de la bibliographie. Enfin, l'étude paramétrique du modèle permet de définir les facteurs influents du procédé et de déterminer des tendances d'évolution.

3. Observation de la structure du produit fini afin de corréler les paramètres procédé à la qualité finale du produit. La taille cristalline et la morphologie des cristaux confèrent au

produit final ses futures qualités d'usage. L'analyse microscopique des produits congelés permet donc de déterminer les paramètres influents et d'étudier les mécanismes de croissance de la glace.

Au delà des résultats scientifiques, mon apport personnel a été de développer des modèles pour des domaines d'application tels que l'agro-alimentaire pour lesquels une large place est souvent laissée à l'empirisme. Sans minimiser les recherches expérimentales, il a fallu convaincre que la modélisation représente un outil intéressant qui s'appuie sur l'analyse de la réalité physique des phénomènes et qui permet d'apporter des solutions novatrices avec un gain de temps et d'argent souvent significatif.

2

Milieux particulaires

2.1 Bibliographie

2.1.1 Contexte

La caractérisation et l'étude du comportement de matériaux granulaires sont nécessaires pour la compréhension de plusieurs phénomènes naturels comme le mouvement des dunes et les avalanches de neige, et de processus industriels tels que l'écoulement et le mélange de poudre. Ainsi, la recherche dans le domaine, que ce soit par l'expérimentation physique ou par la simulation numérique, fédèrent plusieurs communautés scientifiques : génie civil [45], génie des procédés [46], géologie [47], mécanique [48]. En génie des procédés, les matériaux solides divisés présentent une part non négligeable des produits, finis ou intermédiaires, mis en oeuvre dans les tous les secteurs industriels (agro-alimentaires, chimiques, métallurgiques, pharmaceutiques, ...).

Jusqu'à présent, il n'y a pas de théorie complète qui permette de décrire les différents phénomènes observés concernant le comportement de ces matériaux. La discontinuité et le caractère multiphasique sont à l'origine de ces difficultés. En effet, une poudre est un assemblage de particules solides hétérogènes dispersées dans une phase continue gazeuse entre lesquelles s'exerce une multitude d'interaction (Van der Waals, capillaires, électrostatiques, etc.). Le comportement global d'une poudre dépend directement de ces interactions et des caractéristiques des particules solides. Ainsi, la caractérisation d'un système particulaire se situe à l'échelle microscopique (caractéristiques intrinsèques des particules), à l'échelle mésoscopique (propriétés relatives à une population de particules) et à l'échelle macroscopique (propriétés comportementales de l'ensemble du lit granulaire) [49, 50].

D'un point de vue numérique, plusieurs approches ont été adoptées pour modéliser les matériaux granulaires. Par exemple, la mécanique des fluides a été utilisée pour décrire l'écoulement des matériaux granulaires se comportant comme un liquide pour l'étude d'écoulement de particules

45. Zou and Chen, Granular sediment deposition and aggregation upstream of a check dam : A discrete element study, Powder Technology, 307, 90–98, 2017.

46. Mohanty *et al.*, Study of flow through a packed bed using discrete element method and computational fluid dynamics, Journal of the Taiwan Institute of Chemical Engineers, 63, 71–80, 2016.

47. Mead and Cleary, Validation of DEM prediction for granular avalanches on irregular terrain, Journal of Geophysical Research : Earth Surface, 120(9), 1724–1742, 2015.

48. Bourbatache *et al.*, DEM ball bearing model and defect diagnosis by electrical measurement. Mechanical Systems and Signal Processing, 41(1-2), 98–112, 2013.

49. Saleh and Guigon, Caractérisation et analyse des poudres - Propriétés comportementales des solides divisés. Techniques de l'Ingénieur, J2 252, 1–16, 2015.

50. Saleh and Guigon, Caractérisation et analyse des poudres - Propriétés physiques des solides divisés, Techniques de l'Ingénieur, J2 251, 1–14, 2015.

cohésives par exemple, la théorie cinétique a été adaptée pour décrire l'écoulement des matériaux granulaires se comportant comme un gaz pour des particules très dispersées, et la mécanique des sols est souvent utilisée pour l'étude des contraintes dans un matériau granulaire se comportant comme un solide (statique des empilements). Grâce aux progrès réalisés dans les machines de calcul, la méthode des éléments discrets (DEM, "Discrete Element Method") est parmi les outils les plus utilisés à ce jour pour la simulation des milieux granulaires.

2.1.2 La Méthode des Éléments Discrets (DEM)

La DEM est une méthode qui détermine la position, la vitesse et l'orientation de chacune des particules du milieu à chaque pas du temps durant la simulation. De façon générale, la résolution du problème met en oeuvre un schéma itératif dont les étapes fondamentales sont les suivantes [51] :

- la détection des contacts ; cette étape est la plus complexe et la plus coûteuse en terme de temps CPU.
- le calcul des forces de contacts évaluées à partir du mouvement relatif des deux particules et du modèle constitutif utilisé.
- l'estimation du mouvement des particules basé sur la résolution de l'équation du mouvement.

Dans la littérature, les DEMs sont divisées en deux catégories : (i) la Smooth Contact Dynamics (SCD) qui considère une légère interpénétration des corps modélisée par un système de ressorts et d'amortisseurs, (ii) la Non Smooth Contact Dynamics (NSCD) qui est basée sur la conservation de la quantité de mouvement. Sans entrer dans le détail de la résolution des équations, cette méthode a la capacité de simuler le comportement de grains de propriétés physiques et de géométries différentes. L'avantage de la DEM est lié à sa capacité de simuler un grand nombre de particules.

En génie des procédés, l'utilisation de codes de calcul basée sur la DEM est de plus en plus courante. Elle trouve des applications diverses [52] dans les domaines d'écoulement, de mélange, de compaction, d'enrobage et de fluidisation (couplée dans ce cas à des méthodes type éléments finis).

2.1.3 MULTICOR : code de calcul DEM

A partir de 2001, le Laboratoire des Technologies Innovantes a pu disposer d'un code de calcul basé sur la DEM en 2D, MULTICOR, développé par Jérôme Fortin. Ce code de calcul utilise la Non Smooth Contact Dynamics, qui permet entre autre de travailler avec une discrétisation en temps très grande (10^{-3}s), en comparaison avec les codes SCD (10^{-7}s).

Par ailleurs, l'optimisation de l'algorithme de calcul permet la convergence de problèmes à des ensembles de plusieurs dizaines de milliers de corps rigides. A chaque pas de temps, l'ensemble des forces de contact du système est déterminé itérativement par la méthode dite des équilibres successifs qui est basée sur un algorithme de type Gauss-Seidel. Chaque force de contact est calculée en adoptant des valeurs provisoires des forces sur les autres contacts. La convergence est obtenue quand chaque force interparticulaire vérifie la loi de contact unilatéral (relation qui existe, sur la zone de contact, entre les efforts normaux et le mouvement relatif des deux corps

51. Fortin *et al.*, Numerical simulation of granular materials by an improved discrete element method. International Journal for Numerical Methods in Engineering, 62(5), 639–663, 2004.

52. Zhu *and al.*, Discrete particle simulation of particulate systems : A review of major applications and findings. Chemical Engineering Science, 63(23), 5728–5770, 2008.

dans la direction normale) . La figure 20, donnée à titre d'exemple, présente le résultat de la simulation avec le code de calcul MULTICOR développé au LTI par Jérôme Fortin et son équipe, l'impact d'un grain à une vitesse de 5 $m.s^{-1}$ sur un lit de 90000 particules de 1 mm de diamètre.

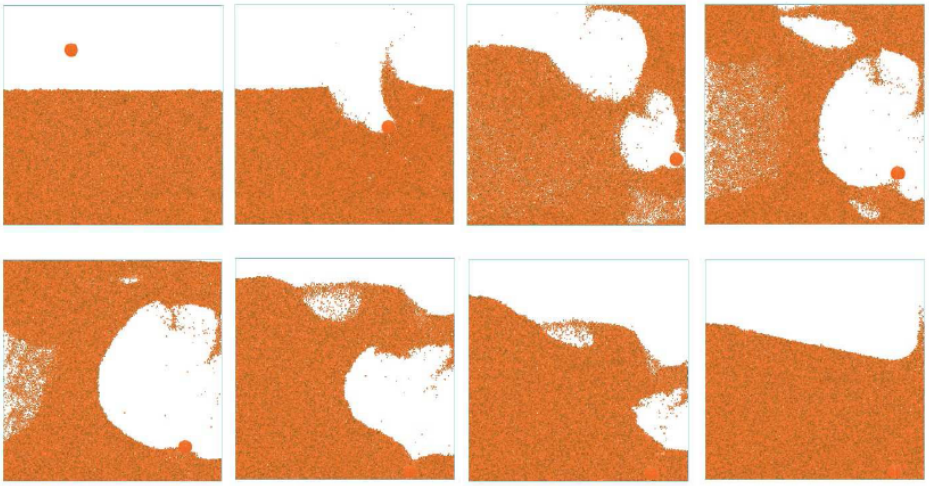

FIGURE *20 – Impact d'une particule sur un lit de 90000 particules.*

Le traitement graphique permet de visualiser le mouvement des grains mais aussi les forces de contact (normales et tangentielles). Le code MULTICOR a été étendu en 3D au cours de la thèse de I. Sanni soutenue en juillet 2006 [53]. De 2004 à 2011, je me suis investie avec les collègues du LTI (J. Fortin, M. Guessasma et E. Bellenger) à introduire les phénomènes thermiques dans le code de calcul (voir section suivante). Depuis 2011, les collègues ont poursuivi le développement du code notamment en couplant d'un point de vue purement mécanique la méthode des éléments discrets à celle des éléments finis [54] et en intégrant des phénomènes électromécaniques pour l'application au diagnostic des défauts dans les roulements à billes [55].

2.2 Utilisation d'outils basés sur la DEM pour la modélisation de milieux complexes

Dans le domaine des matériaux granulaires, mon activité s'est centrée sur la modélisation de matériaux fonctionnels et du comportement thermo-mécanique des milieux granulaires. A ce titre, sur la période 2006-2011, j'ai été membre du GdR MeGe (Couplages multiphysiques et multi-échelles en mécanique géo-environnementale).

Ce travail suppose la détermination des caractéristiques intrinsèques des produits élaborés mais aussi leur comportement sous sollicitations externes. Dans cette partie, je me suis focalisée sur les travaux numériques en utilisant des codes de calcul (MULTICOR, IGED, LMGC90). Les données expérimentales, étape importante pour la validation des modèles, ont été fournies par les diverses collaborations ou des données bibliographiques.

53. Sanni *et al.*, A reliable algorithm to solve 3D frictional multi-contact problems : Application to granular media. Journal of Computational and Applied Mathematics, 234(4), 1161–1171, 2010.

54. Haddad *et al.*, Heat transfer by conduction using DEM–FEM coupling method. Computational Materials Science, 81, 339–347, 2014.

55. Machado *et al.*, Diagnosis of faults in the bearings by electrical measures and numerical simulations. Mechanics & Industry, 15(5), 383–391, 2014.

2.2.1 Modélisation par la DEM des phénomènes thermomécaniques dans les interfaces de contact

Dans le cadre des appels à projets du Pôle "Mécanique, Matériaux et Procédés sûrs" du Conseil Régional de Picardie, nous avons obtenu en octobre 2006 en collaboration avec l'INERIS (Christophe Proust) un financement pour le projet MULTICOR, portant sur l'étude thermomécanique de l'interface de contact entre deux corps solides. Ce projet a fait l'objet de la thèse de Viet-Dung Nguyen de 2006 à 2009, dirigée par Pr. Jérôme Fortin.

Contexte

Le contexte de ce projet est lié à des des enjeux socio-économiques importants tels que les risques industriels induits par un frottement mécanique. En effet, les frottements d'origine mécanique sont une des causes principales d'inflammation des ATmophères EXplosives (ATEX) dans l'industrie. Compte tenu d'une demande sociale vers plus de sécurité, relayée par une évolution de la réglementation, les constructeurs de machine sont à la recherche d'outils suffisamment fiables leur permettant de contrôler in situ la température, d'évaluer les risques d'inflammation et de dimensionner des machines "sûres".

Pour répondre à ce problème, il est nécessaire de se focaliser sur l'interface de contact entre deux corps solides, système complexe dont la dynamique est encore mal connue. Si dans ce domaine, l'apport de la méthode des éléments finis a permis une avancée certaine, certains phénomènes locaux ne sont pas pris en compte. En effet, des études expérimentales ont montré la formation de particules à l'interface de contact, introduisant le concept de troisième corps. L'approche des milieux discrets basée sur le caractère discontinu des systèmes multi-corps permet de mieux comprendre les phénomènes aux échelles les plus fines ainsi que d'approcher la nature de l'interface de contact et son évolution thermique au cours du temps.

Modélisation thermomécanique de l'interface de contact

A partir de données d'entrée telles que la charge imposée, la vitesse de cisaillement, la géométrie et la nature des corps, le but de la modélisation était de déterminer les caractéristiques thermiques à l'interface de contact, mais aussi d'estimer le coefficient de frottement global.

Les transferts thermiques dans un milieu granulaire peuvent être de différentes natures, mais à l'aide de MULTICOR, on s'est principalement intéressé à la modélisation :

- du transfert thermique résultant du contact physique entre les particules. La déformation réelle des particules étant extrêmement complexe à modéliser, le contact est modélisé par une légère interpénétration des particules. On peut alors, grâce la théorie de Hertz, estimer les conductances de contact.

- de la génération de chaleur par frottement des particules. Elle est estimée à partir de la vitesse de glissement et de la force normale entre les particules en contact.

Une des hypothèses principale de la modélisation a consisté à considérer une température uniforme des particules, en supposant que la résistance de transfert thermique au sein d'une particule (transfert par conduction) est significativement plus faible que la résistance thermique entre les particules. Nous avons aussi supposé que l'équation de la chaleur devrait être résolue avec un pas de temps suffisamment faible pour que le flux de chaleur traversant une particule ne se propage pas plus loin que les particules voisines. Différentes validations de l'introduction des transferts thermiques dans le code MULTICOR ont été menées par des comparaisons avec des résultats numériques et expérimentaux relevés dans la littérature.

Application aux interfaces de contact sous contrainte et soumis à un cisaillement

En vue de simuler une machine-outil rotative, la configuration étudiée est celle d'un cisaillement plan. Le milieu granulaire est confiné entre deux parois distantes d'une hauteur H. La paroi inférieure se déplace à la vitesse imposée V et la paroi supérieure est soumise à une charge verticale F (Figure 21). Des conditions de périodicité sont imposées aux limites : on remplace une particule qui sort de la frontière par une autre particule avec les mêmes propriétés dynamiques sur la face opposée. Pour tenir compte de la rugosité, les parois sont constituées de particules "collées". La longueur L de l'écoulement simulée est choisie de telle sorte que les effets de bords soient négligeables.

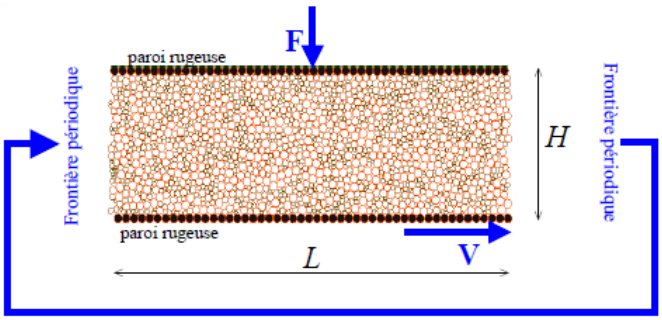

FIGURE *21 – Modèle de l'interface de contact.*

A partir de cette modélisation, la rhéologie du milieu granulaire a été étudiée en fonction des paramètres d'entrée (charge imposée, vitesse de cisaillement, rugosité des parois, coefficient de frottement intrinsèque des particules, granulométrie du milieu). Une attention particulière a été portée sur la variation du coefficient de frottement effectif de l'interface de contact pour caractériser l'écoulement des grains. Il est défini comme le rapport de la force de cisaillement (calculée à partir des réactions de contact normales entre les particules et la paroi inférieure) sur la force imposée. On peut montrer que, dans la limite des grands systèmes, le coefficient de friction effectif dépend d'un seul paramètre sans dimension construit à partir des données du problème, qu'on appelle nombre inertiel [56]. Il peut s'interpréter comme le rapport du temps de ré-arrangement des grains sur le temps qu'une couche de grains met à avancer d'un diamètre moyen sous l'effet de la déformation imposée. On peut classer les régimes d'écoulement en fonction de ce nombre inertiel. Pour un nombre inertiel petit (inférieur à 10^{-2}), il s'agit du régime quasi-statique où le matériau est décrit comme un solide. Pour un nombre inertiel supérieur à 10^{-1}, il s'agit du régime collisionnel, où le milieu est fortement agité et peut être décrit comme un gaz.

L'évolution du coefficient de frottement effectif en fonction du régime d'écoulement a été déterminé numériquement grâce au code de calcul MULTICOR (Figure 22). On note un comportement de type viscoplastique. La friction démarre à une valeur finie et augmente lorsque le nombre inertiel augmente, c'est à dire lorsqu'on cisaille plus vite ou lorsqu'on appuie moins fort. Il existe donc un seuil d'écoulement pour les milieux granulaires : il faut appliquer une contrainte minimum pour cisailler le matériau, c'est l'aspect plastique. Au dessus du seuil, la contrainte due au frottement solide augmente avec la vitesse de déformation, c'est l'aspect visqueux.

En outre, une étude paramétrique a permis de quantifier l'influence des données telles que la rugosité des parois, le coefficient de friction local ou la vitesse de cisaillement, et de démontrer l'occurrence du phénomène de "stick-slip" (collage-glissement en français) caractérisant des instabilités de frottement.

56. Guyon *et al.*, La matière en désordre, Ed. by EDP Sciences, 2014. ISBN 978-2-7598-1069-7.

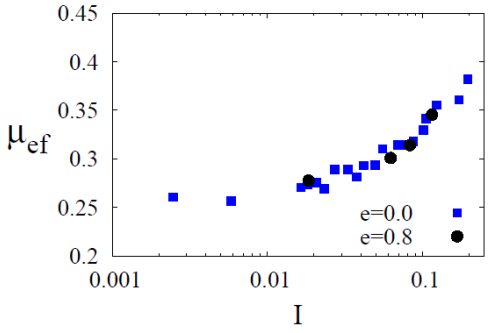

FIGURE *22 – Coefficient de frottement effectif μ_{ef} en fonction du nombre inertiel I (pour deux valeurs du coefficient de restitution noté e).*

D'un point de vue thermique, pour de faibles valeurs du nombre inertiel, les résultats numériques semblent montrer qu'une "bande chaude" se forme initialement près de la paroi mobile pour progresser au cours du temps dans l'épaisseur du lit (Figure 23). Il est intéressant de noter, que dans cette bande chaude, la distribution de la température n'est pas homogène. Il apparaît de façon très localisée des points chauds classiquement démontrés dans les systèmes frottants comme étant à l'origine des phénomènes d'inflammation.

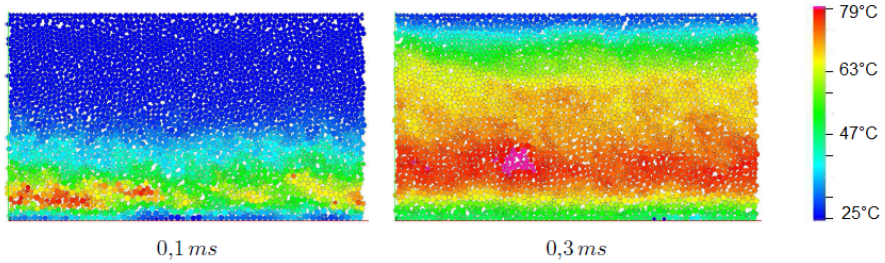

FIGURE *23 – Évolution de la température au cours du temps d'un milieu granulaire soumis à des sollicitations externes.*

Publication associée : [ACL5] (page 112)

Bilan de l'étude

Cette étude a permis de mettre en oeuvre une démarche de modélisation multi-physique à l'aide de la méthode des éléments discrets. Elle couple les calculs dynamiques classiques de la DEM avec la description des transferts thermiques dans un milieu granulaire. Ce travail a nécessité l'introduction de phénomènes tels que le transfert thermique par contact et la génération de chaleur par frottement. Les applications visées concernaient la description mécanique et thermique de l'interface de contact par une couche d'un milieu granulaire représentatif du troisième corps caractéristique en tribologie et elle a été approfondie dans l'étude présentée dans le paragraphe suivant concernant la vidange de silo.

De nombreuses questions se sont posées à la suite de ce travail. Différents axes de poursuite peuvent être envisagés :

- l'étude a été réalisée en 2D, donc il est évident qu'il faut envisager une approche tridimensionnelle pour être plus représentatif.
- les phénomènes de "cohésion-décohésion" du milieu granulaire aux interfaces frottantes ont été expérimentalement mis en évidence, il conviendrait d'en tenir compte numériquement.

- à des températures relativement élevés, les transferts par rayonnement risquent de ne plus être négligeables et devront être intégrés aux équations de difffusion de la chaleur.

2.2.2 Étude de la décharge de silos

Dans la continuité du projet MULTICOR, nous avons poursuivi une étude sans financement en nous focalisant sur la modélisation de la décharge de silos. Notre motivation a été double : la présence d'industriels locaux susceptibles d'être intéressés par des modèles prédictifs pour améliorer la traçabilité des céréales stockées en silo et le savoir-faire du laboratoire TMIR de l'UTC dans la mesure expérimentale de distribution de temps de séjours dans des silos.

Contexte

La problématique concerne le stockage des produits granulaires agricoles et plus particulièrement, les difficultés associées à leur écoulement dans les silos industriels de grande taille. Les problèmes rencontrés se posent aussi bien en termes de qualité du produit soutiré qu'en termes de maîtrise et prévention des risques d'incendie et d'explosion. L'étude vise, en particulier, à établir :

- des modèles prédictifs fiables permettant de décrire l'écoulement des grains céréaliers dans les silos de stockage dans le but de prédire leur distribution de temps de séjour (DTS) en fonction de leurs coordonnées spatiales initiales, autrement dit en fonction de l'état de remplissage du silo ;
- les mécanismes et les cinétiques des processus de dégradations, chimique ou biologique, des grains dûes à des variations thermiques.

Ces études doivent permettre de comprendre les phénomènes mis en jeu lors du stockage et de proposer des solutions de bonnes pratiques pour améliorer, sécuriser et rendre plus robustes le fonctionnement des unités de stockage des produits en question. L'objectif de cette étude en 2010 était de montrer la faisabilité de la démarche et d'amorcer une collaboration entre l'UTC et le LTI pour obtenir un financement.

Étude expérimentale et modélisation de l'écoulement de silos

L'écoulement des produits granulaires dans les silos n'est pas un phénomène simple et peut varier entre deux cas entièrement opposés : (i) un écoulement en masse où le solide est extrait régulièrement (les grains chargés en premier sortiront les premiers), (ii) un écoulement en cheminée où les grains entrés dans le silo en derniers seront les premiers à en sortir. Bien entendu, le premier mode d'écoulement est celui recherché alors que, les silos industriels fonctionnent, pour la plupart, en écoulement cheminée, faute d'une mauvaise conception à la réalisation ou d'une cohésivité élevée du matériau ensilé. Ce type d'écoulement conduit à une dispersion très marquée des temps de séjour des grains mais surtout à l'apparition des zones mortes proches des parois. Si le produit possède une activité physique, physico-chimique, chimique ou encore biologique, plusieurs phénomènes non désirés peuvent apparaître (mottage, auto-échauffement, ...).

D'un point de vue expérimental, l'UTC a développé une technique de traçage validée pour l'écoulement des grains céréaliers. Elle consiste à placer, à des endroits bien précis d'un silo, des grains peints avec des peintures magnétisantes. Le silo est ensuite déchargé sur un tapis défilant en dessous de l'orifice. Les grains sont séparés en petits volume au cours de la décharge puis triés par couleur. Il devient alors possible de déterminer la DTS et donc le temps moyen de séjour ainsi que sa dispersion pour chaque population de traceur.

D'un point de vue numérique, la première étape a consisté à valider le modèle avec des données expérimentales. Différentes configurations ont été envisagées (géométries des trémies, méthode de

remplissage, géométrie et granulométrie des particules, ...) pour un nombre de particules limité à 10^6. A titre d'exemple, sur la figure 24, on compare des résultats numériques à des données expérimentales issues de la bibliographie [57] concernant la décharge de particules non sphériques d'une maquette bi-dimensionnelle.

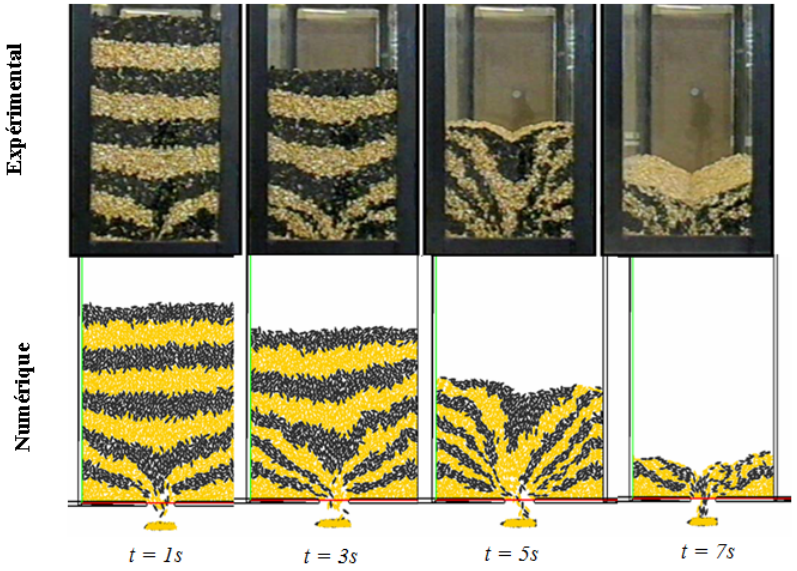

FIGURE *24 – Comparaison qualitative de la décharge d'un silo : étude expérimentale*[57] *et modélisation DEM.*

Les calculs ont montré une bonne adéquation avec les résultats expérimentaux et ont permis de conclure sur les capacités de la DEM à prédire l'écoulement de la matière et son renouvellement au cours des opérations de remplissage et de vidange d'un silo. De même, la formation de zones mortes et les risques associées notamment en cas de remplissage partiel à répétition peuvent être prédits. En pratique, ces zones de stagnation des grains sont les zones où le risque d'auto-échauffement serait le plus présent.

Publication associée : [ACL6] (page 127)

Bilan de l'étude

Si cette pré-étude a permis de montrer le potentiel de la méthode pour prédire les temps de séjour d'un nombre limité de particules, les perspectives d'un point de vue numérique sont encore nombreuses et se situent à deux échelles :

- à l'échelle microscopique, il reste à intégrer les mécanismes gouvernant les transformations chimiques ou biologiques, largement favorisées par l'élévation locale de température.

- à l'échelle macroscopique, il conviendrait d'intégrer un plus grand nombre de particules. Seule une approche hybride basée sur le couplage des méthodes microscopiques (DEM) et macroscopiques (méthodes des éléments finis) peut permettre de traiter de plus grandes quantités de produit.

57. Coetzee and Els, Calibration of discrete element parameters and the modelling of silo discharge and bucket filling. Computers and Electronics in Agriculture, 65(2), 198–212, 2009.

2.2.3 Gestion des flux thermiques dans un matériau composite

De 2008 à 2011, j'ai collaboré à un projet européen PRISTIMAT (Partenariat en Recherches, Innovations et Supports Techniques Interrégionaux en MATériaux). Il s'agit d'une collaboration transfrontalière en recherches dirigées vers les entreprises dans les domaines des matériaux à gradients de composition pour le transport. Ce projet a été financé dans le cadre du programme transfrontalier INTERREG IV France-Wallonie-Vlaanderen. Le porteur de projet était le CRBC (Centre Belge de la Céramique, Mons en Belgique) et j'ai été responsable de la coordination de ce projet pour le LTI. Les autres partenaires étaient le SIRRIS (Centre collectif de l'industrie technologique belge, Charleroi), l'UVHC (Université de Valenciennes et du Hainaut Cambrésis) et le CRITT MDTS (Centre Régional et d'Innovation de Transfert de Technologie spécialisé dans les Matériaux, Dépôts et Traitements de Surface, Charleville-Mézières). Ce projet a fait l'objet du post-doctorat de Nabil Ferguen au sein du LTI (2010-2012).

Contexte

L'objectif est de développer de nouveaux matériaux capables de répondre à des cahiers des charges multi-critères permettant d'allier des propriétés thermiques et mécaniques. Ces matériaux doivent être capables d'assurer et de gérer le transfert des calories de manière à ce que les éléments fonctionnels puissent être maintenus à leur température nominale de fonctionnement. Les applications visées concernent essentiellement l'industrie automobile pour l'évacuation de la chaleur entre les parties chaudes du bloc moteur et les parties connexes en polymère.

Une solution proposée est d'élaborer des matériaux à gradients à base d'alumine (isolant, rigide) et d'aluminium (conducteur, souple) présentant macroscopiquement une gradation dans la répartition des phases. Le procédé d'élaboration, développé par l'UVHC et le SIRRIS, consiste à imprégner d'aluminium des mousses céramiques. Il est possible d'élaborer des structures poreuses à gradient de taille des porosités de 200 à 1000 µm de diamètre (Figure 25) avec des interconnexions contrôlées entre ces pores (de 0,3 à 0,5 fois le diamètre des pores) [58].

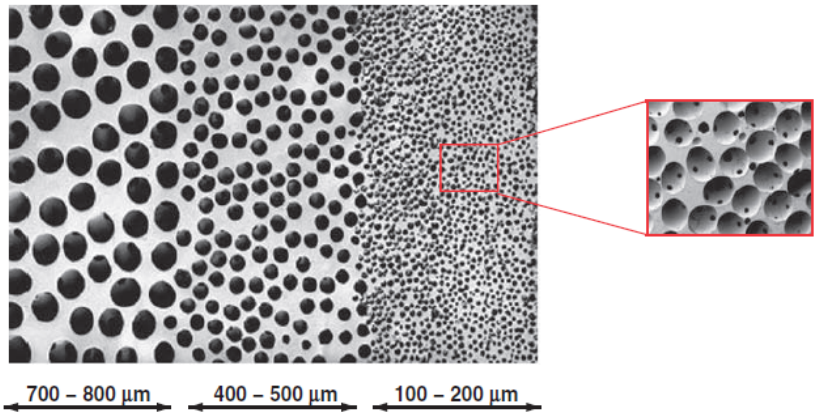

FIGURE *25 – Mousse d'alumine à gradient de composition*[58].

Modélisation

Le travail du LTI a consisté à développer un modèle capable de prédire la conductivité thermique apparente du matériau élaboré afin d'optimiser l'architecture des phases en présence. Le modèle

58. Descamps *et al.*, Manufacture of macroporous β-tricalcium phosphate bioceramics, Journal of the European Ceramic Society, 28(1), 149–157, 2008.

proposé utilise conjointement la méthode des éléments discrets et la méthode des éléments finis. L'algorithme se décompose en six grandes étapes (Figure 26) :

- Génération d'un empilement aléatoire de billes de Polymethylmethacrylate (billes utilisées expérimentalement pour produire les mousses céramiques) à partir d'un code DEM (PFC3D ou Multicor).
- Compression de l'empilement pour créer l'interconnexion souhaitée entre les billes et détermination du rayon de contact entre les billes.
- Récupération des paramètres géométriques et intégration dans un code de calcul par la méthode des éléments finis (SolidWorks, outil de conception assistée par ordinateur) : génération du squelette auquel les propriétés de l'aluminium sont affectées.
- Génération du négatif aux propriétés de l'alumine.
- Assemblage du composite alumine/aluminium.
- Maillage de l'ensemble du matériau.

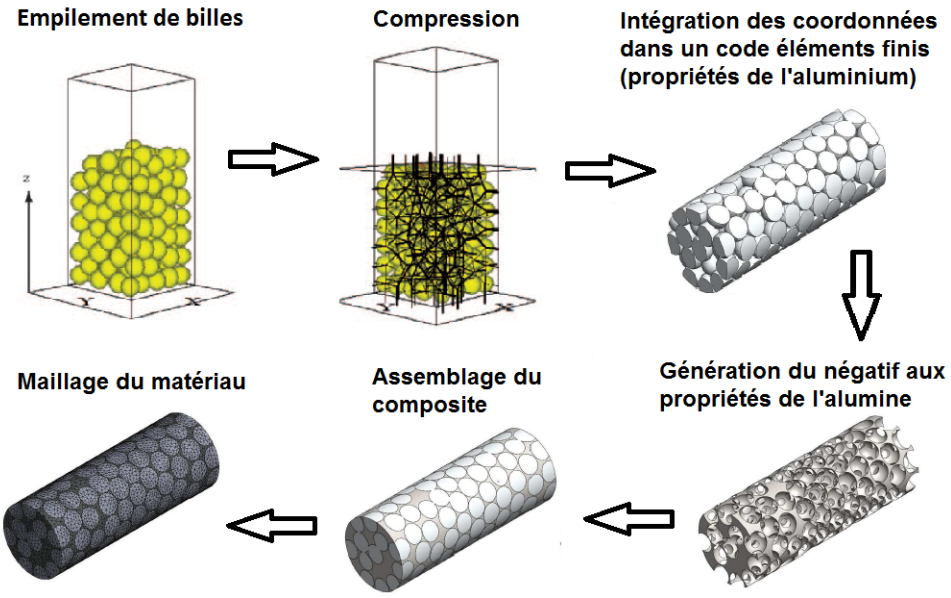

FIGURE *26 – Modélisation du matériau composite.*

En régime stationnaire, l'application d'un gradient de température permet grâce à la loi de Fourier de déterminer la conductivité apparente du matériau. Ainsi, l'influence des fractions volumiques des deux phases et des rayons de contact (interconnexions) sur la conductivité thermique a pu être montrée. L'anisotropie du matériau a également été quantifiée.

Publication associée : [ACL7] (page 135)

Bilan de l'étude

L'utilisation d'un code DEM en trois dimensions en lien avec les outils de conception assistée par ordinateur par la méthode des éléments finis, est adaptée pour la génération d'un matériau composé de cellule d'aluminium et de préforme céramique. Ces outils ont permis d'aider les élaborateurs de ces matériaux (UVHC, CRIBC) à maîtriser l'architecture de la mousse d'alumine

à réaliser, en fonction des capacités technologiques et des applications visées définies par les utilisateurs.

A court terme, les poursuites de ce travail ont permis de définir un volume élémentaire représentatif pour optimiser les temps de calcul. A plus long terme, une comparaison avec des valeurs expérimentales de conductivité thermique a permis de valider le modèle, pour permettre la fabrication d'un prototype de grande taille.

2.3 Bilan général sur les travaux des milieux particulaires

L'approche des milieux discrets basée sur le caractère discontinu des systèmes multi-corps permet de mieux comprendre les phénomènes activés à l'échelle du grain et d'approcher la nature de l'interface de contact et son évolution au cours du temps. La thèse de V.D. Nguyen soutenue en 2009 s'est focalisée sur le comportement thermique de l'interface de contact soumise au cisaillement dynamique. Ce travail sur l'introduction des transferts thermiques dans le code MULTICOR a conduit à une autre application concernant l'étude des écoulements et des phénomènes thermiques générés par frottement lors de la vidange de silos.

Concernant l'étude de matériaux fonctionnels à structure complexe, la forte anisotropie des matériaux générés n'a pas permis d'utiliser un des nombreux modèles analytiques de conductivité thermique issus de la littérature. Une modélisation tri-dimensionnelle tenant compte des répartitions et des interconnexions entre phases a donc été développée. Grâce à la DEM, le modèle développé représente au plus près la géométrie complexe du milieu, en simulant un empilement aléatoire de billes sous contraintes. L'outil développé permet d'aider les élaborateurs dans le choix et le design (taux, taille, forme, interconnexion, ...) des phases en présence.

Dans les deux approches ci-dessus, la DEM a montré ses faiblesses et ses point forts. Si le nombre de particules reste limité malgré le développement des puissances de calcul, la construction de volumes élémentaires représentatifs peut être nécessaire pour la simulation de grands systèmes. Des solutions peuvent également être trouvées par l'approche multi-échelle. La méthode des éléments discrets permet de caractériser les phénomènes locaux pour définir des lois de comportements macroscopiques, tandis que la méthode des éléments finis permet de simuler le milieu granulaire comme un milieu continu (Figure 27).

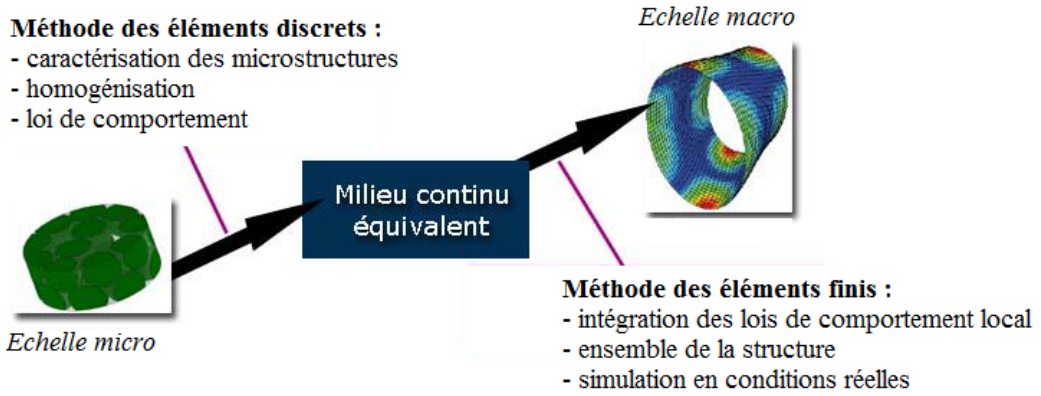

FIGURE *27 – Couplage éléments finis/éléments discrets pour une approche multi-échelle.*

3

Perspectives de recherche : de l'optimisation de procédés vers la modélisation discrète du changement de phase

3.1 Politique du projet de recherche

Dans la continuité de ce qui a déjà pu être construit depuis 13 ans, le projet de recherche que je propose s'appuie sur les concepts suivants :

- la simulation numérique constituant une aide précieuse dans la compréhension de phénomènes complexes, l'effort déjà engagé dans ce domaine pour modéliser les procédés de congélation et le comportement de milieux particulaires devra être poursuivi. Sur la thématique des procédés de congélation, le domaine d'application sera élargi à différents procédés de changement de phases, tels que la cristallisation, le séchage ou la lyophilisation. En s'appuyant sur des études en partenariat avec des industriels du secteur et en collaboration avec d'autres laboratoires français et étrangers, ce projet de recherche vise à développer des approches numériques plus performantes dans la modélisation des transferts avec apparition ou disparition de phases. A court terme, je peux citer la possible implication dans un projet FUI, piloté par la société ICAR concernant le séchage de bétons réfractaires. La tâche qui incombe au LAGEP est la modélisation des transferts et contraintes internes pour éviter la fissuration du matériau.

- les études expérimentales porteront toujours sur le développement des relations entre les qualités d'usage des produits finis et les conditions opératoires de procédé. Néanmoins, les procédés et les outils de caractérisation développés au cours de ces dernières années permettent d'élargir le champ d'application à un domaine plus vaste que celui du génie des procédés. A titre d'exemple, je peux citer la collaboration naissante avec les collègues de l'IRCELYON. La problématique concerne la compréhension des mécanismes et des conditions de formation des aérosols, particules à forte incidence sur le climat et la qualité de l'air. Les compétences complémentaires des deux partenaires permettent d'aborder la problématique à la fois d'un point de vue de la chimie de surface air/mer et d'un point de vue de la cristallisation en considérant la nucléation et la croissance des particules. Une des voies envisagées est d'étudier les cinétiques de formation de particules par cryo-microscopie en condition de pression et de température contrôlée. Ce projet vient d'être financé par l'Institut de Chimie de Lyon.

- le développement de la recherche s'appuyant sur des moyens financiers, mon souhait serait de prendre davantage de responsabilités dans le montage de projets pour l'obtention de crédits. Les thématiques telles que l'environnement ou l'énergie, soutenues par les communautés de recherche académique de la Région Auvergne – Rhône-Alpes sont des pistes

sérieuses. Un co-financement avec l'Agence de l'Environnement et de la Maîtrise de l'Énergie peut également être envisagé.

3.2 Quelques projets à court ou moyen terme

3.2.1 Purification de l'acide phosphorique sur paroi froide

Contexte

L'acide phosphorique ultra-pur est un réactif extrêmement important en microélectronique. Sa principale caractéristique réside dans sa capacité unique à résister à l'oxydation, la réduction et l'évaporation qui le rend particulièrement utile dans l'industrie de l'électronique. Actuellement, il existe deux procédés de la fabrication de l'acide phosphorique ultra-pur : (i) le procédé thermique, utilisé à l'échelle industrielle, consomme une grande quantité d'énergie, (ii) le procédé par cristallisation, qui n'est à ce jour pas développé à l'échelle industrielle vu la difficulté de contrôler la vitesse de cristallisation. Pourtant, cette technique présente de nombreux avantages : propre, sobre, écologique (pas de solvant organique, pas d'additifs chimiques) et moins énergivore par rapport au procédé thermique. C'est dans ce contexte qu'une thèse en co-tutelle avec l'université d'El Jadida au Maroc et l'OCP (l'Organisme Chérifien des Phosphates) a été proposée.

Projet

L'objectif de ce projet est de développer un procédé de fabrication d'acide phosphorique ultra-pur par intégration de la cristallisation et de la nanofiltration pour une application à l'échelle industrielle. Plusieurs travaux sur la purification de l'acide phosphorique par cristallisation sont rapportés dans la littérature. Il en ressort que la zone métastable de la nucléation primaire est très large (elle semble être de plus de 50 °C. La nucléation serait inhibée par les impuretés. De plus, lorsque la nucléation a lieu, la suspension deviendrait très visqueuse et difficilement filtrable. Pour contourner ces difficultés, la technique de cristallisation utilisée par les différents auteurs est une cristallisation en milieu fondu en suspension, avec ensemencement. Ainsi deux modes de cristallisation seront étudiés au cours de la thèse :

- la cristallisation en milieu fondu en suspension avec ensemencement en étudiant l'intérêt d'un éventuel couplage avec la nanofiltation pour limiter l'effet des impuretés ;
- la cristallisation sur paroi froide dans la continuité des travaux développés au LAGEP. Le verrou important lié à cette technologie concernera le contrôle de la nucléation. Le problème risque d'être exacerbé si, du fait de la présence des impuretés, la zone métastable est très large. Une piste pourrait être de tester l'emploi d'ultrasons.

3.2.2 Optimisation énergétique des procédés de séparation par congélation

Contexte

Les récentes recherches menées au LAGEP ont démontré la faisabilité technique du procédé de congélation sur paroi froide à l'échelle pilote d'une part pour des applications de dessalement d'eau et d'autre part pour du traitement d'effluents industriels. La technologie développée présente l'avantage indéniable d'avoir une signature environnementale bien meilleure que celles des autres technologies. Si une conduite optimisée du procédé permet d'obtenir des puretés de glace très correctes, il reste à faire la preuve de sa compétitivité économique sur le plan de la consommation énergétique. Une évaluation économique du procédé complet de dessalement, basées sur des points de fonctionnement expérimentaux, a montré que la consommation énergétique d'une petite installation pourrait être très faible en utilisant une machine frigorifique fonctionnant entre l'unité de ressuage et l'unité de congélation. Il serait alors intéressant d'étudier la rentabilité du

couplage du procédé par congélation à une pompe à chaleur permettant d'agir à des températures comprises entre -10 ° C et +10 ° C.

Projet

L'objectif de cette étude vise à définir une technologie rentable de traitement de l'eau en couplant le procédé par congélation sur paroi froide à une pompe à chaleur permettant d'agir à des températures comprises entre -10 ° C, et +10 ° C. La démarche envisagée pour ce travail, en collaboration avec les collègues automaticiens du laboratoire, se décompose en trois grandes étapes :

- la première consistera à coupler la simulation existante du procédé (transfert de masse et de chaleur avec changement de phase) à la modélisation « Hardware-in-Loop » d'une pompe à chaleur. Il s'agit d'une méthode de simulation caractérisée par l'association de véritables composants, connectés à une partie simulée. L'originalité de ce système est de pouvoir simuler virtuellement le fonctionnement de la pompe à chaleur, de permettre des conditions d'essais poussées à l'extrême et de bénéficier d'une économie de temps et d'argent. Le modèle process + pompe à chaleur permettra de définir en mode simulation intégrale les conditions optimales de séparation.

- la seconde étape consistera à retirer un degré de simulation en intégrant l'émulateur « Hardware-in-Loop » au procédé réel de congélation. Ces tests permettront notamment de prendre en compte les problématiques techniques (temps de réponse, initialisation du modèle, incertitudes paramétriques du modèle, ...).

- enfin, une série d'expériences sera développée pour étudier les avantages et les inconvénients des différentes solutions proposées, en termes de faisabilité technologique, de coût énergétique et de qualité de la séparation.

L'enjeu est double : (i) d'un point de vue technologique, il s'agit de définir une technologie de production de froid optimale (en y incluant les fonctionnements assistés par énergie solaire par exemple), (ii) d'un point de vue scientifique, un modèle dynamique du couplage de la pompe à chaleur avec le procédé de congélation pourrait être proposé en vue de sa commande pour garantir une pureté de glace optimale.

3.2.3 Modélisation de poudre en compression

Contexte

L'équipe pharmaco-technique du LAGEP s'intéresse depuis plusieurs années au comportement de poudres en compression. Deux récentes thèses [59, 60] ont fait état de transformations physiques de principes actifs induites par les étapes de mises en forme telles que la compression. Ces transformations sont problématiques dans le domaine pharmaceutique, puisqu'elles peuvent avoir des conséquences sur les cinétiques de dissolution, sur la biodisponibilté et sur la stabilité du principe actif.

Les investigations expérimentales menées au cours de ces deux thèses ont permis d'évaluer l'impact des conditions opératoires (procédé et formulation) sur la transition polymorphique de la caféine Forme I en Forme II. Par ailleurs, il a été possible d'établir un lien entre le procédé de

59. S. Hubert. Transitions de phases solides induites par un procédé de compression directe : application à la caféine et à la carbamazépine. PhD thesis, Université Claude Bernard Lyon 1, 2012.

60. A. Juban. Transformation Induite au cours d'un Procédé Industriel (TIPI) de compression directe : transition polymorphique de la caféine et propriétés physiques des comprimés. PhD thesis, Université Claude Bernard Lyon 1, 2016.

compression et les propriétés mécaniques du comprimé telles que la contrainte à la rupture et la dureté. Si les résultats expérimentaux sont encourageants et permettent une avancée certaine dans la compréhension des mécanismes de transitions de phases, il est à noter qu'une des thèses a nécessité la fabrication de plus de 4000 comprimés. Pour extrapoler les résultats à d'autres formulations et d'autres procédés, le développement d'un modèle semble utile pour limiter les essais expérimentaux et accéder à des grandeurs difficilement mesurables par l'expérience.

Projet

Dans cette application, le but de la modélisation discrète est de simuler le réseau de forces intergranulaires pour estimer les températures locales du lit de poudre. A titre d'exemple, lors du projet sur l'étude de la décharge des silos, nous avions modélisé ce phénomène pour un système en écoulement. La Figure 28b montre l'influence de la vitesse de vidange imposée sur la température de la paroi conique du silo au cours de l'écoulement. L'augmentation de la température avec la vitesse peut être liée à l'augmentation des vitesses de glissement et à un transfert de chaleur favorisé par la conductance dans des chaînes de forces dominantes (Figure 28a).

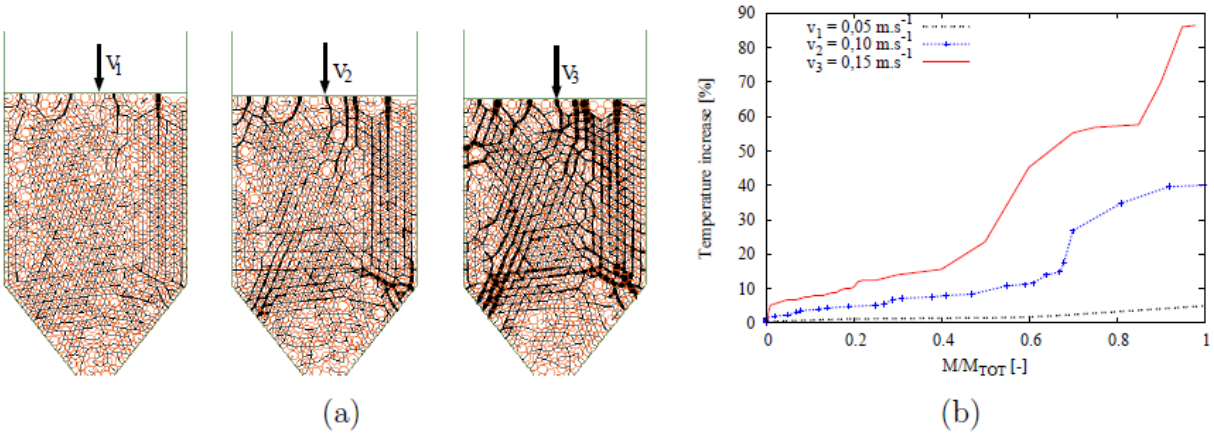

FIGURE *28 – (a) Influence de la vitesse de vidange imposée sur les chaînes de forces, (b) Évolution pour différentes vitesses de vidange de la température sur la paroi conique en fonction de la fraction de poudre écoulée.*

La figure (Figure 28a) montre également qu'une approche continue utilisant des modèles phénoménologiques macroscopiques ne peut pas reproduire correctement l'évolution des contraintes et des déformations à cause des chemins préférentiels suivis par les chaînes de forces. Dans le cas de la compression de poudre, l'intérêt de la méthode des éléments discrets est de prédire un effort localisé au sein d'un milieu granulaire sollicité mécaniquement en modélisant l'interaction entre les grains. De plus, il est envisageable de simuler les différentes étapes du procédé de compression : le remplissage, le tassement et la densification. Si les deux premières phases du procédé peuvent se décrire par des lois de contact plastiques très répandues dans la communauté des milieux granulaires, la difficulté réside dans la modélisation de la densification en fin de compression qui nécessite des lois de contacts pour des valeurs élevées de compacité.

3.2.4 Modélisation de la microstructure cristalline

Contexte

Si les modèles de cristallisation développés au cours de mes activités de recherche permettent de décrire de façon macroscopique des cinétiques de croissance, ils font l'objet d'hypothèses fortes basées sur des considérations thermodynamiques à l'équilibre. En outre, ils ne permettent pas

de décrire les caractéristiques structurales du matériau à l'échelle locale. En effet, ces modèles s'appuient sur la théorie classique de nucléation dont la morphologie cristalline est une donnée d'entrée. Cependant, des instabilités de croissance peuvent se produire au cours du processus de cristallisation pouvant donner naissance à une microstructure complexe. Plusieurs questions restent donc sans réponse sur l'ensemble de mon travail : quelle est précisément la morphologie des cristaux ? Comment-est elle générée ? Quels sont les processus de nucléation et de croissance ?

Projet

Si des travaux expérimentaux sont en cours, le développement d'un modèle s'avère nécessaire pour mieux comprendre les mécanismes mis en jeu. L'idée de base consiste à construire étape par étape un modèle local afin de suivre, à l'échelle mésoscopique, la dynamique des interfaces solution-cristal. La méthodologie adaptée pour cette démarche est la simulation en champ de phase, couramment utilisée dans le domaine de la solidification des alliages. Ces méthodes visualisent toute séparation de phases non pas comme une surface rigoureusement raide, mais comme une interface diffuse. Les phases en présence ainsi que leur interface sont décrites à l'aide d'une fonction, qui prend une valeur constante dans chacune des phases (correspondant à la phase cristalline et à la phase liquide). On passe ainsi d'un modèle discontinu à un champ continu dans l'espace et dans le temps (appelé champ de phase), qui permet de déterminer en tout point et en tout temps l'état du système. La position de l'interface est ainsi implicitement donnée par un contour de valeurs constantes des variables du champ de phase. Il n'est alors pas nécessaire de définir des conditions d'équilibre thermodynamique à l'interface mobile.

D'un point de vue modélisation, en plus des équations classiques de conservation de la masse, de l'énergie et de la quantité de mouvement, s'ajoute une nouvelle équation sur le champ de phase, basée sur les concepts de la thermodynamique irréversible qui assure la minimisation de l'énergie libre. Contrairement aux modèles microscopiques tels que la dynamique moléculaire, dans lesquels le système est décrit à l'échelle de l'atome, en champ de phase, les systèmes seront décrits uniquement par des variables thermodynamiques macroscopiques telles que les concentrations ou la température. Ceci permet d'incorporer tous les phénomènes que l'on peut rencontrer lors d'une transformation de phase. La souplesse de cette approche est particulièrement bien adaptée pour traiter des problèmes de croissance cristalline.

Deuxième partie

Activités pédagogiques et administratives

1

Activités pédagogiques

1.1 Spécificités des IUT

De 2004 à 2011, j'ai enseigné au département GCGP de l'IUT de l'Aisne. Depuis 2011, je suis rattachée au département GCGP de l'IUT Lyon1. Les deux IUT ont chacun leurs propres spécificités :

- à St Quentin, le département se trouve doublement délocalisé, par rapport à Amiens (centre principal de l'Université de Picardie Jules Verne) et par rapport à Laon (direction de l'IUT de l'Aisne). Cela nécessite une forte implication de l'équipe pédagogique dans les tâches administratives. Néanmoins, il permet de compléter l'offre de formation dans la région, puisqu'il n'y a pas de formations concurrentes à bac + 2 dans le domaine de la chimie dans un rayon de 60 kilomètres. En revanche, l'absence de campus (à l'époque) induisait un déficit en terme d'images et de vie universitaire, rendant le recrutement parfois difficile.
- à Lyon, la situation permet de bénéficier des moyens pédagogiques et matériels de l'Université (outils informatiques, installations sportives, restaurants universitaires, activités culturelles, ...) et de l'attractivité de la région Rhône-Alpes, important bassin d'emploi dans le secteur de la chimie. Mais le faible nombre d'enseignants permanents induit une limitation des effectifs.

Dans les deux départements d'IUT, le taux d'encadrement est d'environ 55%. Ce faible taux nécessite un investissement de chacun, et plus particulièrement des enseignants de la spécialité, pour pallier le déficit. Ainsi, depuis 2004, en plus de mon service statutaire, j'effectue chaque année entre 150 heures et 200 heures complémentaires. J'interviens dans les trois années de formation (1A, 2A et LPro). A titre d'exemple, en 2007-2008, j'ai effectué 342H équivalent TD, réparties en 24% de cours magistraux, 40% de travaux dirigés et 36% de travaux pratiques. En 2015-2016, j'ai effectué 456H équivalent TD, réparties en 7% de cours magistraux, 33% de travaux dirigés et 60% de travaux pratiques.

Malgré la charge pédagogique importante, j'apprécie le fonctionnement des IUT. Les moyens développés et l'aspect professionnalisant permettent d'enseigner de façon théorique et pratique le Génie des Procédés en lien étroit avec le milieu industriel.

1.2 Enseignements en DUT

Mes enseignements sont dispensés dans le cadre du programme pédagogique national (PPN) du DUT GCGP. Au cours des années, mes enseignements ont balayé une grande partie du programme dans le domaine du génie des procédés sous forme de cours magistraux, de travaux

dirigés et/ou de travaux pratiques.

Le tableau 2 présente la liste des modules enseignés, en rouge ceux enseignés en continu de 2004 à 2011 à l'IUT de l'Aisne, en bleu ceux enseignés en continu de 2013 à aujourd'hui à l'IUT de Lyon1 et en noir ceux enseignés de façon occasionnelle en fonction des besoins (disponibilités des vacataires, dédoublement de groupes TD/TP, semestrialisation, remplacement, ...).

	Module du PPN 2013		Volume horaire étudiant		
Année	**Référence**	**Nom**	**Cours**	**TD**	**TP**
1A	1102	Mécanique des fluides	–	–	40H
	1103	Bilans	10H	14H	–
	2101	Thermodynamique	–	28H	–
	2103	Transferts thermiques	20H	28H	–
	2102-2104	TP Thermodynamique - Thermique	–	–	48H
	2105	Opérations solide fluide	14H	24H	–
	2106	TP Opérations solide fluide	–	–	24H
	2107	Environnement	–	–	12H
2A	3101	Transfert de matière	25H	35H	–
	3103	TP Transfert de matière	–	–	64H
	33P06C	Simulation et conduite des procédés	–	–	20H
	41P02C	Bureau d'études	–	–	40H
	41P06C	Technologies des procédés	6H	8H	–

Tableau 2 – Modules enseignés en DUT GCGP. En rouge, en continu de 2004 à 2011. En bleu, en continu de 2013 à 2017.

Dans les séances de TP, j'ai essayé de sensibiliser les étudiants aux bonnes pratiques de laboratoire (rédaction du cahier de laboratoire, tri des déchets, sécurité en laboratoire, ...) et de développer l'utilisation d'outils informatiques de simulation (utilisation de Prosim par exemple). Pour l'enseignement des cours magistraux, j'ai écrit un polycopié dans chacun des modules dont j'ai assuré l'enseignement en continu. Pour inciter les étudiants à approfondir les notions développées en cours de façon autonome, j'ai développé depuis 2016 des modules d'auto-évaluation en ligne. La participation est très correcte, mais les retombées sont difficilement quantifiables.

1.3 Enseignements en LPro

Dans la LPro "Métiers de l'eau" de St Quentin sur la période 2006-2011, j'ai mis en place le nouveau cours "Traitement des effluents industriels" (6H CM - 8H TD - 48H TP). Les effluents industriels présentent souvent une charge polluante élevée et nécessitent des traitements complémentaires ou de substitution aux traitements biologiques classiques. Les principales techniques de traitement des effluents liquides, relatives aux opérations unitaires de génie des procédés, sont présentées dans ce module. Une partie du cours est également consacrée aux différentes techniques de dessalement de l'eau de mer. Dans le cadre de ce module, j'organisais une visite au salon Pollutec à Paris. En parrallèle des cours magistraux, j'ai développé six TP dont deux spécifiques à ce module (dessalement d'eau de mer par osmose inverse et Traitement d'une solution de permanganate par oxydo-réduction, précipitation puis décantation).

Dans la LPro "Procédés d'élaboration et de production des solides" de Lyon, j'enseigne depuis 2012 un module sur la connaissance des propriétés des poudres et sur leur manipulation (8H CM - 16H TD). Ce sont les propriétés d'un ensemble de particules qui déterminent le comportement

d'une poudre et son aptitude à l'écoulement, au mélange ou à la fluidisation. La caractérisation de ces propriétés comportementales est plus spécifiquement abordée dans ce module. Une partie est également consacrée à l'étude de la fluidisation d'un lit particulaire.

1.4 Enseignements en Faculté de Pharmacie

Depuis 2016, j'enseigne un module de thermique de 28H équivalent TD (50% CM - 50% TD) aux étudiants de 4ème année de l'Institut des Sciences Pharmaceutiques et Biologiques de l'Université de Lyon1. Le cours de thermique enseigné en DUT a été adapté et enrichi pour les besoins des étudiants en pharmacie.

1.5 Activités de suivi

Chaque année, une partie de mes activités d'enseignement est aussi consacrée à l'encadrement de projets tutorés (en DUT et en LPro) nécessitant un suivi régulier de l'avancement du travail. Par ailleurs, j'assure le suivi de stages (en DUT) et d'apprentis (en LPro) en entreprise. Cela se traduit classiquement par une prise de contact régulière avec le tuteur entreprise, une visite sur site dans la mesure du possible, ainsi que l'évaluation d'un rapport et d'une soutenance.

En moyenne, je suis 3 groupes de projet tutoré par an (2 en DUT et 1 en LPRO), 3 à 5 stages et 2 à 3 alternants de LPRO.

2

Activités d'encadrement

Les stages listés dans les paragraphes suivants se sont déroulés soit à l'IUT, soit au laboratoire (LAGEP ou LTI) pour bénéficier des ressources matérielles et/ou de compétences propres à chaque site. L'encadrement et l'autonomie sont bien entendus très dépendants du niveau d'études du stagiaire ou du thésard, mais j'ai essayé pour chacun d'entre eux de contribuer au bon déroulement de leur apprentissage.

2.1 Stages de 2ème année de DUT et LPRO (3 mois)

Année	Nom	Titre	Financement	Encadr.
2008	T.X. Ho	Mesure expérimentale de conductivité thermique de purée	Projet région Picardie	100%
2010	H.P. Nguyen	Réchauffement d'une bouteille de vin par cristallisation d'un mélange eau/acétate de sodium	Le Creuset	100%
2012	Y. Ros	Mise à jour du document unique et actions de prévention	IUT Lyon1	100%
2013	Y. Goursaud	Mise au point d'un pilote de congélation	LAGEP	30%
2014	K. Bazin	Traitement de l'eau par congélation en régime dynamique	LAGEP	30%
2018	V. Chapot	Etude de la lyophilisation de probiotiques	LAGEP	30%

Tableau 3 – Liste des stages de niveau bac+2.

A ces stages s'ajoute en 2017-2018 l'encadrement de T. Brunier, étudiant en LPRO qui effectue son alternance à 50% du temps chez l'industriel et à 50% du temps au LAGEP. Son sujet porte sur la caractérisation de l'écoulement de poudres industrielles.

2.2 Stages Master

Année	Nom	Titre	Financement	Encadr.
Niveau bac + 4				
2014 (15 jours)	C. Genoulaz B. Leroy P.G. Remy	L'effet Mpemba : L'eau chaude gèle-t-elle plus vite que l'eau froide ?	non (Projet CPE)	50%
2014 (1 mois)	A. El Arabi	Étude expérimentale et modélisation du séchage convectif d'un produit alimentaire	non (Projet CESI)	50%
2014 (2 mois)	E. Daleka	Étude de la congélation de sorbet par ultrasons	bourse Erasmus + obtention d'une bourse UCBL	50%
Niveau bac + 5				
2008 (6 mois)	G. Dehaussy	Introduction de la thermique dans un code Eléments Discrets 3D	LTI	20%
2013 (6 mois)	M. Rodriguez	Construction du diagramme de phase eau-acétone	bourse Erasmus	60%
2014 (6 mois)	L. Bouiaicha	Étude des transitions et de la variation de la structure interne de produits biologiques pendant le séchage	LAGEP	40%
2016 (6 mois)	V. Hong	Modeling of drying food	LAGEP	40%
2018 (6 mois)	M. Rouabah	Modélisation du séchage par la DEM	EZUS Lyon1	30%
2018 (6 mois)	C. Chatre	Etude de la nucléation des aérosols	Institut Chimie Lyon	50%

Tableau 4 – Liste des stages de niveau Master.

2.3 Encadrements de thèses

Co-encadrement de la thèse de Viet Dung Nguyen (2006-2009), "Modélisation par la Méthode des Éléments Discrets des phénomènes thermomécaniques dans les interfaces de contact."
Date de soutenance : 5 novembre 2009. Projet financé par le Conseil Régional de Picardie.
Encadrement : J. Fortin (30%) – E. Bellenger (25%) – M. Guessasma (25%) – **C. Cogné (20%)**

Co-encadrement de la thèse de P.U. Nguyen (2006-2010), "Surgélation par le vide de purées de légumes". Date de soutenance : 4 Mars 2010. Projet financé par le Conseil Régional de Picardie.
Encadrement : J.L. Lanoisellé (60%) - **C. Cogné (20%)** - E. Van Hecke (20%)

Co-direction de la thèse T. Htira (2012-2016), "Traitement d'eaux usées industrielles par congélation sur paroi froide". Date de soutenance : 23 Septembre 2016. Bourse MENRT.
Encadrement : D. Mangin (40%) – **C. Cogné (40%)** – E. Gagnière (20%)

Co-encadrement de la thèse de P. Verlhac (2015-2018), "Étude et Optimisation des Cycles de Lyophilisation de Probiotiques". Bourse MENRT.
Encadrement : S. Vessot (40%) – G. Degobert (40%) – **C. Cogné (20%)**

2.4 Encadrements de Post-doctorats

Encadrement du post-Doctorat de N. Ferguen (2010-2011), "Modélisation du transfert thermique dans des composites Al/Al_2O_2.
Financement FEDER, programme européen INTERREG IV France-Wallonie-Vlaanderen. Encadrement : **C. Cogné (40%)** – E. Bellenger (30%) – M. Guessasma (30%)

Encadrement du post-Doctorat de S. Labouret (2013), "Contrôle par ultrasons de la nucléation de la glace pour l'optimisation des procédés de congélation et de lyophilisation"
Financement ANR. Encadrement : R. Peczalski (70%) – **C. Cogné (30%)**

Encadrement du post-Doctorat de S. Labouret (2014), "Procédé d'intensification de la récupération des phosphates dans les eaux usées par précipitation de struvite"
Financement Programme européen Life+. Encadrement : D. Mangin (60%) – **C. Cogné (40%)**

3

Activités administratives et responsabilités collectives

3.1 Activités administratives

D'un point de vue administratif, les spécificités du site de St-Quentin comme sa structure modeste ou sa délocalisation m'ont offert l'opportunité de prendre rapidement des responsabilités administratives telles que la création et l'animation de formations.

3.1.1 Direction des études

Entre 2004 et 2007, j'ai assuré la direction des études du département GCGP. J'ai effectué les tâches classiques incombant à cette responsabilité : gestion du cursus des étudiants, animation pédagogique, orientation après DUT, suivi des cohortes, participation à la mise en place de la semestrialisation, etc.

3.1.2 Responsabilité de formation

De 2004 à 2006, j'ai porté le dossier de demande d'habilitation d'une licence professionnelle intitulée "Métiers de l'Eau". Cette tâche a consisté à concevoir le projet en relation avec les besoins industriels, à créer une équipe pédagogique et à développer un partenariat avec les professionnels du secteur (académiques et industriels). C'est grâce à l'investissement de l'ensemble des collègues de l'époque que la LPro a été ouverte en septembre 2006 et a été réhabilitée avec succès en 2008.

De 2006 à 2010, j'ai assuré la responsabilité de cette de formation : gestion du cursus des étudiants, animation pédagogique, gestion des emplois du temps, suivi des cohortes, promotion de la formation, renforcement du partenariat industriel, ouverture d'une section d'apprentissage (en 2007), réhabilitation de la formation (2008), organisation de visites d'entreprises et salons...

Depuis 2016, j'assure la co-responsabilité de la licence professionnelle "Procédés d'élaboration et de production des solides divisés" avec Denis Mangin.

3.1.3 Assistante de prévention

Depuis 2012, je suis assistante de prévention pour le département GCGP de l'IUT Lyon1. J'assiste et conseille le chef de département dans la démarche d'évaluation des risques, ainsi que dans la mise en place des règles d'hygiène et de sécurité. De plus, j'évalue et recense les risques avec l'ensemble des permanents, propose des actions de préventions et/ou de corrections et assure leur mise en œuvre. Enfin, je mets à jour annuellement le document unique d'évaluation des risques professionnels du département.

3.1.4 Responsable poursuite d'études

Depuis 2012, je suis responsable "poursuite d'études" pour le département GCGP de l'IUT Lyon1. Dans ce cadre, plusieurs tâches m'incombent :

- informer les étudiants des différents parcours d'études qui s'offrent à eux après l'obtention du DUT GCGP,
- être en lien étroit avec la direction du site pour l'organisation d'un forum poursuite d'études,
- inviter des instituts à venir présenter leurs formations (par l'intermédiaire d'"anciens" du département notamment),
- proposer un entretien individuel pour orienter au mieux l'étudiant en fonction de ses vœux et de ses capacités,
- coordonner la gestion des dossiers de poursuite d'études.

3.2 Responsabilités collectives

Tout au long de ma carrière, j'ai participé à différentes activités d'ordre collectif pour le laboratoire ou pour l'IUT.

3.2.1 Conseil, comité, commission

- Membre élu du Conseil d'IUT Lyon1 de 2014 à 2017.
- Membre interne de comités de sélection pour des postes de MCF : Université de Picardie en 2009 et en 2010 (poste 0316), Université de Lyon1 en 2014 (poste 4247), en 2015 (poste 4297), en 2016 (poste 4359), en 2018 (2 postes)
- Membre externe de comités de sélection : INSA Lyon en 2017 (poste 4187 et 4188), UTC en 2017 (poste 4094), Université d'Artois (2009).
- Membre externe de la commission de spécialistes de la 62ème section CNU de l'Université de Valenciennes et du Hainaut-Cambrésis (2007-2008).
- Membre du conseil de département GCGP de l'IUT de l'Aisne (2004-2011) et de l'IUT Lyon1 de 2011 à aujourd'hui.
- Membre de l'Union en Génie des Procédés du Nord (UGéPé-Nord) de 2009 à 2011.
- Membre de la Société Française de Thermique de 2005 à aujourd'hui.
- Membre du groupe "Formation" de la Société Française de Génie des Procédés depuis 2014 présidé par Marie Debacq.

3.2.2 Animation et diffusion scientifique

De 2004 à 2015, j'ai contribué à la diffusion scientifique auprès de primaires (CM1-CM2) par la participation à la fête de la science à l'IUT de Lyon1 ou par l'accueil d'élèves à l'IUT de l'Aisne. L'intérêt de cette action permet aux étudiants de DUT de présenter la chimie au quotidien et de vulgariser leurs connaissances, aux élèves de primaires de découvrir la chimie et de manipuler dans les laboratoires, et au département de se faire connaître à travers différentes actions de communication.

Dans le cadre du groupe "Formation" de la Société Française de Génie des Procédés, j'ai participé à l'organisation de la journée "Modification des programmes : quel impact sur les formations en génie des procèdes du bac au master ?" le 15/2015/2015 au CNAM à Lyon. De plus, je suis membre du projet "Structuration de la page d'accueil UNIT en Génie des Procédés et amélioration de l'attractivité du Génie des Procédés" financé par UNIT avec Hélène Desmorieux (UCBL), Marie Debacq (CNAM, Paris), Eric Schaer (ENSIC, Nancy), Nouria Fatah (ENSCL, Lille), Nicolas Reignier (ENSCBP, Bordeaux) et Mallorie Tourbin (ENSIACET). Ce projet a donné lieu à une communication orale [ACTN27]. Le site *http ://genie-des-procedes.fr* a été crée dans ce cadre.

En recherche, l'animation et la diffusion scientifique sont des activités récurrentes de notre travail. A titre d'exemple, je peux citer quelques faits marquants :

- 12 mai 2016 à Lyon : organisation du workshop "Récupération du phosphore sous forme de struvite - Contraintes réglementaires pour son utilisation comme engrais" dans le cadre du projet PHORWater. Ce workshop, présidé par Denis Mangin (LAGEP) a réuni environ 60 participants (universitaires, industriels du secteur et collectivités locales) de 7 nationalités différentes.

- du 24 au 27 aout 2014 à Lyon : membre du comité local d'organisation du 19^{th} International Drying Symposium. Ce congrès, présidé par Julien Andrieu, a réuni 330 participants de 25 nationalités différentes.

- du 3 au 6 juin 2014 à Lyon : membre du comité d'organisation du Congrès Français de Thermique (cf. Figure 29), intitulé "Approches multi-échelles pour la thermique, l'énergétique et le Génie des Procédés". Ce congrès, présidé par Pr. Jocelyn Bonjour (CETHIL) et Pierre Laurent (LAGEP), a réuni environ 250 participants.

FIGURE *29 – Congrès SFT 2014.*

- 1er décembre 2009 à St Quentin : organisation d'une conférence de presse dans le cadre du projet PRISTIMAT qui s'est traduit par différents articles dans la presse locale et régionale (cf. Figure 30 à titre d'exemple) ainsi que des entretiens diffusés sur deux stations de radio.

- janvier 2008 : organisation du séjour de Rani Devi, Professeur Indienne invitée pendant un mois au LTI (dossier de demande, accueil, séjour scientifique). Lors de sa venue, en plus d'enseigner à l'IUT de l'Aisne, Rani Devi a amorcé une collaboration en recherche dans le domaine du traitement de l'eau par adsorption.

FIGURE *30 – Extrait des titres d'articles publiés à l'issue de la conférence de presse du projet PRISTIMAT.*

3.2.3 Jurys de thèse

Thouaïba HTIRA : Doctorat de l'Université de Lyon, spécialité Génie des Procédés, soutenue le 23/09/2016.

Titre : Traitement d'eaux usées industrielles par congélation sur paroi froide.

Jury composé de R. Peczalski (PU, UCBL - Président), H. Muhr (DR, Université de Lorraine - Rapporteur), N. Candoni (PU, Université Aix-Marseille - Rapporteure), Y. Cartigny (MCF, Université de Rouen - Examinateur), J.M. Bossoutrot (Docteur Ingénieur, Arkéma - Examinateur), D. Mangin (PU, UCBL - Directeur de thèse), C. Cogné (MCF, UCBL - Co-directrice de thèse), E. Gagnière (MCF, UCBL - Co-directrice de thèse).

Phuong-Uyen NGUYEN : Doctorat de l'Université de Technologie de Compiègne, spécialité Génie des procédés industriels et développement durable, soutenue le 04/03/2010.

Titre : Surgélation par le vide de purées de légumes.

Jury composé de D. Clausse (PU, UTC - Présidente et co-directrice de thèse), J. Andrieu (PU, UCBL - Rapporteur), J.P. Dumas (PU, Université de Pau et des Pays de l'Adour - Rapporteur), J.L. Lanoisellé (PU, UTC - Directeur de thèse), E. Van Hecke (MCF, UTC - Examinatrice), C. Cogné (MCF, UPJV - Examinatrice), A. Maureaux (Directeur scientifique, Groupe Bonduelle - membre invité).

3.2.4 Gestion administrative et financière de contrats

Sur la période 2004-2011, j'ai coordonné pour le LTI les projets "SULTRAPID" et "PRISTIMAT", à la fois dans le montage du dossier, puis dans la gestion du projet.

Le projet "SULTRAPID" a été financé par le Conseil de Picardie et Bonduelle. Pour le laboratoire, ce projet représentait un financement de 23500 €, qui a permis entre autre l'achat de la

licence du logiciel Comsol.

Le projet "PRISTIMAT" a été financé par le programme européen transfrontalier INTERREG IV. Pour le laboratoire, ce projet représentait un budget total de 221000 €, dont 7% de fonds propres, 40% de FEDER et 53% apporté par la valorisation de salaire d'enseignants-chercheurs. Le fonds FEDER a notamment permis d'embaucher un post-doctorat pendant 18 mois. D'un point de vue administratif, ce contrat a nécessité un suivi administratif et financier assez lourd.

3.2.5 Expertises de projets et révisions d'articles

Révision d'articles : Journal of Refrigeration, Powder Technology, Journal of Food Engineering (environ 3 par an).

Comité de relecture : Congrès Français de Thermique, Congrès Français de Génie des Procédés.

Expertises de projets : ECOS Nord 2014 et 2015 (Évaluation orientation de la COopération Scientifique) avec Denis Mangin.

Production scientifique

[ACL] : Articles dans des revues internationales avec comité de lecture

[ACL1] (page 79) **C. Cogné**, J. Andrieu, P. Laurent, A. Besson, J. Nocquet, Experimental data and modelling of thermal properties of ice creams, *Journal of Food Engineering*, 58(4), 331-341, 2003.

[ACL2] (page 90) **C. Cogné**, P. Laurent, J. Andrieu, F. Ferrand, Experimental data and modeling of ice cream freezing, *Chemical Engineering Research and Design*, 81(A), 1129-1135, 2003.

[ACL3] (page 97) A. Caillet, **C. Cogné**, J. Andrieu, P. Laurent, A. Rivoire, Characterization ofice cream structure by direct optical microscopy. Influence off reezing parameters, *Lebensmittel-Wissenschaft und-Technologie*, 36(8), 743-749, 2003.

[ACL4] (page 104) M.A. Bolzinger, **C. Cogné**, L. Lafferère, F. Salvatori, M. Zanetti, P. Ardaud, F. Puel, Effects of surfactants on crystallization of ethylene glycol distearate in oil in water emulsion, *Colloids and Surface A*, 299, 93-100, 2007.

[ACL5] (page 112) V.D. Nguyen, J. Fortin, M. Guessasma, E. Bellenger, **C. Cogné**, Thermomechanical modelling of friction effects in granular flows using the discrete element method, *Journal of Mechanics of Materials and Structures*, 4 (2), 413-426, 2009

[ACL6] (page 127) V.D. Nguyen, **C. Cogné**, M. Guessasma, E. Bellenger, J. Fortin, Discrete modeling of granular flow with thermal transfer : application to the discharge of silos, *Applied Thermal Engineering*, 29, 1846-1853, 2009.

[ACL7] (page 135) N. Ferguen, **C. Cogné**, M. Guessasma, E. Bellenger, C. Pélegris, A numerical model for predicting effective thermal conductivities of alumina/Al composites, *Journal of Composite Materials* , 27, 1-11, 2012.

[ACL8] (page 146) **C. Cogné**, P.U. Nguyen, J.L. Lanoisellé, E. Van Hecke, D. Clausse, Modeling Heat and Mass Transfer During Vacuum Freezing of Puree Droplet, *International Journal of Refrigeration*, 36(4), 1319-1326, 2013.

[ACL9] (page154) O. Louisnard, **C. Cogné**, S. Labouret, W. Montes-Quiroz, R. Peczalski, F. Baillon, F. Espitalier, Prediction of the acoustic and bubble fields in insonified freeze-drying vials, *Ultrasonics Sonochemistry*, 26, 186-192, 2015.

[ACL10] (page 161) **C. Cogné**, S. Labouret, R. Peczalski, O. Louisnard, F. Baillon, F. Espitalier, Theoretical model of ice nucleation induced by inertial acoustic cavitation. Part 1 : Pressure and temperature profiles around a single bubble, *Ultrasonics Sonochemistry*, 29, 447-454, 2016.

[ACL11] (page 169) **C. Cogné**, S. Labouret, R. Peczalski, O. Louisnard, F. Baillon, F. Espitalier, Theoretical model of ice nucleation induced by inertial acoustic cavitation. Part 2 : Number of ice nuclei generated by a single bubble, *Ultrasonics Sonochemistry*, 28, 185-191, 2016.

[ACL12] (page 176) T. Htira, **C. Cogné**, E. Gagnière, D. Mangin, Determination of the Solid Liquid Phase Diagram of the Binary System Propionic Acid/Water, *Journal of Chemical Engineering Data*, 61, 806-812, 2016.

[ACL13] T. Htira, **C. Cogné**, E. Gagnière, D. Mangin, Experimental study of industrial wastewater treatment by freezing, *Journal of Water Process Engineering*, acceptée.

[ACLN] : Autres articles

[ACLN1] **C. Cogné**, J. Andrieu, P. Laurent, Étude et modélisation de la congélation des crèmes glacées commerciales, *Revue Générale du Froid*, 1048, 49-52, 2004.

[ACLN2] J.L. Lanoisellé, A. Maureaux, E. Van Hecke, P.U. Nguyen, E. Baranowski, **C. Cogné**, D. Clausse, Surgélation par le vide des bioproduits : application aux purées de légumes, *Revue Générale du Froid*, 1118, 43-53, 2011.

[ACLN3] Y. Mandri, A. Rich, D. Mangin, A. Rivoire, C. Bebon, T. Bounahmidi, A. Bouhaouss, **C. Cogné**, Dessalement De L'eau De Mer Par Congélation, *Revue Générale du Froid*, 1133, 58-69, 2013.

[OS] : Chapitres d'ouvrages

[OS1] F. Baillon, F. Espitalier, **C. Cogné**, R. Peczalski, O. Louisnard, "Chapter 28 : Crystallization and Freezing Processes Assisted by Power Ultrasound", In *Power Ultrasonics (1st Edition) : Applications of High-Intensity Ultrasound*, Woodhead Publishing Series in Electronic and Optical Materials. Cambridge : Juan A. Gallego-Juárez and Karl Graff, 2015.

[BRE] : Brevet

[BRE1] M-A. Bolzinger, F. Puel, L. Lafferrere, **C. Cogné**, F. Salvatori, P. Ardaud, M. Zanetti ; Cristaux à base de distéarate d'éthylène glycol, leur procédé de préparation et leurs utilisations ; FR2906715 (B1), 2008-11-21 ; WO2008040770 (A1), 2008-04-10 ; RHODIA Recherches et Technologies-UCBL-CNRS.

[BRE2] J. Ferrer, A. Seco, A. Bouzas, R. Barat, L. Borras, N. Marti, L. Pastor, E. Morales, S. Donate, S. Grau, D. Mangin, **C. Cogné**, S. Labouret, E. Gagnière ; Modèle d'utilité "Reactor de cristalización para la obtención de estruvita de las aguas residuales" pour l'Espagne déposé par l'Université de Valence en 2016.

[ACTI] : Communications avec actes dans un congrès international [61]

[ACTI1] **C. Cogné**, P. Laurent, J. Andrieu, Heat transfer model of commercial ice cream freezing, *International Congress on Engineering and Food ICEF9*, Montpellier (France), 2004. Communication orale.

[ACTI2] V.D. Nguyen, J. Fortin, M. Guessasma, E. Bellenger, **C. Cogné**, P. Coorevits, Heat Transfert Modeling by Discrete Element Method, *International Conference LMS2007*, Palaiseau (France), 2007. Communication orale.

[ACTI3] V.D. Nguyen, **C. Cogné**, J. Fortin, M. Guessasma, E. Bellenger, Dynamic thermomechanical modeling for multicontact systems, *9th US National Congress on Computational Mechanics*, San Francisco (USA), 2007. Communication orale.

[ACTI4] V.D. Nguyen, **C. Cogné**, J. Fortin, M. Guessasma, E. Bellenger, Modeling of heat generation by friction in a packed bed, *International Center of Heat and Mass Transfer*, Marrakech (Maroc), 2008. Communication orale.

[ACTI5] V.D. Nguyen, **C. Cogné**, M. Guessasma, E. Bellenger, J. Fortin, Discrete modeling of granular shear flows : parameter study, *World Congress on Computational Mechanics and 5th European Congress on Computational Methods in Applied Sciences and Engineering*, Venise (Italie), 2008. Communication orale.

[ACTI6] P.U. Nguyen, **C. Cogné**, J.L. Lanoisellé, D. Clausse, Freezing of puree droplet due to evaporation : heat and mass transfer modeling, *The 14th IUFoST World Congress of Food Science and Technology*, Pékin (Chine), 2008. Communication orale.

[ACTI7] E. Van Hecke, P.U. Nguyen, **C. Cogné**, J.L. Lanoisellé, D. Clausse, Potential application of calorimetry for control and optimization of a new process, *9th Mediterranean Conference on Calorimetry and Thermal Analysis*, Marseille (France), 2009. Communication orale.

[ACTI8] C. Pelegris, **C. Cogné**, Étude du changement de phase d'une solution d'acétate de sodium, *X^{ème} Colloque Interuniversitaire Franco-Québécois sur la Thermique des Systèmes*, Saguenay (Canada), 2011. Communication orale.

[ACTI9] N. Ferguen, **C. Cogné**, C. Pelegris, O. Rigo, M. Outirite, C. Courtois, A. Leriche, Étude thermique d'un matériau à gradients, *X^{ème} Colloque Interuniversitaire Franco-Québécois sur la Thermique des Systèmes*, Saguenay (Canada), 2011. Communication orale.

[ACTI10] N. Ferguen, **C. Cogné**, M. Guessasma, E. Bellenger, C. Pelegris, Processing and numerical modeling of functionally graded material : architecture optimization and evaluation of the effective thermal conductivity, *Materials Science and Technology Conference and Exhibition*, Columbus (USA), 2011. Communication orale.

[ACTI11] A. Veyrat-Lachenal, H. Desmorieux, **C. Cogné**, P. Lozano, *Nannochloropsis Occulata* Drying characterisation for conductive, convective and radiative drying, *19th International Drying Symposium*, Lyon (France), 2014. Communication par poster.

[ACTI12] T. Htira, **C. Cogné**, E. Gagnière, D. Mangin, Simulation of the freeze wastewater treatment on cold surface, *19th International Drying Symposium*, Lyon (France), 2014. Communication par poster.

61. Le conférencier est souligné.

[ACTI13] T. Htira, **C. Cogné**, E. Gagnière, D. Mangin, Wastewater treatment by freeze concentration : influence of velocity profile on crystal growth and impurities incorporation, *19th International Symposium on Industrial Crystallization*, Toulouse (France), 2014. Communication par poster.

[ACTI14] A. Bouzas, S. Donate, R. Barat, N. Marti, L. Borras, S. Grau, J. Ribes, J. Ferrer, **C. Cogné**, S. Labouret, E. Morales, D. Mangin, A. Seco, L. Pastor, Implementation of P-recovery System in Calahorra Wastewater Treatment Plant, *13th IWA Leading Edge Conference on Water and Wastewater Technologies*, Jerez de la Frontera (Espagne), 2016. Communication par poster.

[ACTN] : Communications avec actes dans un congrès national [62]

[ACTN1] **C. Cogné**, P. Laurent, J. Andrieu, Étude expérimentale et modélisation de la congélation des crèmes glacées industrielles, *Congrès de la Société Française de Thermique*, Grenoble, 2003. Communication orale.

[ACTN2] **C. Cogné**, P. Laurent, J. Andrieu, Experimental data and modeling of ice cream freezing, *9ème Congrès de la Société Française de Génie des Procédés*, Saint-Nazaire, 2003. Communication orale.

[ACTN3] I. Bombard, **C. Cogné**, P. Laurent, J. Lieto, Modélisation numérique de la cuisson sous infrarouge de peinture en poudre, *Congrès de la Société Française de Thermique*, Ile de Ré, 2006. Communication par poster.

[ACTN4] **C. Cogné**, J. Fortin, M. Guessasma, E. Bellenger, P. Coorevits, Modélisation de la thermomécanique dans un système multicontacts, *8ème Colloque National en Calcul des Structures*, Giens, 2007. Communication orale.

[ACTN5] **C. Cogné**, J. Fortin, M. Guessasma, E. Bellenger, P. Coorevits, Modélisation du transfert thermique dans un modèle Éléments Discrets, *18ème Congrès Français de Mécanique*, Grenoble, 2007. Communication orale.

[ACTN6] P.U. Nguyen, **C. Cogné**, J.L. Lanoisellé, D. Clausse, Modélisation de la congélation par évapo-dénte, *Congrès de la Société Française de Thermique*, Toulouse, 2008. Communication par poster.

[ACTN7] V.D. Nguyen, J. Fortin, M. Guessasma, E. Bellenger, P. Coorevits, **C. Cogné**, Modélisation de la thermomécanique dans un système multicontacts, *9ème Colloque National en Calcul des Structures*, Giens, 2009. Communication orale.

[ACTN8] H. Trannois, J. Fortin, M. Guessasma, E. Bellenger, P. Coorevits, **C. Cogné**, Interface Graphique pour exploiter un code Eléments Discrets (IGED), *9ème Colloque National en Calcul des Structures*, Giens, 2009. Communication orale.

[ACTN9] **C. Cogné**, K. Saleh, J. Fortin, M. Guessasma, Modélisation de l'autoéchauffement : application au stockage de grains en silo, *15ème Colloque de la Recherche Nationale en IUT*, Lille, 2009. Communication par poster.

[ACTN10] P.U. Nguyen, **C. Cogné**, J.L. Lanoisellé, E. Van Hecke, D. Clausse, Modélisation de la congélation de purée par évapo-détente, *12ème Congrès de la Société Française de Génie des Procédés*, Marseille, 2009. Communication par poster.

62. Le conférencier est souligné.

[ACTN11] **C. Cogné**, K. Saleh, C. Pelegris, J. Fortin, Modélisation thermomécanique de la décharge d'un silo, *12ème Congrès de la Société Française de Génie des Procédés*, Marseille, 2009. Communication par poster.

[ACTN12] N. Ferguen, E. Bellenger, M. Guessasma, C. Pelegris, **C. Cogné**, M. Outirite, C. Courtois, A. Leriche, O. Rigo, Modélisation thermomécanique d'un matériau composite alumine aluminium : optimisation de l'architecture et calcul de la conductivité thermique apparente, *10ème Colloque National en Calcul des Structures*, Giens, 2011. Communication orale.

[ACTN13] N. Ferguen, E. Bellenger, M. Guessasma, C. Pelegris, **C. Cogné**, M. Outirite, C. Courtois, A. Leriche, O. Rigo, Matériaux composites alumine/aluminium à gradient de fonction : modélisation numérique pour le calcul de la conductivité thermique effective, *20ème Congrès Français de Mécanique*, Besançon, 2011. Communication orale.

[ACTN14] C. Pelegris, **C. Cogné**, P. Laurent, Étude Expérimentale Et Modélisation des transferts thermiques de denrées alimentaires en contact avec un matériau à changement de phase, *Congrès de la Société Française de Thermique*, Bordeaux, 2012. Communication par poster.

[ACTN15] C. Pelegris, **C. Cogné**, Acétate de sodium : Étude calorimétrique et modélisation thermique, *13ème Congrès de la Société Française de Génie des Procédés*, Lille, 2011. Communication par poster.

[ACTN16] M. Outirite, N. Ferguen, C. Pelegris, **C. Cogné**, C. Courtois, A. Leriche, Etude expérimentale et modélisation thermique d'un matériau à gradients, *13ème Congrès de la Société Française de Génie des Procédés*, Lille, 2011. Communication orale.

[ACTN17] **C. Cogné**, R. Peczalski, O. Louisnard, Calcul de la pression et de la température autour d'une bulle en cavitation acoustique, *Congrès de la Société Française de Thermique*, Gérardmer, 2013. Communication par poster.

[ACTN18] Y. Mandri, A. Rich, D. Mangin, **C. Cogné**, A. Rivoire, T. Bounahmidi, A. Bouhaouss, Dessalement de l'eau de mer par congélation sur parois froides : étude paramétrique et dimensionnement du Procédé, *Congrès de la Société Française de Thermique*, Gérardmer, 2013. Communication par poster.

[ACTN19] H. Htira, **C. Cogné**, E. Gagnière, D. Mangin, Etude de faisabilité du traitement des eaux usées industrielles par congélation, *14ème Congrès de la Société Française de Génie des Procédés*, Lyon, 2013. Communication par poster.

[ACTN20] Y. Mandri, A. Rich, D. Mangin, A. Rivoire, C. Bebon, J.P. Klein, T. Bounahmidi, A. Bouhaouss, **C. Cogné**, Congélation d'une solution saline sur paroi froide : modélisation de la diffusion et de la convection naturelle, *Cristallisation et Précipitation Industrielles - Cristal7*, Toulouse, 2013. Communication orale.

[ACTN21] A.D. Mahi, S. Labouret, R. Peczalski, **C. Cogné**, J.P. Valour, Paramètres clés contrôlant la taille des cristaux de glace après congélation initiée par ultrasons , *Congrès de la Société Française de Thermique*, Lyon, 2014. Communication par poster.

[ACTN22] T. Htira, **C. Cogné**, E. Gagnière, D. Mangin, Traitement des eaux usées industrielles par congélation sur paroi froide : modélisation de la convection naturelle, *Congrès de la Société Française de Thermique*, Lyon, 2014. Communication par poster.

[ACTN23] T. Htira, **C. Cogné**, E. Gagnière, D. Mangin, Étude expérimentale et modélisation de la congélation sur paroi froide en milieu stagnant, *Congrès de la Société Française de Thermique*, Toulouse, 2016. Communication par poster.

[ACTN24] S. Labouret, **C. Cogné**, Y. Tahri, E. Gagnière, A. Bouzas, A. Seco, L. Pastor, D. Mangin, Intensification du procédé de précipitation de la struvite, *Cristallisation et Précipitation Industrielles - Cristal8*, Rouen, 2016. Communication par poster.

[ACTN25] T. Htira, E. Gagnière, **C. Cogné**, D. Mangin, Congélation sur paroi froide avec convection naturelle : étude expérimentale et modélisation , *Cristallisation et Précipitation Industrielles - Cristal8*, Rouen, 2016. Communication orale.

[ACTN26] T. Htira, **C. Cogné**, E. Gagnière, D. Mangin, Wastewater treatment by freeze concentration, *16ème Congrès de la Société Française de Génie des Procédés*, Nancy, 2017. Communication orale.

[ACTN27] H. Desmorieux, **C. Cogné**, Marie Debacq, Nouria Fatah, Nicolas Regnier, Eric Schaer, Mallorie Tourbin, Création d'un portail genie-des-procedes.fr, *16ème Congrès de la Société Française de Génie des Procédés*, Nancy, 2017. Communication orale.

[ACTN28] H. Tuyet Vu, H. Desmorieux, **C. Cogné**, A. Fayez, Modeling of thin cylinder spirulina drying, *16ème Congrès de la Société Française de Génie des Procédés*, Nancy, 2017. Communication par poster.

[ACTN29] P. Verlhac, S. Vessot, G. Degobert, **C. Cogné**, J. Andrieu, L. Beney, P. Gervais, Etude et optimisation des cycles de lyophilisation d'une souche modèle probiotique, *16ème Congrès de la Société Française de Génie des Procédés*, Nancy, 2017. Communication orale.

[COM] : Communications orales sans actes dans un congrès international ou national [63]

[COM1] **C. Cogné**, R. Peczalski, F. Baillon, F. Espitalier, O. Louisnard, Calcul Théorique Du Nombre De Nucléis De Glace Générés Par Une Bulle En Cavitation Acoustique Inertielle, *2èmes Journées "Ultrasons : Sonochimie, Procédés et Innovations"*, Chambéry, 2013.

[COM2] **C. Cogné**, S. Labouret, R. Peczalski, O. Louisnard, F. Baillon, F. Espitalier, Ultrasound Assisted Freezing. Theoretical Calculation of the Number of Ice Nuclei Generated by a Single Bubble in Acoustic Cavitation, *14th Meeting of the European Society of Sonochemistry*, Avignon, France.

[COM3] **C. Cogné**, S. Labouret, R. Peczalski, O. Louisnard, F. Baillon, F. Espitalier, Ultrasound Assisted Freezing. Theoretical Calculation of the Number of Ice Nuclei Generated by a Single Bubble in Acoustic Cavitation, *14th Meeting of the European Society of Sonochemistry*, Avignon, 2014.

[COM4] L. Pastor, A. Bouzas, D. Mangin, A. Seco, R. Barat, N. Marti, L. Borras, S. Donate, S. Grau, P. Marques, **C. Cogné**, E. Gagnière, S. Labouret, PHORWater, Phosphorus Recovery from Waste Water Treatment Plants, *2nd European Sustainable Phosphorus Conference*, Berlin (Allemagne), 2015.

63. Le conférencier est souligné.

Bibliographie

Ben Ammar, Lanoisellé, Lebovka, Van Hecke, and Vorobiev. Effect of a pulsed electric field and osmotic treatment on freezing of potato tissue. *Food Biophysics*, 5(3) :247–254, 2010.

Bourbatache, Guessasma, Bellenger, Bourny, and Fortin. DEM ball bearing model and defect diagnosis by electrical measurement. *Mechanical Systems and Signal Processing*, 41(1-2) : 98–112, 2013.

Burke, Georges, and Bryant. *Water relations of foods*, chapter Water in plant tissues and frost hardiness., pages 111–135. New York Academic Press, 1975.

Chassagne-Berces, Fonseca, and Marin. Congélation de produits végétaux - maîtriser la qualité des fruits congelés. *Techniques de l'Ingenieur*, F6 277, 2013.

Chevalier, Le Bail, and Ghoul. Freezing and ice crystals formed in a cylindrical food model : part i. freezing at atmospheric pressure. *Journal of Food Engineering*, 46 :277–285, 2000.

Chevalier, Le Bail, and Ghoul. Evaluation of the ice ratio formed during quasi-adiabatic pressure shift freezing. *High Pressure Research*, 21(5) :227–235, 2001.

Chourot, Macchi, Fournaison, and Guilpart. Technical and economical model for the freezing cost comparison of immersion, cryomechanical and air blast freezing processes. *Energy Conversion and Management*, 44(4) :559–571, 2003.

Coetzee and Els. Calibration of discrete element parameters and the modelling of silo discharge and bucket filling. *Computers and Electronics in Agriculture*, 65(2) :198–212, 2009.

Cornejo, Cornejo, Ramírez, Almonacid, and Simpson. Inverse method for the simultaneous estimation of the thermophysical properties of foods at freezing temperatures. *Journal of Food Engineering*, 191 :37–47, 2016.

Cox, Mazur, and Colbourne. New high pressure low-gwp azeotropic and near-azeotropic refrigerant blends. *International Refrigeration and Air Conditioning Conference*, paper 987, 2008.

Dalvi, Hamdami, Xanthakis, and Le-Bail. Review on the control of ice nucleation by ultrasound waves, electric and magnetic fields. *Journal of Food Engineering*, 195 :222–234, 2017.

Degner, Olson, Rose, Schlegel, Hutkins, and McClements. Influence of freezing rate variation on the microstructure and physicochemical properties of food emulsions. *Journal of Food Engineering*, 119(2) :244–253, 2013.

Descamps, Duhoo, Monchau, Lu, Hardouin, Hornez, and Leriche. Manufacture of macroporous β-tricalcium phosphate bioceramics. *Journal of the European Ceramic Society*, 28(1) :149–157, 2008.

Deville, Viazzi, and Guizard. Ice-structuring mechanism for zirconium acetate. *Langmuir*, 28 (42) :14892–14898, 2012.

Fortin, O. Millet, and de Saxcé. Numerical simulation of granular materials by an improved discrete element method. *International Journal for Numerical Methods in Engineering*, 62(5) : 639–663, 2004.

Freschi, Doran, Malumba, and Blecker. Impact of freezing and thawing processes on wheat and potato starch gel syneresis. *Starch - Stärke*, 66(1-2) :208–215, 2013.

Fuchigami, Kato, and Teramoto. High-pressure-freezing effects on textural quality of carrots. *Journal of Food Science*, 62(4) :804–808, 1997.

Guyon, Hulin, and Bideau. *La matière en désordre*. Ed. by EDP Sciences, 2014. ISBN 978-2-7598-1069-7.

Haddad, Guessasma, and Fortin. Heat transfer by conduction using DEM–FEM coupling method. *Computational Materials Science*, 81 :339–347, 2014.

Hamdami, Monteau, and Le Bail. Simulation of coupled heat and mass transfer during freezing of a porous humid matrix. *International Journal of Refrigeration*, 27(6) :595–603, 2004.

Hickling. Transient, high-pressure solidification associated with cavitation in water. *Phys. Rev. Lett.*, 73(21) :2853–2856, 1994.

Hossein and Sun. Water crystallization and its importance to freezing of foods : A review. *Trends in Food Science & Technology*, 22(8) :407–426, 2011.

Hubert. Transitions de phases solides induites par un procédé de compression directe : application à la caféine et à la carbamazépine. *Thèse de l'Université Lyon 1*, 2012.

Jiang, Li, He, and Wang. Research progress and model development of crystal layer growth and impurity distribution in layer melt crystallization : A review. *Industrial & Engineering Chemistry Research*, 53(34) :13211–13227, 2014.

Juban. Transformation induite au cours d'un procédé industriel (tipi) de compression directe : transition polymorphique de la caféine et propriétés physiques des comprimés. *Thèse de l'Université Lyon 1*, 2016.

Khalil. Etude expérimentale d'un procédé de cristallisation en émulsion huile dans eau : application au distéarate d'éthylène glycol. *Thèse de l'Université Lyon 1*, 2011.

Koch, Seyderhelm, Wille, Kalichevsky, and Knorr. Pressure-shift freezing and its influence on texture, colour, microstructure and rehydration behaviour of potato cubes. *Food / Nahrung*, 40(3) :125–131, 1996.

Lanoisellé, Blel, and Munoz. Application de la technologie des jets d'air à la surgélation des denrées alimentaires. *Revue Générale du Froid*, 1048 :41–48, 2004.

LeBail, Chevalier, Mussa, and Ghoul. High pressure freezing and thawing of foods : a review. *International Journal of Refrigeration*, 25(5) :504–513, 2002.

Lévy, Dumay, Kolodziejczyk, and Cheftel. Freezing kinetics of a model oil-in-water emulsion under high pressure or by pressure release. impact on ice crystals and oil droplets. *LWT - Food Science and Technology*, 32(7) :396–405, 1999.

Machado, Guessasma, Bellenger, Bourbatache, Bourny, and Fortin. Diagnosis of faults in the bearings by electrical measures and numerical simulations. *Mechanics & Industry*, 15(5) : 383–391, 2014.

Mandri, Rich, Mangin, Abderafi, Bebon, Semlali, Klein, Bounahmidi, and Bouhaouss. Parametric study of the sweating step in the seawater desalination process by indirect freezing. *Desalination*, 269(1-3) :142–147, 2011.

Martino, Otero, Sanz, and Zaritzky. Size and location of ice crystals in pork frozen by high-pressure-assisted freezing as compared to classical methods. *Meat Science*, 50(3) :303–313, 1998.

Maureaux, Baranowski, and Luchini. Procédé et installation pour la préparation et conservation de denrée. *Brevet EP1632140 (A1)*, 2006.

Mead and Cleary. Validation of DEM prediction for granular avalanches on irregular terrain. *Journal of Geophysical Research : Earth Surface*, 120(9) :1724–1742, 2015.

Mohanty. Magnetic resonance freezing system. *AIRAH Journal*, 55(6) :28–29, 2001.

Mohanty, Mohanty, and Mishra. Study of flow through a packed bed using discrete element method and computational fluid dynamics. *Journal of the Taiwan Institute of Chemical Engineers*, 63 :71–80, 2016.

Ngapo, Babare, Reynolds, and Mawson. Freezing and thawing rate effects on drip loss from samples of pork. *Meat Science*, 53(3) :149–158, 1999.

Olivera and Salvadori. Effect of freezing rate in textural and rheological characteristics of frozen cooked organic pasta. *Journal of Food Engineering*, 90(2) :271–276, 2009.

Orlowska, Havet, and Le-Bail. Controlled ice nucleation under high voltage DC electrostatic field conditions. *Food Research International*, 42(7) :879–884, 2009.

Otero and Sanz. High-pressure shift freezing. part 1. amount of ice instantaneously formed in the process. *Biotechnology Progress*, 16(6) :1030–1036, 2000.

Otero, Rodríguez, Pérez-Mateos, and Sanz. Effects of magnetic fields on freezing : Application to biological products. *Comprehensive Reviews in Food Science and Food Safety*, 15(3) :646–667, 2016.

Puel, Veesler, and Mangin. Cristallisation - Aspects théoriques. *Techniques de l'Ingénieur*, J2 710 :1–18, 2015.

Rich, Mandri, Mangin, Rivoire, Abderafi, Bebon, Semlali, Klein, Bounahmidi, Bouhaouss, and Veesler. Sea water desalination by dynamic layer melt crystallization : Parametric study of the freezing and sweating steps. *Journal of Crystal Growth*, 342(1) :110–116, 2012.

Rosso, Canals, and Carbonel. Le système binaire eau-acétone. *Comptes rendus hebdomadaires des séances de l'Académie des sciences*, 281 :699–702, 1975.

Saclier, Peczalski, and Andrieu. Effect of ultrasonically induced nucleation on ice crystals' size and shape during freezing in vials. *Chemical Engineering Science*, 65(10) :3064–3071, 2010.

Sadot, Curet, Rouaud, LeBail, and Havet. Modélisation d'un procédé de congélation assistée par micro-ondes. *Congrès Français de Thermique*, Toulouse, Juin 2016.

Saleh and Guigon. Caractérisation et analyse des poudres - propriétés comportementales des solides divisés. *Techniques de l'Ingénieur*, J2 252 :1–16, 2015a.

Saleh and Guigon. Caractérisation et analyse des poudres - propriétés physiques des solides divisés. *Techniques de l'Ingénieur*, J2 251 :1–14, 2015b.

Sanni, Bellenger, Fortin, and Coorevits. A reliable algorithm to solve 3D frictional multi-contact problems : Application to granular media. *Journal of Computational and Applied Mathematics*, 234(4) :1161–1171, 2010.

Sanz, Otero, Elvira, and Carrasco. Freezing processes in high-pressure domains. *International Journal of Refrigeration*, 20(5) :301–307, 1997.

Simpson and Cortés. An inverse method to estimate thermophysical properties of foods at freezing temperatures : apparent volumetric specific heat. *Journal of Food Engineering*, 64 (1) :89–96, 2004.

Soto and Bórquez. Impingement jet freezing of biomaterials. *Food Control*, 12(8) :515–522, 2001.

Torres, Abril, and Casp. Surface heat transfer coefficients for refrigeration and freezing of foods immersed in an ice slurry. *International Journal of Refrigeration*, 28(7) :1040–1047, 2005.

Verboven, Scheerlinck, and Nicolaı. Surface heat transfer coefficients to stationary spherical particles in an experimental unit for hydrofluidisation freezing of individual foods. *International Journal of Refrigeration*, 26(3) :328–336, 2003.

Xanthakis, Le Bail, and Ramaswamy. Development of an innovative microwave assisted food freezing process. *Innovative Food Science & Emerging Technologies*, 26 :176–181, 2014.

Zhu, Ramaswamy, and Le Bail. Ice-crystal formation in gelatin gel during pressure shift versus conventional freezing. *Journal of Food Engineering*, 66(1) :69–76, 2005.

Zhu, Zhou, Yang, and Yu. Discrete particle simulation of particulate systems : A review of major applications and findings. *Chemical Engineering Science*, 63(23) :5728–5770, 2008.

Zou and Chen. Granular sediment deposition and aggregation upstream of a check dam : A discrete element study. *Powder Technology*, 307 :90–98, 2017.

ELSEVIER

Journal of Food Engineering 58 (2003) 331–341

JOURNAL OF FOOD ENGINEERING

www.elsevier.com/locate/jfoodeng

Experimental data and modelling of thermal properties of ice creams

Claudia Cogné [a,b], Julien Andrieu [a,*], Pierre Laurent [a], Alain Besson [c], Jacques Nocquet [b]

[a] *Laboratoire d'Automatique et de Génie des Procédés (LAGEP), UMR CNRS 5007, UCB Lyon 1/ESCPE Lyon, Bât. 308 G, 43, Bd. 11 Nov. 1918, Villeurbanne 69622, France*

[b] *Nestlé PTC, ZI No. 2, Rue Charles Tellier, Beauvais 60000, France*

[c] *Nestlé Product Technology Centre, NESTEC Ltd, Orbe CH-1350, Switzerland*

Received 22 July 2002; accepted 6 October 2002

Abstract

In order to model the heat transfer phenomena which take place during ice cream freezing, predictive correlations of the ice cream thermophysical properties as a function of temperature are needed, principally the specific enthalpy and the thermal conductivity. Due to the fact that these thermal properties are required for various freezing conditions and ice cream formulations, physical models based on large experimental determinations were developed and validated. For a given ice cream formulation, the thermal conductivity was dependent on its density i.e. on the amount of air fraction in the sample and on the temperature whereas the enthalpy is only affected by temperature.

The main objective of this study was to develop physical models that predict the thermal properties of a standard overrun ice cream based on its composition and on the intrinsic thermal properties of each major pure component. In addition, to validate these models, the thermal properties of the ice cream were measured experimentally—the enthalpy by DSC and the thermal conductivity by the transient hot-wire probe method—and the effects of different factors were observed: ice content; temperature and air fraction in the temperature range between −40 and 10 °C. Generally, the predicted thermophysical properties values were in close agreement with those obtained experimentally.

Keywords: Frozen emulsion; Specific enthalpy; Thermal conductivity; Modelling

1. Introduction

A precise knowledge of the various ice cream thermal properties involved is essential for estimating the freezing times and also for simulating the temperature fields variations all through the frozen material during the freezing and the storage periods. These data are essential for controlling the quality and the stability of the frozen food in general and, particularly, in the case of the sorbets and frozen ice creams. Furthermore, the simulation of the freezing process has a great importance for efficiently designing the industrial freezing equipments and for controlling their operating costs. Consequently, the thermal properties of ice cream have been studied and correlated by some authors using various techniques.

The most widely used methods to determine specific heat and enthalpy data of foodstuffs are the adiabatic calorimeter with internal heating and differential scanning calorimetry (DSC) (Ohlsson, 1983; Wang & Kolbe, 1991). With adiabatic calorimeters, the sample, enclosed in a copper capsule, is dropped into the calorimeter adiabatic cell, ensuring that the capsule is in good thermal contact with its copper block. The sample heat capacity is calculated from the copper block temperature change. Then, an internal electric heating device is used to bring the calorimeter to the selected chosen temperature. With good calibration, the precision of the adiabatic calorimeter can be quite high. However, measuring times are quite long and a great care must be taken to insulate the measuring cell adequately.

DSC is also used to determine specific enthalpy data for food. This method is based on a differential heat fluxes measurement between the sample cell and an empty reference cell. The DSC's main advantages rely on rapid and pretty simple measurement and, on the fact that, more valuable information can be obtained by a

* Corresponding author. Tel.: +33-4-72-43-1843; fax: +33-4-72-43-1682.

E-mail address: andrieu@lagep.univ-lyon1.fr (J. Andrieu).

0260-8774/03/$ - see front matter © 2003 Elsevier Science Ltd. All rights reserved.
doi:10.1016/S0260-8774(02)00396-5

Nomenclature

A	constant (Eq. (1)) (°C)
C_P	heat capacity ($J\,kg^{-1}\,°C^{-1}$)
g_1, g_2, g_3	shape factors (–)
H	enthalpy ($J\,kg^{-1}$)
H_{ext}	extrapolated enthalpy ($J\,kg^{-1}$)
H_s	enthalpy for ice solidification ($J\,kg^{-1}$)
L_f	ice fusion latent heat ($J\,kg^{-1}$)
M	molecular weight ($kg\,mol^{-1}$)
Q	linear heat flux ($W\,m^{-1}$)
λ	thermal conductivity ($W\,m^{-1}\,°C^{-1}$)
ϵ	volume fraction, porosity (–)
ρ	density ($kg\,m^{-3}$)
R	perfect gas constant ($J\,mol^{-1}\,°C^{-1}$)
S	sensibility index (%)
T	temperature (°C or K)
T_0	initial freezing temperature of water (°C or K)
T_f	initial freezing temperature (°C or K)
t	time (s)
X	mass fraction (–)

Subscripts

air	air
b	unfreezable water
c	continuous phase
IC	ice cream
ice	ice
j	component
mix	ice cream without air
s	dry matter
w	water

Exponent

model	modelling function
para	modelling with parallel model
serie	modelling with series model

single thermogram, namely the specific enthalpy, the apparent heat capacity and the frozen water fraction. Nevertheless, the sample size is very small and, in the case of heterogeneous materials, sampling should be done with a great care so that the taken and analysed small sample should be well representative of the investigated food.

Concerning the experimental measurement of the food thermal conductivities, two kinds of methods are currently used: the steady state methods and the transient methods (Ohlsson, 1983; Reidy & Rippen, 1971). The first methods are based on the determination of the stationary heat flux through the sample in steady state heat transfer conditions for macroscopic homogeneous and isotropic materials assuming no internal heat generation and no phase change. Based on this principle, the parallel plate method has found some applications: by measuring the total heat flux, the inner and the outer temperature of the plates and the sample thickness, the foodstuff thermal conductivity values can be calculated. Similarly, for concentric cylinders or concentric spheres, the thermal conductivity can be estimated by measuring the temperatures at the inner and outlet radii of the measuring cell. The great advantage of the steady state methods is that a very simple mathematical expression (first Fourier's law) is used to identify the thermal conductivity values but the most important drawback is that it requires long equilibration times for the temperature fields (several hours) and it could be sometimes difficult to shape correctly the sample geometry—particularly for concentric cylinder or concentric sphere shapes—and to eliminate some parasite effects like vaporization or poorly controlled boundary conditions.

The best known transient method is the hot-wire probe method frequently used for a wide range of materials (metals, plastics, composites, etc...). In our laboratory, this method was implemented for frozen foodstuffs, monitored and found adequate and precise for this type of material (Cornillon, 1993; Cornillon, Andrieu, Duplan, & Laurent, 1995; Renaud, Briery, Andrieu, & Laurent, 1992), so it was chosen to measure experimentally the thermal conductivity of frozen overrun ice creams and sorbets. The great advantage of this method relies on its speed (between one and two minutes) and on the relative simplicity of the experimental device and of the probe itself. However, some experimental errors due to theoretical approximations in calculating the thermal conductivity of foodstuffs can occur and can affect its reliability and its precision as pointed out by Gonnet, Andrieu, and Laurent (1987) and, recently by Elustondo, Elustondo, and Urbicain (2001).

Furthermore, the few published literature data on thermophysical properties of commercial ice cream show a pretty large scattering and some discrepancy. Concerning the thermal conductivity data, it was observed that some published values disagree quite often. For example, Willlix, Lovatt, and Amos (1998) used a parallel plate apparatus to determine the thermal conductivity of a model ice cream and these authors proposed a fitting correlation expressing the thermal conductivity values as a function of temperature. Furthermore, Bakshi, Smith, and Gay (1985) investigated the effect of sweeteners and stabilizers on the thermal conductivity of commercial ice creams. Recently, in our laboratory, by using the hot-wire method, Faydi (1999) analysed the effect of the temperature on the thermal conductivity

values of a model ice cream without overrun. Firstly, Olenev (1982) and then Latyshev and Tsirulnikova (1983) and Sastry and Datta (1984) have published data on the effect of temperature on the thermal conductivity values of commercial ice creams with different densities. Note that the data of Sastry and Datta (1984) disagree with the data set of the two other previous authors as concern the temperature influence on thermal conductivity values for samples of the same mean density. The pretty large dispersion of the literature data could not be only due to the different measurement methods but also to the lack of precise and complete information on the sample texture, mainly concerning the air fraction, and also the ice cream basic composition (moisture content, fat content, protein content, etc...).

2. Experimental

2.1. Ice cream preparation

All the major foods components namely proteins, lipids, carbohydrates and water are found in commercial ice cream mix formulations. In our experiments, the thermal properties were determined with the same standard commercial ice cream mix formulation, namely (by weight fractions): milk 11.5%; fat 9%; sugar 18.33%; emulsifiant 0.3% and water 58.87% which correspond to the following weight composition for its basic food components: carbohydrates 26.08%, proteins 5.75%, lipids 9.30% and water 58.87%. Besides, different air ratios—also noted overrun rates by industry manufacturers—were also investigated. In order to obtain a better reproducibility as concern the texture and the structure of the frozen ice cream, the mix was always prepared in the same conditions with the same procedure very precisely controlled (Cogné, 2003). So, the ingredients were mixed at 50 °C. Then, the mix was homogenized under pressure, heated up to 80 °C during a few seconds for pasteurization and, finally, aged quietly for at least 24 h at 4 °C.

The air phase was added during the initial freezing step which takes in a scrapped surface heat exchanger where the mix was pre-crystallized at temperatures in the range between −4 and −6 °C. Depending from the recipe, the porosity of commercial products (by volume fraction basis) could be 0% for water ice, almost 20% for sorbet and more than 50% for commercial ice cream formulations. Then, the ice cream was submitted to a hardening treatment period either inside a cooled air tunnel or inside hardening tunnels with a cooling brining solution at −40 °C.

2.2. Calorimetry

DSC has been used to measure some thermal properties of ice cream. In our case, a commercial Mettler DSC differential scanning calorimeter was used without modulated system. Nitrogen gas was continuously flushed through the cell to eliminate problems associated with water condensation. The apparatus was regularly calibrated with two pure alcanes namely, *n*-decane (melting point −29.7 °C, heat of fusion 199.87 J/g) and *n*-dodecane (melting temperature −9.65 °C, heat of fusion 214.35 J/g). Besides, some regular checking runs were also performed with pure water to check the calorimeter calibration. The ice cream sample was collected before freezing at the exit of the mixing and storage tank, so that it was assumed that the air introduction had not any significant effect on the heat capacity values. A mass of ice cream sample between 10 and 20 mg was sealed in an aluminium DSC pan and very precisely weighed. An identical empty aluminium pan, used as a reference, was exposed to the same temperature rate increase of 1 °C/min for all the experimental runs with frozen samples. All the measurements were carried out by using temperature increase to avoid nucleation and the supercooling problems. Then, these experimental data were analysed in order to derive the enthalpy values according to the temperature changes (Cogné, 2003).

2.3. Hot-wire probe apparatus

The hot-wire probe method was used to measure the thermal conductivity of frozen ice cream. The identification method of the thermal conductivity values was based on a simplified solution of the heat equation for an ideal system composed of an infinite linear heat source immersed in an semi-infinite cylinder geometry medium (Gonnet et al., 1987; Renaud et al., 1992).

The probe itself was made with a medical needle—overall external diameter equal to 3 mm and total length equal to 10 cm—and with a copper-constantan heating wire and a thermocouple placed along the main axial axis, each wire being carefully insulated with an epoxy resin. The hot-wire heating power and the probe temperature rise after a relatively short period of time were the only data required to calculate the thermal conductivity. Assuming a probe of low thermal capacity and a purely radial heat flow, the probe temperature evolution can be simplified and written as follows (Gonnet et al., 1987; Renaud et al., 1992; Cogné, 2003):

$$T = \frac{Q}{4\pi\lambda} \ln t + A \tag{1}$$

where Q represents the heat flux per probe unit length and A is a constant.

Gonnet et al. (1987) extensively discussed the conditions for applying Eq. (1) in calculating the material temperature values. The system was calibrated at regular time periods by using a gel made with pure water and 5% agar-agar to prevent possible convective heat transfer effects. Then, the thermal conductivity values

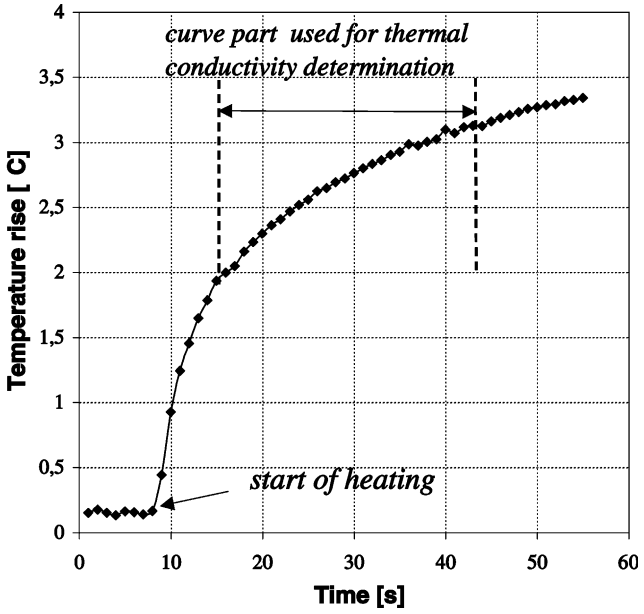

Fig. 1. Hot-wire probe method. Temperature rise during standard runs. $Q = 4\ \mathrm{W\,m^{-1}}$.

were calculated from the linear part of the curve $T = f(\ln t)$. This calibration allowed us to take into account some errors due to the finite dimension of the probe and due to other assumed hypotheses for application of Eq. (1). The ice cream sample was rapidly and directly collected at the outlet of the scrapped heat exchanger at positive temperature—about 5 °C—to overcome filling problems in the hot-wire probe cell related to possible introduction of pockets of air bubbles. Then, the sample was frozen as soon as possible at the chosen temperature and then submitted, for a short time period (Fig. 1), to a constant heating power around 0.4 W, precisely controlled for each measurement run. Then, different classical thermophysical properties models were compared to interpret the observed experimental data in the temperature range from −30 to 10 °C. Nevertheless, not all the data between −10 and 0 °C were collected, because sometimes it was difficult to obtain precise and reproducible thermogram data in this temperature range, due to some possible local thawing phenomena caused by the heating flux at the probe/food interface or to the heterogeneity of the ice cream sample at the local measuring point of the hot-wire probe itself.

3. Modelling

3.1. Enthalpy

The total sample enthalpy was calculated by integration of the DSC signal. It includes both the sensible heat and the latent heat of fusion in the freezing temperature range. As did many other authors, an arbitrary zero reference enthalpy at 0 °C was chosen (Miles, Van Beek, & Veerkaamp, 1983).

Three physical models were used to interpret the ice cream apparent specific enthalpy:

- Additive model by adding the thermal contribution of each pure component.
- Schwartzberg's model and Chen's model based on Raoult's law.

The weight additive model is based on the contribution of the apparent heat capacity of each component and it incorporates the latent heat of fusion as shown below by Eq. (2):

$$C_P = \sum_j X_j C_{Pj} - L_\mathrm{f}(T_\mathrm{f})\frac{\mathrm{d}X_\mathrm{ice}(T)}{\mathrm{d}T} \tag{2}$$

where the subscript j represents the different components (lipid, protein, carbohydrate, water or ice), X_j their mass fraction, C_{Pj} their intrinsic heat capacity values as published by Choi and Okos (1986) and X_ice is the ratio of the mass of ice to the foodstuff total mass. T_f is the initial freezing temperature of the ice cream that was estimated experimentally at −2.5 °C by carrying out some thawing runs on ice cream samples. The term $\mathrm{d}X_\mathrm{ice}/\mathrm{d}T$ was calculated with Miles model (Eq. (12)). The pure ice latent heat of fusion, noted L_f ($\mathrm{J\,kg^{-1}}$), was expressed by the following regression:

$$L_\mathrm{f} = (333.802 + 2.1165T) \times 1000 \tag{3}$$

where the temperature T is expressed in °C.

The second model used to correlate the thermal capacity is Schwartzberg's model based on Raoult's law (Schwartzberg, 1976; Cornillon, 1993):

If $T > T_\mathrm{f}$:

$$C_P = X_\mathrm{s}C_{P\mathrm{s}} + X_\mathrm{w}C_{P\mathrm{w}} \tag{4}$$

If $T < T_\mathrm{f}$:

$$C_P(T) = X_\mathrm{s}C_{P\mathrm{s}} + X_\mathrm{w}C_{P\mathrm{w}} + (X_\mathrm{b} - X_\mathrm{w}).(C_{P\mathrm{w}} - C_{P\mathrm{ice}}) + \frac{M_\mathrm{w}}{M_\mathrm{s}}X_\mathrm{s}\left[\frac{RT_0^2}{M_\mathrm{w}(T_0 - T)^2} - (C_{P\mathrm{w}} - C_{P\mathrm{ice}})\right] \tag{5}$$

where the subscript s represents the dry matter (lipids, proteins and carbohydrates). R is the perfect gas constant, T_0 the freezing point of pure water, T the sample temperature. All temperatures in Eq. (5) are expressed in °C. M_w is the molecular weight of water. Furthermore, the equivalent molecular weight of dry matter, noted M_s was obtained by measuring the freezing point depression:

$$\ln\left(\frac{\frac{X_\mathrm{w}-X_\mathrm{b}}{M_\mathrm{w}}}{\frac{X_\mathrm{w}-X_\mathrm{b}}{M_\mathrm{w}} + \frac{X_\mathrm{s}}{M_\mathrm{s}}}\right) = \frac{L_\mathrm{f}(T_\mathrm{f})M_\mathrm{w}}{R}\left(\frac{1}{T_0} - \frac{1}{T_\mathrm{f}}\right) \tag{6}$$

In this way, the dry matter molecular weight was found equal to 0.55 kg mol^{-1}.

The two next correlations (7) and (8) used to calculate the heat capacity of foods have been initially proposed by Chen (1985) and then used by Cornillon to correlate thermophysical properties of food gels (Cornillon, 1993; Cornillon et al., 1995):

if $T > T_f$:

$$C_P = 4180 - 2299X_s - 627X_s^3 \quad (7)$$

if $T < T_f$:

$$C_P = 1547 + 1254X_s + \frac{X_s}{M_s}\frac{RT_0^2}{(T-T_0)^2} \quad (8)$$

C_P being expressed in J kg^{-1} °C^{-1} and the temperatures T and T_0 in K.

The total enthalpy curve for the three models was calculated by integrating numerically the heat capacity as a function of the sample temperature (Cogné, 2003) and the resulting data are plotted on Fig. 2.

Fig. 2 shows a good agreement between the predictions of the additive model, which is quite equivalent to the empirical Riedel's model (Riedel, 1978) and the experimental data. Nevertheless, we can observe that the two models derived from Raoult's law—without any adjustable parameters—are slightly less accurate in predicting the enthalpy experimental data, particularly in the frozen state.

3.2. Frozen water/unfreezable water

The water contained in the ice cream matrix is either in the state of free water or water bound to the hydrophilic sites of the various components (carbohydrates, proteins, etc...). Only free water can undergo possible state transitions such as ice crystallization. So, the knowledge of the total ice amount is important to understand the behaviour of ice cream during the freezing step and to analyse the morphological and physical structure of the frozen ice cream (Fig. 3).

The determination of the total ice amount as a function of the sample temperature was based on the enthalpy-temperature curves (Faydi, 1999). We assumed that, during the ice freezing phenomenon, the energy changes occurring in the ice cream corresponded only to the freezing of water. Due to this hypothesis, it was possible to express the total enthalpy of ice cream, noted H, as the sum of the enthalpy absorbed by the phase change, due to the water crystallization and the enthalpy absorbed by the sample components due to pure cooling.

All our experimental data have shown that, above 0 °C, the enthalpy increases linearly with the temperature

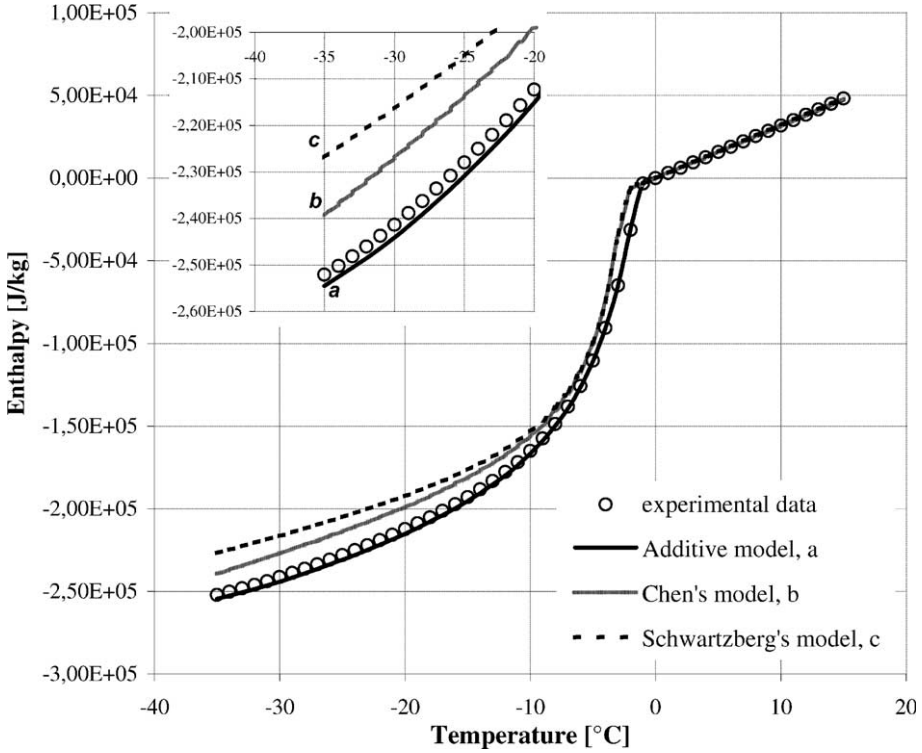

Fig. 2. Comparison between specific enthalpy experimental data and modelling.

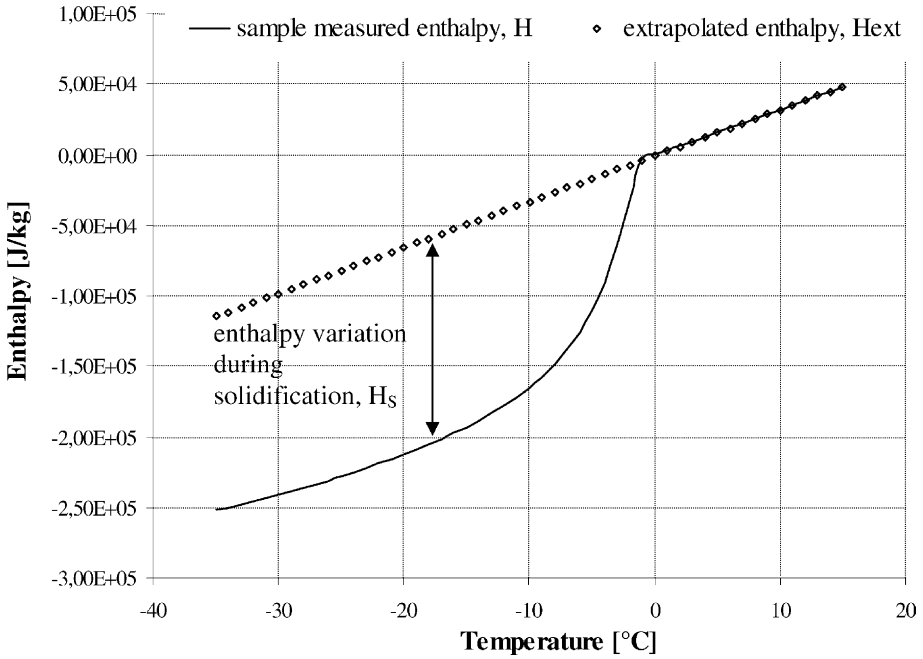

Fig. 3. Enthalpy calculation method for ice fraction determination.

and that it is correlated by a linear regression. So, the resulting straight line can be extrapolated at negative temperatures below the initial freezing point, the extrapolated value, noted H_{ext}, representing a virtual liquid supercooling state of the material. Consequently, the isothermal enthalpy variation $(H_{ext} - H)$ corresponds only to a latent heat variation, noted H_s, resulting from the ice melting in the hypothesis of our analysis (De Cindio, Correra, & Hoff, 1995):

$$H_s = H_{ext} - H \tag{9}$$

Then, the ice weight fraction (mass of ice/total mass of mix) can be estimated by the following relationship:

$$X_{ice}(T) = \frac{H_s(T)}{L_f(T)} \tag{10}$$

Four models derived from Raoult's law, have been successively used to predict the ice weight fraction as a function of temperature.

The first one is only valid for diluted and ideal solutions (Miles et al., 1983):

$$\text{Raoult:} \qquad X_{ice}(T) = (X_w - X_b)\left(1 - \frac{T_f}{T}\right) \tag{11}$$

where T_f represents the initial freezing temperature of the frozen system and T is the ice cream temperature, expressed in °C. Besides, other models have also been checked:

$$\text{Miles:} \qquad X_{ice}(T) = X_w\left(1 - \frac{T_f}{T}\right) \tag{12}$$

$$\text{Heldmann:} \qquad \ln\left(\frac{\frac{X_w - X_b - X_{ice}}{M_w}}{\frac{X_w - X_b - X_{ice}}{M_w} + \frac{X_s}{M_s}}\right) = \frac{L_f(T_0)M_w}{R}\left(\frac{1}{T_0} - \frac{1}{T}\right) \tag{13}$$

$$\text{Chen:} \qquad X_{ice} = \frac{X_s R T_0^2 (T_f - T)}{M_s L_f(T_0)(T - T_0)(T_f - T_0)} \tag{14}$$

where M_w is the water molecular weight, M_s the equivalent dry matter molecular weight, L_f the pure ice fusion latent heat, R the gas constant, T_0 the freezing point of pure water, T_f the initial freezing point of ice cream and T the sample temperature. All temperatures in Eqs. (13) and (14) are expressed in Kelvin. Fig. 4 represents the calculated ice mass fraction—expressed as the mass ratio of ice to the total mass of water—as a function of temperature for these different models. The error bars on experimental data represents the standard deviation between different experimental runs.

The data plotted on Fig. 4 shows that the Raoult's law derived models are in pretty good agreement with experimental data, the most important deviation between the Raoult's law derived model and the experimental data being around 7%. These physical models have the great advantage to be independent of the food formulation, unlike empirical equations that need parameters fitted on experimental data. Besides, it was observed that the initial freezing point of the solution is lower than 0 °C, precisely −2.5 °C, this freezing point

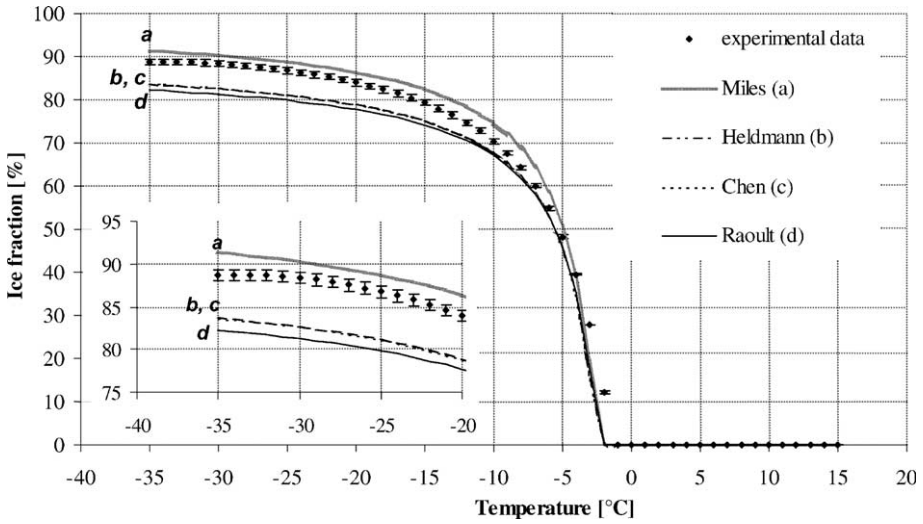

Fig. 4. Ice weight fraction. Comparison between data and modelling.

depression being due to the components dissolved in the mix (sugars, proteins, etc...). After ice crystallization starting, the cryoconcentration of the remaining solution was increased continuously, and hence the freezing point was progressively lowered. This freeze concentration phenomenon continued down to very low temperatures. At −10 °C, only about 70% of the total water was frozen and this ratio reached about 90% at −35 °C. Furthermore, this gradual transformation of water into ice crystals induced a very important variation of the thermal conductivity of the frozen mix.

3.3. Thermal conductivity

Two main factors affect the apparent thermal conductivity of the frozen ice cream: temperature due to its strong influence on the ice fraction—the thermal conductivity of pure ice is about four times higher than that of the liquid water—and the ice cream apparent density due to the greater influence of the air insulation effect.

The main problem in analysing and modelling the actual thermal conductivities of ice cream is that this reconstituted product is a heterogeneous and multiphase material, so that the choice of a specific continuous or dispersed phase was quite arbitrary. As a matter of fact, all the phases, which constitute the frozen ice cream, namely air, ice, fat and the freeze-concentrated continuous phase known as the matrix, contribute to the food thermal properties. However, because the amount of the fat is lower than that of water and that the thermal conductivity of pure ice is higher than that of lipid, the hypothesis that the fat droplets were not in the dispersion but in the matrix phase was adopted.

3.3.1. Thermal conductivity models of ice cream without air

Without air phase, the ice cream was represented as a two-phase material, which consisted of a solid phase (ice crystals) dispersed in a continuous fluid phase made of dry matter and unfrozen water. The thermal conductivity of this continuous phase was modelled either with the series model or with the parallel model by using the intrinsic thermal conductivity values of each main components and their volume fractions estimated from their weight fraction and their density (Choi & Okos, 1986):

$$\lambda_c^{para} = \sum_j \varepsilon_j \lambda_j \qquad \text{parallel model} \tag{15}$$

$$\frac{1}{\lambda_c^{serie}} = \sum_j \frac{\varepsilon_j}{\lambda_j} \qquad \text{series model} \tag{16}$$

with

$$\varepsilon_j = X_j \frac{\rho_c}{\rho_j} \quad \text{and} \quad \rho_c = \frac{1}{\sum_i \frac{X_j}{\rho_j}}$$

where the subscripts c and j represent respectively the continuous phase and each component of this phase (carbohydrate, protein, lipid and unfrozen water). In all cases, it was assumed that the ice crystals were dispersed in the continuous phase. Four different models have been applied to predict the thermal conductivity of this dispersion (Figs. 5 and 6). These simple models (series or parallel) give the lower and the upper limits of the thermal conductivity. Two other classical models were also used to correlate the thermal conductivity of our standard mix at different temperatures. The first one is the Maxwell's model that represents a heterogeneous system as a dispersion of spherical particles in a continuous phase. This model was previously used by

Model	Theoretical equation	Name
heat flux → 	$\lambda_{mix} = (1-\varepsilon_{ice})\lambda_c^{para} + \varepsilon_{ice}\lambda_{ice}$	parallel
heat flux → 	$\frac{1}{\lambda_{mix}} = \frac{1-\varepsilon_{ice}}{\lambda_c^{serie}} + \frac{\varepsilon_{ice}}{\lambda_{ice}}$	series
heat flux → 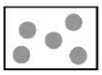	$\lambda_{mix} = \lambda_c^{para}\frac{2\lambda_c^{para} + \lambda_{ice} - 2\varepsilon_{ice}\left(\lambda_c^{para} - \lambda_{ice}\right)}{2\lambda_c^{para} + \lambda_{ice} + \varepsilon_{ice}\left(\lambda_c^{para} - \lambda_{ice}\right)}$	Maxwell
heat flux → 	$\lambda_{mix} = \lambda_c^{para}\frac{1-\varepsilon_{ice} + \varepsilon_{ice}F\frac{\lambda_{ice}}{\lambda_c^{para}}}{1-\varepsilon_{ice} + \varepsilon_{ice}F}$ where $F = \frac{1}{3}\sum_{i=1}^{3}\left[1 + \left(\frac{\lambda_{ice}}{\lambda_c^{para}} - 1\right)g_i\right]^{-1}$ and $\sum_{i=1}^{3} g_i = 1$	De Vries

Fig. 5. Thermal conductivity models.

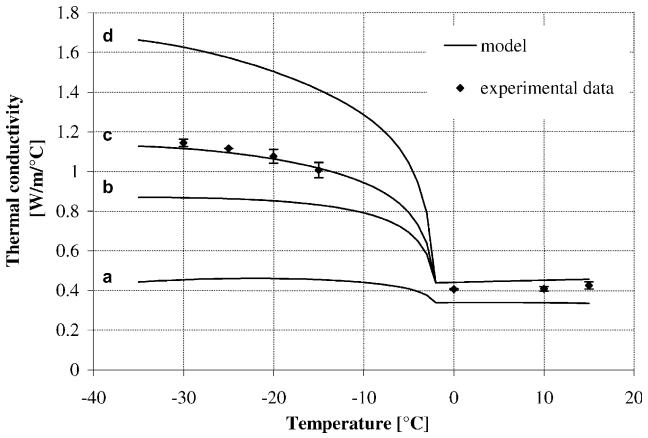

Fig. 6. Ice cream mix (without air) thermal conductivity. Comparison between modelling and experimental data. (a) Series model, (b) Maxwell's model, (c) De Vries's model, and (d) parallel model.

Renaud et al. (1992) and by Cornillon et al. (1995) to interpret the thermal conductivity data of model food gels; these authors observed that it was the most adequate model without any empirical fitting parameter to correlate the conductivity data corresponding to the frozen state. The second one, namely the De Vries's model, which is an extension of Maxwell's equation, introduces two shape factors to take into account the nonsphericity of the ice crystals (Renaud et al., 1992). The values of the two factors obtained by model fitting on experimental thermal conductivity data of nonoverrun ice cream are $g_1 = g_2 = 1/11$, $g_3 = 9/11$ and they correspond to dispersed particles having ellipsoidal shape with a ratio between the major axis to the minor axis equal to 9. These shape factors can be illustrated by the microscopic observation of the ice cream samples frozen from an initial temperature equal to 5 °C that showed an ice morphology with large dentritic crystals (Fig. 7).

Besides, the ice volume fraction was determined from the ice mass fraction estimated by DSC as previously presented. For applying the Maxwell's equation and De Vries's equation, we chose to model the thermal conductivity of the continuous phase by using the parallel model (Fig. 5).

On Fig. 6, the four thermal models were plotted and compared with the experimental data obtained with the standard ice cream mix without air. We could observe that the best fitting between the modelling and the experimental data was obtained with the De Vries's equation. Furthermore, as this model is semi-empirical, we checked it with experimental data obtained with two other solutions containing respectively 25% and 50% sucrose (weight fractions). We introduced the same shape factors as in the case of the ice cream modelling. We still observed that this model described very well the experimental data (Fig. 8). So, it seems very reasonable that this model could be extended with some confidence to different recipes of commercial ice creams.

3.3.2. Thermal conductivity of overrun ice cream

The second step in the analysis and in the modelling of the thermal conductivity of overrun ice creams was to study and to integrate the air phase influence. Usually, the air phase constitutes about 50% by volume of the standard commercial ice cream. As the air intrinsic thermal conductivity is very low, the air porosity has a large influence on the apparent thermal conductivity of commercial frozen ice creams. Besides, the microscopic

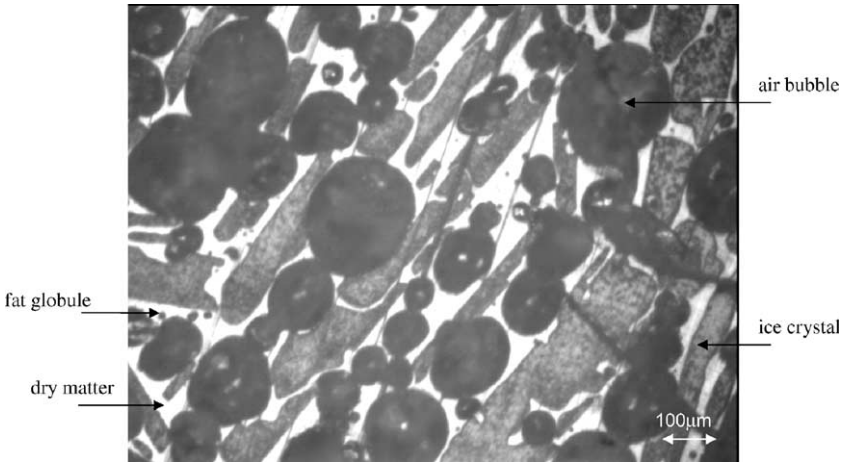

Fig. 7. Microscopic observation of overrun ice cream texture.

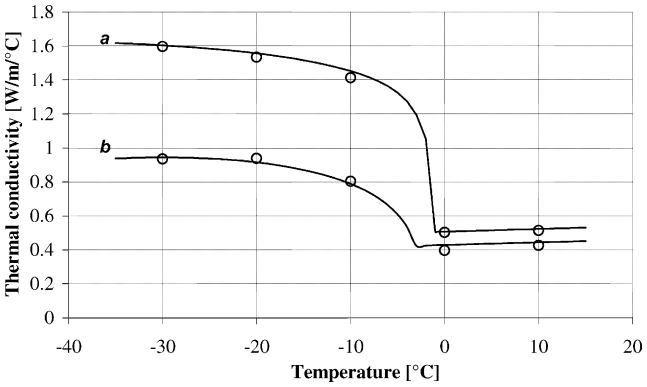

Fig. 8. Thermal conductivity experimental data. Sucrose solutions modelling. (a) 25% weight saccharose, (b) 50% weight saccharose, (○) experimental data, and (—) De Vries's model.

observation of the structure of an overrun ice cream showed that the air phase was dispersed as quite spherical bubbles inside the other phases (Fig. 7). So, the air phase dispersion in the ice cream was modelled by using the following Maxwell's theoretical relationship:

$$\lambda_{\text{ice}}(T) = \lambda_{\text{mix}}(T) \times \frac{2\lambda_{\text{mix}}(T) + \lambda_{\text{air}} - 2\varepsilon_{\text{air}}(\lambda_{\text{mix}}(T) - \lambda_{\text{air}})}{2\lambda_{\text{mix}}(T) + \lambda_{\text{air}} + \varepsilon_{\text{air}}(\lambda_{\text{mix}}(T) - \lambda_{\text{air}})} \quad (17)$$

where ε_{air} represents the air porosity i.e. the volume fraction of the air phase calculated from the frozen ice cream density and λ_{mix} represents the thermal conductivity of a virtual nonoverrun ice cream—composed of unfrozen water, dry matter and ice crystals—modelled by using the De Vries's model previously presented. Fig. 9 presents a summary of the modelling scheme of the thermal conductivity of the frozen ice cream.

A comparison between the experimental data and the model predictions are presented on Fig. 10 as a function of temperature for different air porosities. The error bars on the experimental data represents the standard deviation between different experimental runs. We observed that the model predictions are in pretty good agreement with the experimental data both in the unfrozen domain and in the frozen domain: the mean relative error between the model and the experimental data did not exceed 8%.

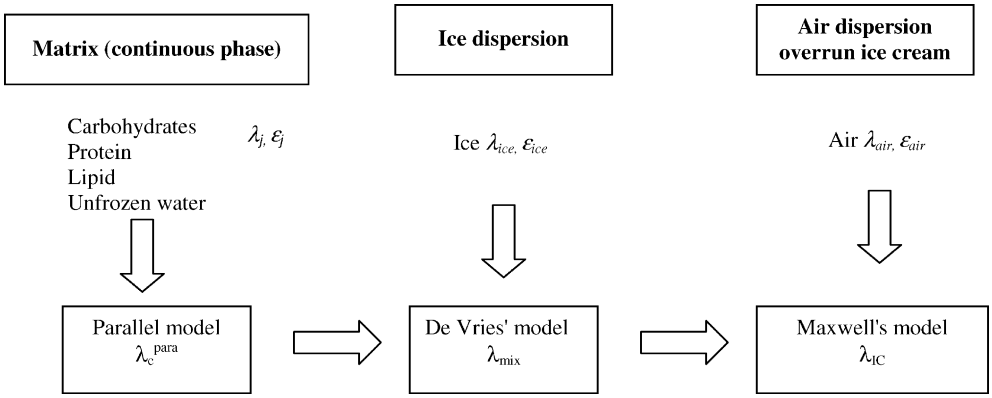

Fig. 9. Scheme describing the thermal conductivity modelling of an overrun ice cream.

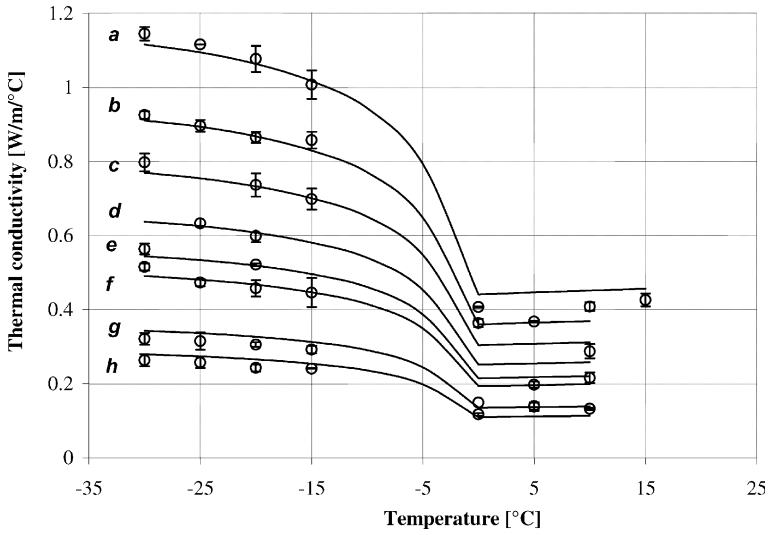

Fig. 10. Thermal conductivity of overrun ice cream. Porosity and temperature influence. Porosity: $a = 0\%$, $b = 13\%$, $c = 23\%$, $d = 33\%$, $e = 41\%$, $f = 46\%$, $g = 60\%$, and $h = 67\%$.

The difference between experimental and predicted thermal conductivity values can be explained by the errors on measured thermal conductivities, by the uncertainties on component mass fraction—problems during the component weights, the water evaporation, the ice determination, the estimation of bound or unfrozen water—and by the estimation of the overrun ratio (porosity).

Furthermore, we also studied the parametric sensitivity of our model by analysing how much a 10% variation of the air porosity or of the ice fraction could influence the ice cream thermal conductivity values. Firstly, we estimated the thermal conductivity with the model as explained above and noted ($\lambda_{0\%}^{\text{model}}$). Secondly, we applied a variation of 10% on the parameter studied ($\lambda_{10\%}^{\text{model}}$) in order to calculate a sensitivity parameter index, noted S. This sensitivity index, defined as the ratio between the thermal conductivity variation resulting from a 10% parameter variation and the nominal value of the thermal conductivity, was expressed as follows:

$$S = \frac{|\lambda_{10\%}^{\text{model}} - \lambda_{0\%}^{\text{model}}|}{\lambda_{0\%}^{\text{model}}} \times 100 \tag{18}$$

We evaluated the average sensitivity index values for three ice cream densities in the frozen state. For high porosities, the porosity parameter was more important than the ice fraction parameter, but the average values of the sensitivity index noted S were quite high, more than 10%. The same study realized with a variation of 10% on the shape factors g_1, g_2 and g_3 in De Vries's model has shown that the sensitivity index value was around 2%. This indicates that we need to determine precisely both the ice fraction and the air fraction to estimate precisely the ice cream thermal conductivity. Besides, the three model parameters—like the shape factors—do not have a great influence on the thermal conductivities of the overrun ice cream.

4. Conclusions

Physical models and empirical equations have been compared to experimental data to predict the thermal properties of standard ice creams with or without air. The models based on Raoult's law have shown a quite good accuracy for correlating the mass ice fraction data as a function of temperature. The predicted enthalpy values with the weight additive model were in pretty close agreement with those experimentally obtained. Concerning the thermal conductivity values, the De Vries' and the Maxwell's models were able to predict very precisely the experimental data obtained with the hot wire probe method at different temperatures and for different overrun ratios in the frozen temperature domain.

It also should be emphasized that all the equations presented and selected in our analysis have a physical meaning so that this modelling seems pretty reliable to be extended to other ice cream formulations than the ones investigated in the present study.

Acknowledgements

The authors are grateful to Nestlé Company and to ANRT (CIFRE programme) for the scientific help and also for the material and financial support received during this work.

References

Bakshi, A. S., Smith, D. E., & Gay, S. A. (1985). Effect of sweeteners and stabilizers on the thermal conductivity of ice cream. *Milchwissenschaft, 40*(8), 449–453.

Chen, C. S. (1985). Thermodynamic analysis of the freezing and thawing of foods. *Journal of Food Science, 50*, 1158–1162.

Choi, Y., & Okos, M. R. (1986). Effects of the temperature and composition on the thermal properties of foods. *Food Engineering and Process Applications*, 93–101.

Cogné, C. (2003). Etude expérimentale et modélisation de la congélation des crèmes glacées foisonnées, Thèse Université Claude Bernard, Lyon I, (à publier).

Cornillon, P. (1993). Mesure et modélisation des différents types d'eau et des propriétés thermophysiques des gels alimentaires congelés. Thèse Université Claude Bernard, Lyon I.

Cornillon, P., Andrieu, J., Duplan, J. C., & Laurent, M. (1995). Use of nuclear magnetic resonance to model thermophysical properties of frozen and unfrozen model food gels. *Journal of Food Engineering, 25*, 1–19.

De Cindio, B., Correra, S., & Hoff, V. (1995). Low temperature sugar-water equilibrium curve by a rapid calorimetric method. *Journal of Food Engineering, 24*, 405–415.

Elustondo, D., Elustondo, M. P., & Urbicain, M. J. (2001). New thermal conductivity probe design based on the analysis of error sources. *Journal of Food Engineering, 48*, 325–333.

Faydi, E. (1999). Etude expérimentale et modélisation de la taille moyenne des cristaux de glace obtenus par congélation unidirectionnelle d'une crème glacée modéle. Thèse Université Claude Bernard, Lyon I.

Gonnet, E., Andrieu, J., & Laurent, M. (1987). Intrinsic thermal conductivities of basic food components. *High Temperatures—High Pressures, 19*, 323–330.

Latyshev, V. P., & Tsirulnikova, N. A. (1983). A method of calculation of thermal conductivity of some dairy products. *Congres of Refrigeration Paris*, 365–369.

Miles, C.A., Van Beek, G., & Veerkaamp, C.H. (1983). Calculation of thermophysical properties of foods. In Jowitt, Escher, Hallström, Meffert, & Spiess (Eds.), Physical Properties of Foods, Vol. 16, pp. 269–312.

Ohlsson, T. (1983). The measurement of thermal properties. In Jowitt, Escher, Hallström, Meffert, Spiess (Eds.), Physical Properties of Foods, Vol. 17, pp. 313–328.

Olenev, Y.A. (1982). Thermal conductivity of ice cream and ice cream mixes. Molochnaya Promyshlennost', URSS, 8.

Reidy, G. A., & Rippen, A. L. (1971). Methods for determining thermal conductivity in foods. *Transactions of the ASAE*, 248–254.

Renaud, T., Briery, P., Andrieu, J., & Laurent, M. (1992). Thermal properties of model foods in the frozen state. *Journal of Food Engineering, 15*, 83–97.

Riedel, L. (1978). Eine Formel zur Berechnung der Enthalpie fettarmer Lebensmittel in Abhängigkeit von Wassergehalt und Temperatur. *Chem. Mikrobiol. Technol. Lebensm., 5*, 129–133.

Sastry, S. K., & Datta, A. K. (1984). Thermal properties of frozen peas, clams and ice cream. *Canadian Institute of Food Science and Technology, 17*(4), 242–246.

Schwartzberg, H. G. (1976). Effective heat capacities for the freezing and thawing of food. *Journal of Food Science, 41*, 152–156.

Wang, D. Q., & Kolbe, E. (1991). Thermal properties of surimi analysed using DSC. *Journal of Food Science, 56*(2), 302–308.

Willlix, J., Lovatt, S. J., & Amos, N. D. (1998). Additional thermal conductivity values of foods measured by a guarded hot plate. *Journal of Food Engineering, 37*, 159–174.

IChemE

www.ingentaselect.com/titles/02638762.htm

0263–8762/03/$23.50+0.00

Trans IChemE, Vol 81, Part A, October 2003

EXPERIMENTAL DATA AND MODELLING OF ICE CREAM FREEZING

C. COGNÉ[1,2], P. LAURENT[1], J. ANDRIEU[1] and J. FERRAND[2]

[1]*Laboratoire d'Automatique et de Génie des Procédés (LAGEP), UMR CNRS 5007, UCB Lyon 1/ESCPE Lyon, Villeurbanne, France*
[2]*Nestlé PTC, Beauvais, France*

In order to optimize the ice cream industrial freezing process, a thermal model has been developed to predict the freezing times. First, physical relationships based on experimental determinations have been validated to interpret the principal ice cream thermal properties involved, namely the specific enthalpy and the thermal conductivity, as a function of the temperature and the density of the product. This theoretical freezing model, based on the numerical resolution of the heat equation, includes both the freezing conditions—ice cream initial temperature, nature of the cooling medium and cooling rate—and the sample composition. Experimental temperature profiles obtained with different freezing conditions were used to validate the model and assess its accuracy. The effect of the freezing conditions on the ice crystal texture was studied. It was shown that the most important operating parameters were the freezing rates and the freezer temperature that govern not only the size but also the ice crystal morphology.

Keywords: ice cream; freezing; thermal properties; modelling; texture.

INTRODUCTION

In the ice cream manufacturing process, freezing is one of the most important steps in determining the final texture and organoleptic properties of this frozen food. Precise knowledge of the various ice cream thermal properties involved is essential for estimating the freezing times and also for simulating temperature evolution during the freezing and the storage periods. These data are essential to control the quality and the stability of frozen foods in general and particularly in the case of reconstituted foods with high water content like ice cream. Furthermore, the simulation of the whole freezing chain is of a great importance for efficiently designing industrial freezing equipment and for controlling their operating costs.

MATERIALS AND METHODS

All the major foods components, namely proteins, lipids, carbohydrates and water, are traditionally found in commercial ice cream mix formulations. In the experimental runs presented here, all the different ice cream samples studied had the same mix standard composition (by weight fractions): water, 61.7%; sugar, 18%; milk solid non-fat, 11%; fat, 9%; emulsifier, 0.3%. The mix was always prepared under the same conditions using the same procedure. The ingredients were mixed at 50°C and were homogenized under pressure at 140 bar in the first stage and at 40 bar in the second stage. Then, they were heated up to 80°C over a period of 25 s for pasteurization and, finally, aged for at least 24 h at 4°C. The air phase was added during the initial freezing step which took place in a batch scraped surface heat exchanger (Hoyer, KF80) where the mix was precrystallized at temperatures in the range −4 to −6°C. Depending on the specific formulation studied, the porosity (by volume fraction basis) of the frozen ice cream samples could vary from 0% for 'water'-type ice creams to 50% for commercial type formulations. The freezing of the ice cream was completed with a hardening treatment period either inside an air cooled tunnel or with cooling brine solutions maintained at −40°C, during which 75–80% of the available water was frozen.

Differential scanning calorimetry (Mettler Toledo DSC 821^e) was used to determine experimentally the thermal properties of the ice cream. The apparatus was regularly calibrated with two pure alcanes namely, *n*-decane (melting point, −29.7°C; heat of fusion, 199.87 J g^{-1}) and *n*-dodecane (melting temperature, −9.65°C; heat of fusion, 214.35 J g^{-1}). In addition, some regular calibration runs were also performed with pure water. The samples were cooled to −40°C at a rate of 10°C min^{-1} and then warmed up to 20°C with a heating rate of 1°C min^{-1}. All the measurements were carried out using temperature increase to avoid the supercooling problems that occurred during nucleation.

The ice cream samples were collected before the freezing step at the exit of the mixing and storage tank, so that it was assumed that the air introduction had not any significant effect on the heat capacity values. Ice cream samples between 10 and 20 mg were sealed in aluminum DSC pans and were weighed to a high level of precision

(balance Mettler Toledo AT 261 Delta range, precision 0.01 mg).

The hot-wire probe method was used to measure the thermal conductivity of the frozen ice creams. The thermal conductivity identification method was based on a simplified solution of the heat equation for an ideal system composed of an infinite linear heat source immersed in a semi-infinite cylinder geometry medium (Gonnet *et al.*, 1987; Renaud *et al.*, 1992). The probe was made with a needle—overall external diameter equal to 3 mm and total length equal to 10 cm—and with a copper–constantan heating wire and a thermocouple placed along the main axial axis, each wire being carefully insulated with an epoxy resin. The hot-wire heating power and the probe temperature rise after a relatively short period of time were the only data required to calculate the thermal conductivity (Cogné *et al.*, 2003a).

An optical microscope with episcopic coaxial lighting inside a cold room at −25°C was used to analyse the ice cream structure (Arnaud *et al.*, 1998; Faydi *et al.*, 2001a). This method is based on the light flux differences reflected by the different interfaces of the material. The reflected light fluxes that determine the image contrasts are determined at the same time by the light fraction of the incident flux absorbed and/or by the light reflected at different interfaces with different orientations, for example at the air bubbles surfaces which are present in commercial ice creams containing air (overrun ice cream).

RESULTS AND DISCUSSIONS

Thermal Properties of Ice Cream

To model the heat transfer phenomena which takes place during the ice cream freezing, predictive correlations of the ice cream thermophysical properties as a function of the temperature are needed, principally the specific enthalpy and the thermal conductivity. Owing to these thermal properties being required for various freezing conditions and for different ice cream formulations, physical models based on a number of experimental determinations were developed and validated.

Enthalpy

The total sample enthalpy was calculated by integration of the experimental DSC signal. It includes both the sensible heat and the latent heat of fusion in the freezing temperature range (Cornillon, 1993). An arbitrary zero reference enthalpy of 0°C was selected as per previous analyses (Miles *et al.*, 1983). Three physical models were used to interpret the ice cream apparent specific enthalpy (Cogné *et al.*, 2003a). The first is the weight additive model, based on the contribution of the apparent heat capacity of each component and incorporating the latent heat of fusion as shown in equation (1):

$$C_P = \sum_j X_j \cdot C_{Pj} - L_f(T_f)\frac{dX_{ice}(T)}{dT} \quad (1)$$

where subscript j represents the different components (lipid, protein, carbohydrate, water or ice), X_j their mass fraction, C_{Pj} their intrinsic heat capacity values as published by Choi and Okos (1986) and X_{ice} is the ratio of the mass of ice to the foodstuff total mass. T_f is the initial freezing temperature of the ice cream that was estimated experimentally at −2.5°C by carrying out some thawing runs on ice cream samples. The term dX_{ice}/dT was calculated from the Miles model (Miles *et al.*, 1983). The pure ice latent heat of fusion, denoted L_f (J kg^{-1}), was expressed by equation (2), where the temperature T is expressed in °C:

$$L_f = (333.802 + 2.1165T) \times 1000 \quad (2)$$

The second model used to correlate the thermal capacity is Schwartzberg's model based on Raoult's law (Schwartzberg, 1976):

$$\text{if } T > T_f: \quad C_P = X_s \cdot C_{Ps} + X_w \cdot C_{Pw} \quad (3)$$

$$\text{if } T < T_f: \quad C_P(T) = X_s \cdot C_{Ps} + X_w \cdot C_{Pw} + (X_b - X_w) \times (C_{P_w} - C_{Pice}) + \frac{M_w}{M_s}X_s \times \left[\frac{RT_0^2}{M_w(T_0 - T)^2} - (C_{Pw} - C_{Pice})\right] \quad (4)$$

where the subscript 's' represents the dry matter (lipids, proteins and carbohydrates), R is the perfect gas constant, T_0 the freezing point of pure water, T the sample temperature. All the temperatures in equation (4) are expressed in degrees Kelvin, M_w is the molecular weight of water. Furthermore, the equivalent molecular weight of dry matter, denoted M_s, was obtained by measuring the freezing point depression estimated experimentally at −2.5°C:

$$\ln\left(\frac{(X_w - X_b)/M_w}{(X_w - X_b)/M_w + (X_s/M_s)}\right) = \frac{L_f(T_f)M_w}{R}\left(\frac{1}{T_0} - \frac{1}{T_f}\right) \quad (5)$$

In this way, the dry matter molecular weight was found to be equal to 0.55 kg mol^{-1}.

The final model used to model the heat capacity was proposed by Chen (1985):

$$\text{if } T > T_f: \quad C_P = 4180 - 2299X_s - 627X_s^3 \quad (6)$$

$$\text{if } T < T_f: \quad C_P = 1547 + 1254X_s + \frac{X_s}{M_s}\frac{RT_0^2}{(T - T_0)^2} \quad (7)$$

The total enthalpy curve for the three models was calculated by integrating numerically the heat capacity as a function of the sample temperature. Figure 1 shows good agreement

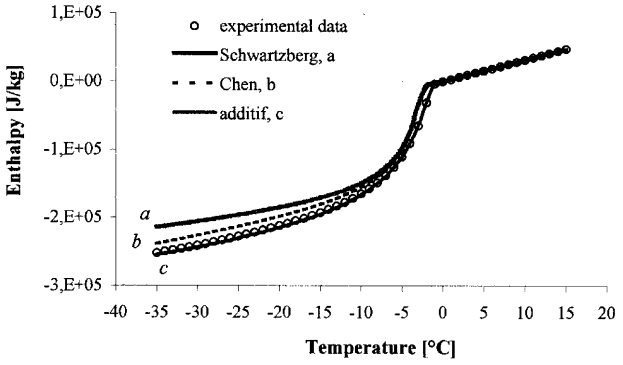

Figure 1. Comparison between specific enthalpy experimental data and modelling.

between the predictions of the additive model and the experimental data. Besides, it can be observed that the two models derived from Raoult's law—without any adjustable parameters—are slightly less accurate in predicting the enthalpy experimental data, particularly in the frozen state.

Apparent thermal conductivity

The experimental results have shown that two main factors affect the apparent thermal conductivity of the frozen ice cream: temperature, due to its strong influence on the ice fraction—the thermal conductivity of pure ice is about four times higher than that of the liquid water—and the ice cream apparent density due to the greater influence of the air insulation effect on this parameter.

A physical model has been developed to interpret the experimental thermal conductivity data and to extrapolate the predictions to other ice cream formulations (Cogné *et al.*, 2003a). This overall model was built from the combination of three elementary models described in Figure 2 and applied at each phase of the ice cream (Renaud *et al.*, 1992; Cornillon *et al.*, 1995):

- the parallel model to predict the equivalent thermal conductivity of the continuous phase;
- the De Vries' model to take account of the nonsphericity of the ice crystals;
- the Maxwell model to express the air phase influence.

The model predictions of the thermal conductivity values are in good agreement with the experimental data both in the unfrozen domain and in the frozen domain; the mean relative error did not exceed 8% (Figure 3).

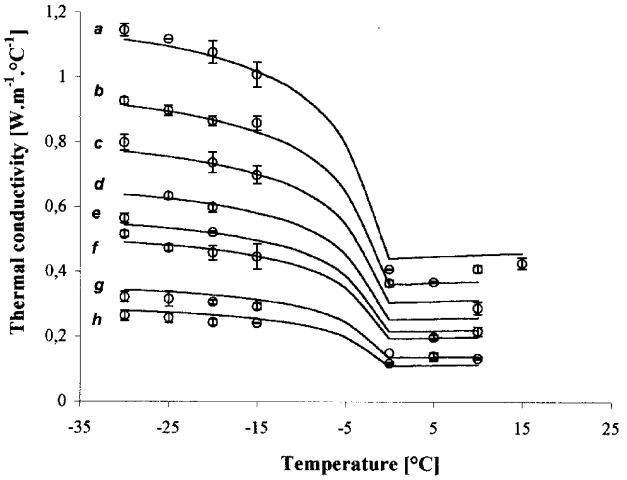

Figure 3. Thermal conductivity of ice cream. Porosity and temperature influence. Circles, experimental data; straight lines, modelling. Porosity: $a=0.05$; $b=0.13$; $c=0.23$; $d=0.33$; $e=0.41$; $f=0.46$; $g=0.60$; $h=0.67$.

Freezing Modelling

Estimation of the food freezing times is a non-linear problem inlvolving heat transfer with simultaneous phase change and temperature-dependent thermophysical properties. A theoretical model has been developed to simulate the freezing kinetics of the ice cream samples and then, this model was validated from freezing experimental data obtained in the pilot plant.

Heat equation numerical integration

The model, developed from the commercial software Ansys, consists of solving numerically the heat equation by the finite element method. For cartesian coordinates, assuming that the thermal properties are isotropic, the classical heat balance equation can be written as:

$$\left[\frac{\partial}{\partial x}\left(\lambda(T)\frac{\partial T}{\partial x}\right)+\frac{\partial}{\partial y}\left(\lambda(T)\frac{\partial T}{\partial y}\right)+\frac{\partial}{\partial z}\left(\lambda(T)\frac{\partial T}{\partial z}\right)\right] = \rho\cdot\frac{\mathrm{d}H}{\mathrm{d}T}\cdot\frac{\partial T}{\partial t} \quad (8)$$

where λ represents the thermal conductivity ($\mathrm{W\,m^{-1}\,°C^{-1}}$), ρ the density ($\mathrm{kg\,m^{-3}}$), H the enthalpy ($\mathrm{J\,kg^{-1}}$), T the temperature (°C), t the time (s) and x, y, z the coordinates (m).

Model	Theoretical equation	Name
heat flux →	$\lambda = \sum_j \varepsilon_j \lambda_j$	parallel
heat flux → Continuous phase (c) / Dispersed phase (d)	$\lambda = \lambda_c \dfrac{2\lambda_c+\lambda_d-2\varepsilon_d(\lambda_c-\lambda_d)}{2\lambda_c+\lambda_d+\varepsilon_d(\lambda_c-\lambda_d)}$	Maxwell
heat flux → Continuous phase (c) / Dispersed phase (d)	$\lambda = \lambda_c \dfrac{1-\varepsilon_d+\varepsilon_d F\frac{\lambda_d}{\lambda_c}}{1-\varepsilon_d+\varepsilon_d F}$ where $F=\frac{1}{3}\sum_{i=1}^{3}\left[1+\left(\frac{\lambda_d}{\lambda_c}-1\right)g_i\right]^{-1}$ and $\sum_{i=1}^{3} g_i = 1$	De Vries

Figure 2. Thermal conductivity models.

The phase change is taken into account by the enthalpy that includes the sensible heat and the latent heat of fusion. The thermal conductivity and the enthalpy data, depending on the temperature, involve a non-linear problem that is resolved using the iterative Newton–Raphson technique.

Initially, the ice cream temperature was assumed to be homogenous and equal to the temperature at the exit of the scraped surface heat exchanger.

Concerning the boundaries conditions, third kind limit conditions were applied, by considering the heat flux continuity on each refrigerated surface, namely:

$$\lambda \left.\frac{\partial T}{\partial n}\right|_{\text{surface}} = h \cdot (T_{\text{surface}} - T_{\infty}) \qquad (9)$$

where λ is the material thermal conductivity ($\mathrm{W\,m^{-1}\,^{\circ}C^{-1}}$), n is the normal direction at the cooled surface, T_{surface} and T_{∞} represent, respectively, the material surface and the fluid refrigerant temperatures (air or brine solution) in °C. The convective heat transfer coefficient noted, h, was estimated using the method of copper blocks: as a result of its high thermal conductivity, a massive copper block having the same shape as the mold and submitted to the same cooling conditions as the ice cream has an approximately uniform temperature. The time derivative from this temperature enabled the heat transfer coefficient to be obtained. These coefficient values were estimated as $20\,\mathrm{W\,m^{-2}\,^{\circ}C^{-1}}$ for freezing experiments in air-cooled tunnels at a speed of $5\,\mathrm{m\,s^{-1}}$ and around $500\,\mathrm{W\,m^{-2}\,^{\circ}C^{-1}}$ for freezing experiments with stirred brine solutions. These values were confirmed from the literature data (Özisik, 1985). However, the heat transfer coefficient is the least accurate parameter of the model with its precision being less than 10%.

The surface, directly in contact with the refrigerant fluid, could be either ice cream or a second material with different thermal properties to ice cream. In the case of stick freezing, a stainless steel mold thermal resistance was added and a perfect contact was assumed between the mold and the ice cream. The contact surface could also have been a plastic packaging, a chocolate waffle, etc.

To minimize the number of nodes and to reduce the computation time, the symmetry of the geometry has been taken into account. Concerning sticks freezing, the geometry was assumed axisymmetrical and 3518 nodes were used to mesh the surface with two-dimensional thermal solid elements composed of eight nodes. For bulk freezing, 2197 nodes were used to mesh one-half volume with three-dimensional thermal solid elements (20 nodes/element). Figure 4 shows the effect of the number of nodes on the accuracy and on the computation time of the simulation of an ice cream bulk sample.

By introducing the thermal properties of the ice cream, namely the thermal conductivity and the total enthalpy, the geometrical characteristics of the ice cream stick and eventually the packaging or the mold thermal resistances, the software was able to calculate the freezing temperature fields in transient state. The total enthalpy was preferred to the heat capacity for numerical stability reasons since the heat capacity function presented a higher discontinuity at the initial freezing temperature. The results can be presented either by plotting the temperature profiles for different locations inside the ice cream stick or by plotting the different isotherms at different freezing times (Figure 5).

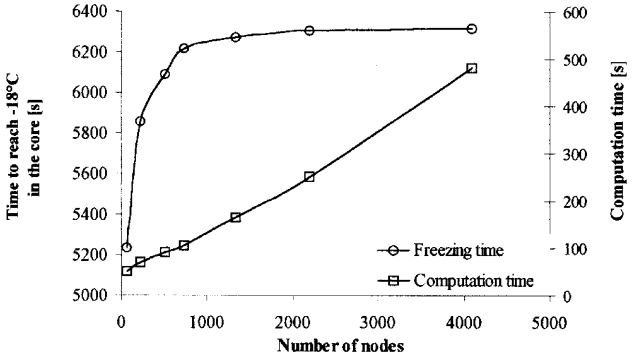

Figure 4. Effect of the number of nodes on the accuracy of the computation. Simulation of a freezing of an ice cream bulk sample. Porosity = 0.50; initial temperature = −5°C; ambient temperature = −28°C; heat exchange coefficient = $20\,\mathrm{W\,m^{-2}\,^{\circ}C^{-1}}$.

Model validation

First, the model was validated for a simple geometrical configuration, i.e. unidirectional heat transfer (Faydi *et al.*, 2001b; Cogné *et al.*, 2003a). Experimental data were collected by recording the temperature field inside the ice cream samples. It was observed that the model was able to predict the experimental freezing kinetics with reasonable agreement (±2°C) in the porosity range 0.05–0.50 and for initial temperatures −2 to −6°C. As a second step, this model was validated for the freezing of ice cream sticks in static brine solutions.

Finally, the model was implemented to simulate bulk freezing experiments in a cold room with samples of different porosities (between 0.05 and 0.50), various mix formulations and air temperatures (−20 to −33°C) at different initial temperatures (between −5 and −8°C). This temperature, adjusted by the evaporation temperature of the refrigerant fluid (ammonia) of the scraped surface heat exchanger and controlled with a thermocouple at the exit of the freezer, was initially considered uniform through the sample bulk. For all these conditions, the theoretical model was able to predict quite precisely (±2°C) the temperature profiles of different ice cream samples (Figure 6).

Freezing times

The freezing time, defined as the time required to reach a core temperature of −18°C, was dependent on the freezing parameters, namely the initial temperature, the refrigeration fluid temperature, the ice cream density and the boundary conditions (Cogné *et al.*, 2003b).

As expected, decreasing the initial and the refrigeration fluid temperature led to lower freezing times. The nature and the flow pattern of the cooling fluid had also a great influence on the freezing kinetics, as shown in Figure 7. The freezing could be five times faster in the case of freezing with forced convection with brine solutions than with air freezing in free convection.

The effect of the porosity was more difficult to interpret. Increasing the air porosity involves a decrease of the sample total density but also a simultaneous decrease of its apparent thermal conductivity (Figure 3). Depending on the ratio volume/cooling surface and on the type of cooling fluid that determines the intensity of the heat fluxes, the ice cream

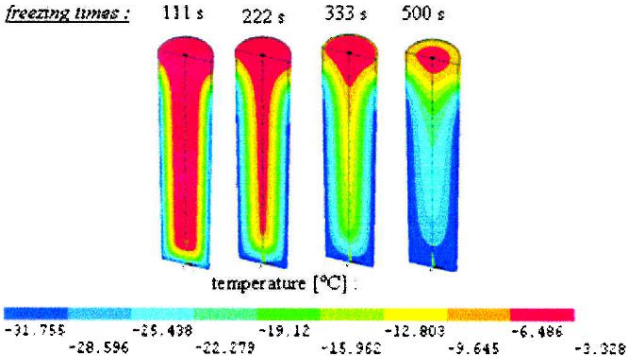

Figure 5. Ice cream sticks freezing kinetics. Isothermal surfaces evolution.

porosity effect could be either to decrease the freezing time—as in the case of freezing with air forced convective—or to increase the freezing time, or to have no significant effect at all, as in the case of freezing in static brine solutions.

Ice Cream Texture Characterization

In the ice cream manufacturing process, the freezing step is the most important step which determines the final texture of this frozen food. The final quality of the product and particularly the smooth texture or the cooling sensation perceived by the consumers when eating ice creams is largely determined, beyond its formulation, by its structure, namely by the distribution, the size and the morphology of the air bubbles and of the ice crystals. To approach the optimization of the quality criteria of the frozen food, the ice cream texture was studied by an original optical microscopy method as previously described (Arnaud *et al.*, 1998; Faydi *et al.*, 2001a; Caillet *et al.*, 2003). For each sample, about 200 crystals were analysed and the ice cristals size distribution curves were plotted with an increment diameter of 10 µm.

Effect of the freezing time on the ice crystal size

The influence of the freezing time on the ice crystal size distribution has been investigated. Six samples of ice cream were produced under the same conditions—porosity equal to 0.50 and temperature at the freezer exit equal to −5°C—but frozen with different rates, between 10 min and

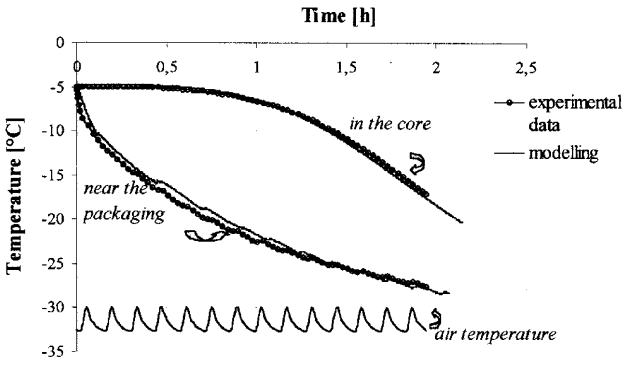

Figure 6. Freezing kinetics of an ice cream bulk sample. Porosity = 0.50; initial temperature = −5°C; ambient temperature = −32 ± 1.5°C.

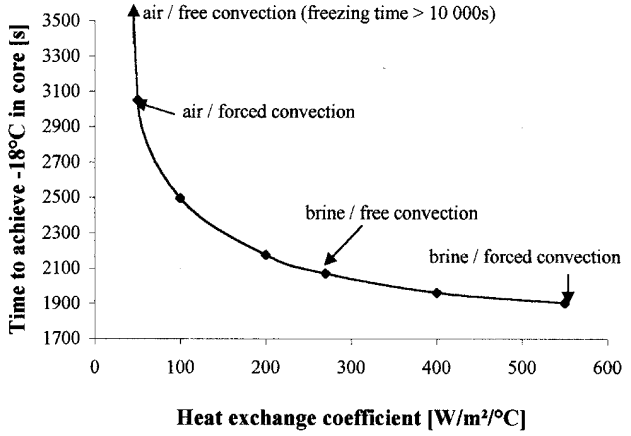

Figure 7. Freezing kinetics of bulk sample. Influence of the heat exchange coefficient. Porosity = 0.50; initial temperature = −5°C; ambient temperature = −40°C.

more than 72 h to reach −18°C in the core of the bulk sample. Then the samples were stored for one week in a cold room at −30°C and analysed by optical microscopy. Figure 8 shows the frequency distribution curve of the ice crystal sizes for the different freezing times. As expected, increasing the freezing times led to a significant increase in the mean diameter of the ice crystals but also to an increase in the standard deviation.

Generally, no new ice crystals were formed after the freezing step inside the scraped surface heat exchanger; the volume of the ice phase increased only through the crystal growth of the already formed crystals. Consequently, a faster rate of cooling during the hardening period will result in a finer distribution of the ice crystal sizes by limiting the ice recrystallization phenomena.

Influence of the porosity on the ice crystal size distribution

To observe the influence of the air ratio on the ice crystal mean size, four samples frozen under the same conditions were studied but with different porosities, namely: 0.05, 0.29, 0.40 and 0.51. Figure 9 shows that the ice crystal mean size decreases as a function of the overrun ratio values with

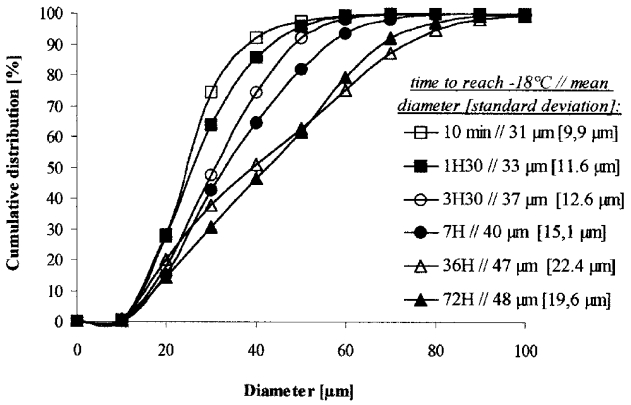

Figure 8. Ice crystal size cumulative distribution curves for different freezing times (time to reach −18°C in the core). Initial temperature = −5°C; porosity = 0.50.

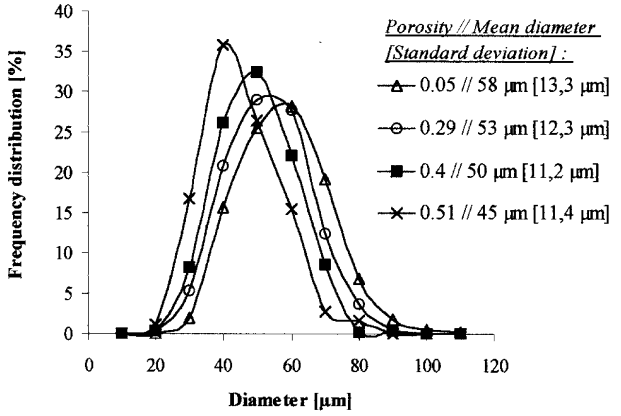

Figure 9. Ice crystal size frequency distribution curves for different porosities. Initial temperature = −5°C; ambient temperature = −20°C.

a larger distribution. This means that the introduction of air resulted in smaller ice crystals sizes and in better stability of the frozen product by reducing the ice crystal growth during the hardening process. Thus, the air overrun process had a double effect, leading to a finer and a more stable structure (Caillet *et al.*, 2003).

Refrigeration temperature influence on the ice crystal size

Decreasing this temperature from −20 to −35°C led to a reduction in the ice crystal mean size; this mean size decreased from 40 µm at −20°C to 33 µm at −35°C for an overrun ice cream (porosity of 0.64) and from 53 to 36 µm for a non-overrun ice cream (porosity of 0.05). This reduction effect was more important in the case of non-overrun ice cream. At low temperatures, the ice crystal sizes were principally governed by the crystal growth kinetics with air incorporation only having a slight influence on the ice crystal size distribution.

Furthermore, the influence of air introduction increased at the higher refrigeration fluid temperature, under which conditions the ice crystal growth kinetics and the recrystallization effects were increased.

CONCLUSIONS

A thermal model has been developed to predict the temperature profiles and the freezing times during the ice cream freezing process. This model includes the thermophysical properties of the ice cream that have been separately determined and then physically modeled. This modelling approach has been validated by comparison of predicted time–temperature profiles with experimental data for different formulations and various freezing operating conditions. An original ice cream texture microscopy analysis has also shown the major influence of the freezing conditions on the ice crystal structure and, consequently, on the ice cream texture and on its organoleptic properties.

NOMENCLATURE

C_P	heat capacity, J kg^{-1}°C^{-1}
g_1, g_2, g_3	shape factors
h	heat exchange coefficient, W m^{-2}°C^{-1}
H	specific enthalpy, J kg^{-1}
L_f	ice fusion latent heat, J kg^{-1}
M	molecular weight, kg mol^{-1}
R	perfect gas constant, J mol^{-1}°C^{-1}
t	time, s
T	temperature, °C or K
T_0	initial freezing temperature of water, °C or K
T_f	initial freezing temperature, °C or K
$T_{surface}$	material surface temperature, °C
T_∞	refrigerant fluid temperature
x	coordinate, m
X	mass fraction
y	coordinate, m
z	coordinate, m

Greek symbols

λ	thermal conductivity W m^{-1}°C^{-1}
ε	air porosity
ρ	density, kg m^{-3}

Subscripts

B	bound water
c	continuous phase
d	dispersed phase
ice	ice
j	component
s	dry matter
w	water

REFERENCES

Arnaud, L., Gay, M., Barnola, J.M. and Duval, P., 1998, Imaging of firn and bubbly ice in coaxial reflected light: a new technique for the characterization of these porous media, *J Glaciol*, 44(117): 326–332.

Caillet, A., Cogné, C., Andrieu, A., Laurent, P. and Rivoire, A., 2003, Characterization of the structure of ice cream by optical microscopy. Influence of freezing parameters on ice crystal structure, *Lebensmittel-Wiss Technol*, 36: 743–749.

Chen, C.S., 1985, Thermodynamic analysis of the freezing and thawing of foods, *J Food Sci*, 50: 1158–1162.

Choi, Y. and Okos, M.R., 1986, Effects of the temperature and composition on the thermal properties of foods, *Food Eng Process Applic*, 93–101.

Cogné, C., Andrieu, J., Laurent, P., Besson, A. and Nocquet, J., 2003a, Experimental data and modelling of thermal properties of ice creams, *J Food Eng*, 58: 331–341.

Cogné, C., Laurent, P. and Andrieu, J., 2003b, Étude expérimentale et modélisation de la congélation des crèmes glacées industrielles, *Thermique et microtechnologies—Congrès SFT 2003*, Marty, Bontemps, Le Person, Ayela (eds), pp 587–592.

Cornillon, P., 1993, Mesure et modélisation des différents types d'eau et des propriétés thermophysiques des gels alimentaires congelés, Thèse Université Claude Bernard, Lyon I.

Cornillon, P., Andrieu, J., Duplan, J.C. and Laurent, M., 1995, Use of nuclear magnetic resonance to model thermophysical properties of frozen and unfrozen model food gels, *J Food Eng*, 25: 1–19.

Faydi, E., Andrieu, J. and Laurent, P., 2001a, Experimental study and modelling of the ice crystal morphology of model standard ice cream. Part I: direct characterization method and experimental data, *J Food Eng*, 48: 283–291.

Faydi, E., Andrieu, J., Laurent, P. and Peczalski, R., 2001b, Experimental study and modelling of the ice crystal morphology of model standard ice cream. Part II: heat transfer data and texture modelling, *J Food Eng*, 48(4): 293–300.

Gonnet, E., Andrieu, J. and Laurent, M., 1987, Intrinsic thermal conductivities of basic food components, *High Temp High press*, 19: 323–330.

Miles, C.A., Van Beek, G. and Veerkaamp, C.H., 1983, Calculation of thermophysical properties of foods, in *Physical Properties of Foods*, Jowitt, Escher, Hallström, Meffert, Spiess, Vos (eds), Vol. 16, pp 269–312.

Özisik, N., 1985, *Heat Transfer: a Basic Approach* (McGraw-Hill, New York, USA).

Renaud, T., Briery, P., Andrieu, J. and Laurent, M., 1992, Thermal properties of model foods in the frozen state, *J Food Eng*, 15: 83–97.

Schwartzberg, H.G., 1976, Effective heat capacities for the freezing and thawing of food, *J Food Sci*, 41: 152–156.

ACKNOWLEDGEMENTS

The authors are grateful to Nestlé Company and to ANRT (CIFRE programme) for its scientific and technical help and also for the material and financial support received during this work.

ADDRESS

Correspondence concerning this paper should be addressed to Dr J. Andrieu, Laboratoire d'Automatique et de Génie des Procédés (LAGEP), UMR CNRS 5007, UCB Lyon 1/ESCPE Lyon, Bât. 308G, 3 rue Victor Grignard, 69622 Villeurbanne, France.
E-mail: andrieu@lagef.cpe.fr

The paper was prepared at the 9th Congress of the French Society of Chemical Engineering held in Saint-Nazaire, France, 9–11 September 2003. The manuscript was received 24 January 2003 and accepted for publication after revision 10 September 2003.

Lebensm.-Wiss. u.-Technol. 36 (2003) 743–749

lwt

www.elsevier.com/locate/lwt

Characterization of ice cream structure by direct optical microscopy. Influence of freezing parameters

Alexandre Caillet, Claudia Cogné, Julien Andrieu*, Pierre Laurent, Alain Rivoire

Laboratoire d'Automatique et de Génie des Procédés (LAGEP), UMR CNRS 5007, Universite Claude Bernard Lyon 1/ESCPE Lyon, UPRES A-Q5007, ESCPE, Bât. 308G, 43 Bd. du 11 November 1918, 69622 Villeurbanne Cedex, France

Received 21 October 2002; accepted 29 April 2003

Abstract

The main objective of this study was to develop and to set up a new optical direct microscopy method, based on the reflected light flux differences, with episcopic axial lighting to characterize the different phases structure of commercial overrun ice creams. Firstly, the results obtained have been validated by two others methods, a destructive method by dispersion and observation by light microscopy and, an indirect method, by scanning electron microscopy after freeze-drying sample. It was observed that the three methods were in agreement and led to the same conclusions concerning the main freezing parameters influence.

So, this technique has been principally used to investigate the effects of the freezing conditions on the ice crystal structure. One of the most important parameters is the freezing rate that governs not only the size, but also the ice crystals texture of the ice cream. The air introduction (overrun) tends to limit the ice crystal growth. Besides, by this method, it was also possible to observe and to quantify the air bubbles size distribution. This direct microscopy method could be extended to other frozen food structure analysis.

Keywords: Ice cream structure; Reflexion photonic microscopy; Ice crystal size; Air porosity

1. Introduction

In the ice cream manufacturing process, the freezing step is one of the most important steps which determines the final texture of this frozen food. The final quality of the product and particularly the smooth texture or the cooling sensation perceived by the consumers when eating ice creams is largely conditioned, beyond its formulation, by its structure, namely by the distribution, the size and the morphology of the air bubbles and the ice crystals. Nevertheless, during hardening, storage and commercial distribution, some important physical changes occur in the ice cream structure. Concerning the air phase, two main mechanisms of the air phase redistribution have been observed: coalescence and drainage (Chang & Hartel, 2002a). Concerning the ice phase, the ice crystal texture is strongly affected by the recrystallization phenomena, which depend principally on formulation factors, on freezing process and on storage temperature conditions (Donhowe & Hartel, 1996). A good quality control of the ice texture and particularly of the ice crystals growth relies on a large number of small crystals. The literature data show that the air bubbles diameter range is located between 30 and 150 μm with a mean diameter around 40 μm (Chang & Hartel, 2002b), and, the ice crystals mean size is between 20 and 75 μm with a mean value around 40 μm (Berger, Bullimore, White, & Wright, 1972; Hagiwara & Hartel, 1996; Hartel, 1996; Russel, Cheney, & Wantling, 1999). Concerning the lipid components, the fat is present in the mix as a fine emulsion which partially coalesces during the freezing. The published data indicate a range of these globule diameter to be 0.04–4.0 μm (Berger et al., 1972).

To approach the quality criteria optimization, various methods types have been used to characterize the texture and the structure of frozen foods. These methods include, for example, sensorial analysis, textural analysis, differential scanning calorimetry, nuclear magnetic resonance spectroscopy or imagery and various microscopic methods. Among these numerous methods, it seems that the microscopic methods are the most

*Corresponding author. Tel.: +33-4-72-43-1843; fax: +33-4-72-43-1682.

E-mail address: andrieu@lagep.univ-lyon1.fr (J. Andrieu).

0023-6438/03/$30.00
doi:10.1016/S0023-6438(03)00094-X

Nomenclature

ε	air porosity or air volume fraction (air volume/total aerated mix volume) (dimensionless)
τ	(air volume)/(nonaerated mix volume) (Eq. (1)) (%)
T_f	mix temperature at the scraped surface heat exchanger (SSHE) exit (draw temperature) (°C)
T_h	hardening temperature (°C)
T_m	mix initial freezing temperature (°C)
X	magnification (dimensionless)

suitable and adequate and, consequently, are the ones most used and implemented in industrial control laboratories.

Three types of microscopic techniques are currently used: destructive methods, indirect methods and direct methods. The first methods type is based on the optical observation of a sample mixed with a suitable medium for dispersing the observed phase (ice crystals or air bubbles) and dissolving the other phases (Donhowe, Hartel, & Bradley, 1990; Sztehlo, 1994). Its great interest relies in the following facts: (1) the experimental time is short and (2) the information on the particles size distribution is easy to collect. Nevertheless, due to the sample dissolution, no data about the relative position and about the volume fractions of the different phases can be obtained. Besides, as the sample is totally destroyed or melted, the images obtained cannot represent all the frozen system texture morphology. The second type are of indirect methods that use mainly electronic microscopy techniques. They provide clear images of the structure and they destroy only partially the sample by cryo-substitution, cryo-fixation, freeze-etching or freeze-drying (Berger & White, 1971; Goff, Verespej, & Smith, 1999; Woinet, Andrieu, Laurent, & Min, 1998). Their main advantage relies on high magnification that allows one to observe fine structural details, but the electron microscopy is expensive and the sample preparation time is quite long.

The last method used to characterize the structure of frozen foods is more original and quite unknown in industrial laboratories. It is the photonic microscopy method with episcopic coaxial lighting that preserves at best the sample original texture of the frozen sample. It is based on direct light reflection on the surface of an ice cream sample. A direct observation in situ at cold temperature allows maintaining the sample in its native state and minimizes the potential artefacts of all the other methods. Compared with the electron microscopy, the main drawback of our method is its low magnification, which does not allow, for instance, the observation of the fat particles. So, to investigate the influence of the freezing conditions on the ice cream structure, the direct optical microscopic method by reflexion was developed and set up in our laboratory (Faydi, Andrieu, & Laurent, 2001) with model ice creams without overrun. In the same project, some experimental data obtained have been checked and validated by indirect and destructive methods. The present paper concerns the extension of this method to commercial ice creams with standard formulations.

2. Material and methods

2.1. Ice cream preparation

In our experimental runs, all the different ice cream samples had he same mix standard composition (g/100 g), namely: water 61.7, sugar 18, msnf 11, fat 9 and emulsifier 0.3. In order to obtain the better reproducibility, the mix was always prepared in the same conditions with the same procedure very precisely controlled. The initial freezing point of our mix was determinated by DSC around $T_m = -2.5$°C (Cogné, Andrieu, Laurent, Besson, & Nocquet, 2003). The ingredients were mixed at 50°C, homogenized at 140 bar in the first stage, and at 40 bar in the second stage, to form tiny fat globules, and pasteurized at 85°C during 25 s. Then, the mix was quickly cooled at 4°C and aged 24 h.

The air phase was added during the initial freezing step which takes place inside the scraped surface heat exchanger (SSHE), type Hoyer KF80, where the mix was pre-crystallized. The hardening step was realized in cold rooms conditioned with convective cold air. The influence of the three process parameters on the ice cream structure was investigated: (1) of the ice cream temperature at the SSHE exit also called draw temperature, noted T_f—the range investigated was between 0°C and −6°C, (2) of the two air cooling temperatures in the cold rooms denoted T_h, −35°C and −20°C and (3) the porosity denoted ε, between the limit values 0 and 0.51. This air porosity or air volume fraction, denoted ε, is related to the industrial overrun ratio, noted τ, by the following relation:

$$\tau(\%) = 100 \times \frac{\varepsilon}{1-\varepsilon}. \quad (1)$$

2.2. Direct optical microscopy observation method

This direct observation method by optical microscopy with episcopic coaxial lighting was originally developed

by the physicists studying the polar ices structures (Arnaud, Gay, Barnola, & Duval, 1998) and this method was adapted in our laboratory by Faydi et al. (2001) to characterize during unidirectional quiescent freezing, the frozen structure of an ice cream mix without overrun.

This method is essentially based on the light flux reflected by the surface of the sample. In fact, the reflected light fluxes that determined the image contrasts resulted, at the same time, from the light fraction of the incident flux absorbed and/or from the light reflected at different interfaces with different orientations, for example at the air bubbles surfaces which are present in the case of commercial ice creams containing overrun (Fig. 1).

After its preparation, the ice cream cups were firstly stored at −25°C. Frozen ice cream cubic samples, a few centimeters long, have been taken and then immersed in liquid nitrogen in order to stop totally the crystallization process and to solidify completely the fat components. Afterwards, the sample was introduced in a cold room maintained around −25°C where the cut surface was meticulously polished, with a microtome (Leica SM2000R) to obtain a very smooth surface with a roughness lower than 1 μm. After obtaining a suitable surface quality, the ice cream sample was directly observed, still at −25°C inside the cold room, with a stereomicroscope (LEICA MZ12), equipped with a digital video camera (Hitachi CCD) and an optical fibre providing the episcopic coaxial lighting. A video monitor was placed inside the cold room and the images were stored with a P.C. located outside the cold chamber. All the optical material in the cold room was placed inside a dry air glove box in slight overpressure with respect to the cold chamber pressure to avoid humidity condensation or frost problems at the frozen sample surface or at the surface of the microscope oculars.

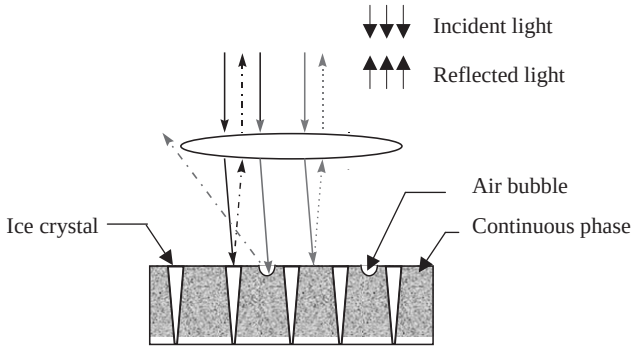

Fig. 1. Principle of photonic microscopy with episcopic coaxial lighting.

Then, the images were recorded with an acquisition data software (Visilog 5.4) and represented in 256 grey levels. Afterwards, they were converted from pixels to micrometers, depending on the magnification selected. Due to problems to separate correctly the three main phases during the image thresholding and to create a representative skeleton, the image analysis was only carried out by tracing with a mouse. Due to irregular shapes of the ice crystals, we measured two characteristic lengths of the ice crystal to evaluate the particle area, in order to calculate the equivalent circle diameter. For each sample, about 200 crystals were analysed and the size distribution curves were plotted with an increment diameter $\Delta d = 10\,\mu m$. Air bubbles, as expected, appeared as dark zones and were of quite spherical shape. Ice crystals appeared in grey colour and the cryoconcentrated continuous phase (containing the dry matter and the unfrozen water), in white levels. Fat globules—with mean diameter values according to literature around 1 μm—could be the dark points round about the air bubbles surface (Fig. 2).

3. Results and discussion

We observed that the ice crystals distribution data depended notably on the microscope magnification. Although the small crystals had a great importance, they

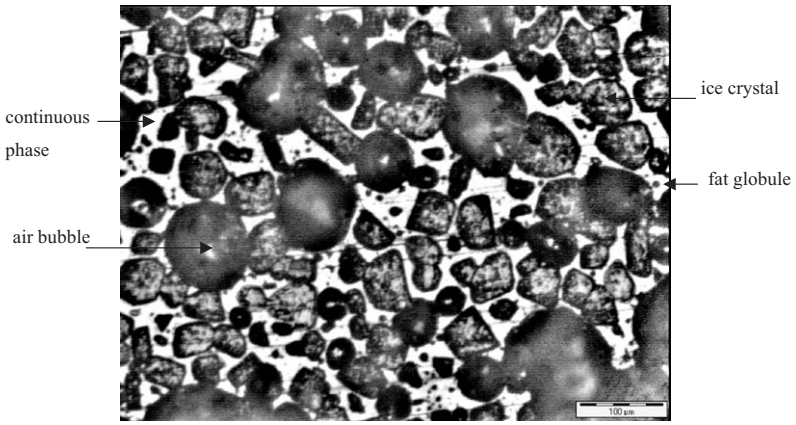

Fig. 2. Structure of ice cream observed by direct microscopy method. $\varepsilon = 0.4$; $T_f = -5°C$; $T_h = -20°C$; $X = 100$.

were not taken into account satisfactorily, particularly, due to the low maximum magnification of our stereomicroscope. For the lower magnification, the ice crystals average diameter was higher than the corresponding values obtained with higher magnification. Finally, to avoid artefacts due to image analysis limitations, we adopted and kept for all the experiments analyses, the same image magnification, namely $X = 100$, except in the case of too large ice crystals sizes.

3.1. Comparison of different observation methods

First, in order to validate our direct observation method, some ice crystal sizes data were compared to data resulting from two others methods, namely a destructive method and an indirect method.

The destructive method was based on mixing the ice cream sample in a suitable medium, dispersed at $-10°C$, and observed with an optical microscope by transmission between two thin layers. Then, the ice crystals were automatically analysed with a software based on the principle of separation of adjacent crystals.

The indirect method adopted was also previously used in our laboratory (Woinet et al., 1998; Faydi et al., 2001). Frozen samples were first freeze-dried at temperatures lower than the glass transition temperature to avoid possible structure modifications during the sublimation step. Then, the freeze-dried samples were polished, sputter coated with a thin gold layer. The samples were transferred under vacuum into the scanning electron microscope, where they were viewed (15 kV accelerating voltage) and photographed by using different magnifications. In the case of samples with overrun, we could differentiate clearly the air bubbles by their spherical shape, and the pores generated after the ice sublimation (Fig. 3).

Fig. 4 compares the ice crystal mean size obtained by the three microscopy methods—i.e. direct, destructive and indirect methods—for ice cream samples frozen under different process conditions. These three methods converge globally to the same data.

3.2. Influence of the ice cream temperature at the SSHE exit on the ice crystal structure

In the case of cooling conditions above the initial freezing temperature, the mix was only whipped on the scraped heat exchanger surface, without any ice nucleation and ice freezing. The electron microscopy (Fig. 5a) showed a dentritic-type pores structure after the ice sublimation confirming the structure observed with the direct method (Fig. 5b). Besides, with the destructive microscopy method (Fig. 5c)—method not really suited for large particles—we observed some important ice crystals agglomeration, so that the quantitative size analysis was very difficult to carry out.

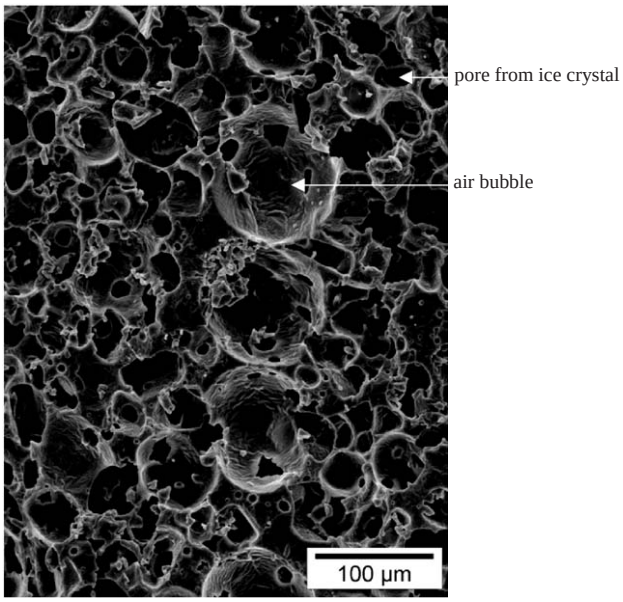

Fig. 3. Ice cream structure image by scanning electron microscopy. $\varepsilon = 0.4$; $T_f = -5°C$; $T_h = -35°C$.

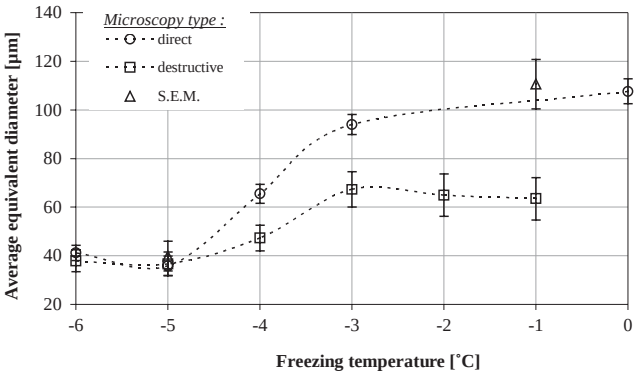

Fig. 4. Comparison of ice crystal mean size with the three microscopic methods.

By contrary, operating the freezing in the SSHE below the mix initial freezing temperature generated ice nuclei and consequently small ice crystals in the final product. In this case, the three methods—scanning electron microscopy (Fig. 6a), direct microscopy (Fig. 6b) and destructive method (Fig. 6c)—led globally to the same qualitative conclusions.

In the same way, we also investigated the influence of the hardening temperature—i.e. the air temperature in the cold room—on ice crystal shape and size structure by the direct optical microscopy method. As expected, decreasing the hardening temperature led to a reduction of ice crystal mean size by limiting the recrystallization phenomena (Miller-Livney & Hartel, 1997; Cogné, 2003).

3.3. Air porosity influence on the ice crystals size

To observe the influence of the air porosity on the ice crystal mean size, we studied four frozen samples in the

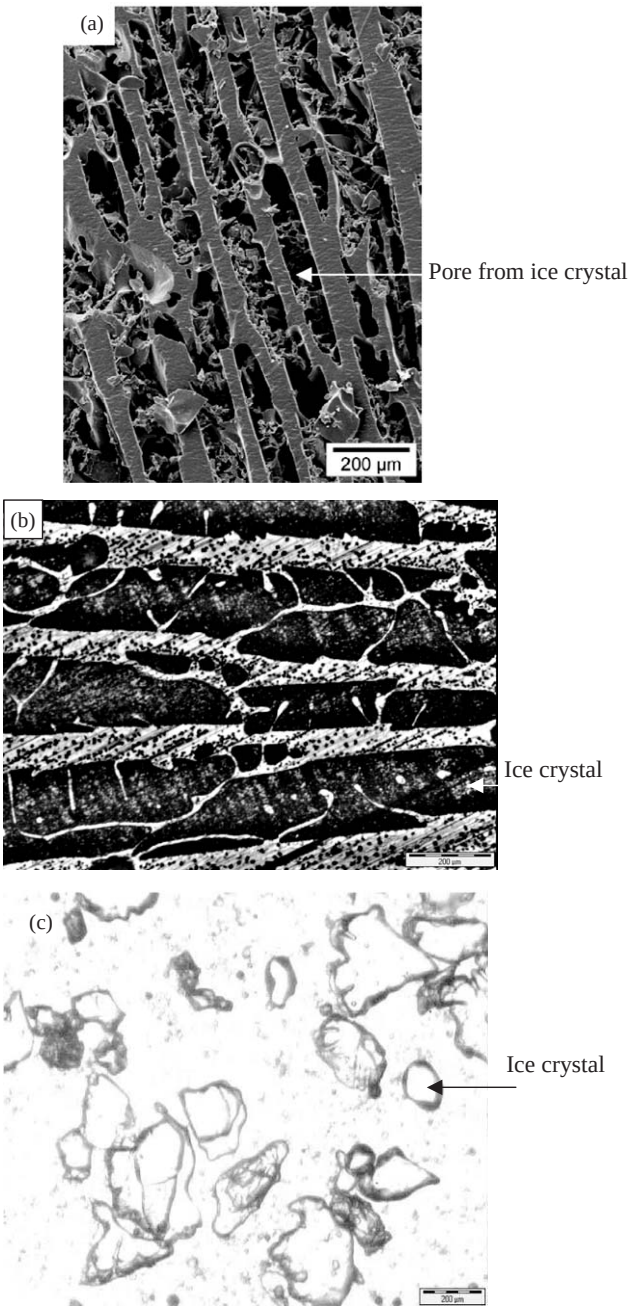

Fig. 5. Nonoverrun ice cream structure: (a) by indirect method, (b) direct method and (c) by destructive method; $T_f > T_m$ ($T_f = -1°C$); $\varepsilon = 0$; $T_h = -35°C$.

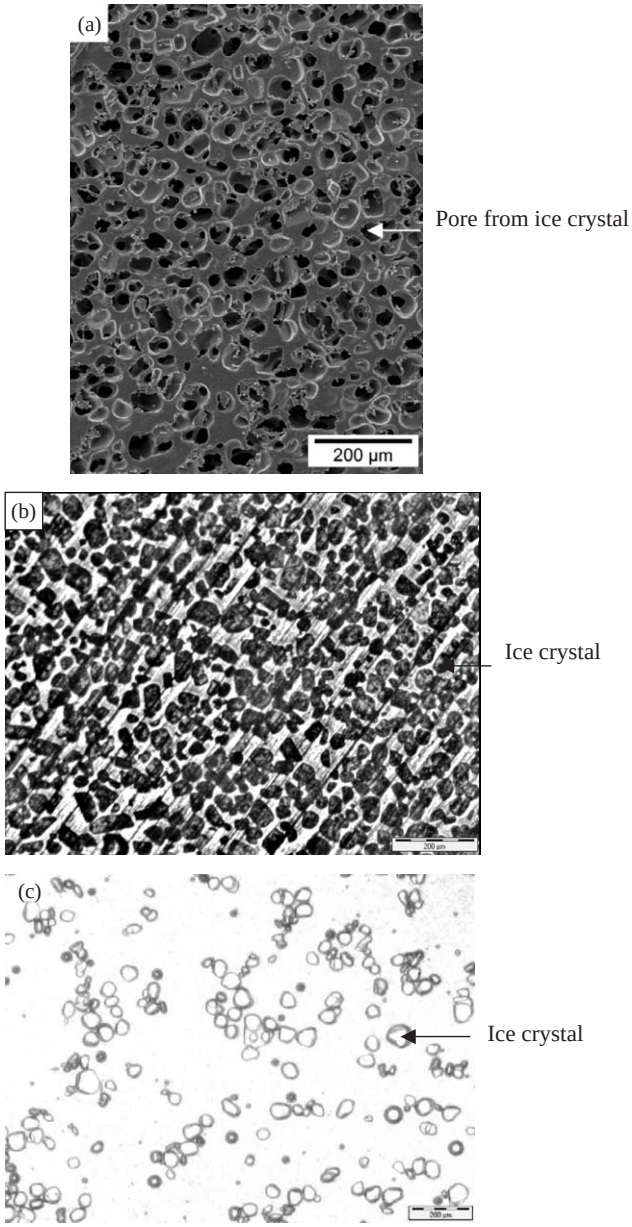

Fig. 6. Nonoverrun ice cream structure: (a) by indirect method, (b) direct method and (c) by destructive method; $T_f < T_m$ ($T_f = -5°C$); $\varepsilon = 0$; $T_h = -35°C$.

same conditions ($T_f = -5°C$; $T_h = -20°C$) but with different porosities, namely: 0.05, 0.29, 0.40 and 0.51. Fig. 7 shows that the ice crystal mean sizes decrease as a function of the porosity values with a more large distribution that means that the air introduction involves smaller ice crystals sizes and a better stability of the frozen product by reducing the ice crystal growth during the hardening process. So, the air overrun processes had the double effect to lead to a finer and a more stable structure. Concerning the heat transfer phenomena, increasing the air porosity induces a decrease of the thermal conductivity due to the air insulation effect, but on the other hand, for a given ice cream sample volume, the mass to freeze is reduced due to the decrease of the ice cream density (Cogné et al., 2003). According to Flores and Goff (1999), a certain amount of air was necessary to have a noticeable impact on the microstructure and that air would not only affect ice cream thermal properties but may also act as a physical barrier during the freezing. Indeed, a well-dispersed air structure reduces the probability of collisions between ice crystals and, by the way, reduces the recrystallization phenomena.

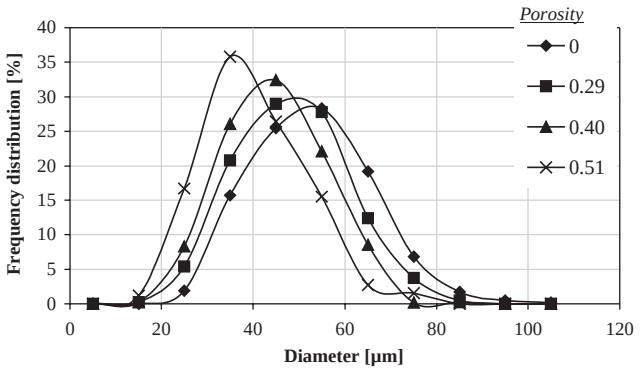

Fig. 7. Ice crystal size frequency distribution curves for different air porosities. $T_f = -5°C$; $T_h = -20°C$.

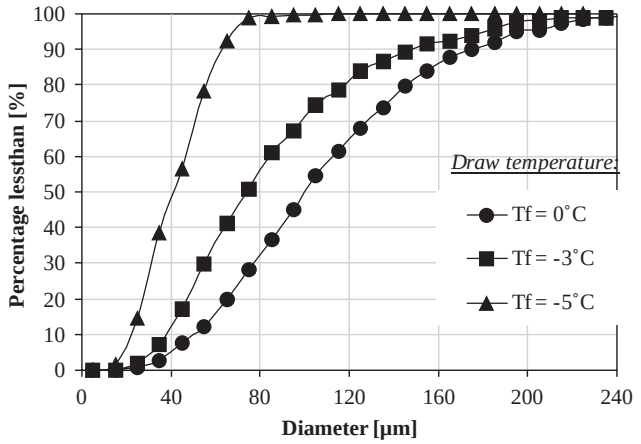

Fig. 8. Air bubbles sizes cumulative distribution curves for different mix SSHE exit temperatures. $\varepsilon = 0.28$; $T_h = -35°C$.

3.4. Air bubbles size distribution

The air bubble size was measured by assuming that the particles are spherical. At least 200 air bubbles for each sample were analysed to ensure an accurate representation of the whole size distribution. Nevertheless, the three-dimensional structure was not take into account: air bubbles were assumed to be fractured at the equatorial plan, but in reality, the spherical particles could be fractured anywhere from the top to the bottom. Contrary to the destructive methods that are based on sample dilution, the direct method enables to observe in situ the air bubbles shape and size inside the frozen ice cream structure which represents a great advantage of this method. So, the qualitative information given by these images is interesting because it was possible to observe the relative position of each phase. Furthermore, we observed, for example that air bubbles are not spread out very uniformly through the other phases.

Fig. 8 compares the cumulative distribution of the air bubbles size for three ice cream samples with the same porosity $\varepsilon = 0.29$ and the same hardening temperature $T_h = -35°C$, but with different ice cream mix temperatures at the SSHE exit, namely 0°C, −3°C and −5°C. So we observed that lowering the SSHE exit temperature involved an important decrease of air bubble mean diameter: from 112 µm for samples only whipped in the SSHE ($T_f = 0°C$) to 47 µm for the samples partially frozen in the SSHE ($T_f = -5°C$). As mentioned by Chang and Hartel (2002c) who observed the same behaviour with ice cream samples directly removed from a batch freezer, the freezing of the mix is necessary for the stabilization of the small air cells. Indeed, by decreasing the SSHE exit temperature, the ice cream viscosity increases what limits the air bubbles coalescence and modifies also the flow pattern of the frozen mix.

4. Conclusions

The direct method of optical microscopy with episcopic coaxial lighting has the advantage to characterize, in situ, the ice cream structure by preserving at best the original properties of the frozen overrun ice cream sample.

Firstly, this technique was compared with other classical techniques more largely used for the characterization of this type of frozen food texture. The data derived with this new original method were found in agreement with each other. Besides, it has the great advantage to be easy to implement with low running costs.

Secondly, we applied this technique to analyse the influence of porosity on the ice crystals distribution and the influence of the freezer exit temperature of the mix on the air bubbles size distributions. The results presented in this study are in agreement with the last literature data. Nevertheless, for the purpose of heat transfer modelling during ice cream freezing, more experimental data and more advanced analyses of the air bubbles size distribution are necessary to estimate precisely the air porosity which is an important parameter influencing the apparent thermal conductivity of the mix.

Finally, this methodology could be extended to other ice cream formulations and to other frozen food types (vegetables, fruits, etc.) for routine exploitation in industrial control laboratories.

Acknowledgements

The authors are grateful to Nestlé Company and ANRT (CIFRE programme) for the scientific help and also for the material and financial support received during this work.

References

Arnaud, L., Gay, M., Barnola, J. M., & Duval, P. (1998). Imaging of firn and bubbly ice in coaxial reflected light: A new technique for the characterization of these porous media. *Journal of Glaciology*, *44*(117), 326–332.

Berger, K. G., Bullimore, B. K., White, G. W., & Wright, W. B. (1972). *The structure of ice cream—Part 1*. Dairy Industries (pp. 419–425) August.

Berger, G., & White, G. W. (1971). An electron microscopical investigation of fat destabilization in ice cream. *Journal of Food Technology*, *6*, 285–294.

Chang, Y., & Hartel, R. W. (2002a). Stability of air cells in ice cream during hardening and storage. *Journal of Food Engineering*, *55*, 59–70.

Chang, Y., & Hartel, R. W. (2002b). Measurement of air cell distribution in dairy foams. *International Dairy Journal*, *12*, 463–472.

Chang, Y., & Hartel, R. W. (2002c). Development of air cells in a batch ice cream freezer. *Journal of Food Engineering*, *55*, 71–78.

Cogne, C. (2003). *Etude expérimentale et modélisation de la congélation des crèmes glacées foisonnées*. Thèse, Université Claude Bernard, Lyon I.

Cogne, C., Andrieu, J., Laurent, P., Besson, A., & Nocquet, J. (2003). Experimental data and modelling of thermal properties of ice creams. *Journal of Food Engineering*, *58*, 331–341.

Donhowe, D. P., & Hartel, R. W. (1996). Recrystallization of ice during bulk storage of ice cream. *International Dairy Journal*, *6*, 1209–1221.

Donhowe, D. P., Hartel, R. W., & Bradley, R. L. (1990). Determination of ice crystal size distributions in frozen desserts. *Journal of Dairy Science*, *74*(10), 3334–3344.

Faydi, E., Andrieu, J., & Laurent, P. (2001). Experimental study and modelling of the ice crystal morphology of model standard ice cream. Part I: Direct characterization method and experimental data. *Journal of Food Engineering*, *48*, 283–291.

Flores, A. A., & Goff, H. D. (1999). Ice crystal size distributions in dynamically frozen model solutions and ice cream as affected by stabilizers. *Journal of Dairy Science*, *82*, 1399–1407.

Goff, H. D., Verespej, E., & Smith, A. K. (1999). A study of fat and air structures in ice cream. *International Dairy Journal*, *9*, 817–829.

Hagiwara, T., & Hartel, R. W. (1996). Effect of sweetener, stabilizer and storage temperature on ice recrystallization in ice cream. *Journal of Dairy Science*, *79*, 735–744.

Hartel, R. W. (1996). Ice crystallization during the manufacture of ice cream. *Trends in Food Science and Technology*, *7*, 315–321.

Miller-Livney, T., & Hartel, R. W. (1997). Ice recrystallisation in ice cream: interactions between sweeteners and stabilizers. *Journal of Dairy Science*, *80*(3), 447–456.

Russel, A. B., Cheney, P. E., & Wantling, S. D. (1999). Influence of freezing conditions on ice crystallisation in ice cream. *Journal of Food Engineering*, *39*, 179–191.

Sztehlo, A. (1994). Investigation of the structure of ice cream by light microscopy. *Microscopy and Analysis*, (September) 85–86.

Woinet, B., Andrieu, J., Laurent, M., & Min, S. G. (1998). Experimental and theoretical study of model food freezing. Part II. Characterization and modelling of the ice crystal size. *Journal of Food Engineering*, *35*(4), 395–407.

Available online at www.sciencedirect.com
ScienceDirect
ELSEVIER
Colloids and Surfaces A: Physicochem. Eng. Aspects 299 (2007) 93–100
COLLOIDS AND SURFACES A
www.elsevier.com/locate/colsurfa

Effects of surfactants on crystallization of ethylene glycol distearate in oil-in-water emulsion

M.A. Bolzinger [a,b], C. Cogne [c], L. Lafferrere [a], F. Salvatori [a], P. Ardaud [d], M. Zanetti [d], F. Puel [a,*]

[a] LAGEP UMR CNRS 5007, Université Lyon 1, Lyon, ESCPE. Bât. 308G, 43 bld. du 11 Novembre 1918, 69622 Villeurbanne Cedex, France
[b] Laboratoire de Dermopharmacie et Cosmétologie, Faculté de Pharmacie (ISPB), Université Lyon 1, Lyon, 8 av Rockefeller, 69373 Lyon Cedex 08, France
[c] Laboratoire des Technologies Innovantes, IUT de l'Aisne, 48 rue d'Ostende 02100 Saint Quentin, France
[d] Rhodia Novecare 40, rue de la Haie Coq, 93306 Aubervilliers Cedex, France

Received 13 July 2006; received in revised form 10 November 2006; accepted 14 November 2006
Available online 19 November 2006

Abstract

Ethylene glycol distearate (EGDS) was forced to crystallize as thin platelet in order to obtain a pearlescent effect. This was possible by performing a cooling surface crystallization in oil-in-water emulsion with the presence of an emulsifier. Under stagnant conditions, nucleation events and growth of faceted crystals in the oil phase were in situ monitored under microscope. After a first primary nucleation of dendritic crystals, a second population of faceted crystals arose by secondary nucleation and seemed to be the prevailing population. In a stirred vessel, the platelet shape of EGDS crystals was driven by the surfactant choice. Only a non-ionic surfactant, located at the liquid interface was supposed to interact with EGDS during the development of the crystals favouring a platelet habit. The nature of the interaction was not yet established. Moreover, the mastery of the platelet shape was lost when the amount of non-ionic surfactant relatively to the EGDS was decreased. This underlined the importance of the non-ionic surfactant for the obtaining of desired shape. The different physical qualities of crystals produced allowed us to confirm relationships between EGDS particle features with their effect of pearlescence of a cold pearl blend.

Keywords: Crystallization; O/W emulsion; Non-ionic surfactant; Ethylene glycol distearate; Cosmetics

1. Introduction

Since several decades, the natural pearl essence was replaced by synthetic pearlescent pigments in a wide range of personal-care formulations in order to enhance their attractiveness. When disperse in a shampoo base, pearlescent pigments having a platelet shape allow a regular multiple reflection of the light. For maximum effect, the particle layers must be aligned parallel to the surface [1,2]. In this configuration, the light is reflected in the most favourable direction and not randomly.

Pearlescent pigments can be grouped into two fields: (1) free substrate particles that consist of basically one optically homogeneous material of high refraction index having a platelet shape; (2) particles that have a layered structure on a substrate [1]. Ethylene glycol distearate ester (EGDS) belongs to the former case. It is a premium quality fatty acid ester. It can be forced to crystallize as thin platelets under definite conditions. The EGDS platelets particles can be obtained by crystallization in a concentrated surfactant based formulation. This suspension usually named cold pearl blend presents the advantage to be simply added to personal-care formulations under mixing at room temperature.

The main manufacturing process widely used in industry to prepare this concentrated suspension of EGDS platelets is a cooling crystallization in emulsion. EGDS is a lipophilic compound with a melting point of 60 °C. Above 60 °C, EGDS constitutes the lipophilic phase of the O/W emulsion. Surfactants are added to stabilize the dispersion. Under cooling EGDS crystallizes and the water constitutes the external phase of the suspension. This crystallization in emulsion is rather complex since the presence of various surfactants at the interface or in the oil phase can

* Corresponding author. Tel.: +33 4 72 43 18 34; fax: +33 4 72 43 16 82.
E-mail address: puel@lagep.univ-lyon1.fr (F. Puel).

0927-7757/$ – see front matter © 2006 Elsevier B.V. All rights reserved.
doi:10.1016/j.colsurfa.2006.11.026

impact the particle shape of EGDS in the medium. The mastery of such operation in industry is characterized by a high level of know-how. A general description of the manufacture of such cold pearl suspension could be found [2]. Nevertheless, the understanding of the role of the emulsifiers on the control of the particle shape has not been yet published in the open literature.

A large amount of publications in the literature on the crystallization of O/W emulsions is available in the field of food science. Its complexity has already been revealed in the rate and extent of crystallization of fats and lipids system [3,4]. In addition to all the classical parameters, which must be accounted for crystallization in a bulk liquid, new factors are imparted by the subdivision of the bulk liquid into droplets. In almost all bulk liquids, some impurities act as the starting point for nucleation and crystallization occurs rapidly by a heterogeneous mechanism. However, when the oil is finely divided into emulsion droplets, the number of droplets may significantly exceed the number of impurities. The oil droplets are impurity free and hence crystallize at higher level of supercooling by a homogeneous mechanism [5]. With an emulsifier, the previous statement is scarcely valid. First, if a chemical affinity between the surfactant alkyl chain and the material which should crystallize is found, the hydrocarbon tails of adsorbed surfactant molecules penetrate into the dispersed oil phase and can increase the nucleation rate. The emulsifier acts as a nucleation site for oil [6]. In this case, nucleation rate is proportional to the interfacial area and not to the volume. Sato and co-workers go further by differencing two types of heterogeneous nucleation processes caused by the surfactants: interface and volume nucleation. The former mechanism occurs at the oil–water interface where the surfactants are absorbed and crystallized during cooling because of their high melting point. The freezing of the lipophilic chain of the absorbed emulsifier membranes can be a template for nucleation of the oil molecule [7,8]. The latter mechanism is due to the nucleation accelerated by the surfactants that are present in the dispersed oil phase [9]. Some additional observations show that solid droplets can induce nucleation in liquid droplets they are physically mixed with, presumably through a collision mechanism (i.e. interdroplet nucleation) [10,11]. Moreover, the presence of surfactants may alter the growth of the crystals in the oil phase leading to a possible change of shape of the particles. In the case of zeolite in non-ionic microemulsions, the surface aspect as well as the aggregate formation may be directed by the presence of surfactant [12]. For a concise view in this domain, we recommend the reviews of Garti and Yano [13] for the roles of emulsifiers and of Povey [3] and Coupland [4] for the study of crystallization of oil-in-water emulsions.

When looking to patents devoted to the manufacture of cold pearl concentrate [14], it appears that several surfactants are used in combination, potentially leading to complex interactions between surfactants and oil. In order to simplify the study, we chose simple formulations, based on EGDS (as the dispersed oil), water (as the continuous phase) and a main surfactant (acting as an emulsifier). The primary objective was to investigate the role of surfactants for the obtaining of thin platelets responsible of the optimal pearlescence. This work aims also to confirm the relationship between EGDS particles shapes and their optical effects.

2. Materials and method

2.1. Raw materials

Commercial EGDS were blends of stearate esters mainly composed of ethylene glycol distearate and ethylene glycol monostearate (EGMS). The percentage of each ester is indicated in the brackets. The first one indicated the EGDS percentage and the second one the percentage of EGMS (ethylene glycol monotearate ester) in the blend.

Experimentally, three commercial EGDS were tested and the pearlescence aspect of the concentrates was compared.

- EGDS 3432 (Croda) ethylene glycol distearate 85% (EGDS/EGMS 85/15);
- EGDS 3496 (Croda) ethylene glycol distearate 95% (EGDS/EGMS 95/5);
- Cutina AGS (Cognis) ethylene glycol distearate 99% (EGDS/EGMS 99/1).

On the same way, three different types of surfactants required for the emulsification stage (one anionic, one non-ionic and the last one amphoteric) were analysed.

- cocamidopropylbetaine (Mirataine BET C-30, Rhodia; active dry matter: 35%);
- sodium trideceth (3) sulfate (Rhodapex EST 30, Rhodia; active dry matter: 75%);
- Lauryl alcohol (7 EO) (Rhodasurf LA-7 Rhodia; active dry matter: 90%).

DMDM Hydantoin (Glydant, Lonza) was used to preserve the final formulations.

2.2. Crystallization procedure

The formulations studied are indicated in Table 1. Formulations A, B and C differed by the surfactant nature. In the C class, C, C1 and C2 differed by their EGDS/surfactant ratio varying from 0.75 to 2.60. C, C3 and C4 were formulated with different EGDS qualities.

EGDS emulsion crystallization was divided in two successive stages. During the first stage, all the ingredients (water, surfactant and commercial EGDS flakes) were introduced in a glass stirred vessel (1 l). The temperature was controlled in the vessel by using a thermostatic bath and a circulating pump, the coolant going through a glass jacket. The mixture was melted at 75 °C under stirring. The second stage corresponded to EGDS crystallization and began at 61 °C until 25 °C. Once nucleated, EGDS crystals grew and got a faceted shape. Before withdrawing the suspension from the vessel with a bottom valve, the preservative was added. The final suspension was made of a population of crystals of EGDS dispersed in a water phase containing the surfactants.

M.A. Bolzinger et al. / Colloids and Surfaces A: Physicochem. Eng. Aspects 299 (2007) 93–100

Table 1
Composition of the formulations

Formulations (mass %)	A	B	C	C1	C2	C3	C4
EGDS/EGMS (85/15)	19	19	19	19	11		
EGDS/EGMS (95/5)						19	
EGDS/EGMS (99/1)							19
Cocamidopropylbetaine	41.8						
Sodium trideceth (3) sulfate		56.3					
Lauryl alcohol 7 EO			16.2	8.1	16.2	16.2	16.2
DMDM Hydantoin	0.5	0.5	0.5	0.5	0.5	0.5	0.5
Deionized water	38.7	24.2	64.3	72.3	72.3	64.3	64.3
Total active matter of surfactant (%)	14.6	14.6	14.6	7.3	14.6	14.6	14.6
Ratio EGDS/surfactant (%)	1.30	1.30	1.30	2.60	0.75	1.30	1.30

In order to evaluate the chemical content of the final water solution, the final suspension was filtered and the mother liquors were dried. The dry residue did not contain EGDS and the amount corresponded to the weight quantity of active matter of surfactants introduced in the batch.

Each run was performed in duplicate in order to assess the process reproducibility. The concentrates were systematically analysed in terms of crystal shape, size distribution measurement and optical aspect of formulations.

2.3. Pearlescence measurement

For pearlescence evaluations, an Aello 1200™ probe was used. Based on the dynamic extinction measurement technique [15], the signal fluctuation was evaluated and allowed to assess the pearlescent aspect. Two standard samples were selected. A pearlescence of 5 was assigned to the most reflecting sample corresponding to a mica dispersion (Timiron Starluster MP-115™ from Merck) known as very pearlescent. A pearlescence of 0 was assigned to the less reflecting dispersion corresponding to a suspension of EGDS crystallized in the absence of surfactant (see Section 3).

The formulation quality was also judged on a simple visual test. The marking of samples from 1 to 5 allowed a relative rank between samples, with 1 corresponding to worst and 5 corresponding to best. The parameter noted by visual rank was correlated to the percentage of reflected light measured by the Aello™ probe (see Fig. 1).

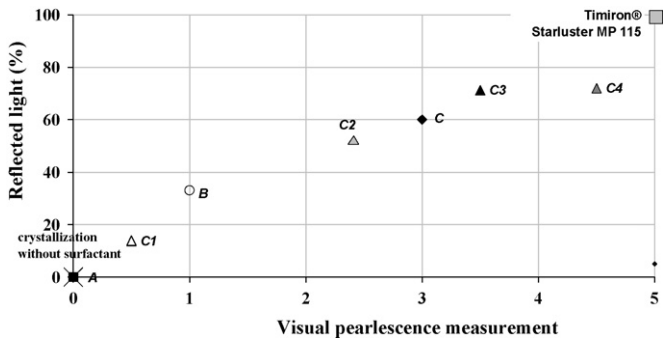

Fig. 1. Pearlescence measurement using the Aello™ probe and a visual ranking.

2.4. Physicochemical controls of the concentrates

2.4.1. Particle size measurement

Particles size distributions were realized using a COULTER LS230™ which offers a special device (Polarization Intensity Differential Scattering PIDS) for the measurement of submicronic particles. Each sample was diluted to 5% in distilled water and then was injected into the measuring cell in optimal quantities making it possible to be under the conditions of measurements defined by the manufacturer (optical concentration ranging between 7 and 12%, concentration of the PIDS ranging between 45 and 55%). The selected optical model was based on Mie theory and required the refractive indexes (1.333 for water and 1.456 for the real part and 0.1 for the imaginary part of the sample).

2.4.2. Crystal shape

The crystal shape and the crystal size were characterized by a scanning electronic microscope (SEM) JEOL 6320 F.

3. Results and discussion

EGDS is a lipophilic compound and its crystallization goes through an aqueous dispersion medium at high temperature. Without any surfactant the EGDS-based dispersion was highly unstable and broke down quickly. Under cooling large crystals (several tens of micrometer) quite thick (few microns) presenting rough surface, not well faceted were formed (see Fig. 2). In comparison to a population of micronic particles the total crystal area was two orders of magnitude lower. The direct reflection of light was not intense. In addition the surface aspect and the edges of the particles promoted diffuse reflection of the light in a random way instead of a direct reflection. In any way, the final concentrate presented pearlescence and the visual rank assigned the quotation 0 to this sample (cross symbol in Fig. 1).

With the absence of surfactant during the crystallization in emulsion of EGDS, the emulsion and the suspension were not stable and the crystals do not fulfil the requirements for the obtaining of pearlescence aspect. So the use of surfactants was absolutely necessary.

We investigated firstly the nature of the surfactant on the crystallization process. We studied different types of surfactant

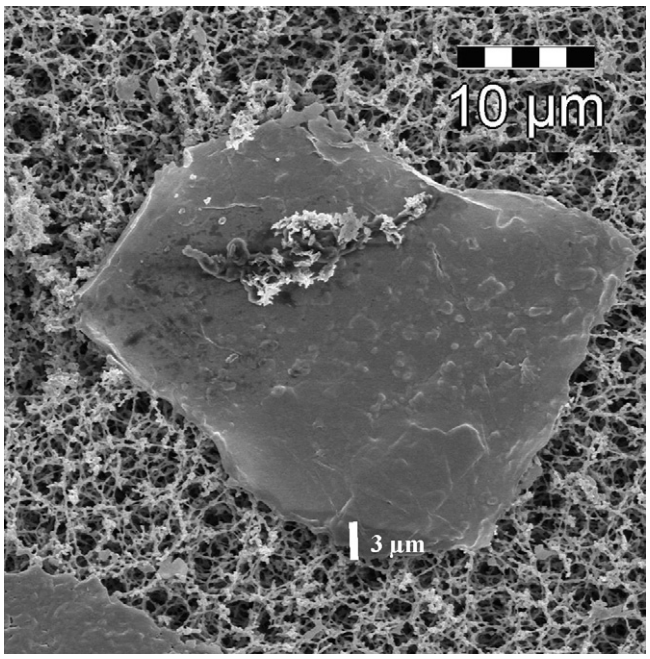

Fig. 2. Crystallization trial without surfactant: final crystals.

some of them being highly hydrophilic (cocamidopropylbetaine and sodium trideceth (3) sulfate) while another one being well-balanced and more amphiphilic (Lauryl alcohol (7 EO)) (HLB 12.4). The main differences between these three surfactants were their hydrophilic character and their capacity to emulsify high percentages of lipophilic phase. These surfactants belong to various chemical classes of emulsifiers (anionic, amphoteric and non-ionic) which are commonly used in cleansing products.

3.1. Location of the crystallization in the emulsion

The EGDS crystallization under cooling of the non-ionic based emulsion (formulation C) was first investigated. The emulsion is generated in the stirred vessel at 75 °C. A small part (10 ml) of this hot emulsion was sampled and poured into a cell thermostated by Peltier effect and placed under a microscope equipped with a video-camera. The cooling profile was then applied until 25 °C. The chemical composition of the liquid phases and the temperature profile are the same between the experiments performed in the Peltier cell and in the agitated reactor. The difference between these two experimental devices come from the agitation: it is a quiescent medium in the thermostated cell, a stirred medium in the reactor. This design allowed to see directly in the formulation the behaviour of the crystallization medium and the different crystallization steps, such as nucleation and crystal growth in quiescent medium. Between 75 and 63 °C, we observed an emulsion where the droplets coalesced (see Fig. 3a). When an emulsion sample was withdrawn from the reactor and cooled below 60 °C a first crystal nucleation in the volume of the droplet appeared. The first crystals grew with a dendritic shape which was already the consequence of a high supersaturation of the medium (see Fig. 3b and c). Few minutes later, during the cooling at lower supersaturation level, a second nucleation arose with crystals exhibiting a faceted habit (see Fig. 3d). Then crystals continue to grow inside the droplets (see Fig. 3e). This second population of particles appeared to be larger than the previous one. The particles obtained with the two devices present the same platelet shape. One could suppose that the mechanisms occurring in each experimental device are similar.

3.2. Amphoteric surfactant: formulation A

Betaines are primary surfactant for shampoos shower gel, liquid soaps and other cleansing products. They offer the advantage of producing particularly fine, stable foam, even in hard water. They are generally used in combination with anionic surfactants because a synergetic effect between them is often observed on the foam quality. The emulsion obtained using Mirataine BET C30 (formulation A) was not stable. Spherical crystals or agglomerates (up to 100 µm) were observed (Fig. 4a) and the width of the crystal size distribution was large (see Fig. 4b). This solid features led to a bad optical aspect which did not confer any pearlescence to the final preparation. The ranking was equal to 0 for this blend (see black square symbol in Fig. 1). Two hypotheses could be made to explain the bad crystal quality. Firstly, cocamidopropylbetaine was poorly efficient to ensure a stable emulsion before cooling and consequently EGDS crystals were very polydisperse in size and not faceted in shape. The large droplet distribution in the emulsion at high temperature led to a large crystal size distribution. Secondly, cocamidopropylbetaine was mainly solubilized in the external aqueous phase and it could be easily hypothesized that during the crystallization process, the surfactant was not in close contact with EGDS oil phase and did not allow directing particles shape (no template effect). Katsugari et al. [7] observed the same phenomenon with a sucrose oleate which had no interaction with *n*-hexadecane phase during crystallization in emulsion and therefore did neither accelerate nucleation nor inhibited crystal growth both in the bulk and in the emulsion system.

3.3. Anionic surfactant: formulation B

As already mentioned with the previous formulation, the anionic surfactant mainly located in the external phase had no impact on the crystals shape. Small spherical agglomerates of crystals (one or two tens of microns) with many submicronic particles were observed (see Fig. 5a and b). Moreover, these crystals exhibited rough surface. The final product presented a low level of pearlescence but looked very matte and opaque. This spherical shape did not transmit light but promoted diffuse reflection and partly absorbed incident light. The particles surface roughness increased phenomenon of diffuse scattering of the incident light and consequently the pearlescence effect was poor. The particle size was small and provided a high covering effect. In summary, the spherical shape associated with the surface roughness and the small size of the particles was responsible for the opacity of the sample. This can be compared to the opaque effect produced by submicronic particles of titanium dioxide.

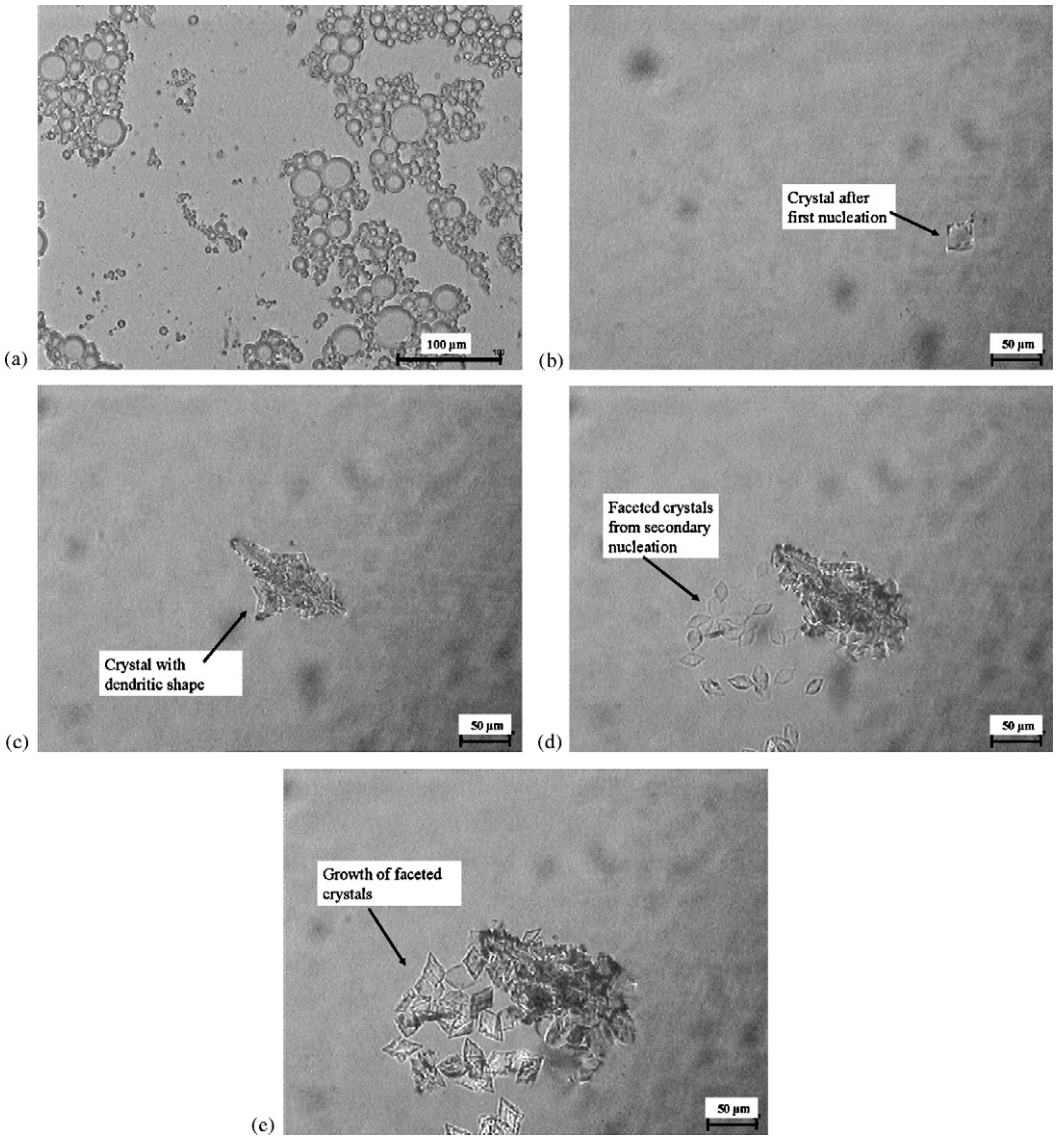

Fig. 3. In situ video monitoring of the start of crystallization of EGDS inside the emulsion: (a) emulsion, (b) first nucleation, (c) dendritic crystals, (d) second nucleation and (e) faceted crystals growing.

3.4. Non-ionic surfactant: formulation C

Non-ionic surfactants are widely used to formulate emulsions. The non-ionic surfactant used in this study led to stable emulsions. EGDS crystals were composed of both thin individual platelets (platelet width, submicronic to micronic size; thickness less than 1 μm) and sand rose agglomerates (global size centred around 10 μm) (see Fig. 6a and b). The rosette form of crystal growth contained thin platelets all growing at different angles: the irregular surfaces and edges could scatter light. Only

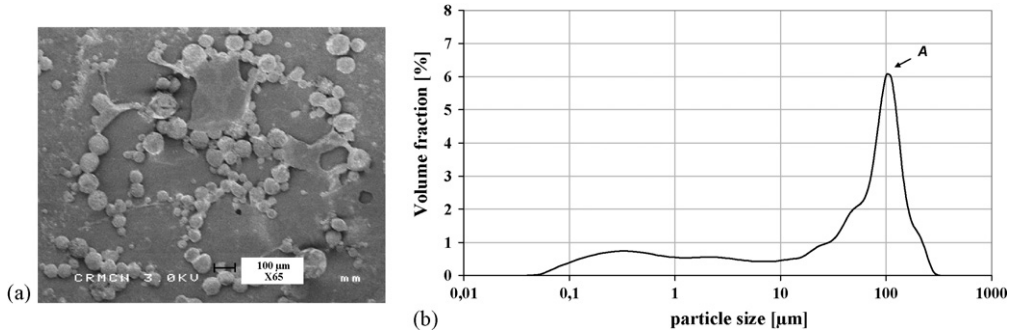

Fig. 4. Formulation A. (a) SEM observation; (b) particles size distribution.

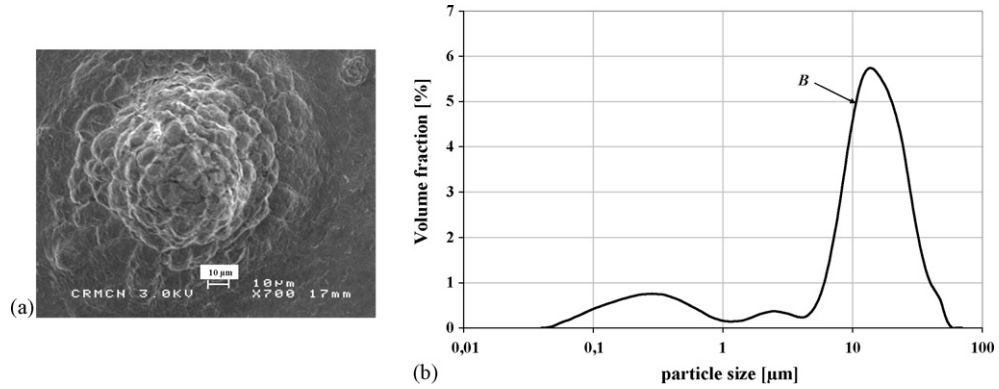

Fig. 5. Formulation B. (a) SEM observation; (b) particles size distribution.

a portion of the incident light was directly reflected. The residual might be transmitted through the platelet to the next layer where it was again reflected. This shape conferred a pearlescence effect to the concentrate. Nevertheless due to the fact that the particles are not perfectly aligned, an important portion of the reflection of the light is lost. This concentrate presented a moderate pearlescence aspect (rank = 3 in Fig. 1). The relationship between particles shapes and optical aspect is yet confirmed.

The experiments carried out under the microscope with this formulation C (see Section 3.1) put the evidence that the crystallization takes place in the oil phase droplet, and not in the bulk aqueous phase. With these experiments, we could not know if the crystallization occured at the interface or in the core of the droplets. However, with the formulation C the oil–water interface was presumed to be covered by the surfactant. This surfactant was hydrophilic (HLB value = 12.4). It was scarcely solubilized in the oil phase and it was mainly adsorbed at the interface and present in the aqueous bulk phase as micelles. As this surfactant acted on the particles shape, the lipophilic tails were presumed to interact with EGDS during the development of the crystal favouring a platelet like habit. Some authors [7–9,13] demonstrated the existence of a template effect. This effect affects mainly the nucleation rate. In this study, it was the relative growth rates of the crystal faces which are modified, since the particle shape is altered. From these observations, it was not possible to evaluate if the mechanism of interaction between the surfactant and the EGDS is the same that the one already described in the literature.

3.5. Quantitative impact of the surfactant

As the choice of surfactant seemed to be a key parameter to obtain the desired particles shape, the parameter, such as the minimal percentage of surfactant necessary for obtaining a pearlescent concentrate was investigated.

Experiments were carried out at constant EGDS percentage (19%) but with different total active matter of surfactants (14.6% for C and 7.3% for C1). The mastery of the platelet shape was almost lost for C1. In Fig. 7a, spherical dense agglomerates of platelets were observed. The shape was close to the formulation B. Due to the decrease of the amount of surfactant relatively to the EGDS content, the interaction between the surfactant and the EGDS was supposed to be lowered, leading to the loss of the platelet shape. Consequently, this cold pearl presented a poor pearlescent effect (rank = 1 in Fig. 1). Lee and Shantz [12] who worked on the monitoring of the shape and size of structured zeolite crystallized in microemulsion systems showed that the surfactant adsorption was essential for aggregate formation at the crystals surface. Surfactant–silicate interactions were suggested to be responsible for the coalescence of the primary particles into aggregate. This effect was dependent on the number of ethoxylated groups present in the surfactant. They had also put in evidence that the decrease of the surfactant content led to rougher surfaces, meaning that the surfactant played a role in controlling surface smoothness without elucidating a possible mechanism of understanding.

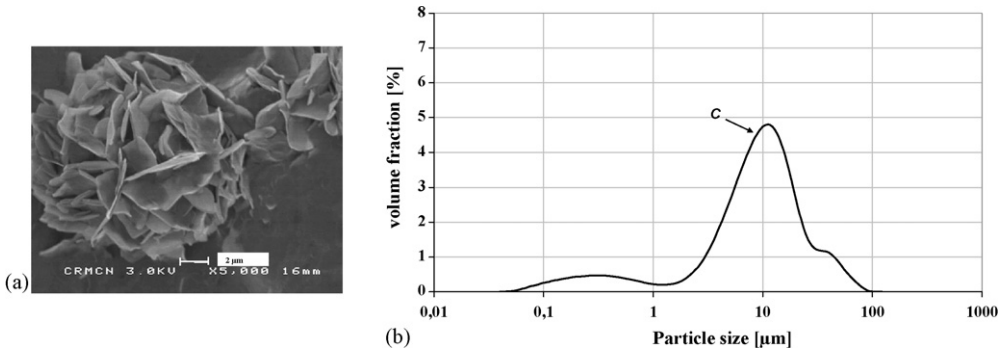

Fig. 6. Formulation C. (a) SEM observation; (b) particles size distribution.

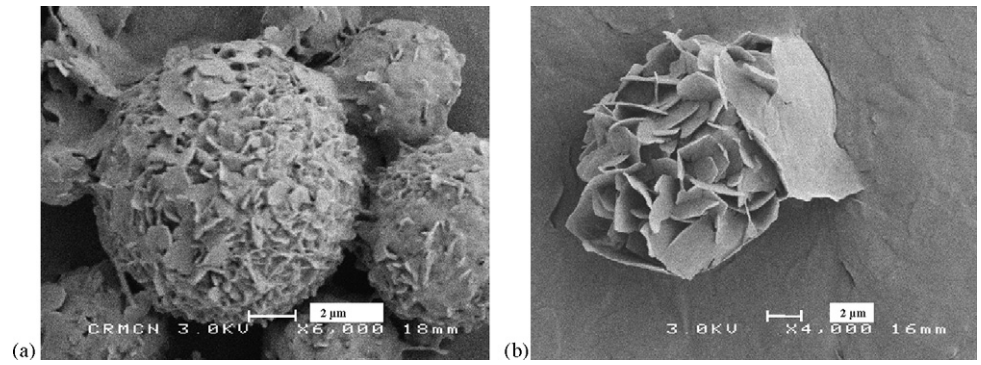

Fig. 7. Influence of surfactant amount. (a) Sample C1 (19% EGDS, 7% surfactant); (b) sample C2 (11%EGDS, 15% surfactant).

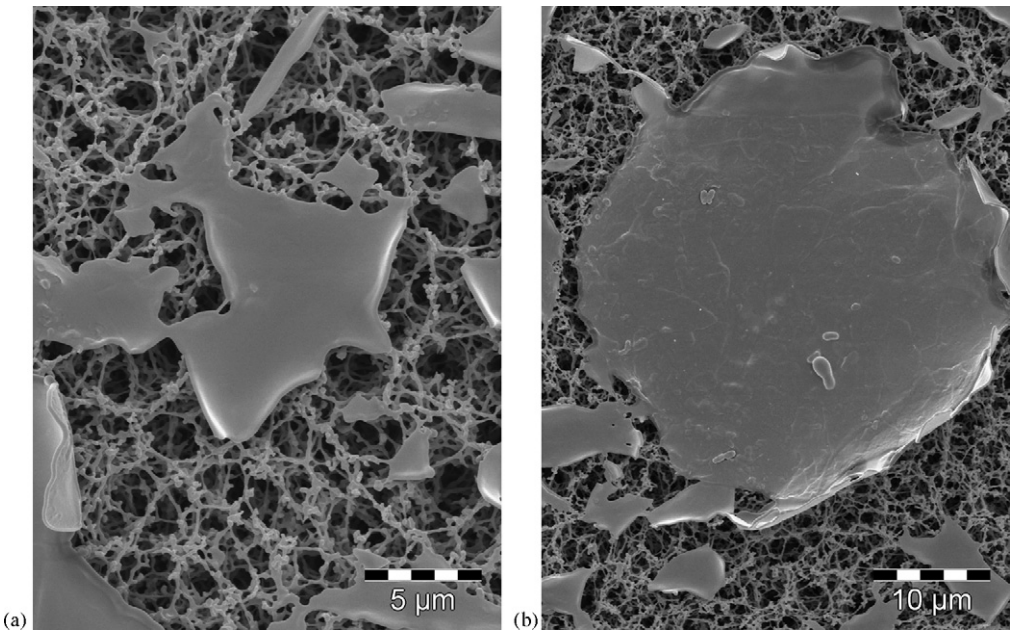

Fig. 8. Influence of EGMS/EGDS ratio. (a) Sample C3 (EGDS/EGMS: 95/5); (b) sample C4 (EGDS/EGMS: 99/1).

3.6. Quantitative impact of the final concentration of solid

The assessment of the influence of the final concentration of solid was performed through the comparison of the formulations C and C2, containing, respectively, 19 and 11% of solid content. The total active matter of surfactant was kept constant. Consequently, the ratio of EGDS/surfactant was decreased to 0.75. Agglomerated platelet crystals were obtained (see Fig. 7b). A slight decrease of the pearlescence from 3.0 to 2.5 was noticed. Despite a significant decrease of solid content, this experiment demonstrated that the one of the major parameters allowing directing the crystals shape and the aggregation of the particles and consequently the pearlescence quality of the cold pearl was the amount of surfactant relatively to the EGDS content.

3.7. Characteristics of the pearlescent agent

From literature review [2], the chemical quality of EGDS (through mono- and distearate ratio) could also affect pearlescence. Experimentally, three commercial qualities of EGDS were tested through the formulations C, C3 and C4 (see Table 1). In all cases, the crystals exhibited thin platelets with smooth surface (see Fig. 8). The particles were less aggregated than those obtained with a raw material having a higher amount of monostearate. The pearlescence increased significantly with the distearate proportion as illustrated in Fig. 1. For the same amount of EGDS crystallized, we could expect a more important specific surface area of the crystals devoted to direct reflection of the light, leading to a more intense pearlescence effect. These microscopic observations were in accordance with the observations reported by Crombie [2] and Hunting [16].

4. Conclusions and perspectives

In the present work, the investigations on EGDS crystallization understanding showed at first the influence of the batch formulation on the final quality of the product. Only a non-ionic surfactant led to a concentrate presenting a pearlescent effect. The ratio EGDS/surfactant was also a key parameter: a minimal surfactant content relatively to the EGDS introduced was

required to control the particle shape and the level of aggregation. In addition, experimental results showed that pearlescence increased with distearate proportion, certainly due to a larger specific area of the platelet generated.

The location of the surfactant seemed also to be a key parameter. It was supposed that the lipophilic tails of surfactant interact with the particle of EGDS in development, maybe through the modification of the growth rates of different crystal faces, like a tailor made additive [17]. From these observations, it was not possible to evaluate precisely the nature of the interaction between the surfactant and the EGDS growing crystals. The nature of this interaction remains in question and will be investigated in the next future.

Moreover, relationships between the crystal features of EGDS formulations and pearlescence quality of the final cold pearl blend have been confirmed. The pearlescence was strongly linked to the shape, the surface aspect, the size distribution of EGDS crystals and their level of aggregation. A platelet shape of several microns of width having a submicronic thickness, combined with a smooth surface allowed a direct reflection of the incident light. This phenomenon increased with the specific area of the particles. That was why an important volume fraction of submicronic and micronic crystals in the population of particles was required. At least, when the platelets were not aligned the pearlescence effect was reduced. This occured when aggregation of platelets became significant.

This work gave new insights on how the EGDS crystallization process could be tuned based on various formulation parameters opening the door to future applications of cold pearls. In the future, it will be possible to choose surfactant in order to guide the particle features and then to tune the desired pearlescent effect.

Acknowledgement

This work has been carried out with the financial support from RHODIA Novecare.

References

[1] G. Pfaff, P. Reynders, Angle-dependent optical effects deriving from submicron structures of films and pigments, Chem. Rev. 99 (1999) 1963–1981.

[2] R.L. Crombie, Cold pearl surfactant-based blends, Int. J. Cosmet. Sci. 19 (1997) 205–214.

[3] M.J.W. Povey, Crystallization of oil in water emulsion, in: N. Garti, K. Sato (Eds.), Crystallization Processes in Fats and Lipids Systems, Marcel Dekker, New York Basel, 2001, pp. 251–288.

[4] J.N. Coupland, Crystallisation in emulsion, Curr. Opin. Colloid Interface Sci. 7 (2002) 445–450.

[5] W. Skoda, M. Van den Tempel, Crystallization of emulsified triclycerides, J. Colloid Sci. 18 (1963) 568–584.

[6] D.J. Mc Clements, S.R. Dungan, J.B. German, C. Simoneau, J.E. Kinsella, Droplet size and emulsifier type affect crystallization and melting of hydrocarbon-in-water emulsions, J. Food Sci. 58 (1993) 1148–1178.

[7] T. Katsugari, N. Kaneko, K. Sato, Effects of addition of hydrophobic sucrose fatty acid oligoesters on crystallization rates of n-hexadecane in oil-in-water emulsions, Colloid Surf. B Biointerfaces 20 (2001) 229–237.

[8] Y. Hamada, I. Kobayashi, M. Nakajima, K. Sato, Optical and interfacial tension study of crystallization of *n*-alkane in oil-in-water emulsion using monodispersed droplets, Cryst. Growth Des. 2 (6) (2002) 579–584.

[9] M. Sakamoto, A. Ohba, J. Kuriyama, K. Maruo, S. Ueno, K. Sato, Influence of fatty acid moiety and esterification of polyglycerol fatty acid esters on the crystallization of palm mid fraction in oil-in-water emulsion, Colloids Surf. B Biointerfaces 37 (2004) 27–33.

[10] D.J. Mc Clements, S.R. Dungan, Effect of colloid interactions on the rate of interdroplet heterogeneous nucleation in oil-in-water emulsions, J. Colloid Interface Sci. 186 (1997) 17–28.

[11] S. Hindle, M.J.W. Povey, K. Smith, Kinetics of crystallization in *n*-hexadecane and cocoa butter oil-in water emulsions accounting for droplet collision-mediated nucleation, J. Colloid Interface Sci. 232 (2000) 370–380.

[12] S. Lee, D.F. Shantz, Zeolite growth of non-ionic microemulsions: synthesis of hierarchically structured zeolite particles, Chem. Mater. 17 (2) (2005) 409–417.

[13] N. Garti, J. Yano, The roles of emulsifiers in fat crystallization, in: N. Garti, K. Sato (Eds.), Crystallization Processes in Fats and Lipids Systems, Marcel Dekker, New York Basel, 2001, pp. 211–250.

[14] P. Chen, J. Niu, S.F. Yoong, Mild Cold Pearlizing Concentrates Patent W0 9713498 (1997).

[15] Wessely B., Altmann J., Ripperger S., Dynamic extinction measurements in presence of particles in sub-micrometer range, Nürnberg, 2001 (reprint Partec 2001).

[16] A.A.L. Hunting, Opacifiers and pearling agents in shampoos, Cosmet. Toiletries 96 (1981) 65–78.

[17] I. Weissbuch, L. Leiserowitz, M. Lahav, Tailor made additives and impurities, in: A. Mersmann (Ed.), Crystallization Technology Handbook, Second ed., Marcel Dekker, 2001 (Chapter 12).

Journal of
Mechanics of
Materials and Structures

THERMOMECHANICAL MODELLING OF FRICTION EFFECTS IN GRANULAR FLOWS USING THE DISCRETE ELEMENT METHOD

Viet Dung Nguyen, Jérôme Fortin, Mohamed Guessasma,
Emmanuel Bellenger and Claudia Cogné

Volume 4, Nº 2 February 2009

mathematical sciences publishers

JOURNAL OF MECHANICS OF MATERIALS AND STRUCTURES
Vol. 4, No. 2, 2009

THERMOMECHANICAL MODELLING OF FRICTION EFFECTS IN GRANULAR FLOWS USING THE DISCRETE ELEMENT METHOD

VIET DUNG NGUYEN, JÉRÔME FORTIN, MOHAMED GUESSASMA,
EMMANUEL BELLENGER AND CLAUDIA COGNÉ

This study deals with the modelling of the thermomechanical phenomena due to friction effects during granular flow. A two-dimensional model using the discrete element method (DEM) and taking into account the contact detection and heat transfers between grains has been developed. Through this study, we have modelled the heat transfer by conductance and the energy dissipation by friction into a granular medium. This modelling enables better understanding of the phenomena at the contact point between grains as well as the energy dissipation by friction of a great number of grains in motion. The validity of the proposed model has been studied by considering some numerical simulations in quasistatic and dynamic regimes.

1. Introduction

The published literature analysis has shown the importance of thermal energy in granular media for industrial processes in applications as diversified as powder metallurgy, chemical reactors (catalysts beds), food technology [Laguerre et al. 2006], thermal insulation [Melka and Bézian 1997], or even simply storing particles in a silo after drying [Ketterhagen et al. 2007]. Only few studies are interested in the understanding of heat transfers resulting from thermomechanical effects. However, these complex phenomena with multiphysical characteristics are an essential stake in the world of industry and transports. For instance, strong frictions (braking, jamming) are responsible for half of ignitions of explosive atmospheres, and are also a dreadful cause of fires in vehicles and accidents. One of the difficulties lies in predicting the friction forces and the temperatures in the friction zone based on the intrinsic properties of bodies in contact.

From a thermal energy point of view, sliding contact is the source of a heat generation by friction, whose distribution between the different bodies is difficult to estimate. Besides, the determination of the contact area, which plays an important role in the value of the transferred heat flow, is also difficult to estimate and depends on various parameters like porosity, rugosity, the distribution of contact forces, and the structure of the media. Mechanical engineers are at the origin of the greatest number of works [Slavin et al. 2002; Vargas-Escobar and McCarthy 2002a; Bahrami et al. 2006]. Slavin et al. [2002] and Bahrami et al. [2006] have developed models to estimate the effective thermal conductivity of a particle packing from the intrinsic properties of solids and fluids. These models enable us to determine the apparent thermal conductivity evolution of a granular medium according to the mechanical loading applied to the particle bed. Vargas-Escobar and McCarthy [2002a] have studied more particularly the influence of contact forces on the apparent conductivity of a bed with a small, but finite, area of contact.

Keywords: heat transfer, contact, conductance, friction, DEM.

The first part of this work consists of using the discrete element method (DEM) for contact detection, determination of contact forces, and kinematic parameters. A computational program, MULTICOR, that can treat an important number of particles (10^6), has been developed to solve the mechanical equations. In the second part, heat transfers by contact as well as energy generation by friction have been studied and implemented in MULTICOR. Finally, through some examples, we underscore the phenomena of thermomechanical interaction.

2. Mechanical resolution by DEM

The conventional DEM allows us to model really deformable particles as well as complex shapes, from the ellipsoid to the polygon. Here, we have studied the simple case of nondeformable and nonpenetrable particles in two dimensions with the computational programme MULTICOR [Fortin et al. 2005]. The coordinates and the Euler rotation angles are the configuration parameters q. The gyroscopic forces are three-dimensional but the centrifugal forces exist even in two-dimensional problems (see Figure 1). The matrix of generalized mass M of the system doesn't depend on q, and hence is a diagonal block. The mechanical equation can be written in the form

$$M\ddot{q} = F_{\text{ext}}(q, \dot{q}, t) + R^{\alpha},$$

where F_{ext} represents the known external forces and R^{α} the unknown interior forces related to contact reactions, with α being the contact number.

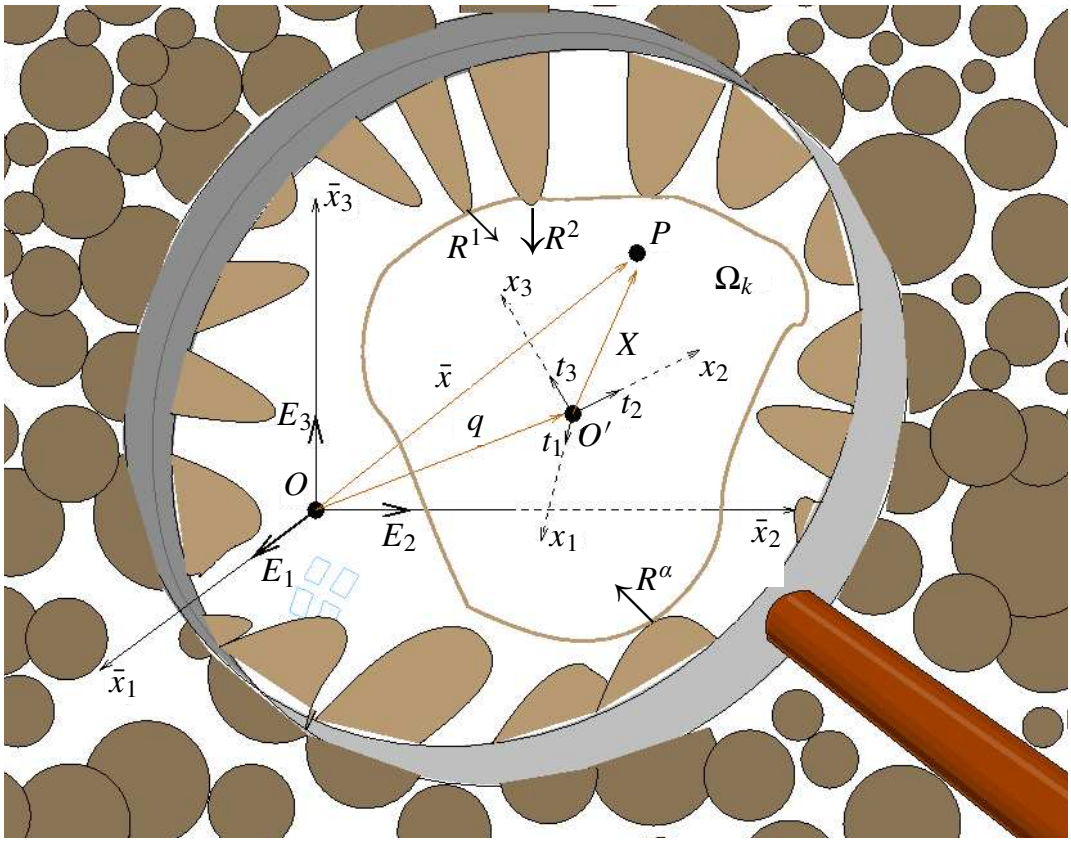

Figure 1. Granular media and its kinematic parameters.

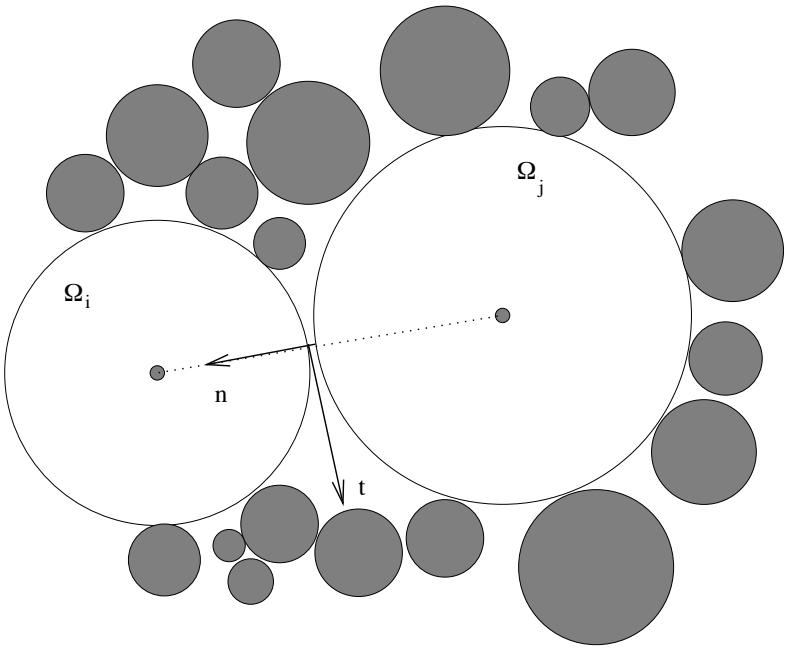

Figure 2. Detection of contact.

In a system composed of p heterogeneous particles (see Figure 1), the critical parameter for the modelling time is the maximum number of interactions between particles. The more the interaction range is important the more we have to test the possible interactions between particles. MULTICOR uses the partitioning method coupled to a connectivity table [Fortin and Coorevits 2004]. This technique allows us to reduce the computational time considerably. In this case, the computational time no longer increases as $O(p^2)$ but only as $O(p)$, which is almost optimal. To each pair of particles Ω_i and Ω_j which may enter in contact, we associated a local reference whose axes are oriented according to the two unit vectors n and t, respectively the normal and tangential vectors in the contact plan (see Figure 2). The normal n is directed from Ω_j to Ω_i. The variables put in duality are $\dot{u}^{ij}$, the relative local velocity of Ω_i with respect to Ω_j, and the contact reaction r^{ij} of Ω_j on Ω_i. In the local base, they are written as

$$\dot{u}^{ij} = \dot{u}_t^{ij}.t + \dot{u}_n^{ij}.n, \qquad r^{ij} = r_t^{ij}.t + r_n^{ij}.n,$$

where $\dot{u}_n^{ij}$ is the normal separation velocity, $\dot{u}_t^{ij}$ the sliding velocity, r_n^{ij} the contact pressure, and r_t^{ij} the friction force.

The introduction of Coulomb's friction μ leads to a nonlinear problem which cannot be solved by a linear programming method. Unlike the usual approach, the bipotential method leads to a single variational principle and an inequality [Fortin and de Saxcé 1999]. Using Usawa's algorithm, we obtain a resolution algorithm of the constitutive law based on the predictive-corrective scheme expressed by

$$\text{predictor}: \tau^{ij} = r^{ij} - \gamma\,[\dot{u}_t^{ij} + (\dot{u}_n^{ij} + \mu||-\dot{u}_t^{ij}||).n], \qquad \text{corrector}: r^{ij} = \text{proj}(\tau^{ij}, K_\mu),$$

where γ is a numerical parameter, and τ^{ij} the projection of Coulomb's cone K_μ leads, according to the value of τ^{ij}, to one of the following states: noncontact, contact with friction, or sliding contact. Conventionally, at each time step, the contact forces in the system are determined repeatedly by the method of successive balances based on a Gauss–Seidel algorithm for the two-dimensional version. Each

contact force is calculated by adopting temporary values over the other contacts. The convergence is obtained when the force satisfies the unilateral contact law with dry friction.

The calculation cycle is a time-stepped algorithm which requires the repetition of the following resolution scheme.

$t = t + \triangle t$
Evaluation of the particle positions q_n
Detection of the contact number α in the system
Evaluation of the particle velocity (without contact)
  $i = i + 1$ (iteration of solver bipotential)
    $\alpha = \alpha + 1$ (contact loop : α is the current index of contact)
      Evaluation of the contact reactions $r^{\alpha,i+1}$
  Indicator of error
Evaluation of the velocity

3. Heat transfer in granular media and thermomechanical formulation

In general, heat transfer in granular media with a stagnant interstitial fluid is assumed to occur by the following physical phenomena:

- Heat conduction through the particles and heat conduction through the fluid between the neighboring particles. Furthermore, in a multicontact system, as considered in this work, we must consider heat conduction through the contact area between two particles Ω_i and Ω_j. Contact conductance refers to the ability to transmit heat across their mutual interface.
- Radiant heat transfer between the fluid within neighboring voids and radiant heat transfer between the surfaces of neighboring particles. For heat transfer by radiation, contact between surfaces is not required. Radiation is linked to the production of electromagnetic waves by a heat surface.
- For fluids, flow heat transfer by interparticle convection can be considered if there is a difference of temperature between the particles and the fluid.

In frictional granular flow regimes, heat transfer occurs from the phenomena presented above. In addition, it is necessary to consider the heat generated by friction between two particles Ω_i and Ω_j. Indeed, sliding contact is an important source of heat generation for the dynamic granular problems considered in this work (see Figure 3, left).

In this paper, we assume that conduction through the solid phase dominates the heat conduction. This assumption is verified when

$$\frac{\lambda_s s}{\lambda_f a} \gg 1,$$

where λ_s and λ_f are respectively the conductivities of the particles and the fluid, a and s are the radius of the particle and the contact area, respectively.

This expression is satisfied for high thermal conductivity solid materials or for solid particles in a vacuum ($\lambda_f \to 0$) [Vargas-Escobar and McCarthy 2002b]. Also, under these conditions, the heat transfer between two adjacent particles Ω_i and Ω_j is only controlled by the contact conductance. In this work, radiant and convective heat transfers are neglected. Therefore, we only consider heat transfer in granular flow by contact conductance and frictional effects (see Figure 3, right).

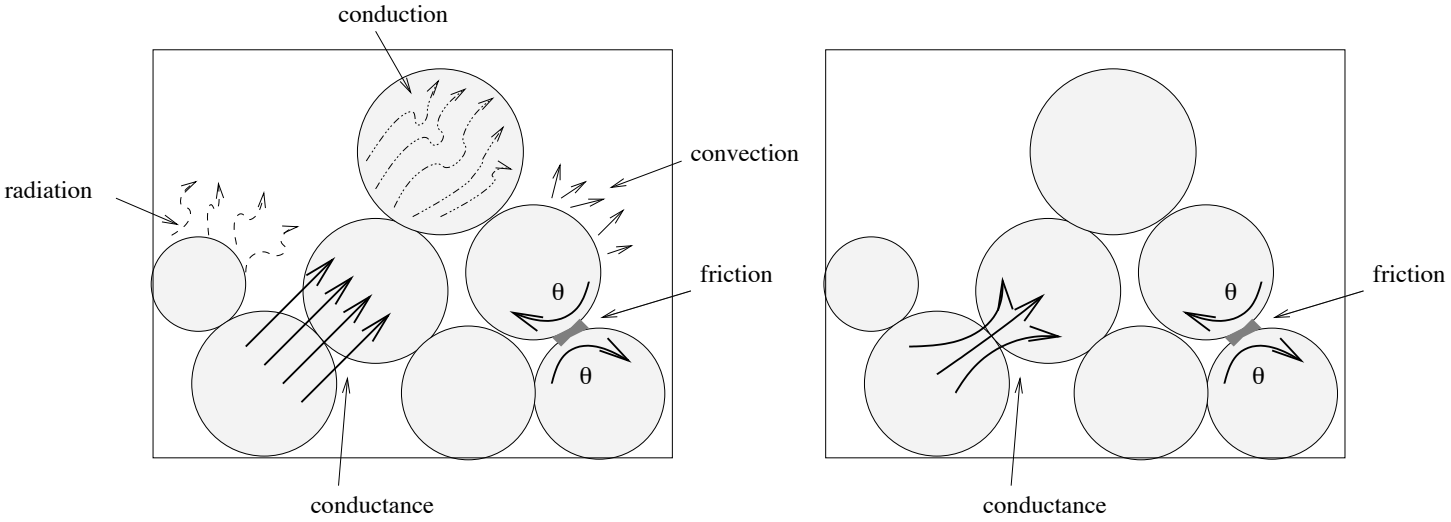

Figure 3. Left: heat transfer mechanisms in granular media. Right: heat transfer in MULTICOR.

3.1. ***Heat transfer by conductance.*** Contact conductance is directly linked to the constriction of the heat flow lines in the contact point [Laguerre et al. 2006]. The thermal contact conductance is defined by the ratio of the heat flow across a contact interface and the magnitude of the temperature discontinuity at the interface,

$$\varphi_{ij} = H_c^{ij}(T_j - T_i),$$

where φ_{ij} is the heat flow transfered between the particles Ω_i and Ω_j, $T_j - T_i$ the temperature difference between the mid-planes of the spheres and H_c^{ij} the contact conductance between the particles Ω_i and Ω_j, with j varying from 1 to the contact number α.

The coefficient H_c^{ij}, which is a function of the compression force, refers to the ability of two materials in contact to transfer heat across their mutual interface (see Figure 4). In our work, contact conductance between particles Ω_i and Ω_j is modeled using Hertz theory as

$$H_c^{ij} = 2\lambda_s \left(\frac{3 r_n^{ij} a^*}{4E^*} \right)^{1/3},$$

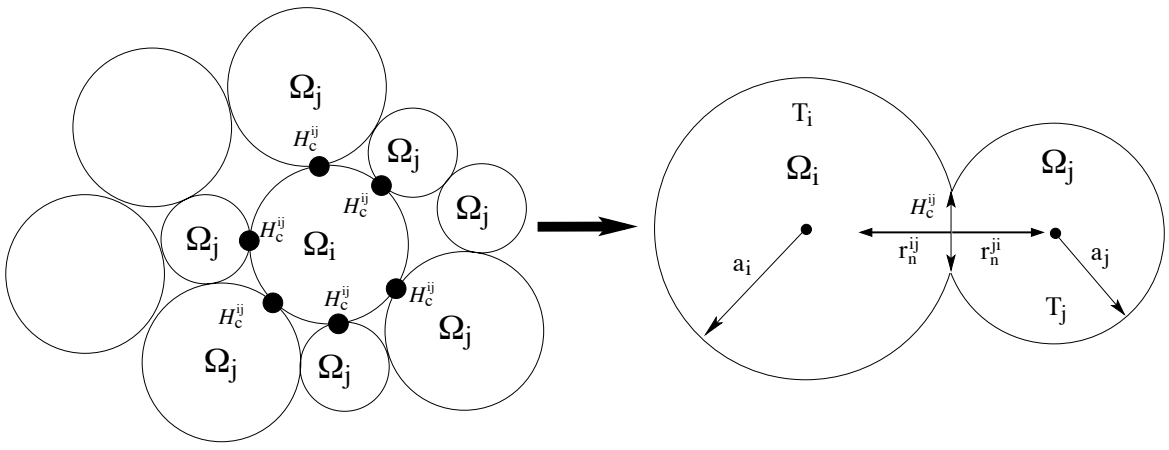

Figure 4. Schematic representation of heat transfer by conductance.

where r_n^{ij} is the normal force, a^* is the equivalent radius, given by $\frac{1}{a^*} = \frac{1}{a_i} + \frac{1}{a_j}$, and E^* is the effective Young's modulus, so that

$$\frac{1}{E^*} = \frac{1-\nu_i^2}{E_i} + \frac{1-\nu_j^2}{E_j},$$

ν being Poisson's ratio.

The contact between two adjacent particles is assumed to be smooth and sliding. The contact conductance is calculated dynamically at each time step and for all contacts of a particle Ω_i.

We recall that the considered particles are nondeformable and nonpenetrable. The use of Hertz's theory only enables us to compute the contact conductance coefficient H_c^{ij}. We assume that the particles remain rigid all the time.

3.2. ***Heat generated by friction.*** In this case, heat flow is generated by dissipation of energy during friction between particles. The deformation is neglected because the particles are assumed rigid. Friction is understood as a continuous mechanical solicitation between two bodies. The heat energy generated by friction, E_{fij}, at the frictional interface during a time step $\triangle t$ is

$$E_{fij} = \mu \dot{u}_t^{ij} r_n^{ij} \triangle t,$$

where μ is the friction coefficient, $\dot{u}_t^{ij}$ the sliding velocity, and r_n^{ij} the normal force.

The modelling of the heat generated by friction requires us to share it between particles in sliding contact. Therefore, we define the partition coefficient of generated heat flow β_{ij}. This coefficient depends on different microscopic parameters like the thermal properties, the sliding velocity, heat generation parameters, and the surface roughness if the contact is not perfect [Linck et al. 2006]. Research in this area has proposed different equations to estimate this coefficient. In our study, this coefficient is obtained from the analytical solution of Mokrani and Bourouga [2005],

$$\beta_{ij} = \frac{1}{2}\left(\frac{\rho_i}{\rho_i + \rho_j} + \frac{\lambda_s^i}{\lambda_s^i + \lambda_s^j}\right),$$

where ρ is the electric resistivity (Ω m).

We assume that the packed bed is made of only one material. The partition coefficient of generated heat flow β_{ij} is then equal to $\frac{1}{2}$.

3.3. ***Thermomechanical resolution.*** Taking into account the various phenomena of heat generation mentioned above, the energy balance and the variation of temperature for a particle during a small time step $\triangle t$ can be written as

$$m_i C_{Pi} \frac{\triangle T_i}{\triangle t} = \sum_{j=1}^{\alpha}\left(H_c^{ij}(T_j - T_i) + \frac{1}{2}\frac{E_{fij}}{\triangle t}\right), \tag{1}$$

where m_i and C_{Pi} are the mass and the heat capacity for Ω_i respectively, and α the contact number.

The temperature evolution between two bodies in contact is governed by Equation (1), representing the balance of the heat energy. For static problems this equation is solved with a time step $\triangle t = 10^{-3}$ s. For dynamical problems (1) is solved with a time step $\triangle t = 10^{-6}$ s, to assume that the temperature of each particle changes slowly so that thermal perturbations do not propagate further than its immediate

neighbors during one time step. The second requirement is that the heat transfer resistance Ω_i (conduction) through a particle is significantly lower than the contact resistance between two particles, Ω_i and Ω_j, provided that

$$Bi = \frac{H_c^{ij}}{\lambda_s a} \ll 1,$$

where Bi is the Biot number.

Equation (1) is discretized in order to compute the temperature T_i at the time step $t + \triangle t$ as

$$T_i^{t+\triangle t} = T_i^t + \frac{\triangle t}{m_i C_{Pi}} \sum_{j=1}^{\alpha} \left(H_c^{ij} (T_j^t - T_i^t) + \frac{1}{2} \frac{E_{fij}}{\triangle t} \right).$$

The general algorithm implemented in MULTICOR is the following:

$t = t + \triangle t$
Evaluation of the particle positions q_n
Detection of the contact number α in the system
Evaluation of the particle velocity (without contact)
  $i = i + 1$ (iterations of solver bipotential)
    $\alpha = \alpha + 1$ (contact loop)
      Evaluation the contact reaction $r^{\alpha,i+1}$
  Indicator of error
Evaluation of T_i^t, H_c^{ij}, E_{fij}
Evaluation of the temperature $T_i^{t+\triangle t}$
Evaluation of the velocity

The resolution of the heat problem requires us to compute at each time step the contact detection, the determination of forces, and the velocities of particles.

4. Numerical simulations

4.1. ***Comparison between DEM and FEM.*** The first application was carried out on a particulate system obtained by a triangular arrangement of 14 particles, with an identical size and a circular shape (1 mm radius). We initially suppose that particle 1 is heated at 100° C and the remaining particles are at a temperature of 20° C (see Figure 5).

From the thermal point of view, this simple modelling allows us to study the diffusion of the heat flow by conductance in granular media. In order to check that this assumption is not too restrictive, we compared MULTICOR's prediction with the results obtained by CAST3M software based on the finite element method (FEM) (see Figure 5). Through this comparison, we could check that the thermal resistance within particles was negligible compared to the thermal contact resistance between particles. This hypothesis could be checked by studying the temperature evolution in particles 1, 5 and 14. The good agreement between MULTICOR and CAST3M seems to validate the assumption about the heat transfer occurring only by conductance.

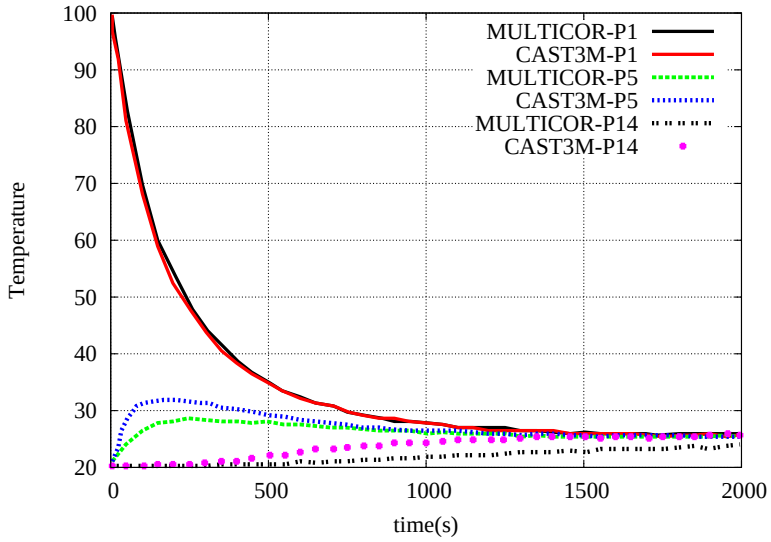

Figure 5. Temperature evolution in particles 1, 5, and 14 obtained by MULTICOR and CAST3M.

4.2. ***Comparison between experiment and MULTICOR prediction.*** In order to validate our thermomechanical model implemented in MULTICOR, we have compared the results with experimental data from [Vargas-Escobar and McCarthy 2002b]. In this study, the authors developed an experimental setup to investigate the heat transfer in a quasistatic configuration. The system is composed of dispersed stainless steel spheres forming a two-dimensional packed bed ($30.4\times\ 45.7\,\mathrm{cm}^2$). The bottom wall is kept at $T_{\mathrm{wall}} = 50°$ C. The top, left, and right walls are insulated (see Figure 6, left). The initial temperature is $T_0 = 25°$ C.

The DEM model shown in the figure was computed by using the thermomechanical properties of stainless steel based on experiments (see Table 1).

In Figure 6, right, we present a part of thermal map after 30 minutes heating. The temperature in the heated granular bed does not propagate uniformly. The front oscillates as force chains appear and disappear along the bed's height.

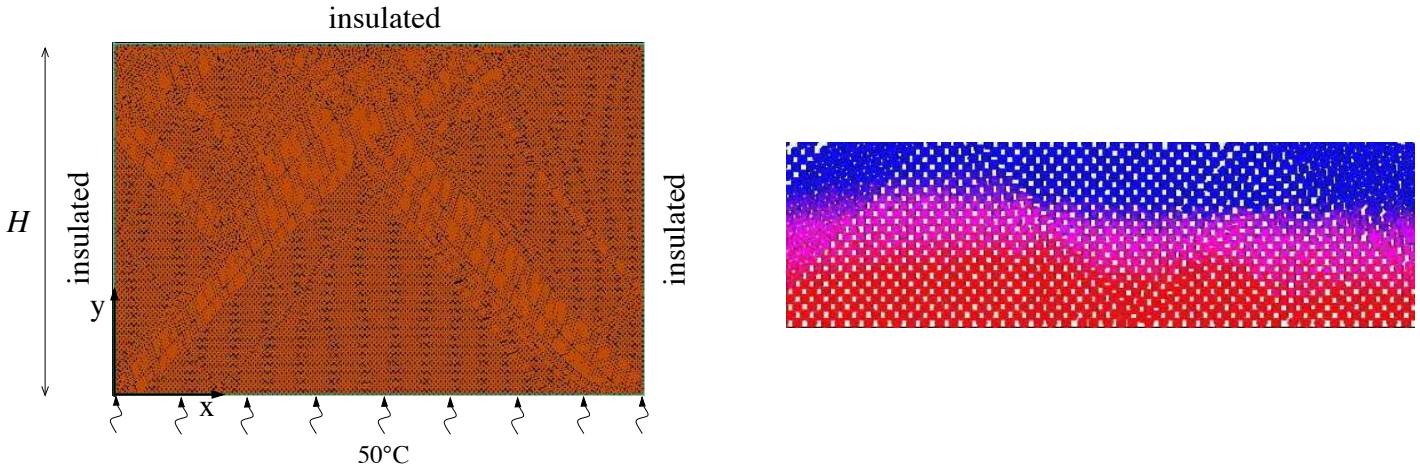

Figure 6. Left: the MULTICOR model. Right: part of the thermal map after 30 minutes heating.

Density	Poisson's ratio	Young's modulus	Particle radius	λ_s
7,500 kg/m^3	0.29	193 GPa	0.003 m	15 W/mK
Number of particles	Length	Height	Friction coefficient	
15,548	0.45 m	0.31 m	0.29	

Table 1. Parameters used in the simulation.

Figure 7 presents a comparison of the temperature as a function of bed's height given by our predictions and the experimental results obtained by Vargas et al. [2002b] after 30 minutes heating. In this figure, θ represents the dimensionless temperature and η the dimensionless height, given by the equations

$$\theta = \frac{T - T_0}{T_{\text{wall}} - T_0}, \qquad \eta = \frac{y}{H}.$$

As shown in Figure 7, the predicted temperature is less accurate for the particles at the bottom of the bed. However, it can be seen that the simulation results matches the experimental curves for dimensionless heights higher than 0.03, which allows us to validate the model prediction in the quasistatic case.

4.3. ***Simulation of heat generation by friction in granular media.*** In this part, we begin to investigate the problem of heat generation in the granular material subjected to shearing solicitation at an imposed velocity. Two cases of shearing will be studied: the quasistatic and dynamic regimes.

The granular material consists of p particles having diameters d (1, 2, and 3 mm). The intergranular contact is characterized by the friction coefficient $\mu = 0.5$.

In the geometry of the shearing plane (see Figure 8), the material is compacted by gravity between two rough parallel walls at a distance H. The top wall is set in motion with velocity V in the positive x direction, and the system is compressed by imposing a uniaxial load F. Periodic conditions are imposed at the lateral boundaries. This means that a particle leaving through one of the boundaries reenters the

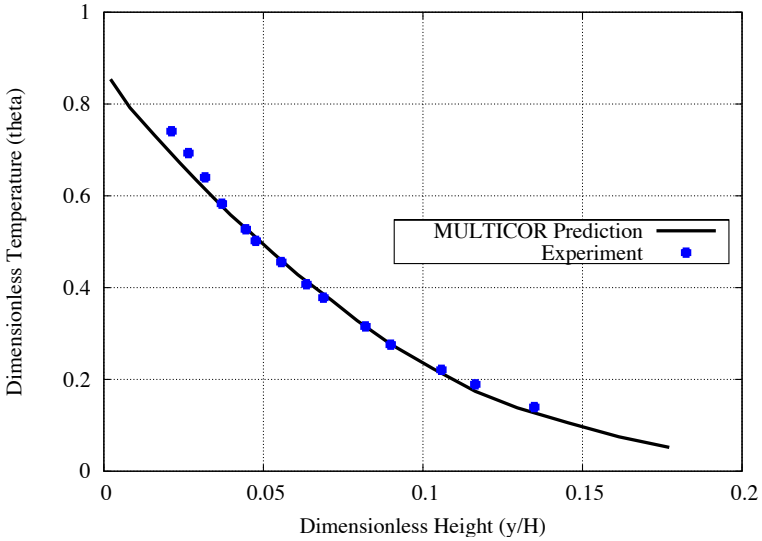

Figure 7. Comparison of experimental data with MULTICOR results after 30 minutes heating.

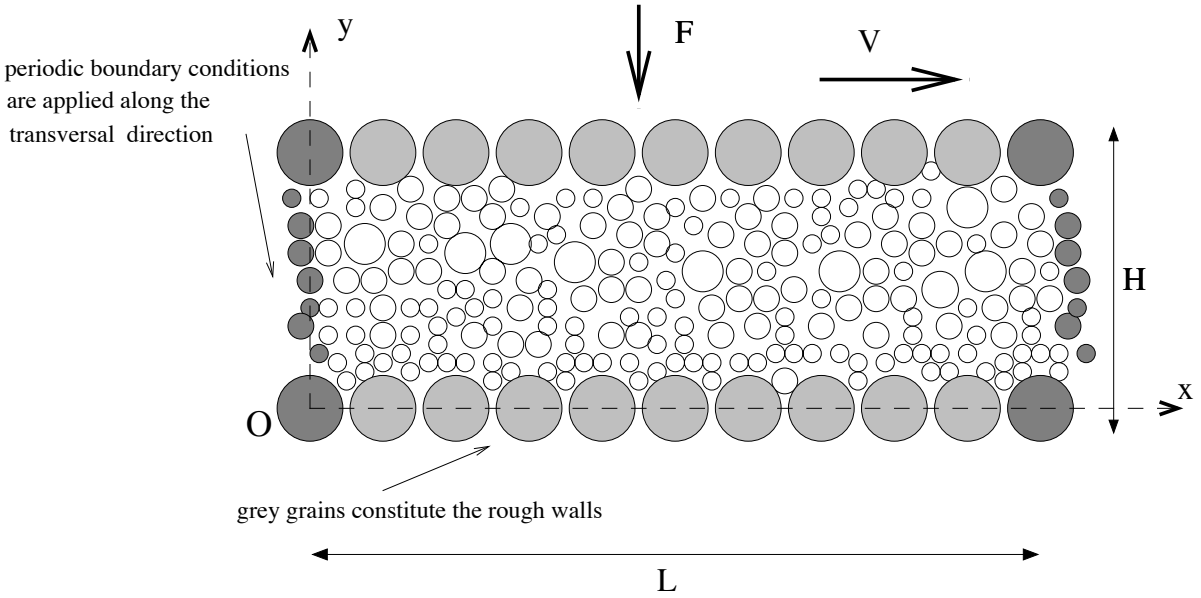

Figure 8. Model of shearing plan with periodic boundaries.

cell at the same vertical location and with the same kinematic and dynamic conditions. L is the length of the simulated flow (equal to 40 particles). This size appears sufficient to neglect the length effects of the simulation box. It is considered here that the roughness of wall surface is modeled by jointed grains having the same characteristics as grains in the flow.

Conventionally, we observe two regimes in granular flows. First we have the quasistatic regime, which usually obeys the constitutive laws in which the effective friction coefficient is constant. Secondly, there is the rapid-flow or dynamic regime, where the particles interact collisionally. In this case, the solid fraction is close to the maximum.

In Figure 9 we present the velocity field of two regimes. On the top two images we note the appearance of small vortices which characterize the quasistatic regime. These disappear in the dynamic regime, observed in the bottom images. In this case, the granular flow becomes stationary. This phenomenon gives us a better understanding of the behavior of granular flow [da Cruz 2004].

Figure 10 shows the contact force distribution across the granular material at the beginning of the simulation and when the stationary regime is established.

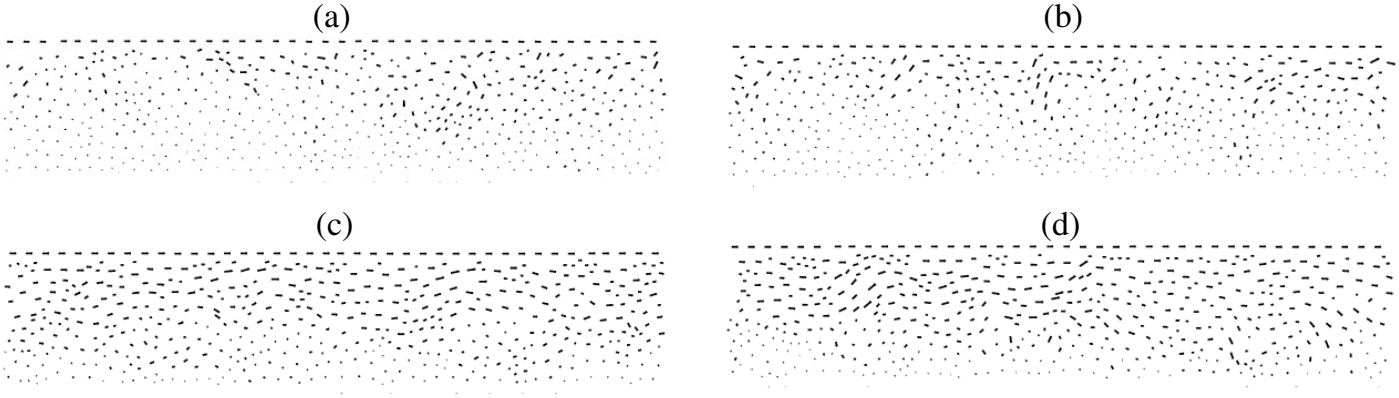

Figure 9. The velocity field in the quasistatic regime with a small vortex (top row), and in the dynamic regime (bottom).

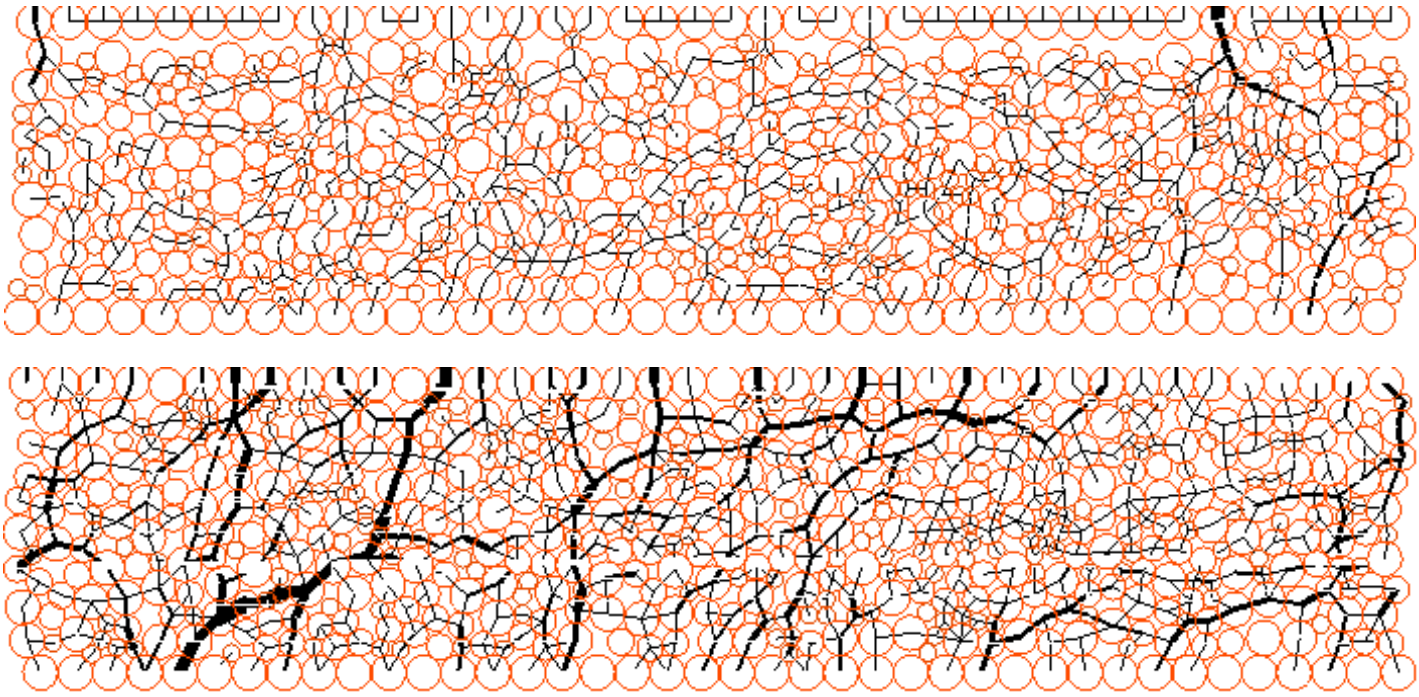

Figure 10. Contact forces field at the beginning of the simulation (top) and when stationary flow is established (bottom).

Another result is concerned with the variation of velocity as a function of the height. We see in Figure 11 that the average velocity agrees well with the curves proposed by da Cruz [2004], **?**], and Vargas-Escobar [2002]. There is no turbulence close to the mobile wall.

The major result of this work is the heat generated by friction between particles and the shearing wall (see Figure 12). Figure 13, left, shows how heat is varies with the granular layer depth. The hottest zone is located in the middle of the flow. These observations are confirmed by Vargas-Escobar [2002], who has shown that the granular temperature profiles illustrate the high-shear zones in the center of the cell.

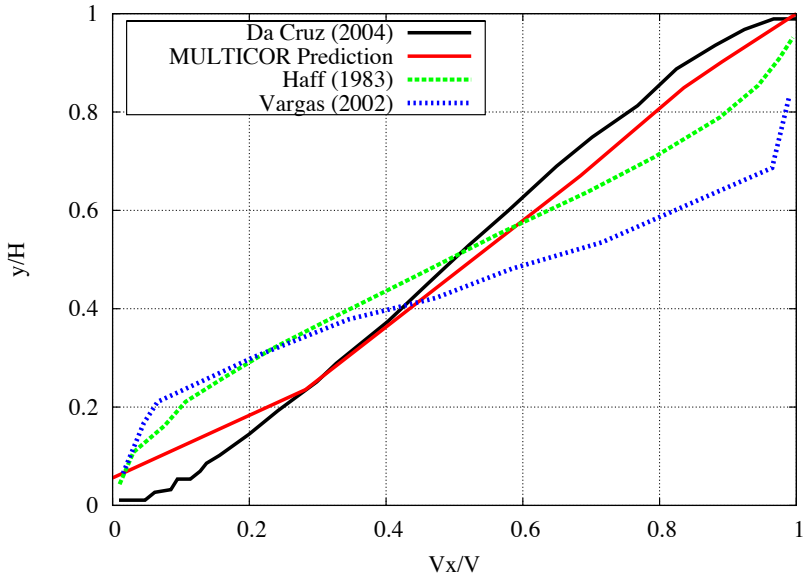

Figure 11. Typical velocity normalized profile.

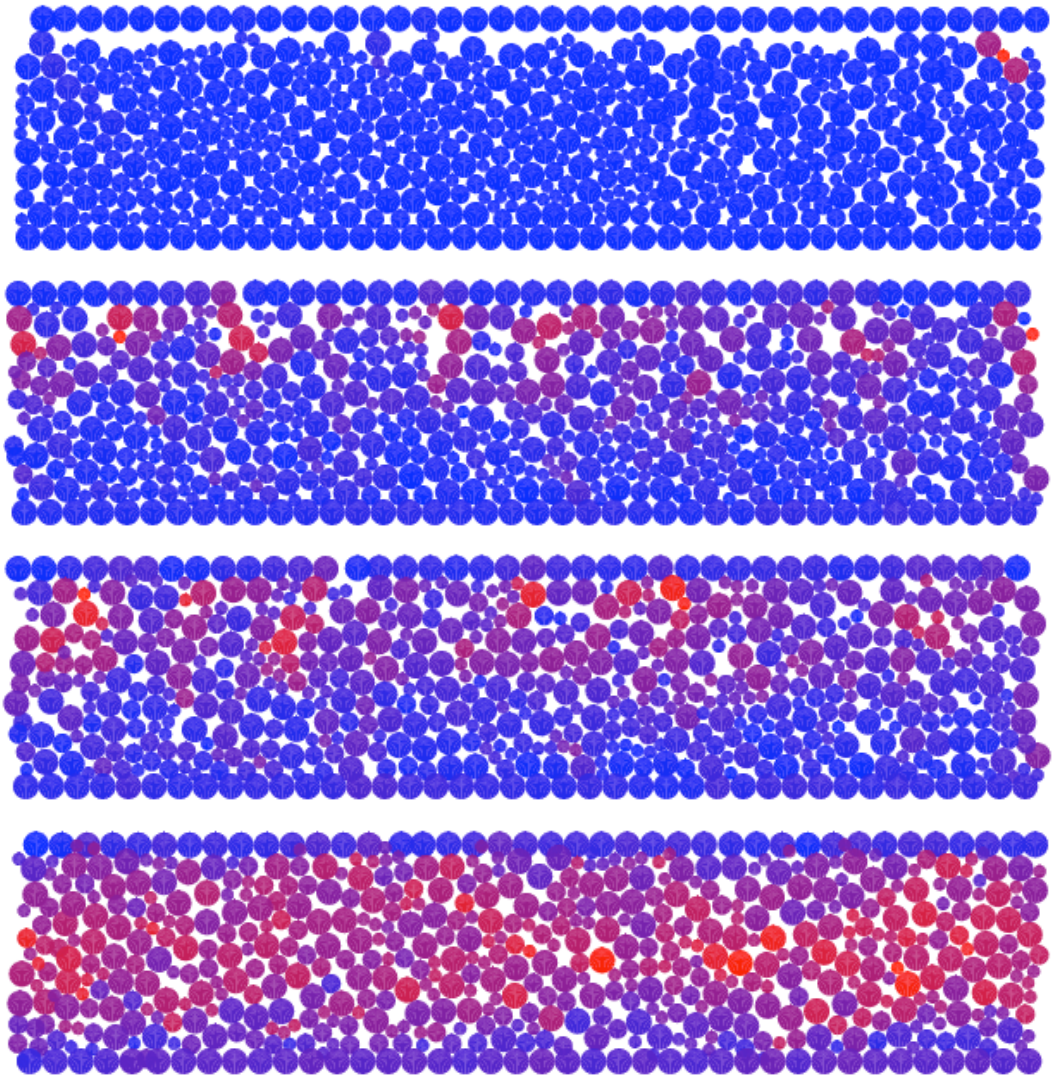

Figure 12. Thermal maps of heat evolution in the quasistatic regime.

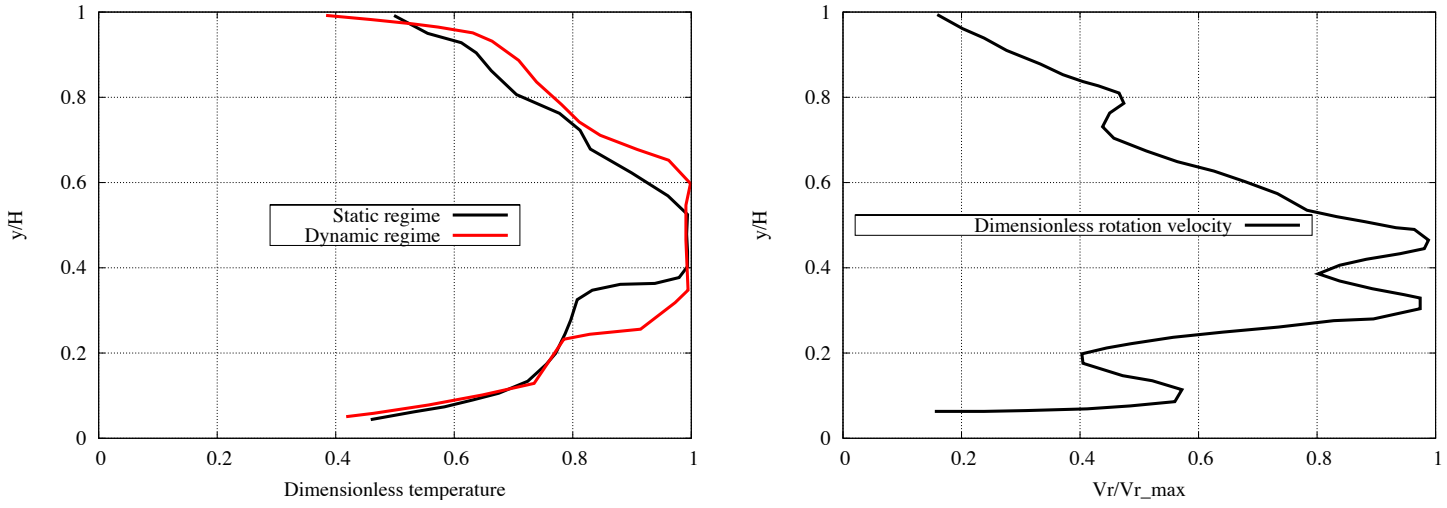

Figure 13. Left: heat profiles. Right: normalized angular velocity.

Here we note that thermal symmetry of the heat profile means that the bottom wall plays an important role in the heat generation. We also note that these profiles correspond with the angular velocity curves, seen on the right in Figure 13.

5. Conclusions

The present work focuses on the modelling of heat transfer and heat generation by friction in a granular material by using DEM. The proposed model has been implemented in MULTICOR software and performed for some examples to check its validity. The numerical predictions obtained with MULTICOR agree with the experimental results and numerical predictions from the literature. Therefore, the proposed assumptions about the predominance of heat transfer by conductance in comparison with other thermal effects has negligible influence on the numerical predictions.

The next step will consist in the incorporation of the other heat transfer phenomena like convection, radiation, and impact effect. Moreover, further studies will focus on the dynamic friction coefficient and its changes with the temperature and the wear in the contact area. An experimental campaign is also planned with our industrial partner Proust et al. [2007].

Acknowledgement

We thank Mrs. Boutinaud-Morel for her advice in the translation of this article.

References

[Bahrami et al. 2006] M. Bahrami, M. M. Yovanovich, and J. R. Culham, "Effective thermal conductivity of rough spherical packed beds", *Int. J. Heat Mass Tran.* **49**:19-20 (2006), 3691–3701.

[da Cruz 2004] F. da Cruz, *Écoulement de grains secs: frottement et blocage*, Ph.D. thesis, École Nationale des Ponts et Chaussées, Paris, 2004.

[Fortin and Coorevits 2004] J. J. Fortin and P. Coorevits, "Selecting contact particles in dynamics granular mechanics systems", *J. Comput. Appl. Math.* **168**:1-2 (2004), 207–213.

[Fortin and de Saxcé 1999] J. Fortin and G. de Saxcé, "Modélisation numérique des milieux granulaires par l'approche du bi-potentiel", *C. R. Acad. Sci. IIb* **327** (1999), 721–724.

[Fortin et al. 2005] J. Fortin, O. Millet, and G. de Saxcé, "Numerical simulation of granular materials by an improved discrete element method", *Int. J. Numer. Meth. Eng.* **62**:5 (2005), 639–663.

[Haff 1983] P. K. Haff, "Grain flow as a fluid- mechanical phenomenon", *J. Fluid Mech.* **134** (1983), 401–430.

[Ketterhagen et al. 2007] W. R. Ketterhagen, J. S. Curtis, C. R. Wassgren, A. Kong, P. J. Narayan, and B. C. Hancock, "Granular segregation in discharging cylindrical hoppers: a discrete element and experimental study", *Chem. Eng. Sci.* **62**:22 (2007), 6423–6439.

[Laguerre et al. 2006] O. Laguerre, S. B. Amara, and D. Flick, "Heat transfer between wall and packed bed crossed by low velocity airflow", *Appl. Therm. Eng.* **26**:16 (2006), 1951–1960.

[Linck et al. 2006] V. Linck, A. Saulot, and L. Baillet, "Consequence of contact local kinematics of sliding bodies on the surface temperatures generated", *Tribol. Int.* **39**:12 (2006), 1664–1673.

[Melka and Bézian 1997] S. Melka and J. J. Bézian, "L'isolation thermique par les materiaux granulaires", *Rev. Gen. Therm.* **36**:5 (1997), 345–353.

[Mokrani and Bourouga 2005] H. Mokrani and B. Bourouga, "Modèle de coefficient de partage du flux généré à une interface de contact électrothermique: approche microscopique en régime permanent", in *12émes Journées Internationales de Thermique* (Tanger, Morocco, 2005), 2005.

[Proust et al. 2007] C. Proust, S. Hawksworth, R. Rogers, M. Beyer, D. Lakic, D. Raveau, P. Hervé, V. Pina, C. Petitfrère, and X. Lefebvre, "Development of a method for predicting the ignition of explosive atmospheres by mechanical friction and impacts (MECHEX)", *J. Loss Prevent. Proc.* **20**:4-6 (2007), 349–365.

[Slavin et al. 2002] A. J. Slavin, V. Arcas, C. A. Greenhalgh, E. R. Irvine, and D. B. Marshall, "Theoretical model for the thermal conductivity of a packed bed of solid spheroids in the presence of a static gas, with no adjustable parameters except at low pressure and temperature", *Int. J. Heat Mass Tran.* **45**:20 (2002), 4151–4161.

[Vargas-Escobar 2002] W. L. Vargas-Escobar, *Discrete modeling of heat conduction in granular media*, Ph.D. thesis, University of Pittsburgh, Pittsburgh, 2002, Available at http://etd.library.pitt.edu/ETD/available/etd-02012002-193942/unrestricted/FinalBW.pdf.

[Vargas-Escobar and McCarthy 2002a] W. L. Vargas and J. J. McCarthy, "Conductivity of granular media with stagnant interstitial fluids via thermal particle dynamics simulation", *Int. J. Heat Mass Tran.* **45**:24 (2002), 4847–4856.

[Vargas-Escobar and McCarthy 2002b] W. L. Vargas-Escobar and J. J. McCarthy, "Stress effects on the conductivity of particulate beds", *Chem. Eng. Sci.* **57**:15 (2002), 3119–3131.

Received 17 Dec 2007. Accepted 7 Mar 2008.

VIET DUNG NGUYEN: vietdung.nguyen@u-picardie.fr
Laboratoire des Technologies Innovantes (EA 3899), Université de Picardie Jules Verne, IUT de l'Aisne, 02100 Saint Quentin, France

JÉRÔME FORTIN: jerome.fortin@insset.u-picardie.fr
Laboratoire des Technologies Innovantes (EA 3899), Université de Picardie Jules Verne, IUT de l'Aisne, 02100 Saint Quentin, France

MOHAMED GUESSASMA: mohamed.guessasma@u-picardie.fr
Laboratoire des Technologies Innovantes (EA 3899), Université de Picardie Jules Verne, IUT de l'Aisne, 02100 Saint Quentin, France

EMMANUEL BELLENGER: emmanuel.bellenger@u-picardie.fr
Laboratoire des Technologies Innovantes (EA 3899), Université de Picardie Jules Verne, IUT de l'Aisne, 02100 Saint Quentin, France

CLAUDIA COGNÉ: claudia.cogne@u-picardie.fr
Laboratoire des Technologies Innovantes (EA 3899), Université de Picardie Jules Verne, IUT de l'Aisne, 02100 Saint Quentin, France

Applied Thermal Engineering 29 (2009) 1846–1853

Contents lists available at ScienceDirect

Applied Thermal Engineering

journal homepage: www.elsevier.com/locate/apthermeng

Discrete modeling of granular flow with thermal transfer: Application to the discharge of silos

V.D. Nguyen [a], C. Cogné [a,*], M. Guessasma [a], E. Bellenger [a], J. Fortin [b]

[a] Laboratoire des Technologies Innovantes, IUT de l'Aisne, 48 rue d'Ostende, 02100 Saint Quentin, France
[b] Laboratoire des Technologies Innovantes, INSSET, 48 rue Raspail, 02100 Saint Quentin, France

ARTICLE INFO

Article history:
Received 15 January 2008
Accepted 10 September 2008
Available online 25 September 2008

Keywords:
Heat transfer
Contact
Friction
Silo
DEM
Particulate beds

ABSTRACT

Heat transfer in particulate beds has an important impact for many industrial processes as well as for the storage of particulate material. This study is aimed at modeling the granular flow and heat transfer between particles during the discharge of a silo. A numerical model based on the detection of contacts and the evolution of heat transfers in particle flow has been developed by using discrete element method (DEM). Through this study, we model the heat flows generated by friction and its transfer by conductance. Influence of the friction coefficient and discharging velocity on the granular flow and heat transfer has been investigated through some numerical examples. This modeling enables to understand better the phenomena at the contact point between particles as well as the heat transfer for a great number of particles in motion from their intrinsic mechanical properties and contact conductance.

1. Introduction

The published literature analysis has shown the importance of heat in granular media for industrial processes in applications as diversified as powder metallurgy, chemical reactors [1], food technology [2], thermal insulation [3] or even simply storing particles in a silo after drying [4]. But few studies are interested in the understanding of thermal transfer during sliding contacts. However these complex phenomena with multi-physical characteristics are an essential element in the understanding of the discharging silo process. One of the difficulty is to be able to predict the forces of friction and the temperatures in the friction zone from the intrinsic properties of grains in contact.

From a thermal energy point of view, the sliding contact is the source of a heat generation, whose distribution between the different bodies is difficult to estimate [5]. Besides, the determination of the contact area, which plays an important role in the value of the transferred heat flow is also difficult to estimate. It depends on various parameters like porosity, particles state, the distribution of contact forces, the nature of each phase and the structure of media. Mechanical engineers are at the origin of the greatest number of works. Slavin et al. [6], Bahrami et al. [7] and Filali [8] have developed models to estimate the effective thermal conductivity of a particles packing, from the intrinsic properties of solids and fluids materials. These models enable to determine the apparent thermal conductivity evolution of a granular media depending on the mechanical forces applied to the particle bed. Vargas et al. [9] has studied more particularly the influence of contact pressure on the apparent conductivity of the bed with a small, but finite area of contact. All these models are considering the state surface of the spheres but only the heat transfers by contact are studied. Laguerre et al. [10] have presented a heat transfer model which took into account radiation phenomena in a packing so as to simulate the cooling of a fruit pile in a cold chamber. In all the above mentioned works, it is assumed that the study is realized in a static bed.

The first part of this work consists in using the discrete element method (DEM) for the contact detection, the determination of contact forces and the kinematic parameters. A computational software MULTICOR, that can treat an important number of particles (10^6 particles in 2D plane), has been developed to solve the mechanical equations. In a second time, the energy dissipation generating by friction and its transfer by contact have been studied and implemented in MULTICOR software. In the last part, through some experimental data and simulations, we underscore the phenomena of thermal and mechanical interaction during the discharge of the silo. We have investigated the influence of friction coefficient in the case of forced flow of granular media. Some phenomenon such as vault effect arising during the discharge of silo are observed and their influence on the heat dissipation into the granular media has been studied throughout numerical simulations.

* Corresponding author.
E-mail address: claudia.cogne@u-picardie.fr (C. Cogné).

1359-4311/$ - see front matter © 2008 Elsevier Ltd. All rights reserved.
doi:10.1016/j.applthermaleng.2008.09.009

2. Mechanical resolution by DEM

The conventional DEM allows to model really deformable particles as well as complex shapes (from the ellipsoid to the polygon). Here, we have studied the simple case of non-deformable and non-penetrable particles in 2D plane with the computational programme MULTICOR, developed by Fortin et al. [11]. The coordinates and the rotations of Euler are the configuration parameters q. The gyroscopic and centrifugal terms are equal to zero in 2D. The matrix of generalized mass M of the system does not depend on q that is diagonal block. The mechanical equation can be written in the following form (Eq. 1):

$$\underline{M}\ddot{q} = F_{ext}(q, \dot{q}, t) + R^{\alpha} \tag{1}$$

where F_{ext} represents the known external forces and R^{α} the unknown interior forces related to contact reactions with α the number of contacts for the considered particle.

In a system composed of p heterogeneous particles, the critical parameter for the modeling time is the maximum number of interactions between particles. The more the interaction range is important the more we have to test the possible interactions between particles. MULTICOR uses the partitioning method coupled to a connectivity table [12]. This technique allows to reduce considerably the computational time. In that case, the computational time no longer increases like $O(p^2)$ but only like $O(p)$, which is almost optimal. For each couple of particles Ω_i and Ω_j which may enter in contact, is associated with a local reference whose axes are oriented according to the two unit vectors n and t, respectively, normal and tangential vectors in the contact plan (Fig. 1). The normal n is directed from Ω_j to Ω_i. The variables put in duality are $\dot{u}^{ij}$, the relative local velocity of Ω_i compared to Ω_j, and the contact reaction r^{ij} of Ω_j on Ω_i. In the local base, they are written by:

$$\dot{u}^{ij} = \dot{u}_t^{ij} t + \dot{u}_n^{ij} n \quad r^{ij} = r_t^{ij} t + r_n^{ij} n, \tag{2}$$

where $\dot{u}_n^{ij}$ is the normal separation velocity, $\dot{u}_t^{ij}$ the sliding velocity, r_n^{ij} the contact pressure and r_t^{ij} the adherence force.

The introduction of Coulomb's friction μ leads to a non-linear problem which cannot be solved by a linear programming method. Unlike the usual approach, the bipotential method leads to a single variational principle and an inequality [11]. By using Usawa's algorithm, we obtain a resolution algorithm of the constitutive law based on the predictive–corrective scheme expressed by Eq. 3:

$$\begin{aligned} &\text{predictor} : \tau^{ij} = r^{ij} - \gamma[\dot{u}_t^{ij} + (\dot{u}_n^{ij} + \mu||\dot{u}_t^{ij}||).n], \\ &\text{corrector} : r^{ij} = proj(\tau^{ij}, K_{\mu}) \end{aligned} \tag{3}$$

where γ is a numerical parameter and $proj(\tau^{ij},K_{\mu})$ the projection of Coulomb's cone which leads, according to the value of τ^{ij}, to one of these states: non-contact, contact with adherence or sliding contact. Conventionally, at each time step, the contact forces in the system are determined repeatedly by the method of successive balances based on a Gauss–Seidel algorithm for the 2D version. Each contact force is calculated by adopting temporary values over the other contacts. The convergence is obtained when the force confirms the unilateral contact law with dry friction.

The calculation cycle is a time-stepped algorithm which requires the repetition of the following resolution scheme (Fig 2).

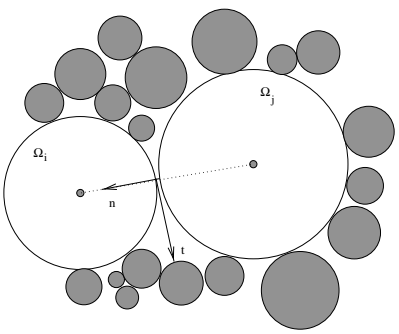

Fig. 1. A local referential.

3. Heat transfer in granular media and thermal formulation

In general, heat transfer in granular media with a stagnant interstitial fluid is assumed to occur because of the following physical phenomena:

- Thermal conduction through the particles and thermal conduction through the fluid between the neighboring particles. Furthermore, in a multi-contact system considered in this work, we must consider thermal conduction through the contact area between two particles Ω_i and Ω_j. Contact conductance refers to the ability of transmitting heat across their mutual interface.
- Radiant heat transfer between the fluid within neighboring voids and radiant heat transfer between the surfaces of neighboring particles. For heat transfer by radiation, contact between surfaces is not required. Radiation is linked to the production of electromagnetic waves by a heat surface.
- For flowing fluid, heat transfer by interparticle convection can be considered if there is a difference of temperature between the particles and the fluid.

In frictional granular flow regimes, heat transfer occurs from the phenomenon presented above. In addition, it is necessary to consider the heat generated by friction between two particles Ω_i and Ω_j. Indeed, the sliding contact is an important source of heat generation for dynamic granular problems considered in this work (Fig. 3a).

In this paper, we assume that conduction through the solid phase dominates the thermal conduction. This assumption is verified when:

$$\frac{\lambda_s s}{\lambda_f a} \gg 1 \tag{4}$$

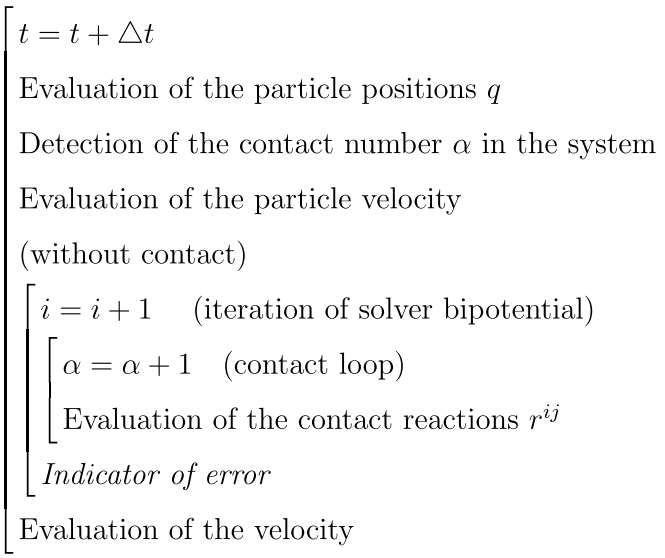

Fig. 2. Algorithm for mechanical resolution.

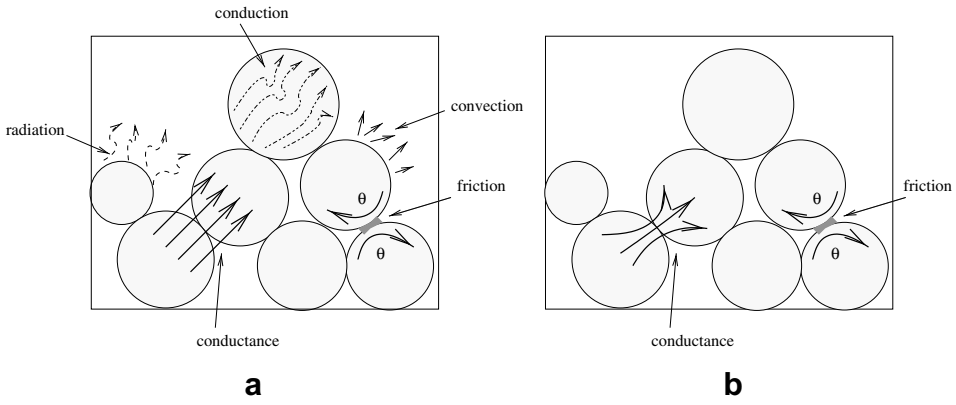

Fig. 3. (a) Heat transfer mechanisms in granular media; (b) heat transfer in MULTICOR software.

where λ_s and λ_f are, respectively, the conductivities of the particles and the fluid, a and s are, respectively, the radius of the particle and the contact area.

This expression is checked for high thermal conductivity of solid materials or for solid particles in a vacuum ($\lambda_f \to 0$) [13]. Under these conditions, the heat transfer between two adjacent particles Ω_i and Ω_j is only controlled by the contact conductance. In this work, radiant and convective heat transfers are neglected. Therefore, we only consider heat transfer in granular flow by contact conductance and friction effect (Fig. 3b).

3.1. Heat transfer by conductance

Contact conductance is directly linked to the constriction of the heat flow lines in the contact point [2]. The thermal contact conductance is defined by the ratio of the heat flow across a contact interface and the magnitude of the discontinuity temperature at the interface (Eq. 5):

$$\varphi_{ij} = H_c^{ij}(T_j - T_i) \tag{5}$$

where φ_{ij} is the heat flow transferred between the particles Ω_i and Ω_j, $T_j - T_i$ the temperature difference between the mid-planes of the spheres and H_c^{ij} the contact conductance between the particles Ω_i and Ω_j with j varies from *1* to the contact number α.

The coefficient H_c^{ij} which is a function of the compression force, refers to the ability for two materials in contact to transfer heat through their mutual interface (Fig. 4). In our work, contact conductance between particles Ω_i and Ω_j is modeled using Hertz's theory (Eq. 6):

$$H_c^{ij} = 2\lambda_s a_H = 2\lambda_s \left(\frac{3r_n^{ij}a^*}{4E^*}\right)^{1/3} \tag{6}$$

where r_n^{ij} is the normal force, λ_s the thermal conductivity of the particle, a_H hertzian contact radius and a^* is the equivalent radius expressed by $\frac{1}{a^*} = \frac{1}{a_i} + \frac{1}{a_j}$, $\frac{1}{E^*} = \frac{1-v_i^2}{E_i} + \frac{1-v_j^2}{E_j}$ the effective Young's modulus (E^* expresses an equivalent Young's modulus between the particles in contact) and v Poisson's ratio.

The contact between two adjacent particles is assumed to be smooth and sliding. The contact conductance is calculated dynamically at each time step and for all contacts of a particle Ω_i.

We remind that the considered particles are non-deformable and non-penetrable. The using of Hertz's theory only enables us to compute the contact conductance coefficient H_c^{ij}. We assume that the particles remain rigid all the time.

3.2. Heat generated by friction

In this case, heat flow is generated by dissipation of energy during friction between particles. This assumption of mechanical energy dissipation is well known in thermomechanical field like braking [14] or high speed machining [15]. The deformation is neglected because the particles are assumed rigid. Friction is understood as continuous mechanical solicitations between two bodies. The heat energy generated by friction $E_{\mu_{ij}}$ at the frictional interface is:

$$E_{\mu_{ij}} = \mu \dot{u}_t^{ij} r_n^{ij} \tag{7}$$

The modeling of the energy generated by friction requires to share the heat between particles in sliding contact. Therefore, we define the partition coefficient of generated heat flow β_{ij}. This coefficient depends on different microscopic parameters like the thermal properties, the sliding velocity, heat generation parameters and the surface roughness if the contact is not perfect [16]. Research in this area has shown different equations to estimate this coefficient

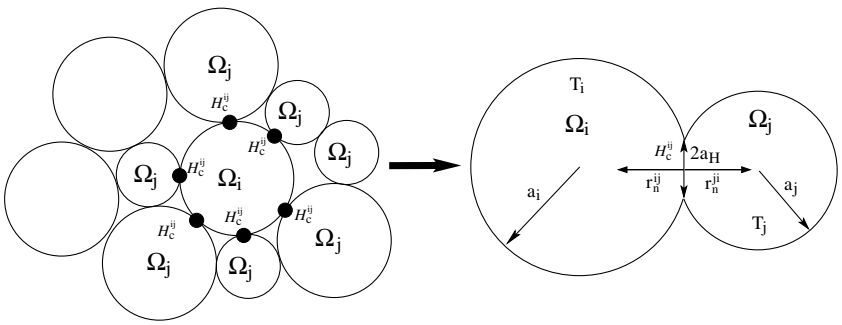

Fig. 4. Schematic representation of heat transfer by conductance.

$t = t + \triangle t$

Evaluation of the particle positions q

Detection of the contact number α in the system

Evaluation of the particle velocity

(without contact)

- $i = i + 1$ (iterations of solver bipotential)
  - $\alpha = \alpha + 1$ (contact loop)
  - Evaluation the contact reaction r^{ij}
  - *Indicator of error*

Evaluation of T_i^t, H_c^{ij}, $E_{\mu_{ij}}$

Evaluation of the temperature $T_i^{t+\triangle t}$

Evaluation of the velocity

Fig. 5. Algorithm for thermal resolution.

[17,18]. In our study, this coefficient is obtained from the analytical solution of Varadi et al. [19] defined as the ratio of the conductivities:

$$\beta_{ij} = \frac{\lambda_s^i}{\lambda_s^i + \lambda_s^j} \tag{8}$$

We assume that the packed bed is made of only one material. The partition coefficient of generated heat flow β_{ij} is then equal to $\frac{1}{2}$.

3.3. Thermomechanical resolution

Taking into account the various phenomena of heat generation mentioned above, the energy balance and the variation of temperature for a particle during a low time step $\triangle t$ can be written as follows (Eq. 9):

$$m_i C_{Pi} \frac{\triangle T_i}{\triangle t} = \sum_{j=1}^{\alpha} (H_c^{ij}(T_j - T_i) + \beta_{ij} E_{\mu_{ij}}) \tag{9}$$

where m_i and C_{Pi} are the mass and the heat capacity for Ω_i, respectively, α the contact number.

The temperature evolution between two bodies in contact is governed by the Eq. (9), representing the balance of the heat energy. This equation is solved with a low time step ($\triangle t = 10^{-3}$ s) to assume that the temperature of each particle changes slowly that thermal perturbations do not propagate further than its immediate neighbors during one time step. The second requirement is that the heat transfer resistance through a particle Ω_i (conduction) is significantly lower than the contact resistance between two particles Ω_i and Ω_j, proved if:

$$Bi = \frac{H_c^{ij}}{\lambda_s a} \ll 1 \tag{10}$$

where Bi is equivalent to the Biot number. The equation used in order to compute the temperature T_i at the time $(t + \triangle t)$ is given as follows:

$$T_i^{t+\triangle t} = T_i^t + \frac{\triangle t}{m_i C_{Pi}} \sum_{j=1}^{\alpha} (H_c^{ij}(T_j^t - T_i^t) + \beta_{ij} E_{\mu_{ij}}) \tag{11}$$

The general algorithm implemented in MULTICOR software is represented in the following scheme (Fig. 5).

The resolution of the heat problem requires to compute the contact detection, the determination of forces and the velocities of particles at each time step.

4. Numerical simulation

MULTICOR software can be used to simulate some industrial processes like sieving, crushing, filtration, etc. In the next sections, we have focused on the discharge of a silo both from a mechanical and in a thermal point of view.

4.1. Mechanical application

In this part, the influence of the initial fill on the discharging process has been investigated. Only mechanical equations have been taken into account for the granular flow modeling in order to correlate MULTICOR predictions with experimental results

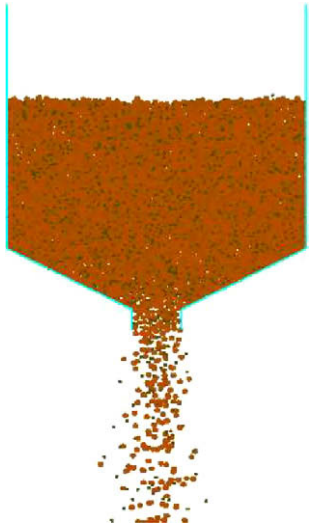

Fig. 6. Hopper discharge of a well-mixed initial fill.

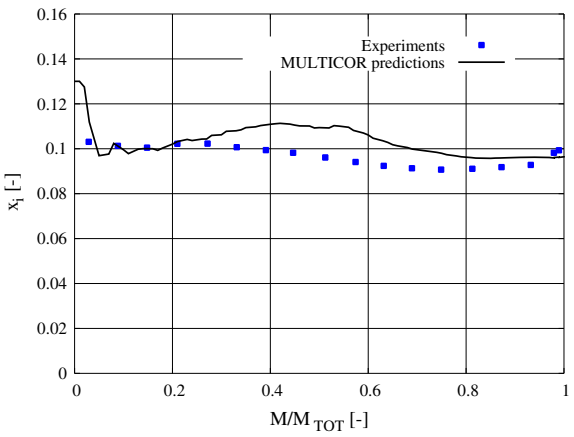

Fig. 7. Comparison of experimental and predicted mass fraction of fine particles during the discharge of a well-mixed initial fill.

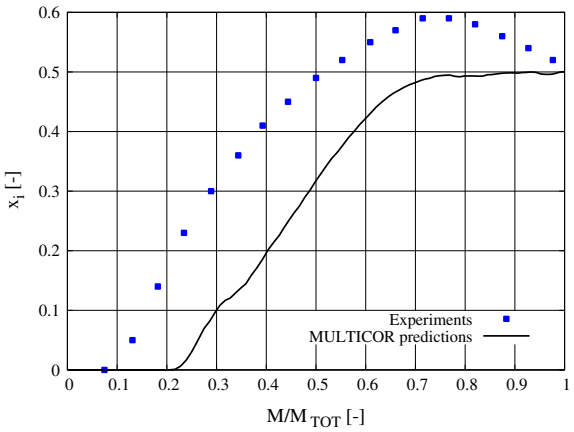

Fig. 8. Comparison of experimental and predicted mass fraction of fine particles during the discharge of a layered initial fill.

developed in the works of Ketterhagen [4]. The experiments have used bidisperse spheres with a mean diameter of 1.6 mm and 0.52 mm. The dimensions of the silo and the properties of the particles are the same than the ones used experimentally by Ketterhagen [4].

The first study is the discharge of the silo with a well-mixed initial charge as shown in Fig. 6. The initial charge contains 10% of fine particles. Computationally, a well-mixed initial fill is relatively simple to obtain by assigning particle positions via a random number generator.

The comparison of experimental results and computational data of discharged fine particles fraction is represented in Fig. 7. M represents the cumulative mass discharge, M_{TOT} the total mass initially charged in the silo and x_i the fine mass fraction of discharged particles.

It should be noted that the discharge of the silo is homogenous but there is an over-prediction of the fine particles concentration by MULTICOR for $0.4 < M/M_{TOT} < 0.7$. The main reason may be due to variation in friction coefficient, particle shapes or homogeneity of the initial fill [4]. Moreover, the simulations have been carried out in two dimensions and do not reproduce perfectly the 3D experiments. Despite these differences, analysis of the weight fractions of the fine particles shows a quite good adequation between

Table 1
Particles properties used in MULTICOR simulations

Parameter	Value
Density	7800 kg m^{-3}
Poisson ratio	0.29
Young's modulus	193 GPa
Particle radius	10^{-3} m
Thermal conductivity	15 W m^{-1} K^{-1}
Number of particle	600
Heat capacity	444 J kg^{-1} K^{-1}

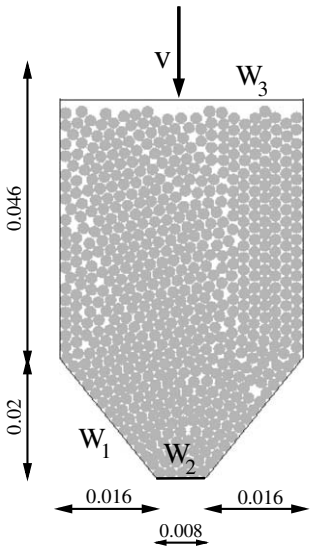

Fig. 10. Scheme of the silo.

modeling and experimental data and allows us to provide a realistic prediction of granular flow during the discharge of silo.

The next example is a layered initial fill. The silo is filled with two horizontal layers, one for each of the particles diameter, fine over coarse particles (Fig. 9). The initial charge contains 50% of fine particles. Fig. 8 represents the evolution of fine particles x_i versus the normalized discharged mass M/M_{TOT}.

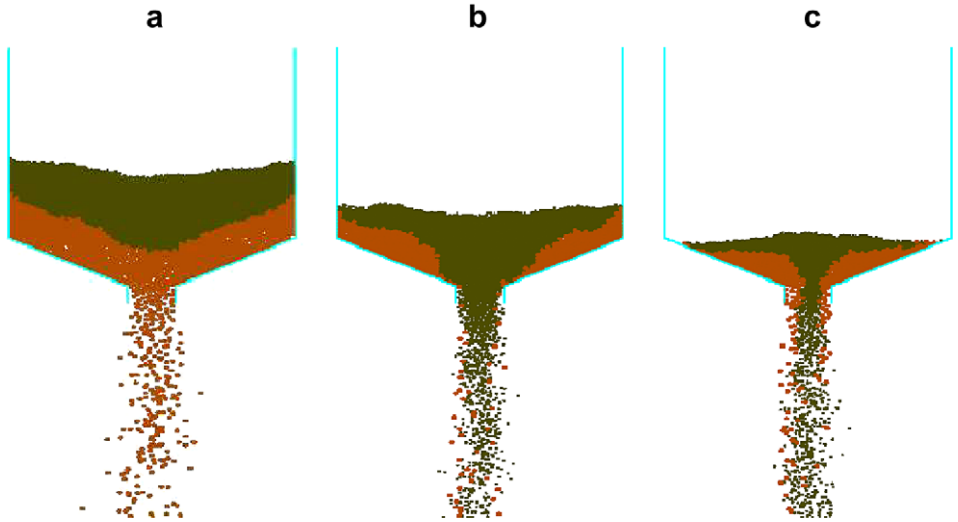

Fig. 9. The three phases of the hopper discharge filled in double layers.

Unlike Fig. 7 that represents an homogenous discharge, three phases may be noted during the process (Figs. 8 and 9):

- Phase 1: at first, only coarse particles are discharged (Fig. 9a).
- Phase 2: as the flow proceeds, the centerline velocities increase and fine particles begin to discharge (Fig. 9b).
- Phase 3: at the end of the discharge, the discharge is quite homogenous (Fig. 9c).

As shown in Fig. 8, the experiments and MULTICOR predictions have the same shape. However, the MULTICOR software gives lower prediction with respect to the experimental results. This difference may be due to the 2D plane modeling which cannot reproduce the same behavior as the experimental test.

After the mechanical validation of MULTICOR software for the discharge of silos, we propose to study heat transfer induced by vault effects during forced flow of granular media.

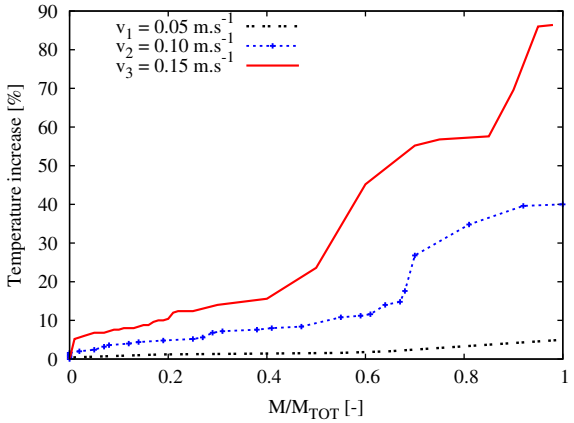

Fig. 11. Influence of the discharge velocity on the temperature increase.

4.2. Heat generation in forced flow of granular media

In this section, MULTICOR software is expanded to include thermal phenomena so that its applications is not limited to isothermal system. Thermal equations are based on the normal force between two particles in contact (Eq. 6) so heat transfer are directly linked to the force chains. We have studied the influence of several parameters (friction coefficient, discharge forces) on the heat generation in granular forced flow. Through this parametric study, we have shown the influence of vault effects on the heat generation. Theses phenomena lead to problems for industrial processes such as hopper discharging [20] or grain conveying in pipes [21]. We precise that in theses works [20,21], the thermal aspects which can be observed for such industrial applications are not discussed.

In MULTICOR, we have assumed that the contact equations and the Hertz theory have been validated with experimental data in a static configuration in a previous work [22]. In the following parts Sections 4.2.1 and 4.2.2, we have focused on the MULTICOR simulations of the forced silo discharging process to investigate the influence of physical phenomena on the temperature increase. The particles properties (steel particles) are summarized in Table 1 and the silo geometry is represented on Fig. 10.

After sedimentation in a closed silo, the wall W2 is opened allowing the beginning of the discharge. The discharging flow is controlled by the velocity v of the superior mobile wall W3. The initial temperature of the system is $T_{ini} = 25°C$. We have considered that the silo walls do not transfer heat with the exterior atmosphere. For each application, we have studied two parameters:

- The percent of the temperature increase on the wall W1 due to friction between particles: $100 \times (T(t) - T_{ini})/T_{ini}$.
- The normalized mass discharged $M(t)/M_{TOT}$,

where T is the averaged temperature of the wall W1, t the time, M is the mass discharged and M_{TOT} the total mass of particles initially in the silo.

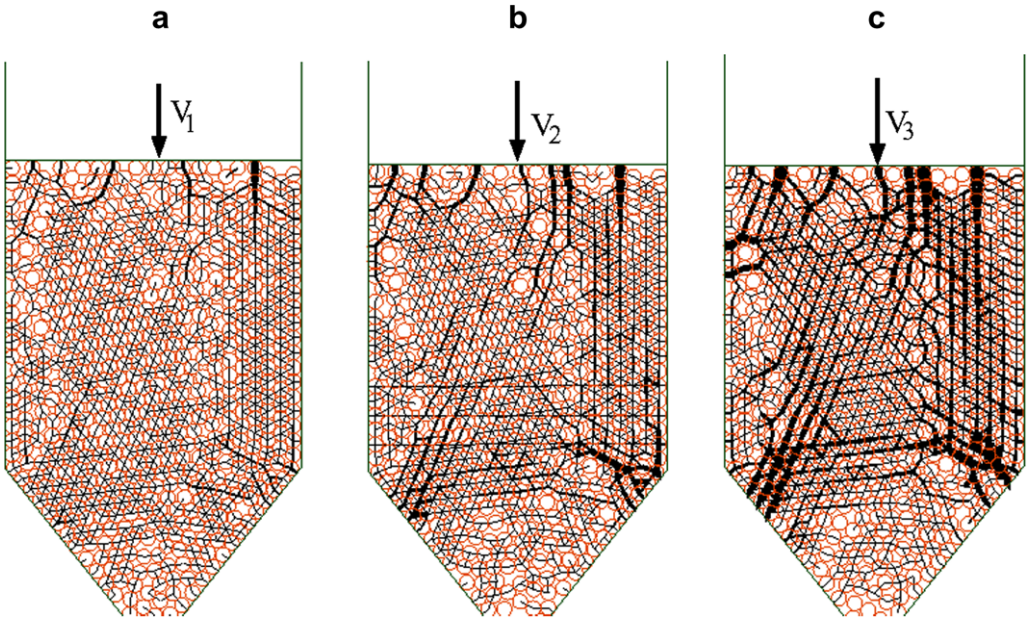

Fig. 12. Influence of the velocity on the force chains after 0.1 s of discharge; (a) $v_1 = 5.10^{-2}\ m\ s^{-1}$; (b) $v_2 = 10^{-1}\ m\ s^{-1}$; (c) $v_3 = 1.5 \times 10^{-1}\ m\ s^{-1}$.

4.2.1. Influence of the discharge velocity

In this part, the friction coefficient is constant ($\mu = 0.3$) and the influence of discharging velocity is explored. Fig. 11 shows the impact of the velocity on the temperature increase inside the silo.

A more striking result is seen in Fig. 12 when we examine the force chains after 0.1 s of discharge for three velocities (5×10^{-2} m s^{-1}, 10^{-1} m s^{-1} and 1.5×10^{-1} m s^{-1}). For an imposed velocity, the contact distribution is not homogenous, forces and also heat transfer follow preferred paths. And we note that the probability of finding contacts, directly linked to the conductance value, increases as the velocity increases.

In this configuration, it is necessary to determine the better conditions of discharge. As represented in Fig. 13, increasing the discharge velocity means a lower discharge time, but in the same time it generates a larger increase of the wall temperature by friction at the end of the discharging process. So depending on the material properties of particles, the discharging flow should be optimized to control the heat generation.

4.2.2. Influence of the friction coefficient μ

Influence of the friction coefficient particle/particle and particle/wall on heat generation and temperature increase is investigated at constant discharge velocity ($v = 0.1$ m s^{-1}). Fig. 14 represents the increase temperature versus the mass discharged for different friction coefficients. As expected, temperature increases significantly in case of large friction coefficients. But the temperature increase is not homogenous, steps can be noted in the heat generation especially for an important friction coefficient ($\mu = 0.35$) that could be explained with the analyze of the force chains. During the discharging flow for $0.4 < M/M_{TOT} < 0.7$, there is no increase of temperature. In this range, the forces chain represented in Fig. 15a shows low forces chains. On the contrary, for $M/M_{TOT} = 0.7$, there is a gap in the temperature increase. In Fig. 15b, we note large force chains with vault effect at the bottom of the silo, generating heat by friction and temperature increase of the wall.

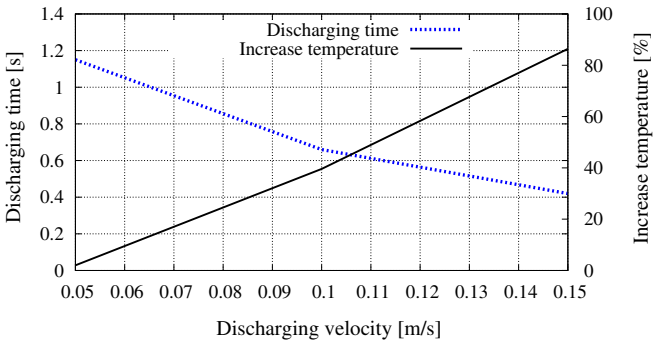

Fig. 13. Discharging time and increase temperature versus the discharging velocity.

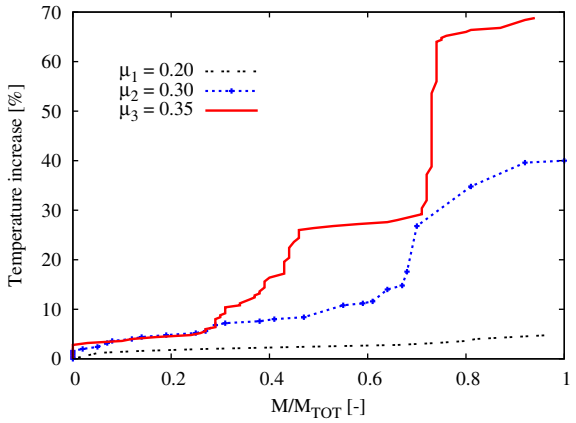

Fig. 14. Influence of the friction coefficient on the temperature increase.

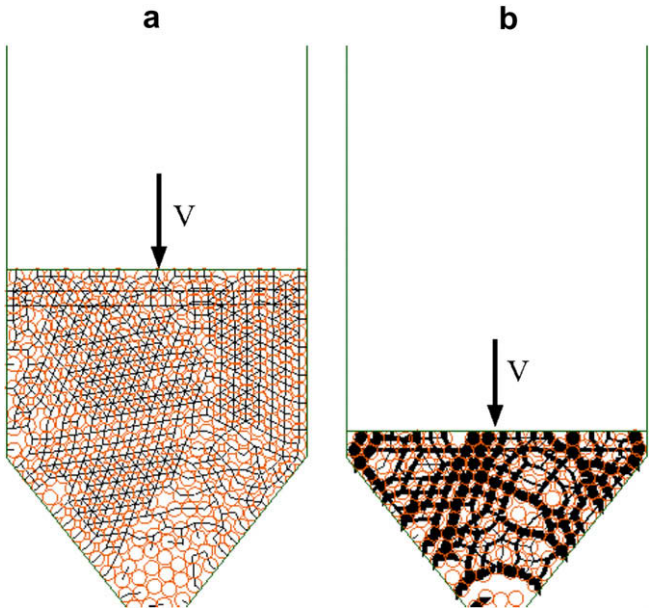

Fig. 15. Force chains; (a) low temperature increase; (b) large temperature increase.

5. Conclusion

The present work focuses on the extend of MULTICOR software, a computational code using discrete elements method, to incorporate heat transfer and heat generation from dissipation of mechanical energy. The results mentioned here show a good adequation with experimental results from the literature, which allows us to validate our assumptions especially in the mechanical field. MULTICOR software also provides good qualitative agreements concerning the influence of the friction coefficient and the discharge velocity on the increase temperature in a silo.

The next step will consist in the incorporation of the other heat transfer phenomena like convection or radiation. Moreover, further studies will focus on the dynamic friction coefficient and its changes with the temperature and the wear in the contact area. An experimental campaign is also planned with our industrial partner INERIS, a French National Institute that has controlled risks for sustainable development, to validate our thermal assumptions in dynamic behavior.

Acknowledgment

The authors are grateful to Dominique Morel for her help in the article redaction.

References

[1] B. Chaudhuri, F.J. Muzzio, M.S. Tomassone, Modeling of heat transfer in granular flow in rotating vessels, Chemical Engineering Science 61 (2006) 6348–6360.
[2] O. Laguerre, S. Ben Amara, D. Flick, Heat transfer between wall and packed bed crossed by low velocity airflow, Applied Thermal Engineering 26 (2006) 1951–1960.
[3] S. Melka, J.J. BTzian, L'isolation thermique par les matTriaux granulaire, Revue GTnTrale de Thermique 36 (1997) 345–353.

[4] W.R. Ketterhagen, J.S. Curtis, C.R. Wassgren, A. Kong, P.J. Narayan, B.C. Hancock, Granular segregation in discharging cylindrical hoppers: a discrete element and experimental study, Chemical Engineering Science 62 (2007) 6423–6439.
[5] P. Chantrenne, M. Raynaud, Study of a macroscopic sliding contact thermal model from microscopic models, International Journal of Thermal Science 40 (2001) 603–621.
[6] A.J. Slavin, V. Arcas, C.A. Greenhalgh, Theoretical model for the thermal conductivity of a packed bed of solid spheroids in the presence of a static gas, with no adjustable parameters except at low pressure and temperature, International Journal of Heat and Mass Transfer 45 (2002) 4151–4161.
[7] M. Bahrami, M.M. Yovanovich, J.R. Culham, Effective thermal conductivity of rough spherical packed beds, International Journal of Heat and Mass Transfer 49 (2006) 3691–3701.
[8] M. Filali, ConductivitT thermique apparente des milieux granulaires soumis a des contraintes mTcaniques: modTlisation et mesure, PhD thesis, Institut National Polytechnique de Toulouse, 2006.
[9] W.L. Vargas-Escobar, J.J. McCarthy, Conductivity of granular media with stagnant intersitial fluids via thermal particle dynamics simulation, International Journal of Heat and Mass Transfer 45 (2002) 4847–4885.
[10] O. Laguerre, S. Ben Amara, D. Flick, Transient heat and mass transfer by free convection in a packed bed of spheres: comparison between two modelling, Applied Thermal Engineering 28 (2008) 14–24.
[11] J. Fortin, O. Millet, G. De Saxe, Numerical simulation of granular materials by an improved discrete element method, Journal of Computational and Applied Mathematics 168 (2004) 207–213.
[12] J. Fortin, P. Coorevits, StratTgie de calcul du pas optimal pour une modTlisation TlTments discrets, In SixiFme Colloque National en Calcul des Structures (2003).
[13] W.L. Vargas-Escobar, J.J. McCarthy, Stress effects on the conductivity of particulate beds, Chemical Engineering Science 57 (2002) 3119–3131.
[14] D. Majcherczak, P. Dufrenoy, M. Nant, Third body influence on thermal friction contact problems: application to braking, ASME Journal of Tribology 127 (2005) 89–95.
[15] E. Guillot, B. Bougoura, B. Garnier, L. Dubar, Experimental study of thermal sliding contact with friction: application to high speed machining of metallic materials, in: Proceedings of ESAFORM Congress, Zaragoza, 2007.
[16] V. Linck, A. Saulot, L. Baillet, Consequence of contact local kinetics of sliding bodies on the surface temperatures generated, Tribology International 39 (2006) 1664–1673.
[17] B. Bougoura, J.M. Briot, J.P. Bardon, Influence de la vitesse et de la charge sur la conductance thermique de transport entre les bagues d'un roulement a rouleaux, International Journal of Thermal Science 40 (2000) 622–637.
[18] C.V. Madhusudana, Thermal conductance of cylindrical joints, International Journal of Heat and Mass Transfer 42 (1999) 1273–1287.
[19] K. Varadi, Z. Neder, K. Friedrich, Evaluation of the real contact areas, pressure distributions and contact temperatures during sliding contact between real metal surfaces, Wear 200 (1996) 55–62.
[20] M. Guaita, A. Couto, F. Ayuga, Numerical simulation of wall pressure during discharge of granular material from cylindrical silos with eccentric hoppers, Biosystems Engineering 85 (1) (2003) 101–109.
[21] A.W. Roberts, M.J. Jones, Analysis of forced flow of granular materials in vertical pipes without and with air permeation, Particulate Science and Technology 21 (2003) 25–44.
[22] V.D. Nguyen, C. CognT, J. Fortin, M. Guessasma, E. Bellenger, Heat transfer modeling by discrete elements method, in: 9th US National Congress on Computational Mechanics, San Francisco, 2007.

Article

JOURNAL OF COMPOSITE MATERIALS

Journal of Composite Materials
0(0) 1–11

DOI: 10.1177/0021998312464081
jcm.sagepub.com

SAGE

A numerical model for predicting effective thermal conductivities of alumina/Al composites

N Ferguen, C Cogné, E Bellenger, M Guessasma and C Pélegris

Abstract

This article describes a novel technique for manufacturing functionally graded materials with tailored properties for thermal management. These materials are ceramic/metal composites with a gradient microstructure, elaborated by producing a porosity gradient preform made of alumina phase subsequently infiltrated by the molten aluminum alloy (Al) phase. In order to model these particulate composites and to evaluate their effective thermal conductivities, a numerical approach based on both discrete element method and finite element method has been developed. The study presented here deals with alumina/Al composites without gradient microstructure and is conducted to numerically investigate the effects of the particle size distributions and the interconnection sizes between particles on the effective thermal conductivity. The situation in which an interfacial thermal resistance is present between both phases of composites to simulate a non ideal contact has also been considered.

Keywords

Ceramic–matrix composites, manufacturing process, thermal conductivity, modeling

Introduction

Functionally graded materials (FGMs) are particulate composites, which present a major interest in the development of various functional materials. FGMs have attracted much attention because their composition and properties can be tailored to suit specific engineering applications, and their advantages over homogeneous materials are apparent.[1,2] This class of composites possesses continuously graded properties and is characterized by spatially varying microstructure created by nonuniform distribution of the reinforcement phase. These materials can be used in a wide range of engineering applications, such as in aircraft for the fabrication of turbine blades for reducing interfacial stresses between dissimilar materials,[1,3] in artificial human implants for biomaterials[4] and in automotive for designing the piston head for high-efficiency engine components.[5]

Several research works regarding the effective thermal conductivity (ETC) for two-phase composite materials can be found in the literatures.[6–12] Maxwell[6] was the first to propose a model for low dispersion particles. Cunningham and Peddicord[8] and Hadley et al.[9] developed an analytical model to determine the thermal conductivity of materials with spherical inclusions. However, many studies[13–19] have shown the existence of an interfacial thermal resistance between phases of composites, which can have drastic effects leading to the reduction of the thermal properties. The imperfect contact between phases of composites can arise from the combination of poor mechanical or chemical adherence at the interface and thermal expansion mismatch,[18] which strongly affect the properties of composites.[20] Hale[13] explains that the effect of the interfacial thermal resistance induces a jump in the temperature field at interphase boundaries and therefore reduces the effective thermal conductivity.

The objective of this work is to develop a new FGM for thermal management applications. The architecture formed by a gradient microstructure will be optimized by controlling the thermal conductivity. The potential uses are for automotive engine blocks. The structure of the composites consists of gradient particle size distributions formed by producing a porosity gradient

LTI EA-3899 Université de Picardie jules Verne, IUT de l'Aisne, France

Corresponding author:
M Guessasma, LTI EA-3899 Université de Picardie jules Verne, IUT de l'Aisne, 48 rue d'Ostende, 02100 Saint-Quentin, France.
Email: mohamed.guessasma@u-picardie.fr

preform of the alumina phase subsequently infiltrated by the molten aluminum alloy phase to get the dense final composite. For this purpose, we have developed a numerical approach using the representative volume element (RVE) method for modeling the architecture of alumina/Al composites and to evaluate their ETCs.

In this article, the numerical approach deals with alumina/Al composites without gradient microstructure. The original approach is based on both discrete element method (DEM) and finite element method (FEM) to understand the phenomena conduction at the particle scale. The method accounts for the effect of the interconnection size between particles and the particle size distributions within composites on the ETC. This article is organized as follows: after the detailed presentation of the manufacturing process in the following section, we describe the numerical approach used to model the process and to generate the architecture of composites in the section. The definition of the RVE and the method of calculation of the critical sizes of RVEs are presented in later section. The FEM of heat transfer in RVEs containing interconnected particles is described in section 'Modeling of the thermal conductivity'. The numerical results are presented and discussed in the section 'Results and discussion'. Final sections are devoted to the conclusions and the future work.

Manufacturing process

The main idea of the process is to realize a spatial distribution of the microstructure formed by producing a porosity gradient preform of the ceramic phase subsequently infiltrated with molten metal phase. The details of the manufacturing process are described below.

Synthesis of the macroporous ceramic

Spherical polymethylmethacrylate (PMMA) particles with fixed granulometric distribution are chemically stuck in order to synthesise a particle skeleton in the shape of a block (Figure 1(a)). The chemical welding is ensured by squeezing and adding a solvent which induces a slow superficial dissolution of polymer. The overlapping between particles is ensured by the realization of bridges at the contact points (Figure 2). The particle skeleton is dried and then immersed into an alumina (Al_2O_3) slurry so that to fill interstitial spaces (Figure 1(b)). Then, the polymer particles are removed by burning them to a temperature of 200°C during 30 h

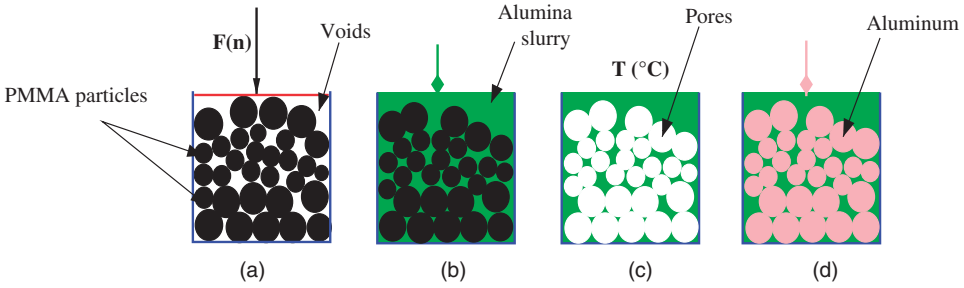

Figure 1. Schematic representation of different steps of the elaboration process: (a) stacking and squeezing of PMMA particles; (b) impregnation into alumina slurry; (c) heat treatments to obtain macroporous alumina; and (d) infiltration of aluminum.

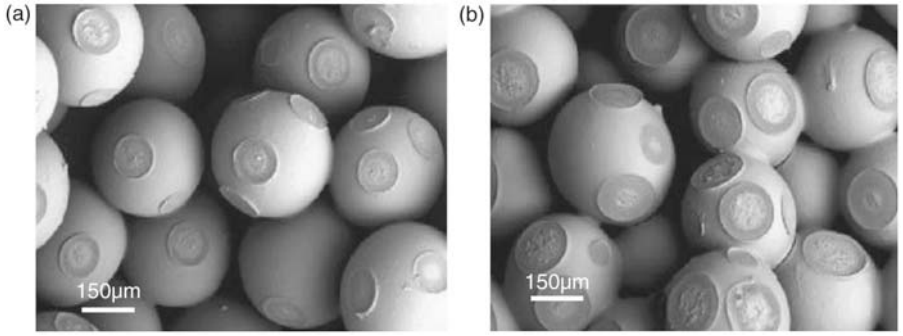

Figure 2. SEM images showing the realizations of bridges between PMMA particles. Size distributions ranging from 400 to 500 μm. The average interconnection sizes between neighboring particles are: (a) 177 μm and (b) 242 μm. Images reproduced from Descamps et al.[21]
SEM: scanning electron microscope; PMM: Spherical polymethylmethacrylate.

leading to the formation of a hollow structure. The residual organic is removed during heating at 400°C for 5 h. An alumina preform with controlled macroporosity is formed (Figure 1(c)). The alumina preform is sintered to a temperature of 1670°C for 3 h for densification and consolidation of the microstructure.[21]

Figure 3 shows the porosity gradient within a ceramic preform (β-tricalcium phosphate), obtained by superimposing slices of PMMA particles with different diameters. Particles which contribute to these pore sizes, have the following size distributions 700–800, 400–500 and 100–200 μm.

Infiltration of a preform by molten aluminum

The porous alumina preform is infiltrated with molten aluminum alloy in vacuum conditions and the temperature of the mould is 720°C (Figure 1(d)). It has been found that the wetting improvement in metal-ceramic systems seems to play an important role in the interfacial bonding of composites materials.[22,23] In order to improve the penetration of the aluminum alloy into the ceramic preform, magnesium is added with controlled quantities into the molten aluminum as wetting agent.[24] It is worth noting that during this process difficulties have been encountered during the infiltration of preforms having interconnection sizes, between pores, lower than 75 μm.

Numerical modeling

Generation of 3D granular systems

In this step, the architecture of the composite represented by the particle skeleton is created from a granular system (Figure 4) using discrete element software PFC3D.[25] The DEM model is a well-established method for predicting the evolution of particle trajectories accounting for interparticle collisions and other relevant forces.[26] The 3D discrete model implemented here involved the following steps. First, particles with fixed radius distributions are generated randomly by sedimentation method in a rigid container in form of a rectangular box (Figure 4(a)). When the equilibrium is reached, the system undergoes a vibration for over a short period of time leading to the rearrangement of the particles to fill void spaces. The increasing of the contact area between particles is ensured by applying an external force (z-direction) to a movable top wall during several cycles that allows interconnecting particles between them, until the desired contact area (Figure 4(b)). At the end of this step, the coordinates of particles and interparticle contact forces are prescribed in a file.

A smooth model is used to describe particle–particle interactions. The model is based on 'soft contact' that allows overlapping of the rigid particles to occur at contact points.[26] The relative deformation (contact overlap) is related to the contact force via the force–displacement law. The constitutive model acting at a contact consists in a stiffness model. The normal stiffness K^n is linked to the normal force F_i^n and the total normal displacement U^n (relative deformation) via equation (1). A thorough discussion of the theoretical background of PFC3D can be found in the software documentation.[25]

$$F_i^n = K^n U^n n_i \tag{1}$$

where n_i is the unit normal vector to the contact plane.

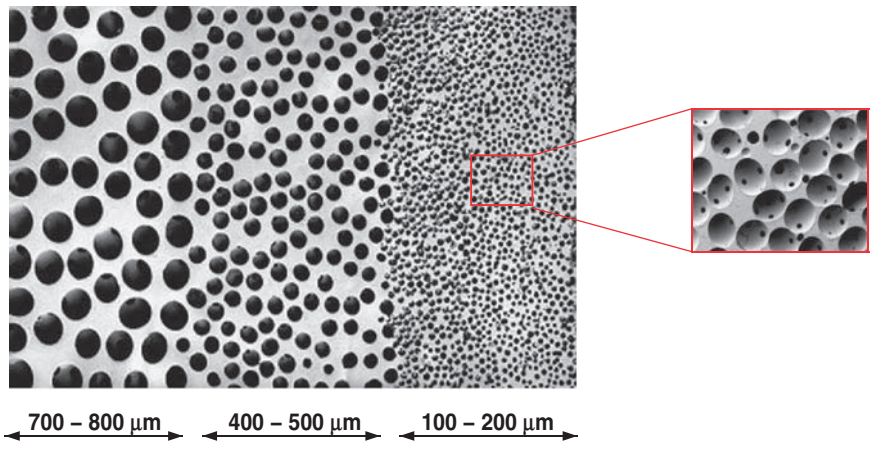

Figure 3. SEM image of the gradient pore within a sintered ceramic preform (β-tricalcium phosphate). The zoomed zone shows several openings between adjacent pores. Images reproduced from Descamps et al.[21]
SEM: scanning electron microscope.

Determination of the contact radius

The contact area of the interconnected particles is determined by calculating the radius of the contact circle. The neighboring particles are interconnected and have a circular intersection with radius noted R_c (Figure 5). Knowing the force acting at each contact point, the overlapped distance U^n and the contact radius R_c can be found using equations (2), (3) and (4).

$$U^n = (R_a + R_b) - D_{ab} \tag{2}$$

$$R_c = \sin(\theta_a)\, R_a \tag{3}$$

$$\theta_a = \arccos\left[\frac{D_{ab}^2 + R_a^2 - R_b^2}{2D_{ab}\, R_a}\right] \tag{4}$$

where D_{ab} is the distance between the sphere particles, R_a and R_b are the radii of particles A and B, respectively, and θ_a is the angle of contact.

Construction of the composite model

A procedure is implemented in conjunction between DEM and the 3D CAD SolidWorks[27] in order to build the particle skeleton, by importing a file which provides the necessary geometric data (coordinates and radius of particles). The particle skeleton has properties of aluminum alloy (Figure 6(a)). Then, a matrix with an interconnected pores network is created having the properties of alumina. This matrix represents the negative image of the particle skeleton (Figure 6(b)). Finally, the two parts are assembled creating the model of alumina/Al composites (Figure 6(c)). The particle volume fraction is systematically calculated when increasing the interconnected sizes between particles. It is defined as the volume of the particle skeleton divided by the total volume of the composite.

RVE size definition

The behavior of heterogeneous materials is often described via the concept of the RVE. It was introduced to correlate the effective or macroscopic properties with the properties of the microscopic constituents and microscopic structures of the materials.[28] Shan et al.[29] did a study on RVE for a ceramic matrix composite, they compared the results of different size RVEs with

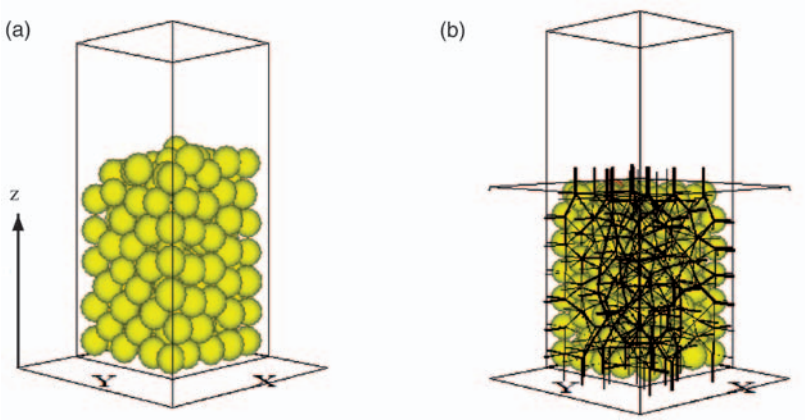

Figure 4. Snapshots of 3D granular system simulation with given particle radius distributions: 900–1000 μm: (a) generated particles by sedimentation method; and (b) compression of the system (contact forces chains are shown by a dark color).

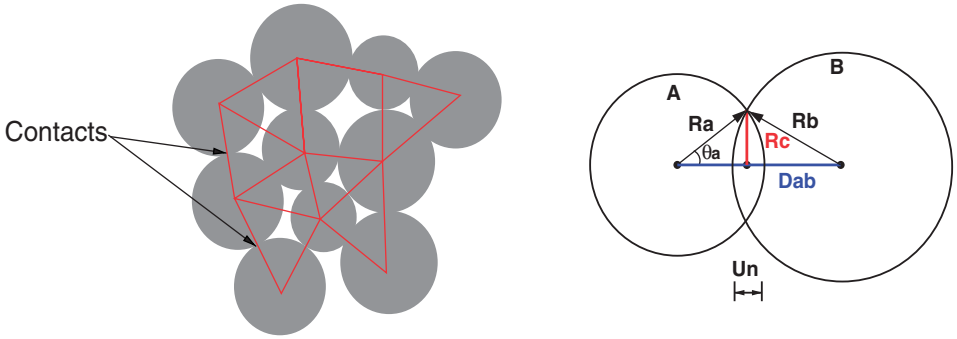

Figure 5. Definition of the interparticle contact conditions in the neighborhood of particle.

experimental results and demonstrated that the effect of the heterogeneous material can be modeled using a RVE. The general point of view is to connect the size of a representative volume of the heterogeneous material to the size of inclusions (reinforcements, grains, etc.). van Mier and van Vliet in their experiments with concrete, for example, suggest the size of the RVE to be approximately equal to at least 3–5 times,[30,31] or 7–8 times the largest inclusion or particle size.[32]

The method of calculation of the effective thermal conductivity of RVE is based on the following: If a large piece of composite is divided into equal halves, both halves will maintain the ETC of the original. If this process is repeated many times, a critical size can be reached so that under this size the ETC will not be retained. The critical size L of the RVE correlated to the particle radius is determined as the smallest size, which is representative of the overall composite. Generally, the RVE is regarded as a volume L^3 of a heterogeneous material that is sufficiently large to be statistically representative of the composite (Figure 7).[10,33]

Modeling of the thermal conductivity

The simulations of the ETC have been performed using finite element analysis (FEA) of the RVEs discretized with second order tetrahedral elements. The calculations were carried out under a steady-state heat flux, a temperature difference ΔT (°C) is imposed between two opposite surfaces whereas the remaining surfaces are assumed to be adiabatic. The total heat flux $\dot{Q}$ (W) resulting from heat conduction, out of the boundary plane, is calculated in order to evaluate the effective thermal conductivity K_{eff} (W/m.K) of the RVE given by Fourier's law in the case of 1D geometry (equation (5)). The numerical results were then compared with an analytical model equations (6) and (7) given by Maxwell[6] for predicting the thermal conductivity of materials consisting of a continuous phase containing spherical inclusions.

$$K_{eff} = \frac{\dot{Q}}{A}\frac{l}{\Delta T} \tag{5}$$

where A is the surface area and l is the thickness of the RVE.

$$\frac{K_c}{K_m} = \frac{\lambda + 2 - 2\phi(1-\lambda)}{\lambda + 2 + \phi(1-\lambda)} \tag{6}$$

and

$$\lambda = \frac{K_d}{K_m} \tag{7}$$

where K is the thermal conductivity, ϕ the volume fraction of the dispersed particles, the subscripts c, m and d

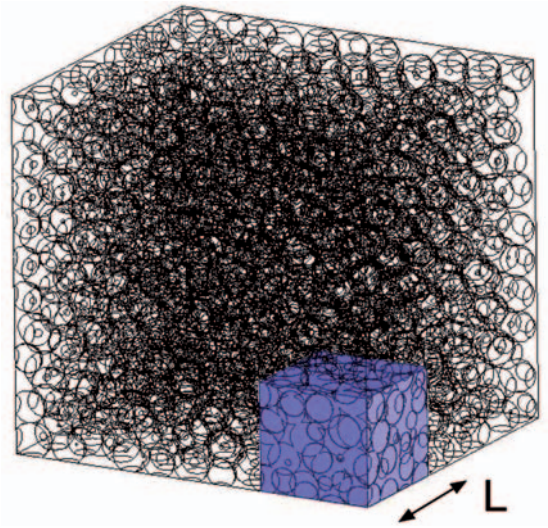

Figure 7. Perspective view of the RVE composed of 1500 interconnected particles (radius distributions ranging from 400 to 500 μm). All edges have been shaded for showing the spatial distribution of the particles.
RVE: representative volume element.

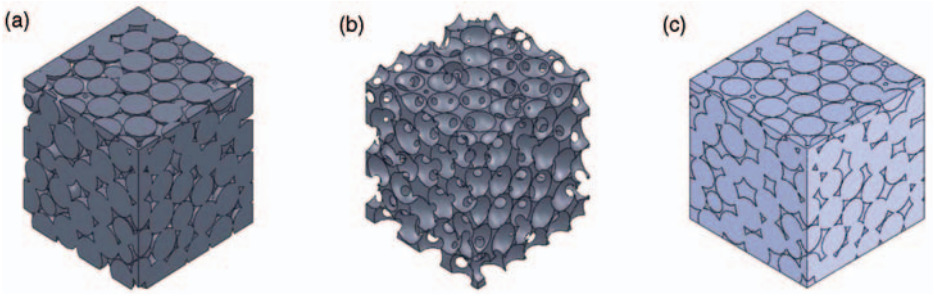

Figure 6. Model of composite obtained by assembly (side of 6 mm): (a) particle skeleton with interconnection; (b) matrix with interconnected pores network; and (c) composite.

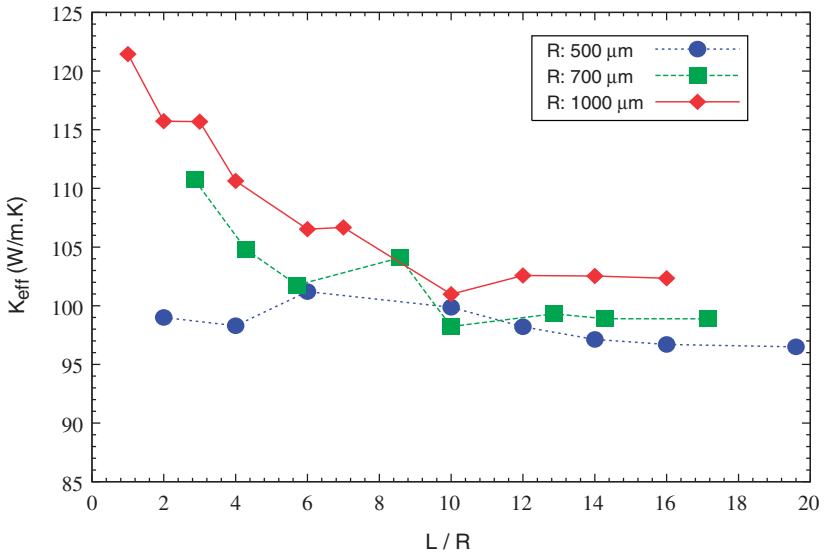

Figure 8. Monosized particles: ETC variation as function of RVE length *L*, normalized by the radius of particles, *R*. Thermal conductivity of particles = 193 W/m.K.
ETC: effective thermal conductivity; RVE: representative volume element.

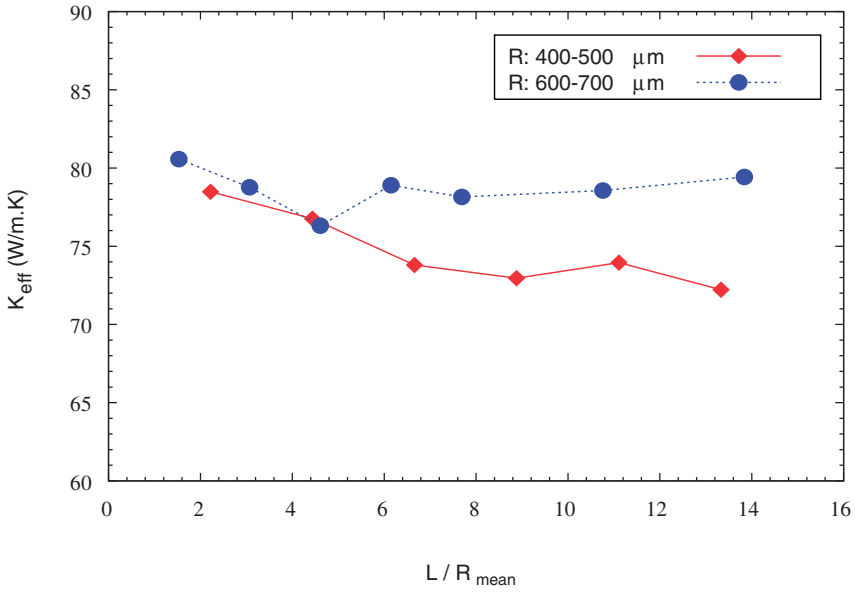

Figure 9. Polysized particles: ETC variation as function of RVE length *L*, normalized by the mean radius of particles, R_{mean}.
ETC: effective thermal conductivity; RVE: representative volume element.

refer to the composite, matrix and dispersed phase, respectively.

Results and discussion

Determination of the RVE size

The numerical studies are conducted to investigate the influence of the RVE size on the ETC of composites. Two types of composite models are generated with monosized and polysized particles. Figures 8 and 9 show the variation of the ETC with the change in the RVE size. For monosized and polysized particles, the RVE size L is normalized by radius R and mean radius R_{mean} of particles, respectively. In the case of monosized particles, the ETC monotonously decreases by increasing the RVE size until it reaches a minimum value and levels off from the ratio $L/R \geq 12$, after which it is assumed to be approximately constant, i.e. the ETC is not affected by the RVE size. In the case of

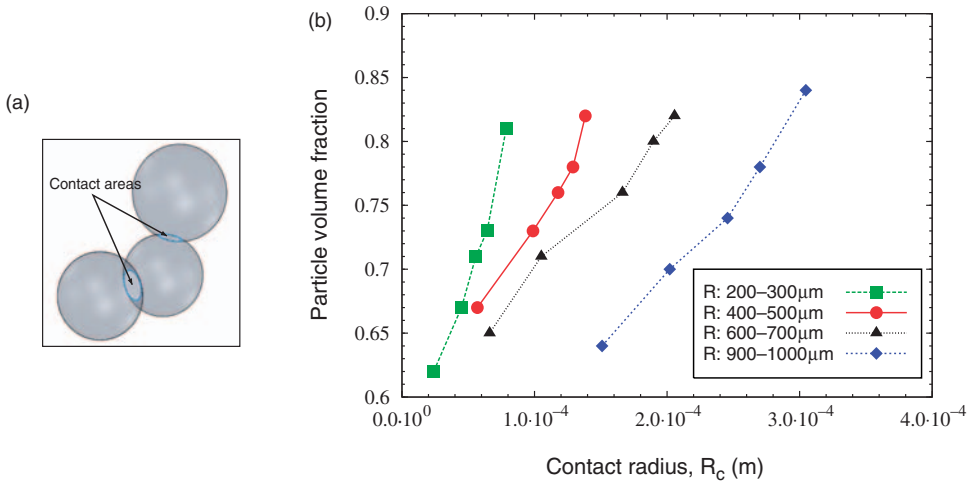

Figure 10. (a) Contact area increasing caused by the particle overlapping at contact points; and (b) dependence of the volume fraction with the increasing of the contact radius between particles.

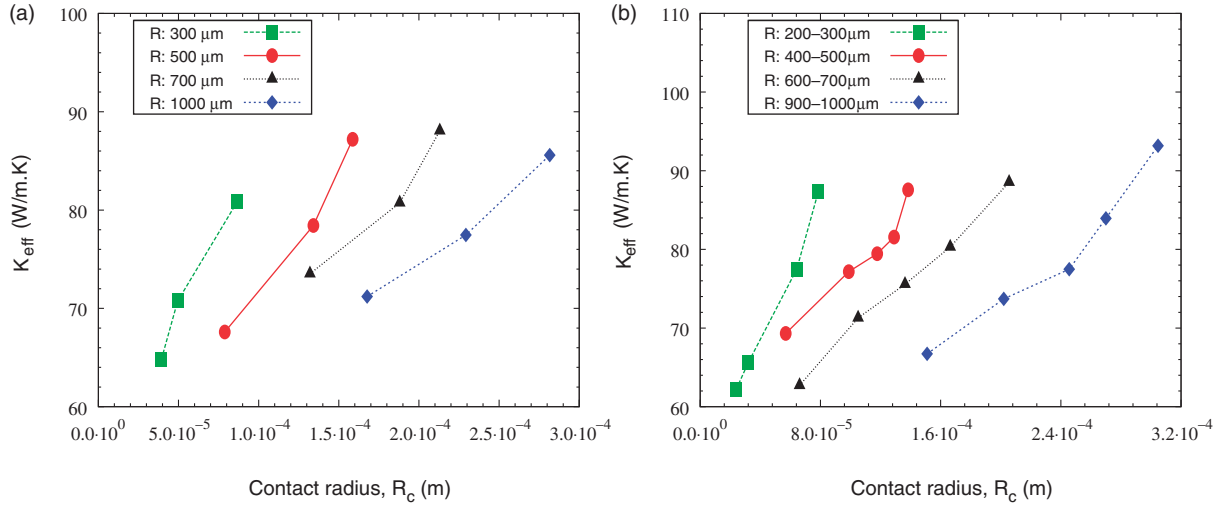

Figure 11. Variation of the ETC in alumina/Al composites with different particle radius distributions: (a) monosized and (b) polysized. Thermal conductivity of particles = 116 W/m.K.
ETC: effective thermal conductivity.

polysized particles the ETC remains nearly constant from the ratio $L/R \geq 6$. In this case, the RVE is smaller due to the polydispersity of the particles and the ETC can be evaluated on the smaller volume L^3 of RVE. From these results, the considered sizes L of RVEs for the calculation of the ETC are 12 and 6 times the mean particle radius for monosized and polysized particles, respectively.

Effect of the contact radius on the ETC

The contact area between particles (Figure 10(a)) is defined by the contact radius R_c and it was varied according to the normalized contact area with regard to the particle radius R. R_c/R is increased from 0.1 to 0.3. The large overlapped particles lead to the densification of the system with an increasing of the particle contact area, which in turn increases the volume fraction of aluminum phase within composites (Figure 10(b)). The predicted thermal conductivity is plotted in Figure 11 as a function of the contact radius. From this figure, it can be seen that when increasing the contact radius the ETC increases accordingly with enhancement in effective conductivity of composites, this indicates that the heat conduction within the composites depends on the contact conditions between particles. Figure 12 shows the comparison between the predictions of Maxwell's model and the simulations. From this figure, the thermal conductivity predicted from the numerical calculations agrees fairly well with the Maxwell's model up to a volume

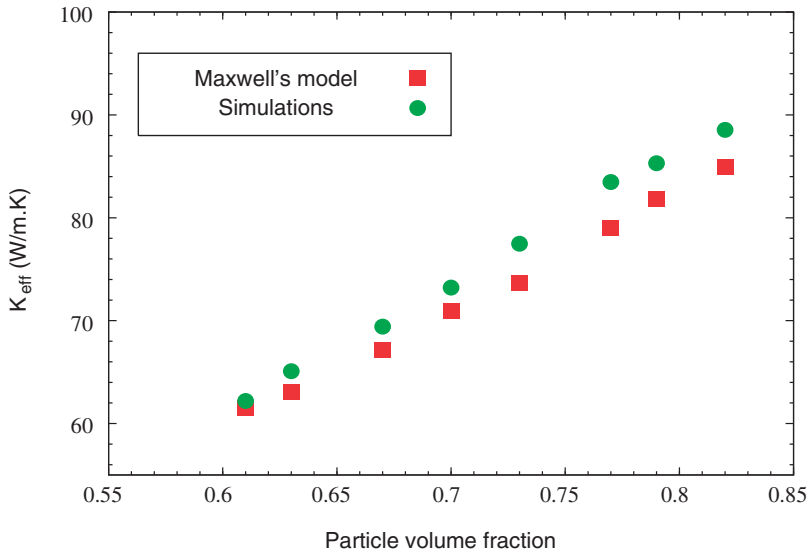

Figure 12. Comparison of Maxwell's model with simulations for predicting the ETC of alumina/Al composites. ETC: effective thermal conductivity.

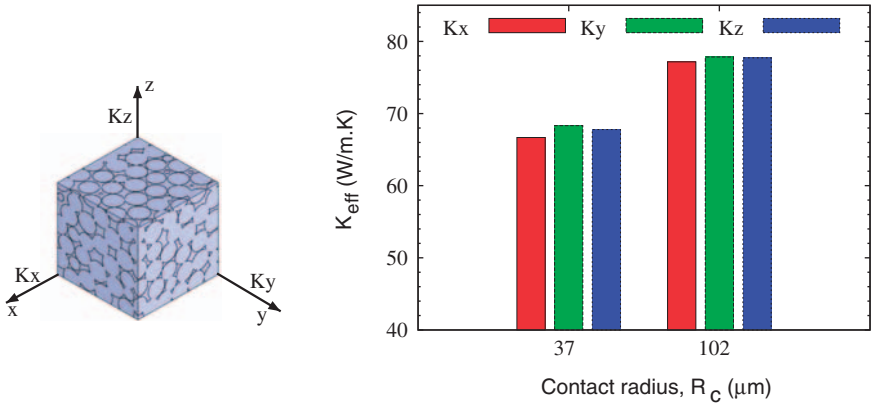

Figure 13. Predicted effective thermal conductivities *Kx*, *Ky* and *Kz* in coordinate directions *x*, *y* and z, respectively.

fraction of particles of about 0.73, from which a small discrepancy occurs between the two approaches. This comparison shows that Maxwell's model fails to predict the ETC for composites having a higher volume fraction of particles.

Isotropic thermal conductivity

In order to investigate the isotropy of the RVEs, the calculations of ETCs values *Kx*, *Ky* and *Kz* in coordinate directions *x*, *y* and *z*, respectively, have been simulated by setting a temperature gradient in the considered direction (Figure 13). The calculations are obtained for two values of contact radius. It is seen that the ETCs values are quite similar in three directions. Theses results show that our numerical approach generates an RVE with statistically homogeneous interconnection size distributions and gives an isotropic thermal conductivity.

Effect of the thermal contact resistance

Two values of Interfacial thermal resistance (*Rth*) are selected, 10^{-3} and 10^{-5} (m^2.K/W) characterize a relative degree of poor adhesion at the interface between phases of the composites. The ETCs are then calculated and compared with the case of composites without interfacial thermal resistance, as shown in Figure 14. From this figure, we can observe that the thermal conductivity is strongly sensitive to the *Rth* values and it is reduced by a factor 2 to 3 compared with the case without *Rth*. When the interconnection sizes is increased significantly so that $Rc/R_{mean} \simeq 0.3$, the distance between curves is getting smaller, i.e. the difference between the ETC for both values of *Rth* is reduced and tend to approach the thermal conductivities of composites without interfacial thermal resistance. The lower thermal conductivity is attributed to the

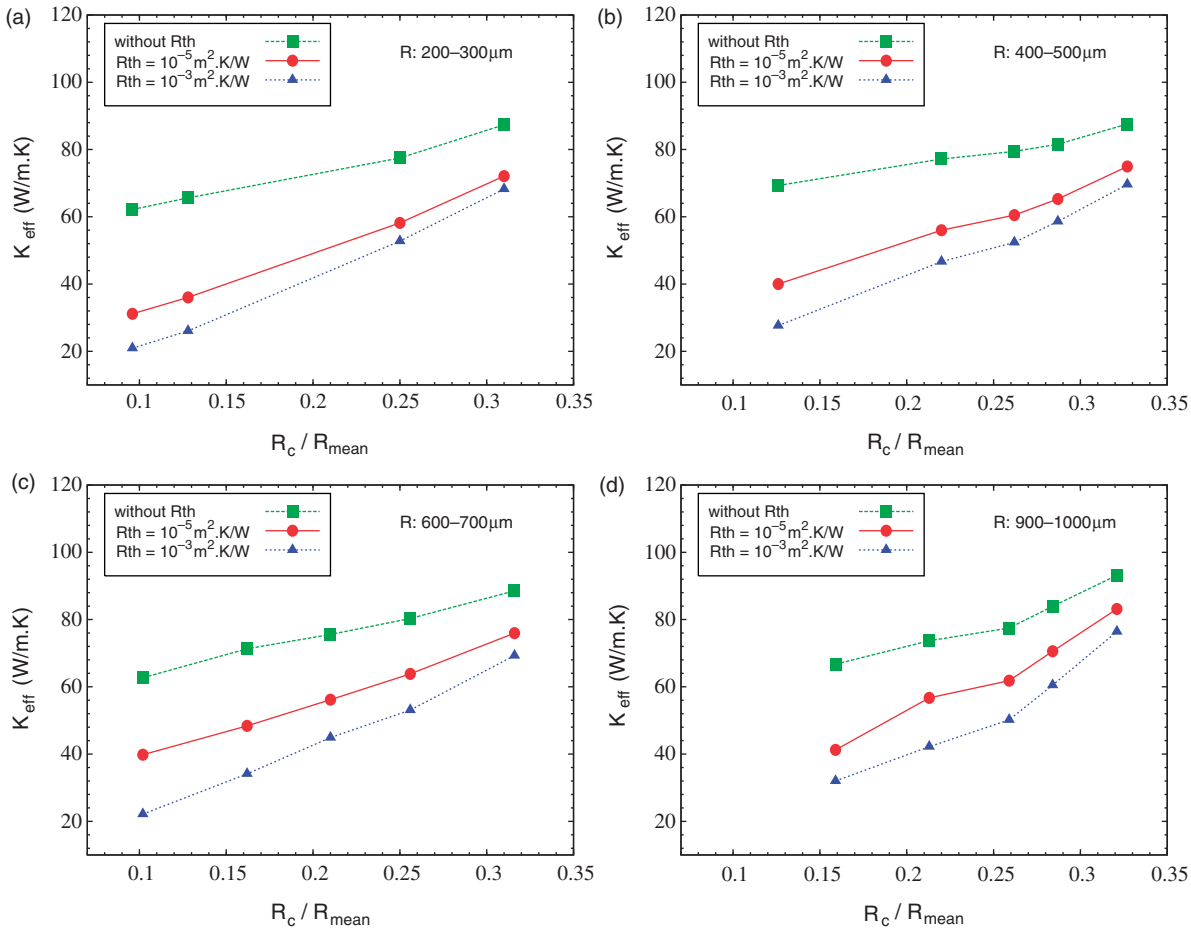

Figure 14. Variation of the effective thermal conductivities of alumina/Al composites without and with interfacial thermal resistance (*Rth*).

presence of the imperfect interfaces between phases by introducing thermal barriers which control the heat conduction within composites.

Conclusions

In this article, a numerical approach was developed in order to investigate the key parameters which control the architecture of alumina/Al composites and predicting their effective thermal conductivities. Systematic FEA of the effects of the interconnection size, particle size distributions and the imperfect interfaces between phases of composites on the effective thermal conductivity have been carried out.

The following general conclusions can be made in this work:

- Different simulations were performed in order to establish the size of RVEs for alumina/Al composites. The size of the RVE is hardly affected by the size of particle, and dependent of the granulometric distribution. The critical size L of RVE in composites with monosized particles is equal to 12 times the particle radius, whereas L is reduced with polysized particles and equal to 6 times the particle mean radius.
- The architecture of composites can be tailored through the control of the interconnection sizes. The thermal conductivity of composite is very sensitive to the presence of imperfect interfaces which can be reduced by a factor 2 to 3, but when increasing the interconnection size between particles the effect of the imperfect interface is attenuated.
- Our numerical model gives acceptable predicted thermal conductivities for RVEs with isotropic thermal properties, but further experimental research is needed to fully understand the influence of parameters controlling the architecture of composites.

Future work

In future work, the modeling approach described herein will be developed on gradient microstructure in order to

design functional alumina/Al composites with tailored properties for thermal management. The architecture of the composites will be optimized by controlling the interconnection size between particles and the gradient microstructure. To take into account the effect of the interfacial thermal resistance on the ETC, the values of *Rth* will be adjusted based on the experimental measures.

Funding

The authors would like to gratefully acknowledge the financial support of the European Union under the INTERREG IV France-Wallonie-Vlaanderen Program PRISTIMAT (No. FW 1.1.19).

Acknowledgements

The authors thank LMPCA (UVHC), SIRRIS, and INISMA-CRIBC (members of EMRA) for supplying the experimental data about the manufacturing process.

Conflicts of interest

None declared.

References

1. Suresh S and Mortensen A. *Fundamentals of functionally graded material*. London: Institute of Materials, 1998.
2. Gandra J, Miranda R, Vilaça P, et al. Functionally graded materials produced by friction stir processing. *J Mater Process Technol* 2011; 211(11): 1659–1668.
3. Shin KH and Dutta D. Constructive representation of heterogeneous objects. *ASME J Comput Inform Sci Eng* 2001; 1(3): 205–217.
4. Anné G, Vanmeensel K, Vleugels J, et al. Electrophoretic deposition as a novel near net shaping technique for functionally graded biomaterials. *Key Eng Mater* 2006; 314: 213–218.
5. Shin KH, Natu H, Dutta D, et al. A method for the design and fabrication of heterogeneous objects. *Mater Design* 2003; 24(5): 339–353.
6. Maxwell JC. *Electricity and magnetism*. Oxford: Clarendon Press Oxford, 1873.
7. Lewis T and Nielsen LE. Dynamic mechanical properties of particulate-filled composite. *J Appl Polym Sci* 1970; 14(16): 1449–1471.
8. Cunningham ME and Peddicord KL. Heat conduction in spheres packed in an infinite regular cubical array. *Int J Heat Mass Transfer* 1981; 24(7): 1081–1088.
9. Hadley G. Thermal conductivity of packed metal powders. *Int J Heat Mass Transfer* 1986; 29(6): 909–920.
10. Torquato S. Morphology and effective properties of disordered heterogeneous media. *Int J Solid Struct* 1998; 35: 2385–2406.
11. Kumar S, Bhoopal R, Sharma P, et al. Non-linear effect of volume fraction of inclusions on the effective thermal conductivity of composite materials: a modified maxwell model. *Open J Compos Mater* 2011; 1: 10–18.
12. Hyun S and Torquato S. Designing composite microstructures with targeted properties. *J Mater Res* 2001; 16(1): 280–285.
13. Hale DK. The physical properties of composite materials. *J Mater Sci* 1976; 11: 2105–2141.
14. Hasselman DPH. Effective Thermal conductivity of composites with interfacial thermal barrier resistance. *J Compos Mater* 1987; 21: 508–516.
15. Benveniste Y. Effective thermal conductivity of composites with a thermal contact resistance between the constituents: nondilute case. *J Appl Phys* 1987; 61: 2840–2841.
16. Geiger AL. Effect of reinforcement particle size on the thermal conductivity of a particulate silicon carbide-reinforced aluminiummatrix composite. *J Mater Sci Lett* 1993; 12: 420–423.
17. Ning QG and Chou TW. Closed-form solutions of the in-plane effective thermal conductivities of woven-fabric composites. *Compos Sci Technol* 1995; 55(1): 41–48.
18. Nan CW, Birringer R, Clarke DR, et al. Effective thermal conductivity of particulate composites with interfacial thermal resistance. *J Appl Phys* 1997; 81: 6692–6699.
19. Xu Y, Tanaka Y, Goto M, et al. Thermal conductivity of SiC fine particles reinforced Al alloy matrix composite with dispersed particle size. *J Appl Phys* 2004; 95(2): 722–726.
20. Andrianov IV, Bolshakov VI, Danishevs'kyy VV, et al. Asymptotic simulation of imperfect bonding in periodic fibre-reinforced composite materials under axial shear. *Int J Mech Sci* 2007; 49(12): 1344–1354.
21. Descamps M, Duhoo T, Monchau F, et al. Manufacture of macroporous β-tricalcium phosphate bioceramics. *J Eur Ceram Soc* 2008; 28: 149–157.
22. Delannay F, Froyen L, Deruyttere A, et al. The wetting of solids by molten metals and its relation to the preparation of metal-matrix composites. *J Mater Sci* 1987; 22: 1–16.
23. Kennedy A and Asavavisithchai S. Effect of ceramic particle additions on foam expansion and stability in compacted Al-TiH_2powder precursors. *Adv Eng Mater* 2004; 6(6): 400–402.
24. Sangghaleh A and Halali M. Effect of magnesium addition on the wetting of alumina by aluminium. *Appl Surf Sci* 2009; 255(19): 8202–8206.
25. Itasca Consulting Group Inc. PFC3D (particle flow code in 3 dimensions). V 4.0, MN: ICG, 2008.
26. Cundall PA and Strack ODL. A discrete numerical model for granular assemblies. *Géotechnique* 1979; 29: 47–65.
27. Dassault systémes. Solidworks: 3d mechanical design and 3d CAD software, 2011. http://www.solidworks.com/
28. Gitman IM, Askes H and Sluys LJ. Representative volume: existence and size determination. *Eng Fract Mech* 2007; 74: 2518–2534.
29. Shan Z and Gokhale A. Representative volume element for non-uniform microstructure. *Comput Mater Sci* 2002; 24: 361–379.

30. van Mier JGM. *Fracture processes of concrete*. Boca Raton: CRC Press Inc., 1997.
31. van Vliet M. *Size effect in tensile fracture of concrete and rock*. PhD thesis, Delft University of Technology, The Netherlands, 2000.
32. van Mier JGM. Microstructural effects on fracture scaling in concrete, rock and ice. In: *IUTAM Symposium on Scaling Laws in Ice Mechanics and Ice Dynamics* (eds Dempsey JP and Shen HH), 2001, pp. 171–182. Dordrecht/Boston/London: Kluwer Academic Publishers.
33. Kanit T, Forest S, et al. Determination of the size of the representative volume element for random composites: statistical and numerical approach. *Int J Solid Struct* 2003; 40: 3647–3679.

INTERNATIONAL JOURNAL OF REFRIGERATION 36 (2013) 1319–1326

Available online at www.sciencedirect.com

SciVerse ScienceDirect

journal homepage: www.elsevier.com/locate/ijrefrig

Modeling heat and mass transfer during vacuum freezing of puree droplet

C. Cogné [a,*], P.U. Nguyen [b], J.L. Lanoisellé [b], E. Van Hecke [b], D. Clausse [b]

[a] Laboratoire des Technologies Innovantes (EA 3899), IUT de l'Aisne, 48 rue d'Ostende, 02100 Saint Quentin, France
[b] Laboratoire Transformations Intégrées de la Matière Renouvelable (EA 4297), Centre de Recherches de Royallieu, BP 20.529, 60205 Compiègne, France

ARTICLE INFO

Article history:
Received 15 September 2011
Received in revised form
31 January 2013
Accepted 6 February 2013
Available online 16 February 2013

Keywords:
Freezing
Vacuum
Modeling
Heat transfer
Mass transfer
Puree

ABSTRACT

A numerical simulation using COMSOL®, a commercial software, has been developed to model heat and mass transfer during vacuum freezing by evaporation of a single puree droplet. The simulations predict local water content, temperature and mass losses during the process. This theoretical model, based on the numerical resolution of heat and mass diffusion equations, includes both the process conditions and the thermophysical properties of the puree. Experimental temperature profiles and dry matter content measurements were used to validate the model and assess its accuracy. From the model, it has been shown that the main parameters that governed the transfer are the droplet diameter, the ambient pressure and the initial temperature.

Modélisation du transfert de chaleur et de masse lors de la congélation sous vide d'une gouttelette de purée

Mots clés : congélation ; vide ; modélisation ; transfert de chaleur ; transfert de masse ; purée

1. Introduction

This current work is dealing with the freezing obtained by a vacuum process of a puree mainly composed of water (92%) and various solid materials. In food technology, vacuum process for cooling is often used when a fast temperature decrease of product is required to comply with safety and quality attributes of the sample (McDonald and Sun, 2000; Landfeld et al., 2002; Sun and Wang, 2004). Its principle consists in removing the evaporating latent heat of water, which implies a fast decrease of the product temperature. To maintain the evaporation process, a continuous pumping inside the equipment is applied. When the pressure of gaseous phase is reduced, the evaporation of the water phase occurs, and the fraction of solid increases, since latent heat for the freezing is supplied by the latent heat of the water

* *Corresponding author*. Tel.: +33 (0)4 72 43 18 62; fax: +33 (0)4 72 43 16 82.
E-mail address: claudia.cogne@univ-lyon1.fr (C. Cogné).
0140-7007/$ – see front matter © 2013 Elsevier Ltd and IIR. All rights reserved.
http://dx.doi.org/10.1016/j.ijrefrig.2013.02.003

Nomenclature

A	constant in Pham's model, J kg^{-1}
B	constant in Pham's model, J K kg^{-1}
c	moisture concentration, kg m^{-3}
C_P	specific heat, J kg^{-1} K^{-1}
D	water mass diffusion coefficient, m^2 s^{-1}
H	enthalpy, J kg^{-1}
H_0	enthalpy at the ice melting point, J kg^{-1}
K	water vapor mass transfer coefficient s m^{-1}
L_v	latent heat of evaporation or sublimation of water, J kg^{-1}
P	pressure, Pa
r	spherical coordinate, m
t	time, s
T	temperature, °C
T_f	ice melting point, °C

Greek letters

λ	thermal conductivity, W m^{-1} K^{-1}
ρ	density, kg m^{-3}

Exponents

LG	liquid/gas equilibrium
SG	solid/gas equilibrium

Subscripts

f	frozen
s	surface
sat	saturated
tot	total
u	unfrozen
w	water vapor
0	initial conditions

evaporation. From the practical point of view, the liquid puree is sprayed at the top of a vacuum tower. At the triple point of the product, gas-liquid-solid three phase equilibrium is achieved. Mass loss caused by vacuum cooling is not a significant problem, it can be carefully controlled by adjusting the initial water content of the product (Maureaux et al., 2008).

Accurate predictions of the temperature and the moisture fields are important for the design of the vacuum equipment and for the optimization of the operating parameters of the process. Models in vacuum cooling are widely used to simulate the fast temperature decrease of the food. The modeling of heat treatments are generally based on the transient heat and mass transfer and are solved by using finite elements methods (Wang and Sun, 2002) or computerized fluid dynamics models for porous foods (Sun and Hu, 2003). However, for the evaporation-boiling phenomena reported in the previous studies, the thermal properties are usually assumed constant with the temperature, hypothesis that could be acceptable for cooling process but not for freezing. Concerning vacuum freezing processes, the modeling and simulation are more complex because adequate models have to take account of vapor generation, evaporation, water phase change during freezing. Therefore, only few studies are focused on this subject. Close to our study, Satoh et al. (2002) and also Shin et al. (2000) presented a detailed description of the freezing of a water droplet due to evaporation and developed a simplified model solved by analytical resolution.

This article is focused on the thermal characterization of the puree, the development of a model to simulate the vacuum freezing, the model validation and a sensitivity study to investigate the main parameters governing this freezing process (Nguyen, 2010).

2. Materials and methods

2.1. Puree preparation

The product studied in this article is composed mainly of carrot (95%) and rice flour which represent 8.8% ± 0.2 of dry matter. It corresponds to a composition of 0.9% proteins, 3.9% carbohydrates, 0.3% fat, 1.5% minerals, 2.4% fiber and 95% water. A second kind of puree has been studied, namely cooked puree with carrot (86%) and cream (4.5%) which represent 12.1% ± 0.6 of dry matter. Both purees concern commercial products that have been thaw at ambient temperature during 24 h. Then, the puree was slowly mixed to obtain a homogeneous product.

2.2. Dry matter content

The dry matter is estimated by drying a sample at 103 °C during 24 h. The measure is done before and after the freezing step. The mass difference between the two measures provides the water loss during the process.

2.3. Enthalpy–temperature relationship

Differential scanning calorimetry (DSC) was used to determine the enthalpy of the puree as a function of temperature. A sample mass between 10 and 20 mg was sealed in an aluminum cell and was weighed to a high level of precision (±0.5 mg). The commercial frozen puree was thawed at 4 °C, 24 h before the measurement. To determine temperature–enthalpy relationship, the samples were cooled to −40 °C and then warmed up progressively up to 20 °C at a heating rate equal to 2 °C min^{-1} with a stabilization period of 400 s for each magnitude of 4 °C (Clausse et al., 2004).

The experimental DSC signal is a heat flow which is proportional to the partial derivative of enthalpy versus time. The total enthalpy of the puree was calculated by integration of the experimental DSC signal after subtraction of a "blank" signal (empty cell in the same conditions). It includes two components, namely the sensible heat and the latent heat of fusion in the freezing temperature range. In the current study, the total enthalpy was preferred to the heat capacity for numerical stability reasons since the heat capacity function presents a higher discontinuity at the initial freezing times. An arbitrary zero enthalpy reference at −40 °C was chosen. Pham's model has been used to model the puree specific

enthalpy versus temperature (Pham, 1996). This model is based on the integration of Schwartzberg equation. It is expressed by two equations (Eqs. (1) and (2)) as follows :

$$T \leq T_f : H = A + C_{pf}T - B/T \quad (1)$$

$$T > T_f : H = H_0 + C_{pu}T \quad (2)$$

where C_{pf} represents the specific heat of frozen sample while C_{pu} is the specific enthalpy of the unfrozen sample. A and B represent arbitrary parameters related to the reference point for enthalpy. H_0 is the mass enthalpy at the freezing point T_f and T in °C is the sample temperature. The parameters A, B, H_0, C_{pf}, C_{pu} and T_f have been evaluated successfully by fitting our experimental data as shown in Fig. 1. The obtained values listed in Table 1 are close to literature values found for vegetables (Amarante, 2004) and are compared to asparagus values that contain the same water amount (Amos et al., 2008).

2.4. Thermal conductivity determination

The hot wire probe method was used to measure the thermal conductivity of the puree. The thermal conductivity identification method was based on a simplified solution of the heat equation for an infinite linear heat source immersed in a semi-infinite cylindrical medium. Practically, the sample was thawed from commercial frozen puree during 24 h at positive temperature about 4 °C. Then, the sample was introduced in the measuring cell and rapidly frozen at the chosen temperature. For a short time period, the sample was submitted to a constant heating power around 0.4 W, precisely controlled for each measurement run. The hot wire heating power and the probe temperature rise were the only data required to calculate the thermal conductivity (Cogné et al., 2003). Fig. 2 illustrates the experimental data obtained with our puree samples depending on the temperature and compared with De Vries model (Cogné et al., 2003). This model which is an extension of Maxwell equation, requires the evolution of ice obtained by DSC and introduces two shape factors to take into account the potential nonsphericity of the ice crystals (Cogné et al., 2003). As explained in this previous work, the values of the shape factor (supposed rotated ellipsoids) leads to spherical particles.

The experimental results have shown that the temperature strongly affects the apparent thermal conductivity of the puree due to its strong influence on the ice fraction: the thermal conductivity of pure ice is about four times higher than the liquid water one (Lide, 2008–2009). Except in the transition phase, the model of De Vries can predict quite good the thermal conductivity of the product.

Concerning the repeatability of the experiments as mentioned in Fig. 2 by the error bars, only a low deviation between the three runs was observed, except around the freezing point. Indeed, in the temperature range [−5/0 °C], it was difficult to obtain precise and reproducible temperature profiles, due to some possible local thawing phenomena caused by the heating flux at the hot wire/food interface. The experimental measures around the freezing point could also be affected by the amount of salt.

Table 1 – Pham's parameters for carrot (fitted on experimental data) and for asparagus (Amos et al., 2008).

Parameter	Carrot	Asparagus	Unity
C_{pf}	1720	2400	J kg^{-1} K^{-1}
C_{pu}	3420	3880	J kg^{-1} K^{-1}
A	61,230	76,400	J kg^{-1}
B	302,440	303,000	J K kg^{-1}
H_0	377,260	368,000	J kg^{-1}
T_f	−0.92	−1.05	°C

2.5. Laboratory vacuum cell

In a first time, an experimental apparatus in static conditions has been set-up in our laboratory to study the feasibility, to quantify freezing times and to secure the scale-up of an industrial process. The experimental cell including a vacuum pump, a vacuum regulator and a vacuum flask has been set-up in our laboratory (Fig. 3). The droplet is formed with a pipet and the diameter is controlled by weighting the sample; the density has been previously measured with a pycnometer (970 kg m^{-3}). The sample is initially introduced into the vacuum flask at a constant temperature of 24 °C. Then the ambient pressure in the flask was set to a fixed value in the range of 200 Pa. The air/water vapor in the flask was suddenly evacuated by opening the regulator valve and just a few seconds were required to reach the set-point. During the experiment, the pressure in the flask and the temperature at the center of the droplet were continuously recorded thanks to

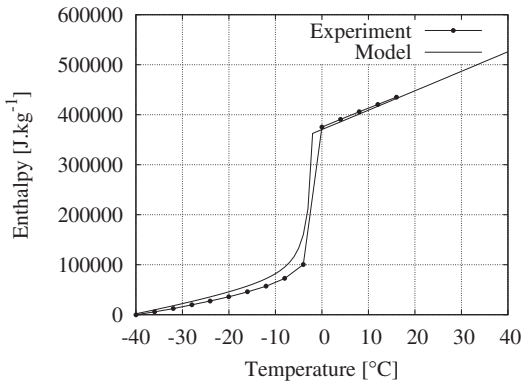

Fig. 1 – Comparison between specific enthalpy experimental data and modeling for puree.

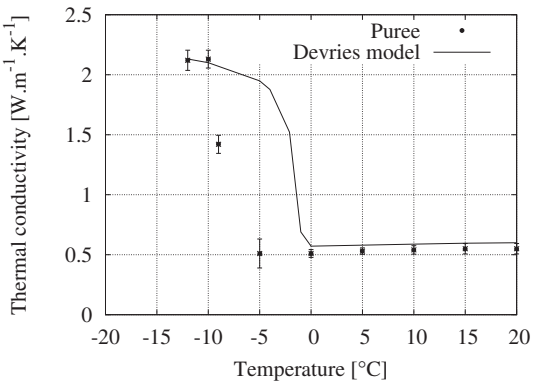

Fig. 2 – Thermal conductivity of puree versus De Vries model. Error bars are standard deviations from 3 replicates.

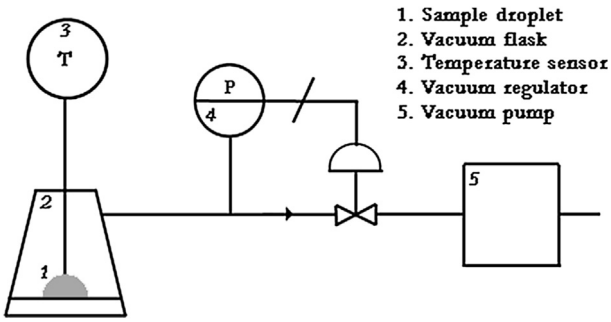

Fig. 3 – Scheme of the experimental apparatus.

the regulator gauge and a thermocouple (type K) of 1 mm in diameter carefully placed at the center of the droplet. Each run has been replicated two times but the precision (±1 °C) is limited by the experimental configuration (thermocouple position, geometry of the sample), the stability to set the pressure and the acquisition of temperature. The puree sample, assumed perfectly half spherical, was insulated on its circular base with a film plastic placed between the droplet and glass wool. This insulator was especially used to limit heat loss to the bottom of the glass flask. With this laboratory cell, investigations on droplet diameters (7.3 mm; 10.5 mm; 12.5 mm) were carried out at a constant pressure (200 Pa).

2.6. *Industrial vacuum process unit*

In a second time, a freezing process with a flow of 50 kg h^{-1} has been developed in dynamical conditions. A new quick-freezing process especially suitable for viscous liquid foods has been proposed and successfully experimented at large scale recently (Maureaux et al., 2008). This consists of spraying the product into a chamber (diameter: 0.8 m; height: 3 m) where a sufficient vacuum is maintained. The subsequent sudden water vaporization due to pressure drop results in a rapid temperature decrease inducing a quasi instantaneous ice nucleation. The vacuum is then broken in a sas and products are quickly removed for analysis of dry matter. A digital video camera is used to capture images of the spraying cone. Thanks to theses images, sprayed droplets are visualized to estimate the size distribution. Due to the difficulty to equip with sensor this industrial vacuum unit, no measure of temperature could have been realized in this unit except the initial temperature just before the spraying. With this industrial unit, investigations on ambient pressures (400 Pa; 500 Pa; 600 Pa) were carried out at a droplet average diameter of 1 mm.

3. Model development

The estimation of food freezing times in the vacuum process is a transient problem involving heat and mass transfer, phase change, and temperature dependent thermophysical properties. A theoretical model using the commercial software COMSOL has been developed to simulate the freezing kinetics of a puree droplet. COMSOL software is a finite element solver used for various physics and engineering applications, especially those involving coupled or multiphysics phenomena.

During the cooling and the freezing processes, water evaporation takes place at the surface of the droplet which generates an internal heat flux by conduction from the droplet centre to its surface due to the heat sink resulting from the latent heat of phase change (vaporisation; freezing). To simulate simultaneous heat and moisture transfer in the droplet, the following assumptions were made:

- the geometry of the puree droplet was perfectly half spherical;
- water was evaporated only at the surface of the droplet;
- there was no shrinkage, the droplet diameter was constant;
- convection and radiation with ambient atmosphere were negligible;
- thermal and mass transfers were radial from the center to the surface of the droplet;
- mass transfer concerned only single species (i.e., only water);
- water supercooling was not taken into account in the model.
- thermodynamical equilibrium exists at the liquid surface between the cooled liquid and its vapor. Further, the surface temperature of the liquid is given by its equilibrium value corresponding to the water vapor pressure of the saturated vapor.

Based on the above assumptions, the freezing process by vacuum was modeled with a heat and mass diffusion model. The model equations were coupled through the thermophysical properties of the product which depend on its moisture concentration and on its temperature.

3.1. *Mass transfer model*

The general mass transfer equation is based on Fick's second law for the internal diffusion of water during freezing (Eq. (3)) (Hamdami et al., 2004; Campanone et al., 2001):

$$\frac{\partial c}{\partial t} = \nabla(D\nabla c) \tag{3}$$

where c is defined as the mass moisture concentration in the puree is he mass of water per volume unit of puree. D, the water mass diffusion coefficient depending on the temperature according to an Arrhenius's law, has been fitted on literature data for similar products (Landfeld et al., 2002; Hamdami et al., 2004; Houska et al., 1996). The vacuum pump removes gases from the vacuum chamber and when the water vapor pressure reaches the saturated vapor pressure corresponding to the temperature T, the water in the product boils. The water vapor pressure difference between the droplet surface and the surrounding atmosphere of the droplet causes some water evaporation. This evaporated water flow is assumed proportional to an overall mass transfer coefficient, noted K, and the water partial pressure difference between the droplet surface and the surrounding (Eq. (4)). This assumption is based on a thermodynamic equilibrium between the vapor and the liquid/solid phase at the surface of the droplet (Landfeld et al., 2002; Hamdami et al., 2004; Houska et al., 1996):

$$-D\nabla c = K(P_{sat}(T_s) - P_w) \tag{4}$$

The water partial pressure P_w corresponds to the chamber pressure, assumed equal to the total pressure experimentally measured. The saturation pressure P_{sat} is related to the surface temperature. All along the freezing temperature range, we assumed a gas/liquid equilibrium at the surface of the droplet. The saturation pressure was also estimated by the following relation (Eq. (5)) of Houska et al. (1996):

$$P_{sat}^{LG} = \exp\left(23.209 - \frac{3816.44}{T_s - 46.44}\right) \quad (5)$$

If the surface temperature is lower than the initial freezing point, the saturation pressure is related to a solid/gas equilibrium estimated by the following equation (Eq. (6)), valid for the pure ice/water vapor system (Perrot, 2006):

$$P_{sat}^{SG} = \left(3.66\cdot10^{12} - 1.31\cdot10^{8}\cdot T_s - 3.38\cdot10^{6}\cdot T_s^2\right)\exp\left(\frac{-6150}{T_s}\right) \quad (6)$$

In the equations (Eq. (5)) and (Eq. (6)), the saturation pressure P_{sat} is given in Pa and the surface temperature T_s in K.

The overall mass transfer coefficient $K = 10^{-4}$s m^{-1} has been fitted on experimental results based on the freezing of water droplet due to evaporation (Satoh et al., 2002). Similar value has been used by He and Li (2003) to simulate the vacuum cooling of spherical foods.

3.2. Heat transfer model

The governing form of the transient heat transfer equation is written as follows (Eq. (7)):

$$\varrho\frac{dH}{dT}\frac{\partial T}{\partial t} = \nabla(\lambda\nabla T) \quad (7)$$

where ρ represents the density, dH/dT is the derivative form of the heat capacity issued from the experimental results (DSC), T the temperature, t the time. The phase change is taken into account by the specific heat that includes both the sensible heat and the latent heat of fusion. The thermal conductivity and the enthalpy data, depending on the temperature, involve a non-linear problem that was resolved using the iterative Newton–Raphson technique. Initially, the puree temperature was assumed to be homogenous and equal to the atomization temperature at the inner of the vacuum tower. Concerning the boundaries conditions, we neglected the external heat transfer resistance due to non significant thermal gradient inside the boundary layer. Third kind limit conditions were also applied, by considering the heat flow continuity on the surface, namely:

$$\lambda\nabla T = L_v K(P_{sat}(T_s) - P_{tot}) \quad (8)$$

If $T \geq T_f$, L_v is the latent heat of water vaporization and P_{sat} is given by the Eq. (5). Else, if $T < T_f$, L_v represents the water latent sublimation heat and P_{sat} is estimated by the relation (Eq. (6)).

3.3. Resolution

The model was applied to simulate the freezing of a puree droplet. The puree contains about 92% water and initially the system is at uniform temperature T_0. Due to the axisymmetry of the droplet, only one half of the planar section was selected for running the simulations. The representative geometry was discretized in 647 triangular elements. As represented in Fig. 4,

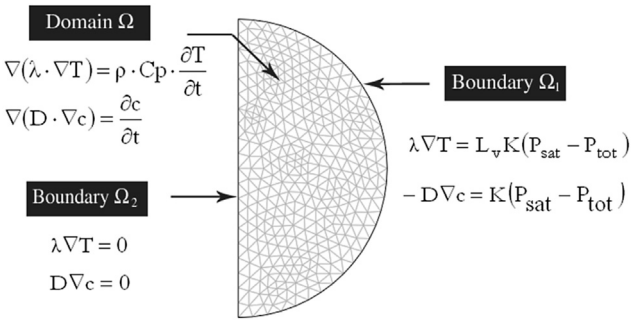

Fig. 4 – Scheme of the meshed geometry used for the modeling.

the boundary Ω_1 represented the surface of the droplet, while the boundary Ω_2 represented the symmetry lines inside the droplet which has a null heat and mass transfer flow conditions. On the domain Ω, diffusive mass and heat transfer equations (Eq. (3) and Eq. (7)) were applied.

Then, the resulting system of nonlinear partial differential equations was solved numerically using the commercial software COMSOL by the finite element method. The finite element method has proved to be powerful in solving differential equations involving irregular geometry, variable boundary conditions, non-homogenous and anisotropic materials in food industry (Puri and Anantheswaran, 1993).

The time-dependent model shows the temperature decrease during the cooling and freezing process. Simulations also model the moisture in the puree droplet. Therefore, the water mass loss during the evaporation is computed from the total change in mass by a volume integration of the water content.

4. Results and discussions

4.1. Experimental validation of thermal transfer

To validate the above thermal simulations, the numerical results have been compared to experimental data from the laboratory vacuum cell. Three samples with different mass were frozen in the laboratory vacuum apparatus presented in Part 2.5. Concerning the modeling, a half spherical sample was taken into account, the diameter depending on the mass sample (100 mg, 300 mg and 500 mg of puree corresponding to a droplet diameter respectively of 7.3 mm, 10.5 mm and 12.5 mm). The experimental pressure has been directly integrated to the model. The initial temperature is taken from the experimental value measured by a thermocouple at the center of the droplet. The experimental temperature and the predicted values are presented in Fig. 5.

Although the model is subject to considerable limitations and data to experimental difficulties, the thermal behaviors are quite similar and the modeling values match the predicted results quite well for the three runs, especially concerning the total freezing times. Profiles have shown both a rapid cooling of the droplet, it can be achieved in under within less than

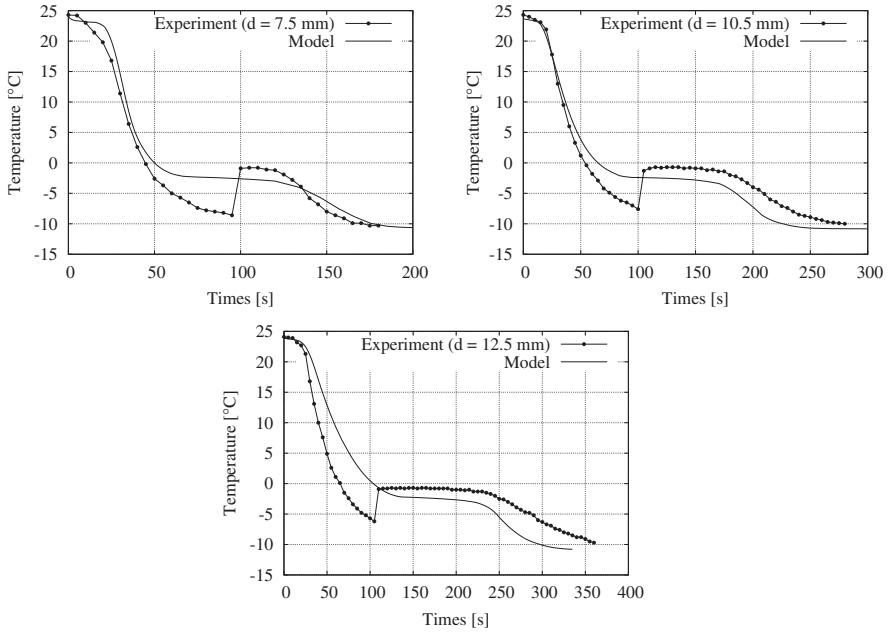

Fig. 5 – Comparison of the predicted center temperature with experimental results for three droplet diameter (7.3 mm; 10.5 mm; 12.5 mm). Pressure setpoint: 200 Pa.

1 min, and the freezing plateau where ice crystals grow. Then, the ice droplet was cooled to a negative temperature. In this temperature range, mass transfer concerns sublimation and explains the final low temperature decrease. We note a larger discrepancy between numerical and experimental data in cooling behavior before freezing for important diameter. It could be explained by the difficulty to stabilize the pressure at the setpoint due to a more important water evaporation flow rate. The nucleation phenomenon – a stochastic process – was not taken in account by our model even if the experimental thermograms show quite clearly its presence.

We noted a repeatability of nucleation temperatures in the range between −5 °C and −10 °C on the experimental profiles corresponding approximatively to the same nucleation time (100 s). In a first time, the agreement between the predicted and the experimental kinetics allows us to validate the model hypothesis and has ensured us a quite good accuracy even if we are aware of the fact that this model is quite simplified in the nucleation range. In a second time, to face this challenge and improve the efficiency of our model, the next steps of this work will be to implement the supercooling as mentioned in the literature (Pham, 2006).

4.2. *Experimental validation of water loss*

In this part, experimental and predicted data of mass loss have been compared for three different pressures (Fig. 6). Experimentally, the mass loss has been estimated by weighing the dry content of the sample before and after the vacuum freezing in the industrial process unit presented in Part 2.6. Numerically, the mass loss was estimated by integration of the amount water in the whole droplet at the beginning and at the end of the freezing at 2500 s. The deviation is quite important but becomes smaller for low pressures. We note that the model predictions are lower than the experimental results, except at 400 Pa. The deviation of the final total mass loss between the measured and the predicted data may be explained by two reasons: firstly, the difficulty to realize the experiments and ensure their reproducibility; secondly, during vacuum freezing process, mass loss comes from water evaporation at the surface of the droplet, but probably also from volume evaporation at the pores of the sample, phenomena which is not taken into account by the model.

4.3. *Parameter sensitivity study*

This part is focused on the exploitation of the mass/thermal model. This model has been extrapolated from the laboratory

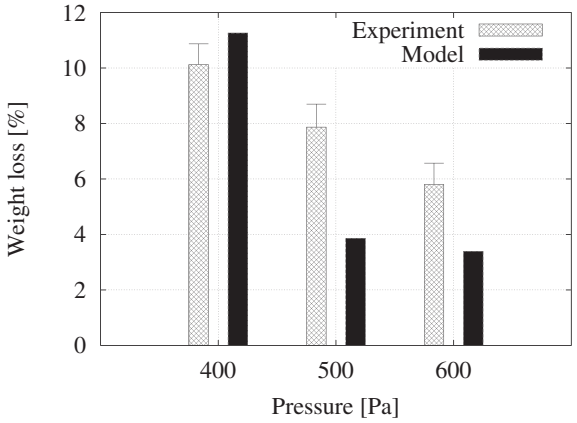

Fig. 6 – Comparison of the mass loss with the experimental data; droplet diameter: 1 mm; initial droplet temperature: 20 °C.

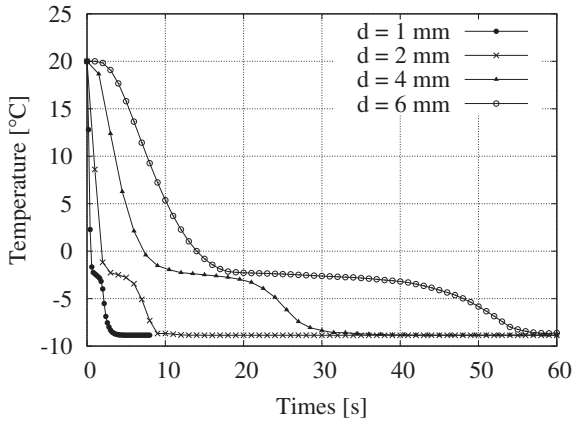

Fig. 7 – Influence of droplet diameter; pressure setpoint: 300 Pa; initial droplet temperature: 20 °C.

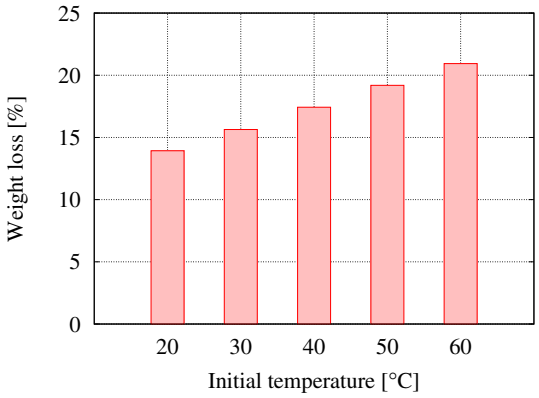

Fig. 9 – Predicted mass loss versus initial temperature; droplet diameter: 1 mm; pressure setpoint: 300 Pa.

conditions to the industrial ones. A parameter sensitivity study has been investigated in order to identify the main factors that govern the industrial vacuum process and to quantify the influence both on the weigh losses and on the freezing times.

Firstly, modeling has been used to point out the influence of the droplet size at a constant total gas pressure of 300 Pa (Fig. 7). As expected, the bigger the droplet diameter, the longer the freezing time. For a droplet which is 6 mm, it takes about 60 s to freeze the whole droplet mass instead of less than 5 s for 1 mm in diameter. On the contrary, the weight loss is not affected by the diameter droplet (data not shown).

The model was also used to investigate the influence of total gas pressure on the freezing kinetics. Fig. 8 presents the predicted temperature under five water vapor pressure conditions imposed from the initial conditions. For the following simulations, the initial temperature of the droplet is 20 °C and its initial diameter droplet was equal to 400 μm.

The freezing times have been found to be strongly affected by the total gas pressure: the lower the vacuum level, the shorter the freezing times. We observed that the freezing temperatures at steady state depend on the initial surrounding pressure. That means that a pressure of 470 Pa in the tower is required in order to freeze the puree into a frozen droplet. For a pressure higher than 500 Pa, the puree droplet is only cooled. In this case, the external water vapor is not enough important to freeze the sample. The simulated results agreed reasonably well with the measured data. From a practical point of view, a pressure around 400 Pa was required to freeze partially the carrot puree and lower than 350 Pa for carrot puree with cream. This could be attributed to a higher resistance to heat transfer inside cooked carrot puree, because its water content is less important (88% ± 0.6).

The last parameter affecting the freezing rate is the initial temperature of the puree. The simulations presented in Fig. 9 concern a droplet of 1 mm diameter and a pressure of 300 Pa. The mass loss increases with the initial temperature, as mentioned also by Zheng and Sun (2005). Indeed, the higher the initial temperature, the more important the pressure difference between the surface and its surrounding. On the contrary, the initial temperature does not affect the freezing times (time to reach −8 °C at the center of the droplet), and the freezing kinetics are only different in the cooling range as shown in Fig. 10.

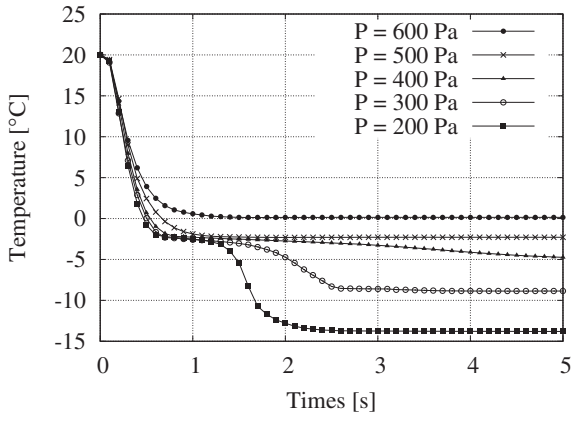

Fig. 8 – Influence of total pressure; droplet diameter: 1 mm; initial temperature: 20 °C.

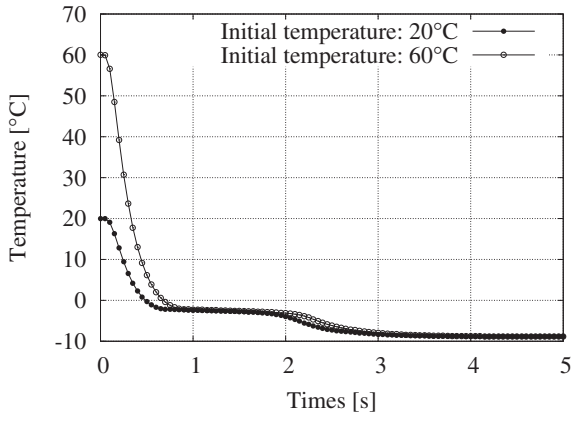

Fig. 10 – Influence of the initial temperature; droplet diameter: 1 mm; pressure setpoint: 300 Pa.

5. Conclusion

A mass and heat transfer model has been developed to predict the temperature and diffusion in a single puree droplet during a pure static freezing process by water evaporation. This modeling approach led to conclusions confirmed by experimental results, both in freezing times and in mass losses. A sensitive study has been carried out to determine the key parameter of the process. The freezing kinetics are governed by the water vapor pressure gradients between the sample and the surrounding atmosphere. The freezing times are also strongly affected by the droplet diameter and the masses loss by the initial droplet temperature.

With further steps in the development of the model like the integration of shrinkage and nucleation, such a model could be later used to optimize freezing conditions and facilitate the control of food quality and safety.

Acknowledgments

The authors would like to acknowledge the Conseil Regional de Picardie and the Groupe Bonduelle for the scientific help and also for the material and financial support.

REFERENCES

Amarante, A., 2004. Application de la mesure de densité de flux de chaleur à la caractérisation du procédé de surgélation des denrées alimentaires. Ph.D thesis, Université de Technologie de Compiègne, France.

Amos, N., Willix, J., Chadderton, T., North, M., 2008. A compilation of correlation parameters for predicting the enthalpy and thermal conductivity of solid foods within the temperature range of −40 to +40°C. Int. J. Refrigeration 31, 1293–1298.

Campanone, L., Salvadori, V., Mascheroni, R., 2001. Weight loss during freezing and storage of unpackaged foods. J. Food Eng. 47 (2), 69–79.

Clausse, D., Lanoisellé, J., Toumi, S., 2004. Ice nucleation in bulk and dispersed water. Application to freezing of foods. In: IX International Symposium On the Properties Of Water, Mar Del Plata, Argentina.

Cogné, C., Andrieu, J., Laurent, P., Besson, A., Nocquet, J., 2003. Experimental data and modelling of thermal properties of ice creams. J. Food Eng. 58, 331–341.

Hamdami, N., Monteau, J., Bail, A.L., 2004. Simulation of coupled heat and mass transfer during freezing of a porous humid matrix. Int. J. Refrigeration 27, 595–603.

He, S., Li, Y., 2003. Theoretical simulation of vacuum cooling of spherical foods. Appl. Therm. Eng. 23, 1498–1501.

Houska, M., Podloucky, S., Zitny, R., Gree, R., Sestak, J., Dostal, M., Burfoot, D., 1996. Mathematical model of the vacuum cooling of liquids. J. Food Eng. 29, 339–348.

Landfeld, A., Houska, M., Kyhos, K., Qibin, J., 2002. Mass transfer experiments on vacuum cooling of selected pre-cooked solid foods. J. Food Eng. 52, 207–210.

Lide, D., 2008–2009. Handbook of Chemistry and Physics. CRC Press.

Maureaux, A., Baranowski, E., Luchini, F., 2008. Process and apparatus for the preparation and conservation of products such as food and/or biological products. European Patent EP 1 632 140. The Bonduelle Company, Assigned, (2006).

McDonald, K., Sun, D., 2000. Vacuum cooling technology for the food processing industry: a review. J. Food Eng. 45, 55–65.

Nguyen, P., 2010. Surgélation par le vide de purées de légumes. Ph.D thesis, Université de Technologie de Compiègne, France.

Perrot, P., 2006. Propriétés thermodynamiques de l'eau. Techniques de l'Ingénieur. K 585v2.

Pham, Q., 1996. Prediction of calorimetric properties and freezing time of foods from composition data. J. Food Eng. 30, 95–107.

Pham, Q., 2006. Modelling heat and mass transfer in frozen foods: a review. Int. J. Refrigeration 29, 876–888.

Puri, V., Anantheswaran, R., 1993. The finite element method in food processing: a review. J. Food Eng. 19, 247–274.

Satoh, I., Fushinobu, K., Hashimoto, Y., 2002. Freezing of water droplet due to evaporation-heat transfer dominating the evaporation-freezing phenomena and the effect of boiling on freezing characteristics. Int. J. Refrigeration 20, 226–234.

Shin, H.T., Lee, P., Jurng, J., 2000. Spherical-shaped ice particle production by spraying water in a vacuum chamber. Appl. Therm. Eng. 20, 439–454.

Sun, D., Hu, Z., 2003. CFD simulation of coupled heat and mass transfer through porous foods during vacuum cooling process. Int. J. Refrigeration 26, 19–27.

Sun, D., Wang, L., 2004. Experimental investigation of performance of vacuum cooling for commercial large cooked meat joints. J. Food Eng. 61, 231–240.

Wang, L., Sun, D., 2002. Modelling vacuum cooling process of cooked meat – part 2: mass and heat transfer of cooked meat under vacuum pressure. Int. J. Refrigeration 25, 862–871.

Zheng, L., Sun, D., 2005. Vacuum cooling of foods. In: Emerging Technologies for Food Processing. Elsevier Academic Press, London, UK (Ch. 5).

Ultrasonics Sonochemistry 26 (2015) 186–192

Contents lists available at ScienceDirect

Ultrasonics Sonochemistry

journal homepage: www.elsevier.com/locate/ultson

Prediction of the acoustic and bubble fields in insonified freeze-drying vials

O. Louisnard [a,*], C. Cogné [b], S. Labouret [b], W. Montes-Quiroz [a], R. Peczalski [b], F. Baillon [a], F. Espitalier [a]

[a] Centre RAPSODEE, UMR CNRS 5302, Université de Toulouse, Ecole des Mines d'Albi, 81013 Albi Cedex 09, France
[b] Université Claude Bernard Lyon 1; LAGEP, UMR CNRS 5007, Campus de la Doua, Bt. CPE, 69616 Villeurbanne, France

ARTICLE INFO

Article history:
Received 6 November 2014
Received in revised form 6 March 2015
Accepted 9 March 2015
Available online 13 March 2015

Keywords:
Acoustic cavitation
Bubble structures
Propagation in bubbly liquids
Wave attenuation
Sono-freezing
Sono-crystallization

ABSTRACT

The acoustic field and the location of cavitation bubble are computed in vials used for freeze-drying, insonified from the bottom by a vibrating plate. The calculations rely on a nonlinear model of sound propagation in a cavitating liquid [Louisnard, Ultrason. Sonochem., 19, (2012) 56–65]. Both the vibration amplitude and the liquid level in the vial are parametrically varied. For low liquid levels, a threshold amplitude is required to form a cavitation zone at the bottom of the vial. For increasing vibration amplitudes, the bubble field slightly thickens but remains at the vial bottom, and the acoustic field saturates, which cannot be captured by linear acoustics. On the other hand, increasing the liquid level may promote the formation of a secondary bubble structure near the glass wall, a few centimeters below the free liquid surface. These predictions suggest that rather complex acoustic fields and bubble structures can arise even in such small volumes. As the acoustic and bubble fields govern ice nucleation during the freezing step, the final crystal's size distribution in the frozen product may crucially depend on the liquid level in the vial.

1. Introduction

Acoustic cavitation has been recognized as a useful method to trigger the nucleation of ice in supercooled water [1–9]. The mechanism underlying this effect at the microscopic scale is still a matter of debate, and two opposite theories exist [10–13]. Inertial cavitation, involving bubbles collapsing radially, is believed to be a necessary condition. However, single-bubble experiments have shown that non-inertial cavitation could also trigger ice nucleation [14], whereas other similar experiments showed the opposite [15].

Whatever the mechanism involved, this phenomenon can be used to control ice nucleation. Ultrasound-induced cavitation allows to trigger ice nucleation at low levels of supercooling, which is unfeasible in normal conditions, owing to the stochastic character of nucleation. This has interesting consequences for example in freeze-drying processes, where nucleation at moderate supercooling yields larger crystals and therefore enhances sublimation rates [7,9]. Moreover, controlling the nucleation temperature by ultrasound allows for inducing ice crystallization simultaneously in all processed samples and thus for decreasing the dispersion of the crystal properties.

A commonly used industrial freeze-drying system consists of cold shelves, which allow to freeze simultaneously hundreds or thousands of glass vials containing the solution (typically a few mL). Andrieu and co-workers have combined this system with a vibrating plate, which transmits ultrasound to the vials through the vibration of the glass walls [7]. The system has been improved and instrumented, and a design experiment has been performed in order to study the influence of the ultrasonic power and supercooling level [9].

Unfortunately, in such experiments, the amplitude and spatial distribution of the acoustic pressure field is generally not known, and the bubble field is difficult to visualize, because of the presence of crystals. This makes the comparison with existing "single-bubble theories" difficult. Empirical correlations between various controllable experimental parameters (frequency, ultrasound amplitude, geometry, type of ultrasonic transducer, temperature) and the observable quantities (nucleation temperature, size and shape of crystals) can be made, but bypassing the knowledge of the acoustic and bubble fields. Yet, it is well known that cavitation fields are never spatially homogeneous and self-organize as localized bubble structures [16]. It is therefore interesting to gain more knowledge on the location of the bubbles in the vibrated vials used for freeze-drying of aqueous solutions. Moreover, in order to

* Corresponding author.
E-mail address: louisnar@enstimac.fr (O. Louisnard).

http://dx.doi.org/10.1016/j.ultsonch.2015.03.008
1350-4177/

design and optimize new experimental setups, it would be useful to predict the conditions under which cavitation is really produced in the vial, for example a lower bound on the required vibration amplitude. Predicting the effect of other experimental parameters, such as the filling level in the vials, would also be welcome.

These issues are not specific to sono-crystallization and arise in all applications of acoustic cavitation, for example sonochemistry. Predicting the bubble and acoustic field ab initio has long been thought unfeasible (see [17] for a review), owing to the complexity of the physics involved. However, a recent model of acoustic wave propagation in cavitation fields has shown its ability to capture the main features on some well-known bubble structures [18,19]. In this communication, the latter model is used in the conditions of past sono-freezing experiments in vials [7,9]. The relative simplicity of the model is drawn on to vary the experimental parameters.

2. Model

The occurrence of acoustic cavitation is known to produce a self-attenuation of the acoustic field [20,21]. Therefore, correct modelling of acoustics in a cavitating liquid requires to account for the mechanical energy dissipated by the cavitation bubbles. This energy dissipation has two physical origins: thermal conduction in the gas/vapor contained in the bubble, and viscous friction in the violent radial motion around the bubbles. For inertial cavitation, involving bubble collapses, a correct estimation of these two contributions can only be made on the basis of a real nonlinear bubble dynamics [22].

Under some reasonable approximations, a model accounting for this energy dissipation was proposed [18]. It is based on Caflish equations [23] describing the propagation of a finite-amplitude pressure wave in a dilute bubbly mixture. This model, following the early idea of Foldy [24], expresses the effective pressure field at a given location by adding the average pressure waves radiated by neighboring bubbles to the primary field [25]. The system is closed by a non-linear equation of bubble dynamics, in which the local pressure field acts as the driving term. We emphasize that, by construction, such models do account for the bubble–bubble interaction, and essentially contain the same physics as discrete models of bubble clouds [26–29], which exhibit similar damping phenomena [27]. This issue is discussed briefly in Appendix A.

Since Caflish equations are difficult to solve in the range of acoustic pressures yielding inertial cavitation, they were reduced to a simpler form in [18], by retaining only the fundamental part of the acoustic field $p(\mathbf{r},t) = P(\mathbf{r})e^{j\omega t}$. The complex amplitude $P(\mathbf{r})$, which carries the amplitude and phase of the field, was found to approximately obey a nonlinear Helmholtz equation:

$$\nabla^2 P + k^2(|P|)P = 0. \tag{1}$$

The complex wavenumber can be obtained from:

$$\Re(k^2) = \frac{\omega^2}{c_l^2} + \frac{4\pi R_0 \omega^2 N}{\omega_0^2 - \omega^2}, \tag{2}$$

$$\Im\left(k^2\right) = -2\rho_l \omega N \frac{\Pi_v + \Pi_{th}}{|P|^2}, \tag{3}$$

where ω is the angular frequency, c_l the sound velocity of the pure liquid, and ρ_l its density. The quantities Π_v and Π_{th} are the average power dissipated by the bubble over one acoustic cycle, by viscous friction in the liquid, and by heat conduction in the bubble, respectively. The relation between $\Im(k^2)$ and the latter quantities constitute the key point of the model, and allow to obtain realistic estimations of the attenuation coefficient of the wave $\alpha = -\Im(k)$ [22,18].

The bubbles are assumed to have an ambient radius R_0. The bubble density N is assigned to zero in the zones where the acoustic pressure is less than the Blake threshold, and to a constant value N_0 in the opposite case.

$$N = \begin{cases} N_0 & \text{if } |P| > P_B \\ 0 & \text{if } |P| < P_B \end{cases}. \tag{4}$$

This model has been shown to catch reasonably well the so-called cone bubble structures, visible under large area transducers [30–32], and the flare-like structures [16] in ultrasonic baths, with some reasonable choices, albeit arbitrary, of the free parameters R_0 and N_0 [19].

Another technical difficulty in acoustic models of sono-reactors is the way solid boundaries are handled. Precedent studies based on linear acoustics showed that modelling the latter by infinitely soft or infinitely rigid boundaries is not convenient [33,34]. Therefore, continuity equations are used to couple the wall vibrations to the liquid acoustic field, as detailed in Ref. [34].

In order to calculate $\Pi_v(|P|)$ and $\Pi_{th}(|P|)$, bubble dynamics simulations were performed in conditions close to the experiments described in Refs. [7,9]. The bubble dynamics model used was taken from Toegel et al. [35], as in Ref. [18]. The bubbles ambient radius was set to $R_0 = 5\,\mu m$, the frequency was $f = 35,890$ Hz, the ambient pressure $p_0 = 101,300$ Pa, and the driving pressure $|P|$ was varied between $0.1\,p_0$ and $3\,p_0$. The properties of supercooled water were taken at $-5\,^\circ C$: density $\rho_l = 1000\ kg/m^3$ [36], surface tension $\sigma = 76.3\ mN\ m^{-1}$ [37], sound velocity $c_l = 1380\ m\ s^{-1}$ [38] and viscosity $\mu_l = 2 \times 10^{-3}$ Pa s [36]. As in earlier work [18], Π_{th} was found negligible compared to Π_v and the latter can be fitted in non-dimensional form by:

$$\frac{\Pi_v(|P^*|)}{|P^*|^2} = p_0 V_0 \omega \exp\left[A + B\tan^{-1}\left(\frac{|P^*| - P_0^*}{\Delta P^*}\right)\right], \tag{5}$$

where p_0 is the ambient pressure, $|P|^* = |P|/p_0$ is the dimensionless acoustic pressure amplitude and $V_0 = 4/3\pi R_0^3$ is the bubble ambient volume. In the considered conditions, the set of fitting parameters in (5) was found to be $A = -2.207$, $B = 5.337$, $\Delta P^* = 0.2223$, $P_0^* = 0.9628$.

The problem was solved with COMSOL Multiphysics. The geometry and boundary conditions are described in Fig. 1. Axisymmetry allows to represent only a 2D longitudinal section of the vial. All external solid boundaries were assumed free, except the contact surface between the plate and the vial, where a displacement U_0 was imposed. The mathematical formulation of these boundary conditions can be found in Ref. [34]. Finally, the free surface of the liquid was modelled by an infinitely soft wall.

The domains were meshed with triangular elements, whose maximum size was 1 mm in the liquid, and 0.5 mm in the solid. The mesh was refined near the vial bottom because large gradients of acoustic pressure were expected in this zone. Finally, a mesh convergence study has been performed in a typical case, to ensure that the mesh was sufficiently fine.

In all simulations, we considered bubbles of ambient radii $R_0 = 5\,\mu m$, yielding the Blake threshold P_B of $1.056\,p_0$. The bubble density was arbitrary fixed to $N_0 = 50$ bubbles/mm^3. The influence of these parameters will be discussed below.

3. Results

3.1. Results display.

For each simulation case presented hereinafter, all results will be presented as on Fig. 2, which is obtained as follows. First, a color plot of the peak dimensionless acoustic pressure $|P^*| = |P|/p_0$ is

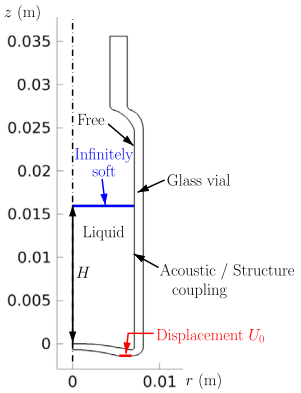

Fig. 1. Geometry and boundary conditions of the vial filled with liquid. The liquid level H is measured from the on-axis inner side of the vial wall.

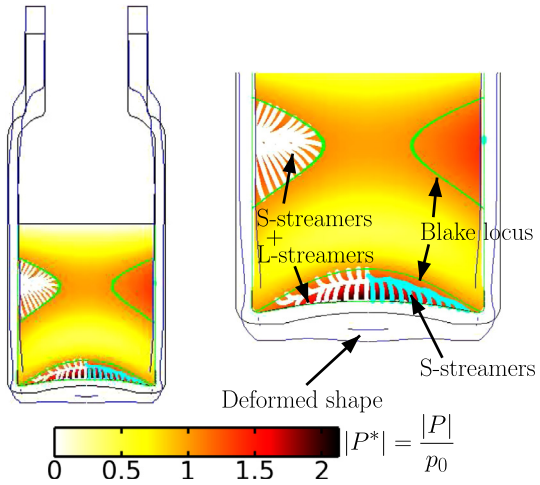

Fig. 2. Example of simulation results ($U_0 = 1$ µm , $H = 16$ mm, $f = 35,890$ Hz). The right graph is a zoom on the left one. Color plot: peak dimensionless acoustic pressure $|P^*| = |P|/p_0$. Lines on the left part of figure (white): streamlines of the Bjerknes force field launched from any point where the Blake threshold is exceeded. Lines on the right part of figure (light-blue): streamlines of the Bjerknes force field launched from any solid surface where the Blake threshold is exceeded. The line limiting the former set of streamlines materializes the Blake threshold locus (green). The deformed shape of the glass wall is also represented (blue) at phase $\omega t = \pi$. (For interpretation of the references to colour in this figure legend, the reader is referred to the web version of this article.)

displayed and the locus of the Blake threshold ($P_B^* = 1.056$) is materialized by a green line. The blue line represents the deformed shape of the vial, at phase $\omega t = \pi$, that is, when the contact surface is at its lowest position. Finally, the Bjerknes force field is deduced from the amplitude and phase of the pressure field, as detailed in Ref. [19]. Similarly to the latter reference, the streamlines of this field are sketched as follows, in order to materialize the plausible bubble paths in the liquid:

- streamlines are launched from those parts of the solid surfaces where the acoustic pressure exceeds the Blake threshold. These streamlines were named "S-streamers" in Ref. [19], and are displayed in the right part of the bottle (light-blue online);
- streamlines are launched indifferently from any point where the acoustic pressure exceeds the Blake threshold (displayed on the left part of the bottle, white lines). This set of streamlines includes the set of S-streamers, and the difference between the two sets are the streamlines originating from the Blake locus. The latter were called "L-streamers" in Ref. [19].

Experiments on cone or flare structures evidenced that S-streamers are always visible, whereas the set of L-streamers may be less dense. However, the latter reproduced reasonably well the filamentary structures located near the pressure antinodes, for example in ultrasonic baths. The relation between the Bjerknes force field and the actual location of bubbles remains an open issue, and for now, we chose to present both sets systematically.

3.2. Influence of vibration amplitude

First, the liquid height H was set to 7 mm, as in the experiments of Refs. [7,9], while the vertical displacement U_0 of the contact surface was varied from 0.009 µm to 1 µm. The results are displayed on Fig. 3, in which a zoom on the liquid has been made for clarity. For the lowest amplitude (upper left plot), the pressure field is everywhere lower than the Blake threshold, so that there are no bubbles, and the acoustic field is essentially predicted by linear acoustics. As the amplitude is increased, the acoustic pressure increases in the bottom zone of the liquid and starts to exceed the Blake threshold. Bubbles can nucleate on the latter and travel toward the vial bottom, which remains attractive (on the three first graphs in Fig. 3). Thus, in this case, no S-streamers are visible. Above $U_0 = 0.08$ µm (five last graphs in Fig. 3), some parts of the vial bottom start to be repulsive for bubbles, because the latter produce a large traveling contribution in the wave [18], which strongly repels bubbles from the solid surface [39,16,40,19], and forms S-streamers [(light-blue online) lines on the right part of the graph]. As amplitude increases, the S-streamers progressively invade the whole vial bottom and increase in height.

The self-saturation of the field can be clearly seen on Fig. 4, which displays the pressure profiles on the symmetry axis, non-dimensionalized by $\rho_l c_l \omega U_0$, for the eight values of U_0 used in Fig. 3. If the field were given by linear acoustics, all profiles would merge on a universal curve (represented by square symbols). It is seen that for the lowest amplitude $U_0 = 0.005$ µm, for which no cavitation is predicted, the pressure profile indeed merges with this curve. However, for increasing amplitude the dimensionless pressure profiles progressively decrease, down to approximately 2% of the universal curve for the highest amplitude $U_0 = 1$ µm (lowest curve on Fig. 4, corresponding to the rightmost bottom plot of Fig. 3). This clearly illustrates that linear acoustics would predict unrealistic huge values of the acoustic pressure field in the vial.

The displacement amplitude of the vial wall boundaries depends on the point considered and the driving level. It ranges from values close to U_0 for large drivings, to about 40 U_0 for low drivings, where no cavitation occurs (see Supplementary material, Fig. S1 and caption).

Finally, in the context of sono-freezing, these results for the liquid level used in experiments [7,9] yields two important conclusions. First, the cavitation field always appears at the bottom of the vial, and this promotes the nucleation of smaller ice crystals in the bottom part. This reinforces the effect of thermal gradients that necessarily arise when the sample is cooled from below [7,41]. This suggests that a different insonification method should be designed if one wish to avoid this synergetic effect, resulting in very broad crystal size distributions. On the other hand, because of self-saturation, it can be seen that a large increase of the driving amplitude does not produce large variations neither of the acoustic field amplitude, nor of the cavitation field extension. There might be therefore an optimum amplitude level sufficient to trigger ice nucleation.

3.3. Influence of liquid height

For a given amplitude $U_0 = 1$ µm, the liquid height has been varied between 6 mm and 20 mm. The resulting acoustic field

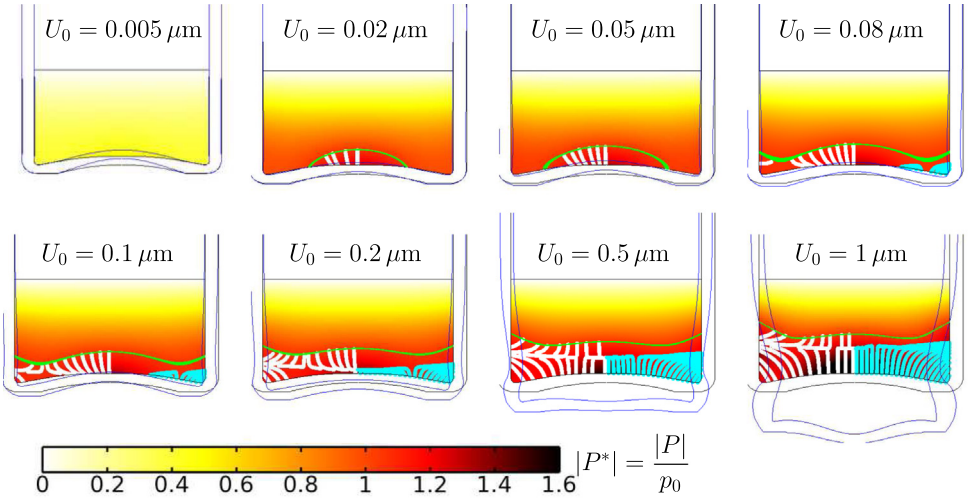

Fig. 3. Acoustic field and bubble paths for increasing driving amplitudes U_0 and a water level $H = 7$ mm, at $f = 35,890$ Hz. The figures zoom on the liquid for clarity. From left to right and top to bottom: $U_0 = 0.005, 0.02, 0.05, 0.08, 0.1, 0.2, 0.5, 1$ μm. See Fig. 2 for description.

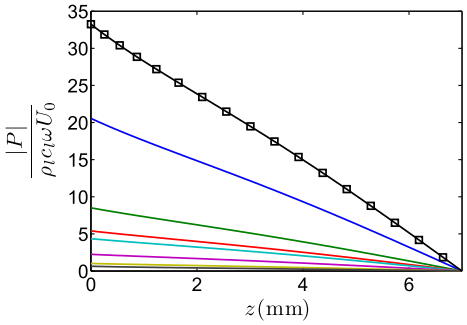

Fig. 4. Dimensionless acoustic pressure along the symmetry axis, in the conditions of Fig. 3. From top to bottom: $U_0 = 0.005, 0.02, 0.05, 0.08, 0.1, 0.2, 0.5, 1$ μm. The squares (merging exactly with the curve $U_0 = 0.005$ μm) correspond to the universal line predicted by linear acoustics.

and bubble paths are represented on Fig. 5. Above a critical liquid level, the region where the Blake threshold is exceeded splits in two parts (from $H = 10$ mm and above on Fig. 5). A dome-shaped region appears on the vial bottom, and a toroidal region builds up along the vertical glass wall, with a pressure antinode against the wall. The latter remains approximately at a constant distance from the liquid free surface as the level is increased. The streamlines in this region show that a classical streamer can be formed, with bubbles attracted by the wall pressure antinode. Conversely, at the vial bottom, the shape of S-streamers show that the wall is repulsive for the bubbles in a dome-shaped region extending almost up to the Blake locus.

On the two last graphs of Fig. 5 (H = 18 and 20 mm), it can be seen that the Blake threshold is exceeded in a small region on the axis, so that the toroidal region finally fills in the whole width of the vial. This occurs because the liquid level is large enough to enable the formation of a longitudinal standing wave, as evidenced by the axial pressure profiles displayed on Fig. 6 (solid lines). Moreover, for the largest level (H = 20 mm), it can be seen that a very small conical S-streamer appears near the wall, which means that the latter becomes repulsive. This is due to the fact that in this small region, the bubble dissipation becomes large enough to convert the local standing wave into a radial traveling wave. A zoom on the potentially resulting structure is displayed on Fig. 7, where streamlines of the Bjerknes force field have been launched from arbitrary points. The result shows some similarity with the flare structures described in Refs. [16,19].

These results suggest that changing the supercooled liquid level in the vial can have important consequences on the bubble field, and therefore on ice nucleation locations, and finally on the crystalline structure of the frozen product. The bubble structure appearing near the wall for high levels, exemplified in Fig. 7, may trigger ice nucleation in this region. In such a case, one would expect that the freezing front would not only travel upwards from the vial bottom, as observed in past experiments, but that another front would start from the vertical walls and travel towards the vial axis. This should have visible consequences on the morphology of ice crystals

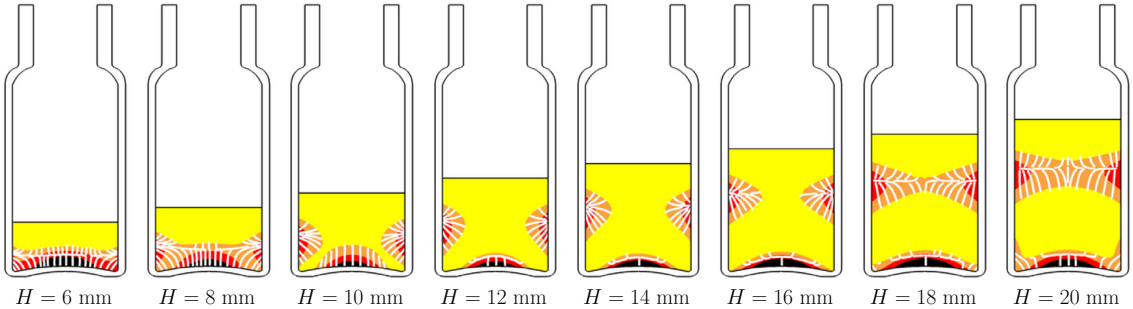

Fig. 5. Acoustic field and bubble paths for an amplitude $U_0 = 1$ μm and a liquid level $H = 6$ mm,8 mm,10 mm,12 mm,14 mm,16 mm,18 mm,20 mm from left to right, at $f = 35,890$ Hz. See Fig. 2 for description. For readability, the color plot is restricted to 4 levels, corresponding to $|P^*|$ in the intervals (from lightest to darkest shade): $[0, P_B^*]$, $[P_B^*, 1.25]$, $[1.25, 1.5]$, $|P^*| > 1.5$, where $P_B^* = 1.056$ is the dimensionless Blake threshold.

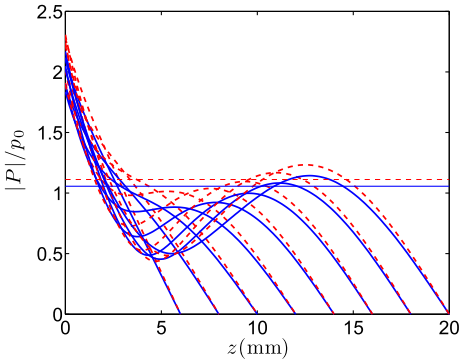

Fig. 6. Acoustic pressure profile along the symmetry axis, in the conditions of Fig. 5. Solid lines (blue): $R_0 = 5$ μm; dashed lines (red): $R_0 = 3$ μm. All curves end at $z = H$ and are therefore self-explanatory. The horizontal thin lines indicates the respective Blake thresholds for $R_0 = 5$ μm and $R_0 = 3$ μm. (For interpretation of the references to colour in this figure legend, the reader is referred to the web version of this article.)

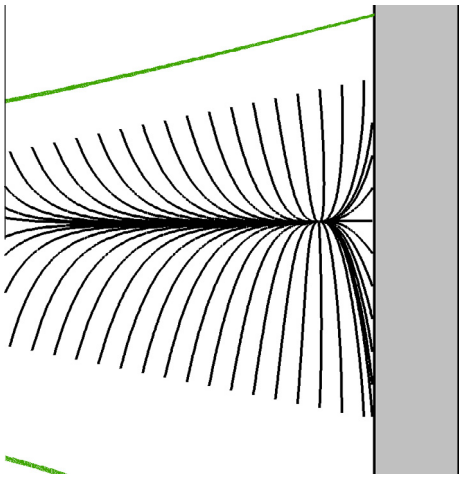

Fig. 7. Zoom on the flare-like structure appearing near the vial wall for $H = 20$ mm (rightmost graph on Fig. 5). The slanted lines (green) are the Blake loci. The vial wall is represented in gray. (For interpretation of the references to colour in this figure legend, the reader is referred to the web version of this article.)

nucleated in this region. A specific experimental campaign should be performed in order to confirm these predictions.

3.4. Influence of parameters R_0 and N_0

The calculations of Section 3.3 have been repeated in exactly the same conditions, but assuming bubbles of ambient radius $R_0 = 3$ μm. The resulting axial pressure profiles are represented with dashed lines on Fig. 6. They are slightly larger than the ones obtained for $R_0 = 5$ μm, but their global evolution for increasing liquid levels remains unchanged.

On the other hand, the calculations were repeated for $R_0 = 5$ μm, $H = 16$ mm, $U_0 = 1$ μm, and varying the bubble density N_0 from 20 to 200 bubbles/mm^3 by steps of 30. Similar ranges of bubble densities have been reported in bubble clouds under horn-type transducers [27]. As expected, the resulting pressure profiles along z (Fig. 8) decrease for increasing N_0, which is the logical consequence of an increased interaction between bubbles as they are more densely distributed. However,all profiles on Fig. 8 maintain the same shape. It can be noted that for the lowest bubble density ($N_0 = 20$ bubbles/mm^3), the Blake threshold is exceeded near $z = 10$ mm, because less bubbles produce less wave

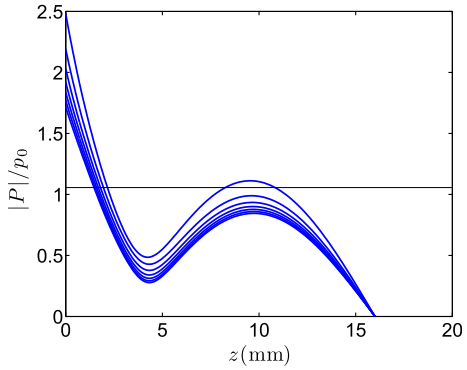

Fig. 8. Acoustic pressure profile along the symmetry axis, at $f = 35,890$ Hz, for $U_0 = 1$ μm, $H = 16$ mm, and a bubble density $N_0 = 20, 50, 80, 110, 140, 170, 200$ bubbles/mm^3 (from top to bottom). The horizontal thin line indicates the Blake threshold.

attenuation. This means that keeping all parameters constant, lower bubble densities would favor the appearance of the bubble structure in the middle of the liquid (similar to the ones visible on the two rightmost graphs of Fig. 5). This result is interesting and rather counter-intuitive, and suggests that in some configurations, injecting less bubbles in the model yields more bubbles-populated regions in the liquid.

4. Conclusions

Calculations of the acoustic and bubble fields have been performed in a vial insonified from the bottom by a vibrating plate, in the conditions of past sono-freezing experiments. The results confirmed that the bubble field was located at the bottom of the vials for low liquid levels, but evidenced also a more complex, non trivial bubble structure as the liquid level increases. Although these results must be validated against experiments, it has been demonstrated that even in such small samples involved by freezing aqueous solutions in glass vials, spatial variations of the crystal sizes and shapes may occur because of the inhomogeneity of the acoustic and bubble fields. The knowledge of the latter cannot therefore be disregarded in such experiments. The influence of other parameters, such as the clamping of some part of the vial, could also be studied. On the other hand, it has been shown that linear acoustics calculations yield unrealistic predictions in such problems.

Acknowledgments

The authors acknowledges the support of the French Agence Nationale de la Recherche (ANR), under grant SONONUCLICE (ANR-09-BLAN-0040–02) “Ice nucleation control by ultrasounds for freezing and freeze-drying processes optimization”.

Appendix A. On the bubble–bubble interaction in the model

Following a suggestion of a reviewer, this appendix examines whether the model used in this paper, which is a simplified version of Caflish equations [23], accounts in some way for the interaction between bubbles, as do “discrete” models describing the mutual influence of bubbles oscillating in pairs [26] or in clusters [27]. This discussion intends to clarify briefly and as simply as possible this issue, at the price of mathematical rigor. The main lines of the discussion are borrowed to Prosperetti [25].

Interacting bubble models, such as Eq. (7) in [26], or Eq. (2) in the cluster model of Yasui and co-workers [27], consist in a bubble radial dynamics equation written as:

$$R\ddot{R}+\frac{3}{2}\dot{R}^2=\frac{1}{\rho_l}(p_L-p_S(\mathbf{r},t)-p_\infty)\\ -\sum_{i=1}^{N-1}\frac{1}{d_i}\left(2\dot{R}_i^2R_i+R_i^2\ddot{R}_i\right), \tag{A.1}$$

where for simplicity, we have omitted refining terms accounting for liquid compressibility and for water evaporation/condensation at the bubble wall. The first line in Eq. (A.1) is a classical Rayleigh equation, where R is the bubble radius, ρ_l is the liquid density, p_L is the pressure in the liquid at the bubble wall, $p_S(t)=p_A(\mathbf{r})\sin\omega t$ is the driving acoustic pressure field at the bubble centroid location $\mathbf{r}$ if the latter were absent, and p_∞ is the static pressure. The additional term in the second line of Eq. (A.1) describes the pressure fields radiated by $N-1$ neighboring bubbles, among which the i^{est} one is located at a distance d_i from the bubble described by (A.1), and has an instantaneous radius $R_i(t)$.

Eq. (A.1) therefore states simply that the "effective" pressure field driving the described bubble is basically:

$$p_{\text{eff}}(\mathbf{r},t)=p_S(\mathbf{r},t)+\rho_l\sum_{i=1}^{N-1}\frac{1}{d_i}\left(2\dot{R}_i^2R_i+R_i^2\ddot{R}_i\right). \tag{A.2}$$

Assuming further that the $N-1$ other bubbles are identical, their dynamics $R_i(t)$ are solutions of equations formally similar to (A.1). Furthermore, assuming that bubbles are numerous enough so that they can be described by a bubble density $n(\mathbf{r}_0)$, and noting that $2\dot{R}^2R+R^2\ddot{R}=\ddot{V}/4\pi$, the discrete sum in Eq. (A.2) can be replaced by a volume integral:

$$p_{\text{eff}}(\mathbf{r},t)=p_S(\mathbf{r},t)+\rho_l\iiint_{\mathcal{V}}\frac{\ddot{V}(\mathbf{r}_0,t)}{4\pi|\mathbf{r}-\mathbf{r}_0|}n(\mathbf{r}_0)d\mathbf{r}_0, \tag{A.3}$$

where $V(\mathbf{r}_0,t)$ is the instantaneous volume of the (numerous) bubbles located at $\mathbf{r}_0$.

Now, having in mind a model describing the spatial variations of p_{eff}, we note that the Green function for the Laplacian can be readily recognized in the integral, so that taking the Laplacian of Eq. (A.3), we get:

$$\nabla^2p_{\text{eff}}(\mathbf{r},t)=\nabla^2p_S(\mathbf{r},t)-\rho_l\iiint_{\mathcal{V}}\ddot{V}(\mathbf{r}_0,t)\delta(\mathbf{r}-\mathbf{r}_0)n(\mathbf{r}_0)d\mathbf{r}_0\\ =\nabla^2p_S(\mathbf{r},t)-\rho_ln(\mathbf{r})\frac{\partial^2V}{\partial t^2}(\mathbf{r},t),$$

where δ stems for the Dirac function. In this equation, p_S is the acoustic pressure field that would drive the bubble if it were alone (in absence of interaction), and satisfies therefore a standard linear propagation equation in the pure liquid. Thus, the above equation finally writes:

$$\frac{1}{c_l^2}\frac{\partial^2p_S}{\partial t^2}(\mathbf{r},t)-\nabla^2p_{\text{eff}}(\mathbf{r},t)=\rho_ln(\mathbf{r})\frac{\partial^2V}{\partial t^2}(\mathbf{r},t),$$

where c_l is the sound velocity in the pure liquid. If we replace p_S by p_{eff} in the first term of the LHS of this equation,[1] we get exactly the first equation of the Caflish model ([23,42]):

$$\frac{1}{c_l^2}\frac{\partial^2p_{\text{eff}}}{\partial t^2}(\mathbf{r},t)-\nabla^2p_{\text{eff}}(\mathbf{r},t)=\rho_ln(\mathbf{r})\frac{\partial^2V}{\partial t^2}(\mathbf{r},t), \tag{A.4}$$

of which our model is an approximation (see Ref. [18] for details).

The Caflish model is then closed by calculating the bubble volume $V(\mathbf{r},t)=\frac{4}{3}\pi R^3(\mathbf{r},t)$ from a bubble dynamics equation driven by the local *effective* pressure field $p_{\text{eff}}(\mathbf{r},t)$, exactly in the same way as in (A.1), R_i is calculated as a solution of (A.1) itself!

The continuous path between the two approaches summarized above shows that the bubble interaction is indirectly included in our model (as for any model derived from Caflish equations), but in a global fashion. As detailed in [18], what we call "the acoustic field" is the first harmonic part of the effective field p_{eff} from (A.4), or from (A.1). It is spatially damped because as shown in [18], part of the effective field energy is dissipated by viscous friction in the radial motion of the liquid around the bubbles (and to a lesser extent by heat transfer in the bubble).

As a final comment, these remarks might also shed light on one major result of Ref. [27] (Section V and Fig. 6). It is found there that the actual pressure profile on the axis (solid line) is far less than that predicted by the analytical solution of linear acoustics for a circular piston [Eq. (15) in the latter reference]. This is exactly the result that we obtain in all the simulations with our model, either in the present paper (see Fig. 4), or in Ref. [18] (Fig. 6). We suggest therefore that in Section V of Ref. [27], if the peak value of $p_{\text{eff}}(x)$ from Eq. (A.2) had been evaluated instead of $p_a(x)$, the authors might have recovered values close to the solid line of their Fig. 5.

Following the same line of reasoning, we also note that if we were to reproduce Figs. 9–11 of Ref. [27] with our model, we would obtain the dashed line by driving the bubble with the linear acoustic prediction $p_S(t)$, and the solid line by driving the bubble with the pressure field $p_{\text{eff}}(t)$ calculated with our model.

We conclude therefore that both approaches contain in fact the same physics, and that our model (being a derived product of Caflish Model) catches the bubble–bubble interaction at least approximately. The informal comments of this appendix would probably deserve to be revisited more thoroughly, and possibly extended to more complex configurations, such as mixtures of bubbles of different sizes [29]. This may motivate a dedicated study. We thank the reviewer for suggesting this interesting discussion.

Appendix B. Supplementary data

Supplementary data associated with this article can be found, in the online version, at http://dx.doi.org/10.1016/j.ultsonch.2015.03.008.

References

[1] S.L. Hem, Ultrasonics 5 (4) (1967) 202–207.
[2] J.D. Hunt, K.A. Jackson, Nature 211 (1966) 1080–1081.
[3] T. Bhadra, Indian J. Phys. 42 (2) (1968) 91.
[4] S.N. Gitlin, S.S. Lin, J. Appl. Phys. 40 (12) (1969) 4761–4767.
[5] T. Inada, X. Zhang, A. Yabe, Y. Kozawa, Int. J. Heat Mass Transfer 44 (23) (2001) 4523–4531.
[6] R. Chow, R. Blindt, R. Chivers, M. Povey, Ultrasonics 43 (4) (2005) 227–230.
[7] K. Nakagawa, A. Hottot, S. Vessot, J. Andrieu, Chem. Eng. Process. 45 (9) (2006) 783–791.
[8] B. Lindinger, R. Mettin, R. Chow, W. Lauterborn, Phys. Rev. Lett. 99 (4) (2007) 045701.
[9] M. Saclier, R. Peczalski, J. Andrieu, Chem. Eng. Sci. 65 (10) (2010) 3064–3071.
[10] J.D. Hunt, K.A. Jackson, J. Appl. Phys. 37 (1966) 254–257.
[11] R. Hickling, Nature 206 (1965) 915–917.
[12] C.P. Lee, T.G. Wang, J. Appl. Phys. 71 (1992) 5721–5723.
[13] R. Hickling, Phys. Rev. Lett. 273 (1994) 2853–2856.
[14] R. Chow, R. Mettin, B. Lindinger, T. Kurz, W. Lauterborn, in: D.E. Yuhas, S.C. Schneider (Eds.), Proceedings of the IEEE International Ultrasonics Symposium, vol. 2, IEEE, 2003, pp. 1447–1450.

[1] This assumption is linked to an hypothesis of dilute liquid-bubble mixture, in which we will not enter in details here

[15] K. Ohsaka, E.H. Trinh, Appl. Phys. Lett. 73 (1) (1998) 129–131.
[16] R. Mettin, in: A.A. Doinikov (Ed.), Bubble and Particle Dynamics in Acoustic Fields: Modern Trends and Applications, Research Signpost, Kerala (India), 2005, pp. 1–36.
[17] I. Tudela, V. Sáez, M.D. Esclapez, M.I. Díez-García, P. Bonete, J. González-García, Ultrason. Sonochem. 21 (3) (2014) 909–919.
[18] O. Louisnard, Ultrason. Sonochem. 19 (2012) 56–65.
[19] O. Louisnard, Ultrason. Sonochem. 19 (2012) 66–76.
[20] L.D. Rozenberg, in: L.D. Rozenberg (Ed.), High-Intensity Ultrasonic Fields, Plenum Press, New-York, 1971.
[21] M.M. van Iersel, N.E. Benes, J.T.F. Keurentjes, Ultrason. Sonochem. 15 (4) (2008) 294–300.
[22] O. Louisnard, Congress on Ultrasonics, Santiago de Chile, January 2009, Phys. Procedia 3 (1) (2010) 735–742.
[23] R.E. Caflish, M.J. Miksis, G.C. Papanicolaou, L. Ting, J. Fluid Mech. 153 (1985) 259–273.
[24] L.L. Foldy, Phys. Rev. 67 (3–4) (1944) 107–119.
[25] A. Prosperetti, in: S. Morioka, L. van Wijngaarden (Eds.), IUTAM Symposium on Waves in Liquid/Gas and Liquid/Vapour Two-Phase Systems, Kluwer Academic Publishers, 1995, pp. 55–65.
[26] R. Mettin, I. Akhatov, U. Parlitz, C.D. Ohl, W. Lauterborn, Phys. Rev. E 56 (3) (1997) 2924–2931.
[27] K. Yasui, Y. Iida, T. Tuziuti, T. Kozuka, A. Towata, Phys. Rev. E 77 (1) (2008) 016609.
[28] K. Yasui, J. Lee, T. Tuziuti, A. Towata, T. Kozuka, Y. Iida, J. Acoust. Soc. Am. 126 (3) (2009) 973–982.
[29] K. Yasui, A. Towata, T. Tuziuti, T. Kozuka, K. Kato, J. Acoust. Soc. Am. 130 (5) (2011) 3233–3242.
[30] A. Moussatov, C. Granger, B. Dubus, Ultrason. Sonochem. 10 (2003) 191–195.
[31] C. Campos-Pozuelo, C. Granger, C. Vanhille, A. Moussatov, B. Dubus, Ultrason. Sonochem. 12 (2005) 79–84.
[32] B. Dubus, C. Vanhille, C. Campos-Pozuelo, C. Granger, Ultrason. Sonochem. 17 (2010) 810–818.
[33] K. Yasui, T. Kozuka, T. Tuziuti, A. Towata, Y. Iida, J. King, P. Macey, Ultrason. Sonochem. 14 (2007) 605–614.
[34] O. Louisnard, J.J. González-García, I. Tudela, J. Klima, V. Saez, Y. Vargas-Hernandez, Ultrason. Sonochem. 16 (2009) 250–259.
[35] R. Toegel, B. Gompf, R. Pecha, D. Lohse, Phys. Rev. Lett. 85 (15) (2000) 3165–3168.
[36] P.G. Debenedetti, J. Phys. Condens. Matter 15 (45) (2003) R1669.
[37] D. Kashchiev, J. Chem. Phys. 125 (4) (2006) 044505.
[38] E. Trinh, R.E. Apfel, J. Acoust. Soc. Am. 63 (3) (1978) 777–780.
[39] P. Koch, D. Krefting, T. Tervo, R. Mettin, W. Lauterborn, in: Proc. ICA 2004, vol. Fr3.A.2, Kyoto, Japan, 2004, pp. V3571–V3572.
[40] R. Mettin, in: T. Kurz, U. Parlitz, U. Kaatze (Eds.), Oscillations Waves and Interactions, Universitätsverlag Göttingen, 2007, pp. 171–198.
[41] A. Hottot, S. Vessot, J. Andrieu, Chem. Eng. Process. 46 (7) (2007) 666–674.
[42] K.W. Commander, A. Prosperetti, J. Acoust. Soc. Am. 85 (2) (1989) 732–746.

Ultrasonics Sonochemistry 29 (2016) 447–454

Contents lists available at ScienceDirect

Ultrasonics Sonochemistry

journal homepage: www.elsevier.com/locate/ultson

Theoretical model of ice nucleation induced by acoustic cavitation. Part 1: Pressure and temperature profiles around a single bubble

C. Cogné [a], S. Labouret [a], R. Peczalski [a,*], O. Louisnard [b], F. Baillon [b], F. Espitalier [b]

[a] University of Lyon, France, Université Claude Bernard Lyon 1, Laboratoire d'Automatique et de Génie des Procédés (LAGEP UMR CNRS 5007), Campus de la Doua, Bât. CPE, 69616 Villeurbanne, France

[b] University of Toulouse, France, Ecole Nationale Supérieure des Mines d'Albi-Carmaux, Centre de Recherche d'Albi en génie des Procédés des Solides Divisés, de l'Énergie et de l'Environnement (RAPSODEE UMR CNRS 5302), Campus Jarlard, 81013 Albi, France

ARTICLE INFO

Article history:
Received 5 February 2015
Received in revised form 27 April 2015
Accepted 11 May 2015
Available online 27 May 2015

Keywords:
Ultrasound
Cavitation
Single bubble
Heat transfer
Fluid mechanics
Modeling

ABSTRACT

This paper deals with the inertial cavitation of a single gas bubble in a liquid submitted to an ultrasonic wave. The aim was to calculate accurately the pressure and temperature at the bubble wall and in the liquid adjacent to the wall just before and just after the collapse. Two different approaches were proposed for modeling the heat transfer between the ambient liquid and the gas: the simplified approach (A) with liquid acting as perfect heat sink, the rigorous approach (B) with liquid acting as a normal heat conducting medium. The time profiles of the bubble radius, gas temperature, interface temperature and pressure corresponding to the above models were compared and important differences were observed excepted for the bubble size. The exact pressure and temperature distributions in the liquid corresponding to the second model (B) were also presented. These profiles are necessary for the prediction of any physical phenomena occurring around the cavitation bubble, with possible applications to sono-crystallization.

1. Introduction

1.1. Context and aim of the study

The unstable (inertial) acoustic cavitation of micron size gas bubbles in a liquid medium and especially their violent collapses induce extreme physical conditions (pressures up to tens of GPa, temperatures up to tens of thousands K), inside and in the close vicinity of the bubbles. These conditions are at the origin of spectacular effects like: sonoluminescence, hydroxyl radicals generation, solid surface erosion but also promote the crystallization of solutes in super-saturated solutions or of solvent in super-cooled solutions [1].

In order to keep these phenomena under control, one needs to know exactly the evolution of physical parameters (pressure, temperature, composition) of the gas inside the bubble but also that of the liquid outside as the two are tightly linked one to another.

However, the first concern of most of the studies on acoustic cavitation devoted to interpret sonochemistry and sonoluminescence was the behavior of the gas in the bubble and not that of the surrounding liquid. Thus an approximate way to describe the gas thermal behavior, the heat transfer at the interface and on the liquid side was often adopted in order to obviate the solution of a full set of energy and motion equations in the liquid. In most cases the gas pressure inside the bubble was considered uniform and the motion of the liquid was described by the classical Rayleigh–Plesset equation corrected for liquid compressibility [2–4]. The gas behavior depends strongly on the heat transfer rate across the bubble wall. In a very simplified approach, the slow bubble expansion can be considered as isothermal, while the fast collapse as adiabatic. From that point the basic modeling approach was to describe the gas state by a polytropic equation with a coefficient depending on the Peclet number [5]. As concerns heat transfer in the liquid surrounding the bubble, the simplest assumption was to neglect any thermal gradient and to keep the bubble wall temperature constant at the ambient value [4,6,7]. Another kind of simplified thermal approach was to consider the continuity of the heat flux across the bubble wall and to adopt an arbitrary liquid temperature profile in order to evaluate the heat flux outside the bubble [8,9].

A trend for a more in depth description of the heat transfer between the gas and the liquid was dictated by the recognition of the very important role that plays water vapor in the physics of a collapsing bubble [10–12] and thus the need to take into account the phase change (condensation or evaporation) at the bubble wall and consequently to incorporate a heat balance at the wall in the global model.

* Corresponding author.
E-mail address: peczalski@lagep.univ-lyon1.fr (R. Peczalski).

http://dx.doi.org/10.1016/j.ultsonch.2015.05.038
1350-4177/

The first aim of this study was to calculate accurately the pressure and temperature at the bubble wall and in the liquid adjacent to the wall just before and just after the collapse, starting from the mathematical description of the gas behavior and of the bubble wall motion already established and validated in the literature.

The second aim was to show the importance of the assumptions concerning heat transfer at the bubble wall and in the surrounding liquid, by considering two different modeling approaches briefly presented below:

(A) Inside the bubble, a thermal gradient was supposed to exist in the gas over a thin boundary layer near the bubble wall, with a thickness varying accordingly to the wall dynamics. A constant bubble wall (liquid–gas interface) temperature equal to the far field liquid temperature was assumed, with no thermal gradient on the liquid side.
(B) Inside the bubble, the same hypothesis as for case A was adopted. Outside the bubble, a non-linear temperature profile in the liquid was introduced, determined as an approximate analytical solution of the heat conduction–advection equation. Moreover, the wall temperature was evaluated from the heat balance at the wall including water liquid–vapor phase change effect.

1.2. Bibliographical review

In this section a short review of the recent literature concerning the pressure and temperature profiles inside and outside the bubble will be given.

Kwak and Na [8] calculated density, pressure and temperature distributions inside an air bubble by solving analytically the conservation PDEs but neglecting the viscous dissipation and water vapor. The time evolution of the bubble radius was obtained from the Keller–Miksis equation. The heat flux on the liquid side of the bubble wall was expressed by the boundary layer approximation with the layer thickness being a fitting parameter.

Yasui [10] used thoroughly the boundary layer approach in order to evaluate the time profiles of gas temperature, gas pressure, water content and bubble wall temperature for an argon bubble. As concerns the heat transfer between the gas and the liquid, he adopted an arbitrary layer thickness on the gas side and an exponential profile on the liquid side with one fitting parameter and he considered a heat balance at the wall including the phase change effect.

Toegel et al. [6] aimed at determining the amount of water vapor trapped in the bubble during the collapse and its impact on sonoluminescence. They used the boundary layer approach and considered a model consisting of 3 ODEs. The bubble wall radius was evaluated by the Keller–Miksis equation which takes water compressibility into account, the amount of water vapor inside the bubble was derived from a Fickian diffusion flux at the wall, the gas temperature was obtained from an energy balance which takes the heat conduction flux at the bubble wall into account. The mass and heat fluxes on the gas side were calculated using a boundary layer thickness evaluated as diffusion length at a characteristic time scale of the bubble motion. The gas pressure was derived from the van der Waals equation of state. The temperature at the bubble wall was supposed constant and equal to the far liquid one.

Kim et al. [9] solved the rigorous set of PDEs on the gas side but adopted the Keller–Miksis equation for the bubble wall motion and considered a priori a parabolic temperature profile in a thermal boundary layer on the liquid side. The thickness of the liquid boundary layer was estimated by means of an ODE obtained by the integration of the advection–conduction heat transfer equation over the layer. On this basis, the temperature profiles inside and outside an air bubble (without water vapor) were finally determined.

The approach of Vuong et al. [13] was very similar, excepted that no arbitrary temperature profile was adopted on the liquid side. The heat transfer equation in the liquid was transformed by the Plesset–Zwick method and simplified assuming a thin boundary layer (large Peclet's number) in order to obtain finally a linear diffusion equation in Lagrangian boundary layer coordinates which was solved numerically. Vuong et al. [13] used this model to determine the radial gas temperature profiles and bubble wall temperature time profiles for an argon bubble.

Yuan et al. [14] also transformed the advection–conduction equation on the liquid side into a purely diffusive one by means of the Plesset–Zwick variable change but made no further simplification to solve it. He calculated numerically the radial profiles of gas pressure, temperature, velocity and density for a bubble containing only air. The equations of liquid motion were not solved, the Keller–Miksis equation was used to describe the wall dynamics and the liquid compressibility was neglected in the heat transfer equation.

As concerns the heat transfer on the liquid side, Hauke et al. [15] adopted the less restrictive approach as compared to the already cited works. They solved numerically the full set of governing PDE on the gas side and the heat advection–conduction equation on the liquid side (neglecting only the liquid compressibility in the heat transfer equation) using the Keller–Miksis formulation to describe the bubble wall motion. They provided the radial profiles of temperature, pressure and water vapor content inside the bubble as well as the radial temperature profile outside the bubble.

In the context of therapeutic ultrasound, cavitation and bubble dynamics imply very high acoustic pressures and frequencies as well as elevated temperatures. In such conditions, the mass and heat transfer at the bubble wall are particularly important. To address the relevant physics, a reduced-order model of a single, spherical bubble was proposed by Kreider et al. [12] that incorporates phase change at the liquid–gas interface as well as heat and mass transport in both phases. Two approaches for heat transfer on the liquid side were modeled and compared. In the "scaling" approach (SCL model), uniform liquid temperature was assumed everywhere outside of a boundary layer near the bubble wall and a Fickian expression was used for calculating the thermal flux within the boundary layer. A fitting parameter was needed for estimating the boundary layer thickness. In the second approach the Plesset–Zwick analytical solution was used for describing thermal conduction in the presence of advective liquid flow due to bubble wall displacement. The idea of applying the Plesset–Zwick model for heat transfer on the liquid side used in several studies cited above was adopted for this study.

The applied acoustic driving conditions (P_{ac} – acoustic pressure amplitude, f – acoustic frequency, R_0 – initial bubble radius) and the corresponding gas temperature (T_g) as well as gas–liquid interface temperature (T_i) and pressure (P_{li}) at the collapse are presented in Table 1 for the considered publications and compared with the results of this study.

Independently of the conditions considered and thus of the maximal gas temperature obtained in each particular case, all the results shown above can be roughly classified in two groups: a first group where the bubble wall temperature is of the same order of magnitude than the bubble core one [8–10,12] and the second group where the wall temperature is one order of magnitude lower than the core one [13–15]. It is a very marked difference. Furthermore, again in a rough manner, it can be claimed that the results of the first group are based on simplified modeling approaches (boundary layer approximations, arbitrary liquid temperature profiles, analytical solutions) while those of the second group are based on a more comprehensive and rigorous

Table 1
Selected published acoustic cavitation simulations.

Refs.	Gas	P_{ac} (bar)	f (kHz)	R_0 (μm)	T_g (K)	T_i (K)	P_{li} (GPa)
[8]	Air	1.3	26.5	4.5	25,000	17,000	0.8
[10]	Argon and vapor	1.35	20.6	5	10,000	8000	
[14]	Air	1.275	26.4	4.5	15,000	500	4
[13]	Argon	1.3	26.5	4.5	106,000	4000	
[16]	Argon and vapor	1.3	16	5	15,000	293	
[9]	Air	1.33	12.9	5	28,000	13,500	
[15]	Argon and vapor	1.2	22.3	19.3	4300	360	0.13
[12]	Argon	1.2	26.5	4.5		4200	
This study, model A	Air and vapor	1.4	29	5	9300	263	18
This study, model B	Air and vapor	1.4	29	5	11,300	620	23

approaches (spatial variables distributions, no imposed profiles, numerical solutions). The results of the second group should be considered as the reference. It's obvious then that some degree of refinement is needed in order to catch correctly the thermal behavior of the system and this was the start point of our study.

2. Modeling

The exact description of the bubble dynamics during acoustic inertial cavitation can be only achieved by numerical solution of the full set of mass, momentum and energy conservation PDEs on both the gas and liquid side. Nevertheless, it had been proven that mathematically simplified approaches gave satisfactorily precise results [16]. The most straightforward simplification leading to a set of ODEs is the boundary layer approximation where the temperature and species profiles inside the bubble are supposed to be uniform with the exception of a thin boundary layer near the bubble wall [6,12].

In order to keep both mathematical simplicity and physical relevance, the basic concept of our single bubble model is based on Toegel's [6] (see 'Section 1.2') but substantial modifications have been made. First a more realistic representation of the heat transfer at the bubble wall was introduced through an energy balance involving the interfacial phase change heat flux and a conductive heat flux on the liquid side. Second a rigorous thermal and mechanical description was applied to the liquid, with the solution of the heat conduction–advection equation by the Plesset–Zwick [17] method and of the mass and momentum local conservation equations by the Gilmore's [2] method.

In the following subsections, the equations used to describe the acoustic inertial cavitation of a single bubble containing water and air will be presented, with the emphasis on the two approaches adopted in this study for heat transfer at the wall and in the liquid.

2.1. Thermodynamics of the gas

In this study, the focus is on the physics of liquid surrounding the bubble and the goal is to provide reasonably exact liquid pressure and temperature space profiles after the collapse. For this purpose a very fine model for the gas in the bubble is not necessary and thus global balances and state equations were used on the inner side of the bubble. The gas pressure P_g was considered uniform and evaluated by the classical equation of state with the van der Waals's correction for an incompressible (hard) core:

$$P_g = \frac{(N_v + N_a)\Re T_g}{\frac{4\pi}{3}(R^3 - R_{hc}^3)} \tag{1}$$

where N_a is the number of air moles, N_v the number of water vapor moles within the bubble, R the bubble radius, R_{hc} the hard core radius and T_g the gas temperature. While N_a was considered constant, N_v was considered to vary due to vapor diffusion through the air in the bubble from or to the wall. The vapor quantity balance in the bubble was based on a Fickian expression and a boundary layer assumption:

$$\frac{dN_v}{dt} = \frac{3D_{va}}{R\delta_{mg}}\left(\frac{4\pi R^3 P_{vsat}(T_i)}{3\Re T_i} - N_v\right) \tag{2}$$

where D_{va} is the water vapor in dry air diffusivity and P_{vsat} is the saturated water vapor pressure. The gas temperature T_g was considered uniform except in the close vicinity of the bubble wall and obtained from an overall bubble energy balance where the heat flux at the wall was evaluated by the boundary layer approximation:

$$(C_{vv}N_v + C_{va}N_a)\frac{dT_g}{dt} = -P_g 4\pi R^2 \frac{dR}{dt} + \lambda_g 4\pi R^2 \frac{T_g - T_i}{\delta_{tg}} + \frac{dN_v}{dt} \times (C_{pv}T_i - C_{vv}T_g) \tag{3}$$

where C_v or C_p are specific heat capacities for constant volume or constant pressure and T_i is the time dependent temperature at the bubble wall which must be obtained like a part of the solution of the global bubble cavitation model.

The boundary layer thicknesses for mass (δ_{mg}) and heat (δ_{tg}) transfer at the bubble wall were evaluated as a diffusion length during the characteristic time scale of the bubble oscillation:

$$\delta_{mg} = \min\left(\sqrt{D_{va}\frac{R}{|\dot{R}|}}, \frac{R}{2}\right) \tag{4}$$

$$\delta_{tg} = \min\left(\sqrt{\alpha_g\frac{R}{|\dot{R}|}}, \frac{R}{2}\right) \tag{5}$$

The pressure and temperature correlations for gas properties involved in the above equations: water vapor mass diffusivity in air D_{va}, vapor–air mixture heat conductivity λ_g, vapor–air mixture heat diffusivity α_g, saturated vapor pressure P_{vsat}, heat capacities C_{vv}, C_{va} C_{pv}, were all extracted from the well-known compilation of Poling et al. [18].

2.2. Mechanics of the wall and of the liquid

A single spherical gas bubble surrounded by liquid water is considered. The radial coordinate r originates at the center of the bubble. The mass and momentum conservation equations (Navier–Stokes equations) for a spherically symmetric liquid flow write respectively:

$$\frac{\partial \rho_l}{\partial t} + \frac{\partial}{\partial r}(\rho_l u_l) + \frac{2\rho_l u_l}{r} = 0 \tag{6}$$

$$\frac{\partial u_l}{\partial t} + u_l\frac{\partial u_l}{\partial r} + \frac{1}{\rho_l}\frac{\partial P_l}{\partial r} = 0 \tag{7}$$

where u_l is the liquid velocity, P_l is the liquid pressure and ρ_l its density. The boundary conditions associated to these equations are the liquid pressures and velocities at the wall and far away from the wall:

– at the bubble wall (underscript i) the velocity is determined by the wall motion, the pressure can be expressed by considering the mechanical forces balance involving the pressure force exerted by the gas, the surface tension force and the viscous friction force:

$$u_{li} = U = \frac{dR}{dt} \tag{8}$$

$$P_{li} = P_g - \frac{2\sigma_{gl}}{R} - \frac{4\mu_l}{R}\frac{dR}{dt} \tag{9}$$

where σ_{gl} is the gas–liquid surface tension and μ_l is the liquid dynamic viscosity;

– in the liquid far away from the bubble (underscript ∞), the velocity vanishes and the pressure is the sum of the ambient pressure and the driving acoustic pressure:

$$u_{l\infty} = 0 \tag{10}$$

$$P_{l\infty} = P_0 - P_{ac}\sin(\omega t) \tag{11}$$

As first demonstrated by Gilmore [2], these PDEs governing liquid mechanics around a spherical bubble can be reduced to a set of ODEs by using the Kirkwood–Bethe hypothesis. This hypothesis states that the quantity denoted here by z:

$$z = r\left(h_l + \frac{u_l^2}{2}\right) \tag{12}$$

is constant along any path traced by a point moving outward from the bubble wall with a varying total velocity which is a sum of the sound velocity in the liquid and of the liquid velocity ($c_l + u_l$). Such a path is called a characteristic and the position of the point is described by:

$$\frac{dr}{dt} = c_l + u_l \tag{13}$$

According to the above equations, differentiation along the characteristic gives:

$$\frac{dz}{dr} = \left(\frac{\partial}{\partial r} + \frac{1}{c_l + u_l}\frac{\partial}{\partial t}\right)z = 0 \tag{14}$$

In order to introduce the liquid sound velocity and the liquid enthalpy the following definitions are used:

$$c_l^2 = \frac{dP_l}{d\rho_l} \tag{15}$$

$$dh_l = \frac{dP_l}{\rho_l} \tag{16}$$

After combining the above definitions and the liquid state equation (Tait's equation, see below) with the starting mass and momentum conservation equations, the velocity and the pressure in the liquid are finally described as follows:

$$\frac{du_l}{dt} = \frac{1}{c_l - u_l}\left(-\frac{2c_l^2 u_l}{r} + \frac{(c_l + u_l)}{r^2}Z\right) \tag{17}$$

$$\frac{dP_l}{dt} = \frac{1}{c_l - u_l}(m(P_l + \beta)^{1/m})\left(\frac{4c_l^2 u_l^2}{r} - \frac{(c_l + u_l)^2}{r^2}Z\right) \tag{18}$$

where Z is the z value evaluated at the bubble wall and then:

$$Z = R\left(H_l + \frac{1}{2}\frac{dR^2}{dt}\right) \tag{19}$$

Following the same mathematical lines, the bubble wall motion is written as:

$$R\frac{dU}{dt}\left(1 - \frac{U}{C_l}\right) + \frac{3}{2}U^2\left(1 - \frac{U}{3C_l}\right) = H_l\left(1 + \frac{U}{C_l}\right) + \frac{R}{C_l}U\frac{dH_l}{dR}\left(1 - \frac{U}{C_l}\right) \tag{20}$$

$$\frac{dR}{dt} = U \tag{21}$$

where U is the bubble wall velocity, H_l and C_l are respectively the liquid enthalpy and sound velocity at the bubble wall.

Using the Tait's form of state equation for liquid which writes:

$$\rho_l(P,T) = \rho_{l0}(T)\left(\frac{P_l + \beta}{P_{l0} + \beta}\right)^{1/m} = \frac{\rho_0}{[1 + c(T - T_0)^d]}\left(\frac{P_l + \beta}{P_{l0} + \beta}\right)^{1/m} \tag{22}$$

the enthalpy and the sound velocity can be evaluated everywhere in the liquid (and specifically at the bubble wall) as a function of pressure by the following expressions:

$$h_l = \int_{P_{l\infty}}^{P_l}\frac{dP_l}{\rho_l} = \frac{m}{m-1}\frac{(P_{l0} + \beta)^{\frac{1}{m}}}{\rho_{l0}(T)}[(P_l + \beta)^{\frac{m-1}{m}} - (P_{l\infty} + \beta)^{\frac{m-1}{m}}] \tag{23}$$

$$c_l = \left(\frac{dP_l}{d\rho_l}\right)^{\frac{1}{2}} = \left(\frac{m(P_{l0} + \beta)}{\rho_{l0}(T)}\right)^{\frac{1}{2}}\left(\frac{P_l + \beta}{P_{l0} + \beta}\right)^{\frac{m-1}{2m}} \tag{24}$$

The coefficients of the Tait's equation for the low pressure domain were directly read from the study of Ridah [19] and are given in Table 2. The coefficients for the high pressure domain were obtained by fitting the Tait's equation to the data compiled by Choukroun and Grasset [20]. The density correction for temperature (function $\rho_{l0}(T)$) was adopted from the same study (see Table 2). The water gas–liquid interfacial energy σ_{gl} and the liquid water dynamic viscosity μ_l were also correlated to pressure and temperature [21–23]. It is worth noting that even in case of studies proposing complex models, published simulations were mostly realized with constant fluid properties, especially concerning the liquid. One of the advantages of the present study is that the gas and liquid properties are systematically correlated to pressure and temperature, even for very high pressures (as far as data exist).

2.3. Heat transfer at the wall and in the liquid

2.3.1. Model A

The heat flux between the gas bubble and the ambient liquid must be known for a proper evaluation of the bubble thermodynamics, motion and chemistry. For this purpose, according to the equations presented above, the fundamental issue is the evaluation of the bubble wall (or gas–liquid interface) temperature. The question arises if there is a simple way of estimating this temperature near the collapse. At this special moment, the variation of the gas temperature is very rapid and the hypothetical thermal boundary layer very narrow. Thus, in a first attempt one can consider the classical case of two semi-infinite solid bodies at different initial temperatures which are bring into contact. The heat conduction textbook's solution of this problem states that the ratio of temperature differences between the far and interface temperature for each of the two bodies corresponds to the square root of the ratio of their thermal effusivities (the effusivity is the product of density, thermal conductivity and specific heat capacity). For standard

Table 2
Coefficients of the state equation for liquid water (ρ: kg/m^{-3}, T: K, P: MPa).

	ρ_0	T_0	P_0	c	d	β	m
$P < 1000$	1007	180	0.1013	2.963×10^{-9}	3.17	303.9	7
$P > 1000$	Same as above					80	12.5

values of thermophysical properties of liquid water and air, the temperature gradient at the liquid side will be 2 or 3 order of magnitude smaller than the one at the gas side and so the interface temperature should be very close to the far liquid temperature. This estimation may justify the assumption of constant interface temperature used by several authors (see 'Section 1') for acoustic cavitation modeling. Such an assumption was adopted also for the simplest thermal model considered in this study (model A). It writes simply: $T_i = T_{1\infty} = \text{constant}$.

In this model, the bubble wall temperature is maintained at its lowest possible level and thus the cooling effect of the liquid is maximal.

2.3.2. Model B

The approach presented above is not really satisfactory because during the collapse the gas thermodynamical state is very far away from the standard one, the huge bubble volume reduction resulting in an enormous gas density increase and consequently thermal effusivity increase. The gas effusivity can be expected to become comparable to the liquid one at the collapse and the interface temperature to shift toward to the core gas temperature. Moreover, a vapor–liquid phase change takes place at the bubble wall and a heat balance equation involving the energy sink (or release) due to water evaporation (or condensation) is needed. A more rigorous approach accounting for these effects and also for the bubble dynamics is proposed below.

According to the mechanics of inertial cavitation (see preceding section), the bubble radius R is a given function of time. Due to the radial movement of the bubble wall the liquid is displaced in the vicinity of the bubble. The heat transfer equation for incompressible liquid with constant thermal properties involving molecular diffusion and advection due to liquid motion is written as:

$$\frac{\partial T_l}{\partial t} + u_l \frac{\partial T_l}{\partial r} = \frac{\alpha_l}{r^2} \frac{\partial}{\partial r}\left(r^2 \frac{\partial T_l}{\partial r}\right) \tag{25}$$

where the heat diffusivity is defined as $\alpha_l = \lambda_l/(\rho_l c_{pl})$ and the liquid velocity for incompressible flow is given by:

$$u_l = \frac{R^2}{r^2}\frac{dR}{dt} \tag{26}$$

For the determination of the temperature profile, the liquid incompressibility is assumed, but for determination of the pressure profile the compressibility of liquid has been accounted for as explained in preceding subsection.

The initial and boundary conditions for the above equation are given by:

– boundary condition at the bubble wall: $r = R(t)$

$$-\lambda_l \frac{\partial T_l}{\partial r} = \frac{\Phi_{li}(t)}{4\pi R^2(t)} \tag{27}$$

– boundary condition in far liquid: $r = \infty$

$$T_l = T_{l\infty} \tag{28}$$

– initial condition: $t = 0$

$$T_l = T_{l\infty}$$

The time dependent heat flux at the bubble wall Φ_{li} corresponds to the conductive heat flux in the gas inside the bubble and the latent heat flux of water evaporation/condensation at the wall:

$$\Phi_{li}(t) = 4\pi R(t)^2 \lambda_g \frac{T_g(t) - T_i(t)}{\delta_{tg}(t)} - \frac{dN_v}{dt} M_v \Delta h_{vap}(T_i) \tag{29}$$

In order to solve analytically this problem, independent variable changes will be operated according to the Plesset–Zwick method (see 'Section 1.2').

First, the spatial variable r will be replaced by a new variable y defined by:

$$y = \frac{r^3 - R^3(t)}{3} \tag{30}$$

The new variable corresponds dimensionally to a volume of liquid and (if liquid incompressibility is assumed) is associated to a material point moving along with the displacement of the bubble wall. The new variable is thus a Lagrangian one and the transfer equation will lose its advective term and will become a strictly diffusive one:

$$\frac{\partial T_l}{\partial t} = \alpha_l \frac{\partial}{\partial y}\left[\left(3y + R^3(t)\right)^{4/3} \frac{\partial T_l}{\partial y}\right] \tag{31}$$

In the limit $y \ll R^3$, what means that the temperature in the liquid is supposed to vary significantly only in a small distance from the bubble wall, the above equation becomes:

$$\frac{1}{R^4(t)}\frac{\partial T_l}{\partial t} = \alpha_l \frac{\partial^2 T_l}{\partial y^2} \tag{32}$$

Now using a new temporal variable τ defined by

$$\tau = \int_0^t R^4(t)dt \tag{33}$$

the heat transfer equation transforms simply to:

$$\frac{\partial T_l}{\partial \tau} = \alpha_l \frac{\partial^2 T_l}{\partial y^2} \tag{34}$$

what is a canonical parabolic PDE which solution obtained by the Laplace transform can be found in the references cited above but also in heat conduction textbooks. This solution, for a prescribed time dependent heat flux Φ_{li} at the boundary, writes:

$$T_l(y,\tau) - T_{l\infty} = \frac{\sqrt{\alpha_l}}{4\pi^{3/2}\lambda_l} \int_0^\tau \frac{\Phi_{li}(x)}{R^4(x)\sqrt{\tau - x}} \times \exp\left(-\frac{y^2}{4\alpha_l(\tau - x)}\right)dx \tag{35}$$

The above approach based on the Plesset–Zwick approximation was adopted for the final thermal model of this study (model B). The literature expressions of heat conductivity λ_l [24] and specific heat capacity c_{pl} [20] as function of temperature were used. The influence of pressure on these two parameters was neglected.

The model is very sensitive to mass diffusivity (D_{va}) and heat diffusivities on the gas side (α_g) and on the liquid side (α_l). As concerns the bubble interior, the gas thermal properties are rather well known and well correlated to pressure and temperature [18]. Moreover, the boundary layer approach inside the bubble was proven to give satisfactory results compared to a full solution considering a radial temperature profile inside the bubble [16]. However, the boundary layer approximation outside the bubble suffers from a lack of generally accepted time scale definition for the diffusion length evaluation and from a lack of reliable liquid thermal data, especially for high pressures. In the frame of this study, a boundary layer approach for heat diffusion on the liquid side was tried applying the same time scale as on the gas side (see Eqs. (4) and (5)). That resulted in a not realistic very high temperature at the bubble wall (around 1700 K) at the moment of the collapse and this approach was abandoned. Kwak and Na [8], Yasui [10] and Kreider et al. [12] have used an arbitrary temperature profile or a boundary layer thickness with a fitting parameter. The

Plesset–Zwick approximation [12–14] adopted here avoids introducing such a kind of workarounds.

2.4. Numerical solution of the problem

The bubble dynamics was simulated by solving simultaneously the Eqs. (2), (3), (20) and (21) as a system of first order ODEs by means of MATLAB routine ODE113. At any time t, the solution provided the bubble radius R, bubble wall velocity U, the gas temperature inside the bubble T_g and the vapor quantity inside the bubble N_v. The gas pressure P_g inside the bubble was then calculated by Eq. (1) and the liquid temperature T_i at the bubble wall by Eq. (35). This last equation provided also the liquid temperature distribution all around the bubble.

The liquid dynamics around the bubble was simulated by solving simultaneously the Eqs. (13), (17) and (18) as a system of first order ODEs (MATLAB routine ODE45). The calculations were carried out along a characteristic, each characteristic originating at the bubble wall. Starting from the given conditions at the bubble wall (R, H_l, C_l), for any time subsequent time t, the solution provided the corresponding radial position r along the characteristic and the value of the liquid pressure P_l and liquid temperature T_l at this position. Many characteristics had to be used in order to cover the entire geometrical domain around the bubble.

3. Results and discussion

3.1. Pressure and temperature at the bubble wall

In this section the simulations obtained with the two thermal models (A and B) will be compared. The temporal evolutions of the bubble wall position, the internal gas temperature, the liquid temperature and pressure at the bubble wall are presented on Figs. 1–3. The Figs. 2 and 3 are focused on the first collapse. The gas pressure inside the bubble and the liquid pressure at the bubble wall were found to be quite identical at the collapse and only the liquid pressure was shown. The acoustic and ambient conditions used for the calculations are given in Table 3. The ambient temperature is below zero because this model was intended to be applied later to the case of water freezing induced by ultrasound.

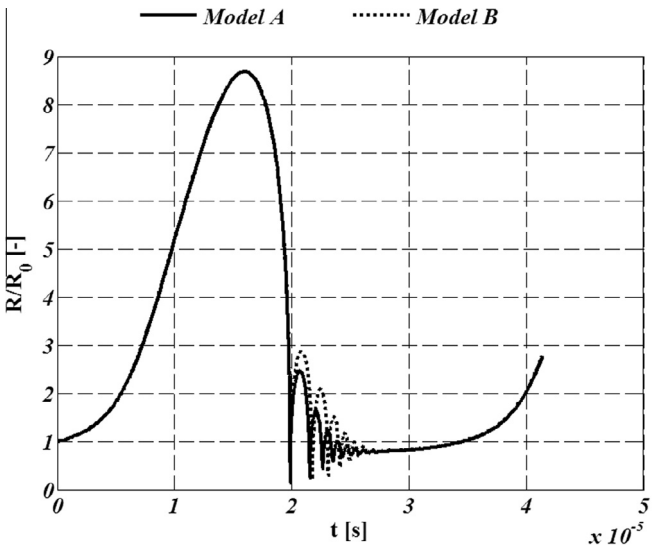

Fig. 1. The time profiles of the bubble radius (R) over one period of the acoustic excitation.

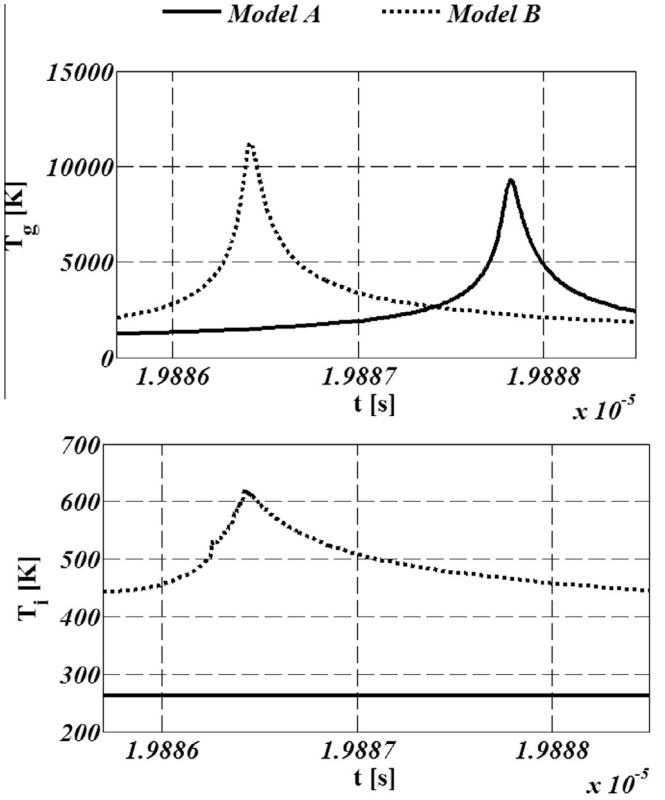

Fig. 2. The time profiles of the internal gas temperature (T_g) and the interfacial liquid temperature (T_i) at the collapse.

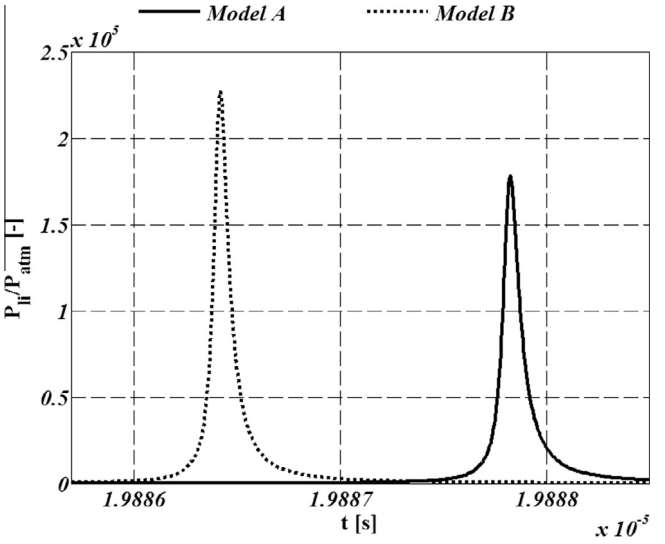

Fig. 3. The time profiles of the interfacial liquid pressure (P_{li}) at the collapse.

Table 3
Parameters of the simulations.

R_0 (μm)	$T_{l\infty}$ (°C)	P_{ac} (bar)	f (kHz)
5	−10	1.4	29

As reported elsewhere, during inertial cavitation the bubble expands rather slowly to several times its initial size and then collapses violently. The huge nearly adiabatic compression of the gas due to the collapse heats up very strongly the bubble core

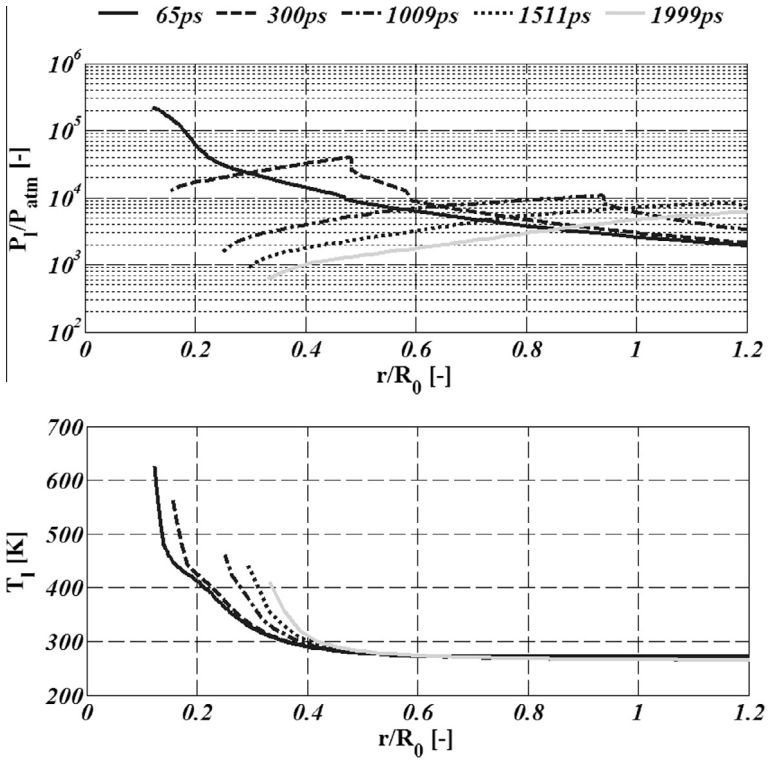

Fig. 4. The radial profiles of liquid pressure (P_l) and liquid temperature (T_l) around a bubble for different times after the collapse.

inducing a temperature and pressure peaks. According to Fig. 1, the thermal model did not affect sensibly the dynamic behavior of the bubble wall, excepted for the post-collapse rebounds. However, the thermal model affected considerably all the thermodynamic variables inside the bubble and at the wall. The temperature of the gas inside the bubble was found to be 20% lower for the model A (9300 K) than for model B (11,300 K). This can be justified by the fact that model A corresponded to a stronger cooling rate of the bubble (see Fig. 2). Consequently, the pressure of liquid at the wall (nearly equal to the internal gas pressure at the collapse) was also 20% lower for case A (18 GPa) than for case B (23 GPa) as shown on Fig. 3. The time of the collapse was slightly different for the two cases.

The thermal model had by evidence the strongest impact on the temperature at the bubble wall. According to Fig. 2, this interfacial temperature for comprehensive model B was rather moderate (620 K) and did not reach the critical value for water (647 K). It was much closer to the far liquid (ambient) temperature (263 K) than to the core temperature (11,300 K). However, substituting the interfacial temperature by the ambient temperature appears clearly as a not realistic hypothesis, especially if temperature sensitive physical and chemical phenomena in the liquid are studied. This result corroborates those corresponding to the most elaborate models and numerical simulations published in the literature (see Table 1), with some caution because of different parameters (acoustic frequency, gas specie).

The bubble interior energy balance (Eq. (3)) does not include the heat effect of chemical reactions. However, the water vapor trapped within the bubble undergoes rapid reactions when the temperature exceeds 3000 K and leads to the production of hydroxyl radicals. Several authors included chemical reactions in their cavitation model and concluded that the endothermic dissociation of water vapor significantly reduced the bubble core peak temperatures (T_g) achieved at the collapse. According to Hauke et al. [15] (argon and vapor, P_{ac} = 1.2 bar, f = 22.3 kHz, R_0 = 19.3 μm) vapor dissociation accounts for 10% of the core temperature (T_g) reduction and according to Storey and Szeri [25] (argon plus vapor, P_{ac} = 1.2 bar, f = 26.5 kHz, R_0 = 4.5 μm), it accounts for up to 30%. But the liquid temperature (T_l) at the bubble wall was supposed and shown to be much less impacted. Supplementary simulations with our model B showed that a 30% decrease of T_g corresponded to a 5% decrease in T_l. So the error of calculating T_l due to chemical reactions omission would be no more than 5%, which is in the range, or even below, of the error induced by the uncertainty on gas and liquid thermo-physical properties.

The model B proposed in this study comprehends all the relevant thermal phenomena and at the same time it writes mathematically rather simply. The thermal model B coupled with the fluidics and thermodynamics model of cavitation proposed in this study writes as a set of ODE's and solves more conveniently (MATLAB) and quickly than a full multi-physics model based on PDE's which requires a finite element software. At the same time, this model gives realistic results, similar to those provided by complex models and sophisticated solvers. It could be a useful tool for fast prediction of pressure and temperature conditions around a single cavitating bubble, with applications to sono-chemistry and sono-crystallization. In the next part of this paper, only simulations obtained with model B will be presented.

3.2. Liquid pressure and temperature near the bubble

The spatial distributions of the temperature and pressure in the liquid outside the bubble just after the collapse are presented on Fig. 4. The first considered time (65 ps) corresponds to the time of maximum pressure at the bubble wall, the time zero being the time of the collapse defined as the maximum of bubble wall velocity.

As observed on liquid pressure profiles, a pressure peak which can be assimilated to a shockwave propagates in the liquid at a very high speed and is attenuated as moving away from the

bubble. As concerns liquid temperature, the spatial profiles present 2 different zones: a very narrow (100–200 nm) zone with a very steep quasi-linear gradient and a broader (1–2 μm) zone with a progressively decreasing gradient. The occurrence of these two zones and the important spatial extension of the second one invalidates a simple calculation of the heat flux in the liquid based on a linear temperature profile over a thermal boundary layer and proves well the necessity of a very fine description of heat transfer between the bubble and the liquid.

Besides, according to Fig. 4, the zone of strong temperature variation was roughly two times smaller than the zone of very high pressures (above 1 GPa). That means that an area with already nearly ambient temperature but still very high pressure existed near the bubble after the collapse. This conjunction could promote sono-crystallization processes, in solutions [26] or melts [7].

4. Conclusion

On the ground of a literature review, a mathematically simple but physically comprehensive model of inertial acoustic cavitation and especially of a single gas bubble collapse was developed. Two different approaches were proposed for modeling the heat transfer between the ambient liquid and the gas: the simplified approach (A) with liquid acting as perfect heat sink, the rigorous approach (B) with liquid acting as a normal heat conducting medium. The values of the bubble radius, gas temperature, interface temperature and pressure corresponding to the above models were calculated in a time interval encompassing the collapse and compared. Important differences were observed for gas and liquid temperatures and may be interpreted as a rebuttal against the simplified heat transfer description, often used in cavitation models. The exact pressure and temperature distributions in the liquid after the collapse, calculated with the second model (B), were presented. The temperature at the bubble wall was found much closer to the ambient liquid one than to the bubble core one. An area with already nearly ambient temperature but still very high pressure was observed near the bubble just after the collapse. These results are the basis for the prediction of any physical phenomena occurring around the bubble, especially of the dissolved or melted phase crystallization, and thus the basis for the control of industrial processes relying on acoustic cavitation. An application to ice sono-crystallization in aqueous solutions will be described in the second part of this paper.

Acknowledgment

This work was financially supported by the French governmental research funding agency ANR in the frame of the project '09-BLAN-0040-SONONUCLICE'.

References

[1] F. Baillon, F. Espitalier, C. Cogné, R. Peczalski, O. Louisnard, Crystallization and Freezing Processes Assisted by Power Ultrasound, in: Juan A. Gallego-Juárez, Karl Graff (Eds.), Power Ultrasonics: Applications of High-Intensity Ultrasound, first ed., Woodhead Publishing, Cambridge, 2014.
[2] F.R. Gilmore, The growth or collapse of a spherical bubble in a viscous compressible liquid, California Institute of Technology Pasadena (Technical Report, unpublished), 1952.
[3] J.B. Keller, M. Miksis, Bubble oscillations of large amplitude, J. Acoust. Soc. Am. 68 (2) (1980) 628–633.
[4] A. Prosperetti, Y. Hao, Modelling of spherical gas bubble oscillations and sonoluminescence, Philos. Trans. R. Soc. London 357 (1999) 203–223.
[5] M.S. Plesset, A. Prosperetti, Bubble dynamics and cavitation, Ann. Rev. Fluid Mech. 9 (1977) 145–185.
[6] R. Toegel, B. Gompf, R. Pech, Does water vapor prevent upscaling sonoluminescence?, Phys Rev. Lett. 85 (15) (2000) 3165–3168.
[7] M. Saclier, R. Peczalski, J. Andrieu, A theoretical model for ice primary nucleation induced by acoustic cavitation, Ultrason. Sonochem. 17 (2010) 98–105.
[8] H. Kwak, J. Na, Hydrodynamic solutions for a sonoluminescing gas bubble, Phys. Rev. Lett. 77 (1996) 4454–4457.
[9] K. Kim, B. Byun, H. Kwak, Temperature and pressure fields due to collapsing bubble under ultrasound, Chem. Eng. J. 132 (2007) 125–135.
[10] K. Yasui, Alternative model of single-bubble sonoluminescence, Phys. Rev. 56 (6) (1997) 6750–6760.
[11] A.J. Szeri, B.D. Storey, A. Pearson, J.R. Blake, Heat and mass transfer during the violent collapse of nonspherical bubbles, Phys. Fluids 15 (2003) 2576–2586.
[12] W. Kreider, L.A. Crum, M.R. Bailey, O.A. Sapozhnikov, A reduced-order, single-bubble cavitation model with applications to therapeutic ultrasound, J. Acoust. Soc. Am. 130 (5) (2011) 3511–3530.
[13] V.Q. Vuong, A.J. Szeri, D.A. Young, Shock formation within sonoluminescence bubbles, Phys. Fluids 11 (1) (1999) 10–17.
[14] L. Yuan, H.Y. Cheng, M.C. Chu, P.T. Leung, Physical parameters affecting sonoluminescence. A self-consistent hydrodynamic study, Phys. Rev. 57 (4) (1998) 4265–4280.
[15] G. Hauke, D. Fuster, C. Dopazo, Dynamics of a single cavitating and reacting bubble, Phys. Rev. E 75 (2007) 1–14.
[16] B.D. Storey, A.J. Szeri, A reduced model of cavitation physics for use in sonochemistry, Proc. R. Soc. A Math. Phys. Eng. Sci. 457 (2001) 1685–1700.
[17] M.S. Plesset, S.A. Zwick, A nonsteady heat diffusion problem with spherical symmetry, J. Appl. Phys. 23 (1) (1952) 95–98.
[18] B.E. Poling, J.M. Prausnitz, J.P. O'Connell, The properties of gases and liquids, fifth ed., McGraw-Hill, New York, 2001.
[19] S. Ridah, Shock waves in water, J. Appl. Phys. 64 (1986) 152–158.
[20] M. Choukroun, O. Grasset, Thermodynamic model for water and high-pressure ices up to 2.2 GPa and down to the metastable domain, J. Chem. Phys. 127 (2007) 124506.
[21] E. Mezger, Loi de variation de la tension superficielle avec la température, Journal de physique 10 (1946) 303–309.
[22] M.L. Huber, R.A. Perkins, A. Laesecke, D.G. Friend, J.V. Sengers, M.J. Assael, I.N. Metaxa, E. Vogel, R. Mares, K. Miyagawa, New international formulation for the viscosity of H20, J. Phys. Chem. Ref. Data 38 (2) (2009) 101–125.
[23] E.H. Abramson, Viscosity of water measured to pressure of 6 GPa and temperatures of 300 °C, Phys. Rev. E 76 (2007) 051203.
[24] M.L.V. Ramires, C.A. Nieto de Castro, Y. Nagasaka, A. Nagashima, M.J. Assael, W.A. Wakeham, Standard reference data for the thermal conductivity of water, J. Phys. Chem. Ref. Data 24 (1995) 1377–1381.
[25] B.D. Storey, A.J. Szeri, Water vapour, sonoluminescence and sonochemistry, Proc. R. Soc. London A Math. Phys. Eng. Sci. 456 (2000) 1685–1709.
[26] C. Virone, H.J.M. Kramer, G.M. van Rosmalen, A.H. Stoop, T.W. Bakker, Primary nucleation induced by ultrasonic cavitation, J. Cryst. Growth 294 (1) (2006) 9–15.

Ultrasonics Sonochemistry 28 (2016) 185–191

Contents lists available at ScienceDirect

Ultrasonics Sonochemistry

journal homepage: www.elsevier.com/locate/ultson

Theoretical model of ice nucleation induced by inertial acoustic cavitation. Part 2: Number of ice nuclei generated by a single bubble

C. Cogné [a], S. Labouret [a], R. Peczalski [a,*], O. Louisnard [b], F. Baillon [b], F. Espitalier [b]

[a] University of Lyon, France, Université Claude Bernard Lyon 1, Laboratoire d'Automatique et de Génie des Procédés (LAGEP UMR CNRS 5007), Campus de la Doua, Bât. CPE, 69616 Villeurbanne, France

[b] University of Toulouse, France, Ecole Nationale Supérieure des Mines d'Albi-Carmaux, Centre de Recherche d'Albi en génie des Procédés des Solides Divisés, de l'Énergie et de l'Environnement (RAPSODEE UMR CNRS 5302), Campus Jarlard, 81013 Albi, France

ARTICLE INFO

Article history:
Received 8 May 2015
Received in revised form 9 July 2015
Accepted 20 July 2015
Available online 20 July 2015

Keywords:
Ultrasound
Cavitation
Single bubble
Liquid undercooling
Ice
Nucleation rate

ABSTRACT

In the preceding paper (part 1), the pressure and temperature fields close to a bubble undergoing inertial acoustic cavitation were presented. It was shown that extremely high liquid water pressures but quite moderate temperatures were attained near the bubble wall just after the collapse providing the necessary conditions for ice nucleation. In this paper (part 2), the nucleation rate and the nuclei number generated by a single collapsing bubble were determined. The calculations were performed for different driving acoustic pressures, liquid ambient temperatures and bubble initial radius. An optimal acoustic pressure range and a nucleation temperature threshold as function of bubble radius were determined. The capability of moderate power ultrasound to trigger ice nucleation at low undercooling level and for a wide distribution of bubble sizes has thus been assessed on the theoretical ground.

1. Introduction

1.1. Context and aim

Controlling the distribution of ice crystal sizes is a key issue in industrial freezing and freeze-drying processes. Ultrasound is already known to be able to initiate the nucleation of ice in undercooled aqueous solutions and to make the freezing reproducible at the desired temperature. But ice crystals' size predictive tools are still missing for design and optimization of ultrasound assisted freezing processes.

As concerns sono-crystallization from solutions, quantitative theoretical prediction of nucleation was pioneered by Virone et al. [1] and applied to ammonium sulphate crystals. However as concerns crystallization from melts and to our best knowledge, Saclier et al. [2] were for the time being the only authors proposing a fully predictive model of ice nucleation triggered by inertial acoustic cavitation. Their model was applied to a 1 ml pure water sample with a known (measured) bubbles' size distribution and the total number of nuclei was calculated as function of the acoustic pressure and water temperature. The model involved however several simplifications and approximations, especially concerning heat balance of the bubble, heat transfer in the water around the bubble and water thermo-physical properties at very high pressures. The goal of this study was to develop a finer and more comprehensive modeling and to propose nucleation thresholds for bubbles of different initial radii.

The authors of the present study have chosen to continue working with the 'pressure rise effect' [3] (see next section) as the nucleation mechanism and set up a comprehensive theoretical model starting from the bubble wall motion induced by inertial cavitation (see part I) and finishing with the number of nuclei generated by the collapse of a single bubble. In the previous paper [4] (part 1), the pressure and temperature fields close to a bubble undergoing inertial acoustic cavitation were simulated and it was shown that extremely strong liquid water pressures but quite moderate temperatures were reached near the bubble wall just after the collapse.

The next step described in this paper (part 2) was to develop a model of ice nucleation and integrate the nucleation volume rate equation over space and time, using the pressure and temperature profiles induced by the collapse of the bubble in order to obtain finally the number of generated nuclei.

As concerns nucleation kinetics, the classical equation for primary stationary homogeneous nucleation was applied [5], but the parameters of this equation had to be made pressure and temperature dependent.

* Corresponding author.
E-mail address: peczalski@lagep.univ-lyon1.fr (R. Peczalski).

http://dx.doi.org/10.1016/j.ultsonch.2015.07.019
1350-4177/

1.2. Bibliographical review

In this section a short literature review concerning first the experimental evidence of the effect of ultrasound on ice crystallization and second the theories about the ice nucleation mechanism by ultrasound, will be presented.

Inada et al. [6] and Zhang et al. [7] studied the potential application of ultrasonic waves to produce ice slurries. They found out that applying ultrasound greatly increased the probability of phase change from undercooled water to ice at a given initial water temperature. The probability of phase change was calculated as the ratio of the number of successful freezing tests to the total number of tests in given conditions. The occurrence of phase change induced by ultrasound increased with the total number of gas bubble nuclei in undercooled water, independently of other experimental conditions.

Chow and co-authors [8,9] evaluated the effect of ultrasounds on the primary and secondary nucleation of ice in sucrose solutions. They presented direct optical observations of crystals formed around an immersed sonication probe, around a single levitating and cavitating bubble and in a special ultrasonic cold stage. They pointed out that the primary nucleation of ice in sucrose solutions can be achieved at higher nucleation temperatures in the presence of ultrasound. It was also shown that the nucleation temperatures of ice increase with increasing ultrasonic power. It was observed that pre-existing ice crystals could be fragmented by ultrasound, which modifies the size distribution and generates nucleation sites.

Nakagawa et al. [10] and Hottot et al. [11] carried out freezing and freeze-drying experiments with an aqueous solution of mannitol in a small glass tube (vial). The vials were cooled down and sonicated by means of a cold vibrating plate. Ice crystals were observed using reflected-light optical microscopy over frozen samples in transversal and longitudinal sections. It was shown that the nucleation could be readily triggered at selected sample temperature values below the equilibrium freezing temperature and that small and numerous ice crystals were obtained at lower nucleation temperature (higher undercooling level), while large and directional ice crystals (dendrite type) were obtained at a higher nucleation temperature (lower undercooling level). Saclier et al. [12] continued the work on mannitol solution sono-freezing in vials. Using the same apparatus and methodology, they confirmed the above qualitative results but further adopted a second order experimental design and quantitatively assessed the effect of both the nucleation temperature and the acoustic power on the final crystal size and shape. The ice crystal size was found to decrease with both the level of undercooling and the acoustic power level, whereas their circularity was found to increase with these parameters.

Kiani et al. [13] studied ultrasound-assisted nucleation of pure water, sucrose solution, and agar gel samples inserted in tubing vials. The vials were immersed in an ultrasonic bath. Ultrasound was applied continuously for different durations and at different sample temperatures in the range up to 5 °C below the freezing point. They observed that ultrasound can trigger ice nucleation with high repeatability at the targeted temperatures and hence can be used to control the onset of nucleation. In a continuation of this study [14], the effect of ultrasound intensity on the nucleation of ice in agar gel samples was additionally studied. It was observed that ultrasound irradiation was able to initiate nucleation at different undercooling levels of the gel if optimum intensity and duration of ultrasound application were chosen.

Although ultrasound has long been used to initiate nucleation in undercooled aqueous solutions, the exact mechanism that explains this effect is not yet well known. Acoustic cavitation (the sudden formation and collapse of gas bubbles in liquids by means of ultrasound) appears to cause the nucleation of ice. There is a distinction between stable cavitation when a bubble pulsates about an equilibrium radius over many acoustic cycles and inertial cavitation when the bubble grows extensively and finally collapses [15].

According to the theoretical study by Hickling [3] very high positive pressures occurring during the final stage of the collapse of a bubble in inertial cavitation increase the equilibrium temperature of water and ice (VI or VII, denser than liquid water), thus enhancing nucleation of a specific ice solid phase. The weak point of this scenario is the uncertainty about a subsequent transformation of the nucleated high pressure ice phase into low pressure regular ice Ih. According to another model [16], nucleation is caused by negative pressures that follow the collapse of the cavitation bubble. This effect will produce low pressure ice Ih, but this idea was questioned by the experiments of Ohsaka and Trinh [17].

On the ground of the Hickling's hypothesis, Inada et al. [6] made an attempt to deduce the probability of phase change from undercooled water to ice from the probability of inertial acoustic cavitation of a given bubble population. But in order to fit their experimental results, they needed to adjust two parameters and their model was not predictive.

According to some other experimental results [9], the moderate oscillation of a bubble in stable cavitation may also induce ice nucleation. These authors suggest micro-streamings as a factor promoting nucleation. The other possible nucleation mechanism is the concentration and agglomeration of ice clusters near the bubble due to pressure diffusion (transfer mechanism driving the densest species toward high-pressure zones). On the basis of theoretical considerations, Grossier and co-workers [18,19] argued that the very high pressure gradients that are needed for pressure diffusion to be effective are attainable only for collapsing bubbles. They thus indirectly refuted stable cavitation as a nucleation initiator.

As suggested by Kordylla et al. [20] and Yasui et al. [21], the occurrence of gas/liquid interface (at the bubble wall) in a supersaturated sonicated solution may induce a kind of heterogeneous nucleation, by reducing interfacial solid–liquid tension and thus reducing the nucleation energy barrier (ΔG_c) according to the classical nucleation theory (CNT). Kordylla et al. [20] has in fact identified the contact angle minimizing a least-square error between experimental and theoretical values. This is however rather a 'curve fitting' approach than a real physical model of sono-nucleation. Some studies have demonstrated that single bubbles do not exhibit this effect [8].

More importantly, applying CNT in a global manner for sono-crystallization is not straightforward, since this theory relies on a (metastable) equilibrium hypothesis. At the scale of a bubble, there exists huge pressure gradients (and to a lesser extent temperature gradients) near the bubble, so that the supersaturation itself is distributed over space and time. Thus, considering the nucleation work (ΔG_c) as constant is a somewhat rough approximation in this situation. Possibly, one could invoke a local equilibrium hypothesis, calculate a spatio-temporal profile $\Delta G_c(r,t)$ around the bubble, and deduce a local instantaneous nucleation rate. This is the idea underlying the 'pressure effect' tentatively quantified in the literature [1,2] and developed in this study.

However, even when accounting for such refinement, the hypothesis of stationary nucleation is always done. In fact, local supersaturation varies on the same time scale as the bubble radius (or shorter in the case of shock waves). If this time scale is of the same order of magnitude as the so-called nucleation time lag, nucleation may be in fact transient. Thus, estimations based on quasi-stationary nucleation may be largely overestimated [22].

A quite novel idea about the nucleation mechanism has arisen very recently [23]. The physics of inertial cavitation states that the bubble interior heats up due to a quasi-adiabatic compression just before the collapse, but then cools down due to a

quasi-adiabatic expansion of the bubble just after the collapse. According to simulations, the temperature of the gas mixture inside the bubble falls to between −30 °C and −60 °C after the collapse, depending on operating conditions. According to the water state diagram, this means that all the water vapor is in a highly metastable undercooled state and could easily transform into ice Ih. This raises two issues, however: is the metastable water period long enough to induce ice nucleation? And how might the ice nuclei invade the surrounding liquid, breaking the bubble wall?

Even if different theories exist and some experimental results were published, no quantitative predictive modeling approach has been proposed until now to assess the impact of ultrasound on nucleation and crystallization of ice in undercooled aqueous solutions, except for the work of Saclier et al. [2].

2. Modeling

2.1. Nucleation kinetics

Nucleation is the process of random generation of small (nano-metrical) aggregates (nucleus) of the new phase that have the ability for irreversible growth to macroscopically large sizes. The driving force for nucleation is the difference of chemical potential of the considered component in the old (liquid) and the new phase (solid). In the case of crystallization from melt by cooling, this driving force is expressed as a function of the so-called 'undercooling' which is the difference between the actual temperature of the liquid T and the theoretical melting temperature of the solid phase T_m [5]:

$$\Delta\mu = -L_m(P)\frac{T - T_m(P)}{T_m(P)} \tag{1}$$

where L_m is the solid phase melting enthalpy per unit mass, P is the liquid phase pressure. Atypically $\Delta\mu$ is expressed here in J/kg. The subscript 'm' points out values in solid–liquid thermodynamical equilibrium conditions. The expression above should have been corrected with a term involving the difference between liquid phase and solid phase specific heat capacity (Δc_{pm}) for very high 'undercoolings' ($\Delta T > 2L_m/(\Delta c_{pm})$). But due to the important uncertainty about the ice heat capacity values at high pressures, this correction had not been applied. The ice melting enthalpy can be expressed with the slope of the equilibrium temperature curve by the classical Clausius–Clapeyron equation:

$$L_m(P) = \left(\frac{dT_m}{dP}\right)^{-1} T_m(P)\left[\frac{1}{\rho_{lm}(P)} - \frac{1}{\rho_{sm}(P)}\right] \tag{2}$$

where L_m is expressed in J/kg and ρ is the mass density of liquid (l) or solid phase (s).

In this study only primary homogeneous nucleation was considered, which is occurring when the clusters of the new phase are in contact only with the old phase and with no other phases or species. According to the classical nucleation theory [5], the rate of formation of such clusters is basically controlled by the energy barrier a cluster has to overcome in its evolution to a stable solid phase and by the frequency of new molecule attachment to the cluster. The energy barrier is calculated as the Gibbs free energy variation necessary for a cluster to reach its critical size (minimum radius of a stable spherical nucleus). The total free energy variation of a cluster is a sum of the free-energy gain due to the liquid–solid phase change and the free-energy loss associated with the creation of the liquid–solid interface. The total free-energy function has a maximum at the critical cluster size. This maximum corresponds to the energy barrier for cluster formation and is inversely proportional to the square of the undercooling of the melt. The Gibb's free enthalpy of one critical size cluster formation writes:

$$\Delta G_c(T,P) = \frac{16\pi}{3}\frac{\sigma_{sl}^3(T,P)}{\rho_s^2(T,P)\Delta\mu^2(T,P)} \tag{3}$$

where ΔG_c is expressed in J (per cluster) and σ_{sl} is the liquid–solid surface tension.

The primary homogenous nucleation rate J is defined as the number of nuclei generated per unit of volume of the liquid and per unit of time. The nucleation rate represents the frequency of appearance at time t of supercritical clusters per unit of volume. At an absolute temperature T, the fraction of clusters that have the size greater than the critical one (by just a single molecule) can be calculated from statistical mechanics and is given by the Boltzmann distribution based on the hypothesis that the probability of some state arising by fluctuation is proportional to the negative exponential of the entropy change involved. The nucleation rate writes then:

$$J(T,P) = J_0(T,P)\exp\left[-\frac{\Delta G_c(T,P)}{kT}\right] \tag{4}$$

where k is the Boltzmann constant. It is expressed here in number per m^3 and per s.

The pre-exponential factor J_0 describes the rate of adjoining new molecules to existing critical clusters (aggregation). The diffusion of critical clusters in the liquid is usually assumed as the aggregation rate limiting mechanism. If the diffusion coefficient is expressed by the Stokes–Einstein formula (of spherical particles through a liquid with low Reynolds number), the dynamic viscosity of the liquid η_l appears as a key parameter. The kinetic factor of aggregation writes then [5]:

$$J_0(T,P) = \frac{4[\sigma_{sl}(T,P)kT]^{1/2}[\rho_s(T,P)N_A]^{5/3}}{\eta_l(T,P)(6M)^{5/3}\pi^{1/3}}\exp\left[-\frac{L_m(P)M}{kN_AT_m(P)}\right] \tag{5}$$

where M is the molecular mass of the liquid, N_A the Avogadro number.

2.2. Number of nuclei

As shown in equations presented above, the nucleation rate is a function of liquid pressure and temperature. By means of the model developed in the part 1 of this study, the pressure and temperature in the liquid adjacent to the bubble wall just before and just after the collapse can be calculated as function of time t and radial distance from bubble center r. In this way the nucleation rate $J(P, T)$ becomes a function of radius and time $J(r, t)$ and can be integrated over a liquid volume surrounding the bubble and over time in order to calculate the number of nuclei N generated by the bubble.

$$N = 4\pi\int\int_{R,t}^{\infty} J(r,t)r^2 dr dt \tag{6}$$

For each time step the integration was started at the bubble wall and was stopped at a distance where no more nuclei were produced ($N < 1$). In the same way the time integration was started at the collapse and stopped when the number of generated nuclei became constant.

Eq. (5) is valid only for quasi-stationary nucleation. The necessary condition for stationary nucleation is that the time scale of driving force variation is greater than the time scale τ of new phase particle diffusion to the cluster. It can be written as:

$$d/dt\left[\frac{\Delta G_c(t)}{kT(t)}\right] < \frac{16}{\pi^3\tau(t)} \tag{7}$$

and

$$\tau(t) = \frac{9N_A\eta_l(\Delta G_c)^{4/3}\rho_s^2L_m^2}{8\pi^2M\sigma_{sl}^3}\exp\left[-\frac{L_mM}{kN_AT_m}\right] \tag{8}$$

As the time available for nucleation after a bubble collapse is extremely short, this condition was verified at every time step of the simulation. The nuclei generated in non-stationary conditions were discarded.

2.3. Water and ice properties

In the context of a bubble collapse event inducing very strong pressure and temperature gradients in the neighboring liquid, all the parameters of the equations given above had to be made pressure and temperature dependent. The parameters varying the most with pressure were the equilibrium ice-water temperature (which determined the undercooling level), the ice-water surface energy, the ice melting enthalpy and ice density. The great difficulty was to feed the model with reliable thermo-physical properties of water and ice as literature data are scarce in the very high pressures range involved by the bubble collapse (up to 60 GPa).

The solid–liquid equilibrium temperature (ice melting temperature) for water was calculated piece by piece for different types of ice compiling data from different sources: Choukroun and Grasset [24] for ice Ih, Wagner et al. [25] for ices III, V, VI and Lin et al. [26] for ice VII. The expression relating the equilibrium temperature to the liquid pressure for all pressure domains writes:

$$T_m(P) = T_0\left(\frac{P - P_0}{a} + 1\right)^{1/b} \tag{9}$$

and the corresponding coefficients are given in Table 1. The plot of the above function is given in Fig. 1.

The data concerning the liquid water and ice density were obtained from the work of Choukroun and Grasset [24] for ice Ih, III, V, VI and from the study of Frank et al. [27] for ice VII. Liquid water dynamic viscosity was read in Huber et al. [28] for pressure below 1 GPa and in Abramson [29] for pressure above 1 GPa (with extrapolation above 6 GPa).

It was finally possible to collect quite reliable pressure dependent data for all properties of liquid water and ice, with the exception of the water solid–liquid surface tension for which a very approximate and not fully validated formula was used. This pressure correction consisted to simply consider the surface tension as proportional to the melting enthalpy. According to Lee and Wang [30] the following expression may be postulated:

$$\frac{\sigma_{sli}^3(P,T)}{\rho_{si}^2(P,T)} = \frac{\sigma_{sli}^3(P_{0i},T)}{\rho_{si}^2(P_{0i},T)}\left[\frac{L_{mi}(P)}{L_{mi}(P_{0i})}\right]^3 \tag{10}$$

However, even if one accepts the postulate, this formula should be applied separately for each ice type (represented by the underscript i, P_{0i} being the lower limit pressure for ice i). As the starting values for the different ices other than Ih are not available (to our best knowledge), this formula was used all over the entire pressure domain starting from ice Ih. The temperature dependence of ice-water surface tension was accounted for using the correlation of Pruppacher [31]. The surface tension has a huge influence on the nucleation rate since it enters to the third power in an exponential in Eq. (3). The uncertainty about this parameter for high pressures is thus a serious drawback of the proposed model.

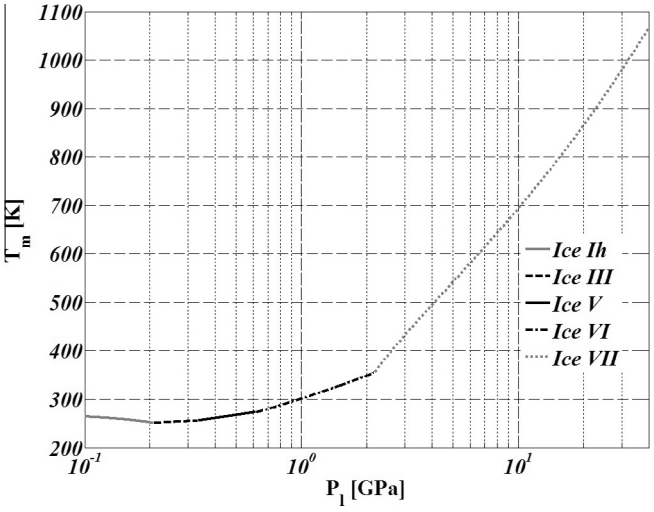

Fig. 1. Water solid–liquid equilibrium (melting) temperature versus pressure. (Data from [24–26]).

3. Results and discussion

3.1. Undercooling

The 'undercooling', defined as the difference between the liquid temperature and the melting (solid–liquid transition) temperature: $T_l - T_m$, is the nucleation driving force in a freezing process according to the classical nucleation theory adopted in this paper. The first concern was to determine the undercooling range around the collapsing bubble. The liquid temperature T_l profiles near the bubble wall were calculated and shown in part 1 [4] of this paper. The melting temperature T_m profiles were obtained from the liquid pressure profiles (see part 1 [4]) using the water solid–liquid equilibrium curve (see Eq. (9) and Fig. 1). Finally, the $T_l - T_m$ temperature difference was determined at each radial location around the bubble and for times just following the collapse and was plotted on Fig. 2. When this difference was negative, the liquid was 'undercooled' and the nucleation was possible. To make the undercooling value negative or positive is only matter of convention; in simulation the absolute value was used.

In Fig. 2, the first plotted line (65 ps) corresponds to the time of maximum pressure at the bubble wall, the time zero being the time of the collapse defined as the maximum of bubble wall velocity. As observed on this graph, the collapse induces a huge local undercooling, up to −370 K just at the time of maximum pressure, which may trigger nucleation. However, the high undercooling domain (over −50 K) is very limited in time (around 1 ns after the collapse) and in space (around 2 μm from the bubble wall). According to the results obtained in part 1 of this paper, the liquid temperature T_l at the bubble wall can reach around 620 K (R_0 = 5 μm, f_{ac} = 29 kHz, P_{ac} = 140 kPa) with the far field temperature $T_{l\infty}$ set as 263 K. The melting temperature T_m value at the bubble wall can attain around 900 K because of the liquid pressure P_l reaching 23 GPa. But the maximum undercooling (−370 K) is not

Table 1
Coefficients of correlation for water solid–liquid equilibrium temperature (T: K, P: MPa).

Parameter	Ice Ih [24] 0–209.9 MPa	Ice III [25] 209.9–350.1 MPa	Ice V [25] 350.1–632.4 MPa	Ice VI [25] 632.4–2170 MPa	Ice VII [26] 2170–22000 MPa
P_0 (MPa)	611.657×10^{-6}	209.5	355	618.4	2170
T_0 (K)	273.15	251.15	256.43	272.73	355
a	−414.5	101.1	373.6	661.4	850
b	8.38	42.86	8.66	4.69	3.47

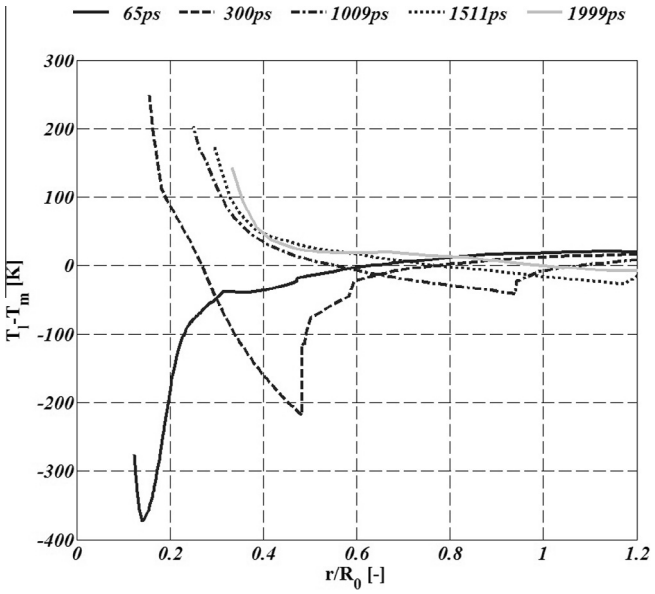

Fig. 2. Liquid undercooling versus the radial position around the bubble and for different times after the collapse (R_0 = 5 μm, f_{ac} = 29 kHz, P_{ac} = 140 kPa).

exactly at the bubble wall, but a little bit away (see Fig. 2) where the pressure is still very high but the T_l temperature have already steeply dropped.

3.2. Nucleation rate

The volumetric nucleation rate J calculated according to Eqs. (1–5) is plotted as function of liquid pressure and temperature in Fig. 3. This plot is not specific to a collapse event but shows generally how the nucleation rate behaves with changing liquid pressure and temperature in the very high pressures range. For comparison, the J value at −40 °C and atmospheric pressure is 30 $\mu m^{-3} \cdot ns^{-1}$. As shown on Fig. 3, the nucleation rate J curves have a maximum located around 2.3 GPa. The occurrence of this maximum and the significant gradients of J with regard to pressure are due to the contradictory influence of water and ice thermo-physical properties (see also Section 2).

The influence of liquid temperature on the nucleation rate is straightforward. If the temperature is decreased, the increase of the thermodynamic driving force of the phase change (undercooling) is prevailing in spite of the decrease of the values of the kinetic coefficient of the aggregation process. The influence of liquid pressure on the nucleation rate relies on two opposite effects. If pressure is increased, the increasing undercooling, solid density and melting enthalpy tend to increase the nucleation rate. But the influence of these parameters is offset by the substantial increase of the solid–liquid surface tension with pressure which results in a decrease of J for pressures above 2.3 GPa. Indeed, the surface tension is proportional to the melting enthalpy which depends on the equilibrium temperature curve and density curve and strongly increases with pressure especially for ice VII. There is in particular a step change of the value of ice density and of the slope of the equilibrium curve (see Fig. 1) because of the transition from ice VI to ice VII.

3.3. Nuclei number

The integration of J over the time elapsed after collapse and over space around the bubble (see Eq. (6)) gives the number of nuclei produced by a single collapse event. The results are presented first as a plot of isopleths of the nuclei number (in the pressure–temperature coordinates) generated by an air bubble with an initial radius of 5 μm driven by an ultrasonic sinusoidal wave at the frequency of 29 kHz (see Fig. 4). The practical integration limits for this case were roughly from 1 to 5 μm for radius and from 0 to 2 ns for time.

According to our results, the nucleation could be triggered starting from an undercooling as low as 5 K for bubbles of initial radius of 5 μm (or around 4 K for 8 μm bubbles, see Fig. 5) if an acoustic pressure amplitude of around 220 kPa is applied. For moderate acoustic pressures up to 220 kPa, the number of generated nuclei was found to increase with the undercooling level and with the acoustic pressure, which was in good qualitative agreement with already published experimental results [6,7,9]. However, for acoustic pressures above 220 kPa and for a given liquid super-cooling level, the number of nuclei was found not to vary any more with pressure. There is thus a range of acoustic pressure where the ultrasound is the most efficient and increasing the pressures beyond is not useful.

The difficulty in quantitative comparison of the present data and those from literature comes from the different methods used to measure the acoustic power (often confused with the electrical

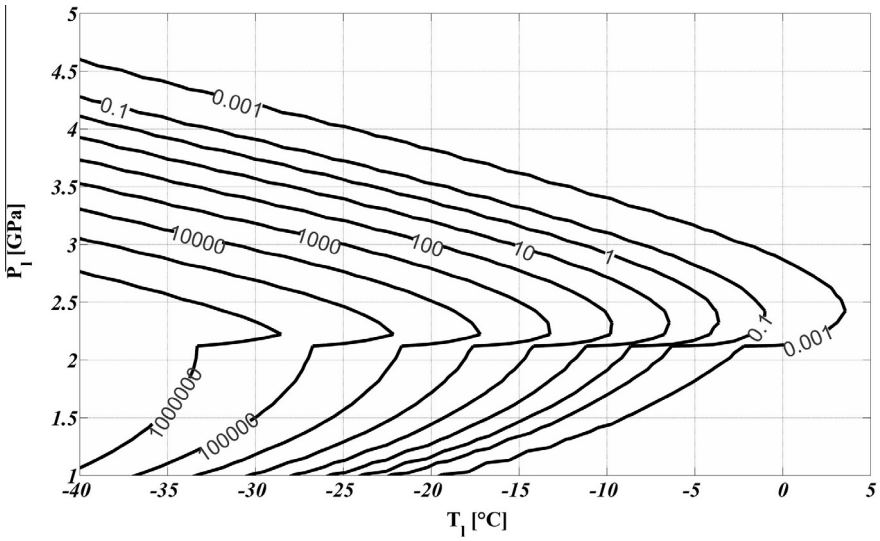

Fig. 3. Nucleation rate per unit volume [$\mu m^{-3} \cdot ns^{-1}$] versus liquid temperature and pressure.

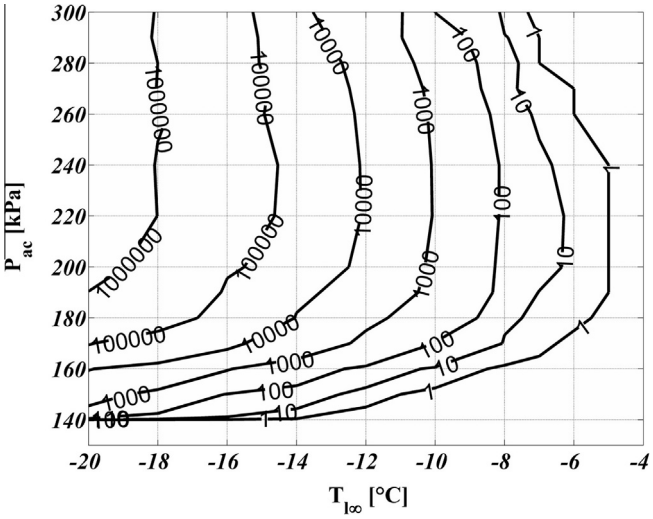

Fig. 4. Number of nuclei as function of initial liquid temperature and acoustic wave amplitude.

power delivered to the transducer) and different output parameters (nucleation probability or nucleation temperature) used to evaluate the nucleation rate (see Section 1). For instance, for the same operating conditions, the nucleation probability of 100% according to Inada et al. [6] corresponds roughly to a nuclei number of 10, according to our results.

Moreover, if it is supposed that the greater the number of nuclei, the smaller the crystal size, then the trends predicted by the theoretical model described above corresponded quite well, qualitatively speaking, to those given by an empirical model based on an experimental design proposed previously by Saclier et al. [12] (see preceding paragraph). A quantitative validation of the theoretical model was not possible, however, because the responses of the experimental design and of the simulations were not directly comparable. The former provided a number of ice nuclei in initial undercooled liquid, and the latter the size of ice crystals in the final frozen solid. A necessary continuation of this work will be therefore the further reconciliation of experimental and model predicted data.

Finally, the ice nucleation temperature threshold is given as function of acoustic pressure and initial bubble radius at the frequency of 29 kHz. The contour curves corresponding to several initial liquid temperatures and representing the conditions for generation of at least one nucleus are plotted on Fig. 5, along with the line corresponding to inertial cavitation threshold. The latter was obtained by using the dynamic equation of bubble wall motion (part 1, [4]) and the cavitation criterion of bubble radius expanding at least twice its initial value. Each contour curve has an upper and lower branch and the zones of possible nucleation lie within these branches. This figure shows even more clearly the existence of an optimal pressure range centered on 225 kPa, especially for low undercooling. There is also an optimal bubble size range centered on 8.5 μm. Nucleation can be already achieved at −5 °C over a large size domain (radius from 3 to 13 μm) providing the appropriate acoustic pressure. The influence of the initial radius on nucleation threshold reflects the nonlinear evolution of the bubble dynamics with the initial radius. Even if it is not as critical as the applied acoustic pressure, the control of initial bubble size may be helpful for achieving nucleation at a desired temperature.

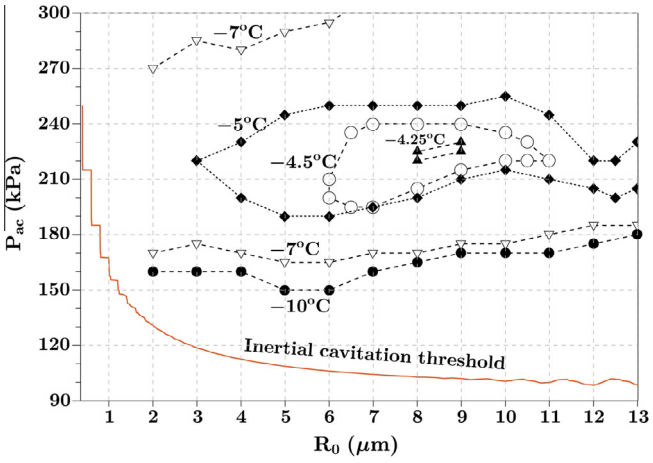

Fig. 5. Isotherms of nucleation threshold as function of initial bubble radius and acoustic pressure.

4. Conclusion

In the preceding paper (part 1), a theoretical model of acoustic inertial cavitation was developed on the ground of a literature survey. The pressure and temperature fields close to a bubble undergoing inertial cavitation were simulated and it was shown that strong liquid water undercooling was reached locally just after the collapse.

Starting from the Hickling's 'pressure rise effect' hypothesis, the goal of this study was to evaluate rigorously the number of ice nuclei generated by the collapse of a single gas bubble driven by an ultrasonic wave in initially undercooled water (temperature below 0 °C). First, the previous model was extended to incorporate the pressure and temperature dependent kinetic model of primary homogeneous ice nucleation. Second, an integration of the nucleation rate over the liquid volume around the bubble and over time after the collapse was performed in order to get the number of nuclei. The calculations were performed for different driving acoustic pressures, ambient liquid temperatures and bubble initial radius.

It was proved that nucleation could be triggered at low undercooling levels and for a wide distribution of bubble sizes, as far as the applied acoustic pressure lies in a specific appropriate range. Nucleation was found to occur at a higher liquid temperature for larger bubbles up to a certain bubble size. Thus the control of nucleis (crystals) number would be facilitated by the control of the bubble population which might be achieved by saturating the liquid sample with air or by pre-sonicating the sample with ultrasound of adapted frequency and amplitude. As the number of nuclei determines the size of crystals for a given liquid volume, the model developed in parts 1 and 2 allows for predicting trends of ice crystals size variation as function of operating conditions. It provides guidance for using ultrasound to control ice crystals size in frozen products and thus for optimal design of industrial freezing processes.

Acknowledgements

This work was financially supported by the French governmental research funding agency ANR in the frame of the project '09-BLAN-0040-SONONUCLICE'.

References

[1] C. Virone, H.J.M. Kramer, G.M. van Rosmalen, A.H. Stoop, T.W. Bakker, Primary nucleation induced by ultrasonic cavitation, J. Cryst. Growth 294 (1) (2006) 9–15.

[2] M. Saclier, R. Peczalski, J. Andrieu, A theoretical model for ice primary nucleation induced by acoustic cavitation, Ultrason. Sonochem. 17 (2010) 98–105.

[3] R. Hickling, Transient, high pressure solidification associated with cavitation in water, Phys. Rev. Lett. 73 (21) (1994) 2853–2856.
[4] C. Cogné, S. Labouret, R. Peczalski, O. Louisnard, F. Baillon, F. Espitalier, Theoretical model of ice nucleation induced by acoustic cavitation. Part 1: Pressure and temperature profiles around a single bubble, Ultrason. Sonochem. (2015), http://dx.doi.org/10.1016/j.ultsonch.2015.05.038.
[5] D. Kashchiev, Nucleation: Basic Theory with Applications, Butterworth-Heinemann, Boston, 2000.
[6] T. Inada, X. Zhang, A. Yabe, Y. Kozawa, Active control of phase change from supercooled water to ice by ultrasonic vibration 1. Control of freezing temperature, Int. J. Heat Mass Transfer 44 (2001) 4523–4531.
[7] X. Zhang, T. Inada, A. Yabe, S. Lu, Y. Kozawa, Active control of phase change from supercooled water to ice by ultrasonic vibration 2. Generation of ice slurries and effect of bubble nuclei, Int. J. Heat Mass Transfer 44 (2001) 4533–4539.
[8] R. Chow, R. Blindt, R. Chivers, M. Povey, The sonocrystallisation of ice in sucrose solutions: primary and secondary nucleation, Ultrasonics 41 (8) (2003) 595–604.
[9] R. Chow, R. Blindt, R. Chivers, M. Povey, A study on the primary and secondary nucleation of ice by power ultrasound, Ultrasonics 43 (4) (2005) 227–230.
[10] K. Nakagawa, A. Hottot, S. Vessot, J. Andrieu, Influence of controlled nucleation by ultrasounds on ice morphology of frozen formulations for pharmaceutical proteins freeze-drying, Chem. Eng. Process. 45 (9) (2006) 783–791.
[11] A. Hottot, K. Nakagawa, J. Andrieu, Effect of ultrasound-controlled nucleation on structural and morphological properties of freeze-dried mannitol solutions, Chem. Eng. Res. Des. 86 (2) (2008) 193–200.
[12] M. Saclier, R. Peczalski, J. Andrieu, Effect of ultrasonically induced nucleation on ice crystals' size and shape during freezing in vials, Chem. Eng. Sci. 65 (10) (2010) 3064–3071.
[13] H. Kiani, Z. Zhang, A. Delgado, D. Sun, Ultrasound assisted nucleation of some liquid and solid model foods during freezing, Food Res. Int. 44 (9) (2011) 2915–2921.
[14] H. Kiani, D. Sun, A. Delgado, Z. Zhang, Investigation of the effect of power ultrasound on the nucleation of water during freezing of agar gel samples in tubing vials, Ultrason. Sonochem. 19 (3) (2012) 576–581.
[15] R.T. Knapp, J.W. Daily, F.G. Hammitt, Cavitation, McGraw-Hill, New York, 1970.
[16] J.D. Hunt, K.A. Jackson, Nucleation of solid in an undercooled liquid by cavitation, J. Appl. Phys. 37 (1) (1966) 254–257.
[17] K. Ohsaka, E.H. Trinh, Dynamic nucleation of ice induced by a single stable cavitation bubble, Appl. Phys. Lett. 73 (1) (1998) 129–131.
[18] R. Grossier, O. Louisnard, Y. Vargas, Mixture segregation by an inertial cavitation bubble, Ultrason. Sonochem. 14 (4) (2007) 431–437.
[19] O. Louisnard, F.J. Gomez, R. Grossier, Segregation of a liquid mixture by a radially oscillating bubble, J. Fluid Mech. 577 (2007) 385–415.
[20] A. Kordylla, T. Krawczyk, F. Tumakaka, G. Schembecker, Modeling ultrasound induced nucleation during cooling crystallization, Chem. Eng. Sci. 64 (8) (2009) 1635–1642.
[21] K. Yasui, T. Tuziuti, K. Kato, Numerical simulations of sonochemical production of $BaTiO_3$ nanoparticles, Ultrason. Sonochem. 18 (5) (2011) 1211–1217.
[22] G. Shi, J.H. Seinfeld, K. Okuyama, Transient kinetics of nucleation, Phys. Rev. A 41 (4) (1990) 2101.
[23] W. Montes-Quiroz, F. Baillon, J.J. Letourneau, F. Espitalier, O. Louisnard, Freezing conditions in inertial cavitation bubbles during post-collapses expansions, in: Proceedings of the 13th Meeting of the European Society of Sonochemistry ESS13, Lviv Ukraine, OC-48, 2012.
[24] M. Choukroun, O. Grasset, Thermodynamic model for water and high-pressure ices up to 2.2 GPa and down to the metastable domain, J. Chem. Phys. 127 (2007) 124506.
[25] W. Wagner, A. Saul, A. Pruss, International equations for the pressure along the melting and along the sublimation curve of ordinary water substance, J. Phys. Chem. Ref. Data 23 (3) (1994) 515–527.
[26] J.-F. Lin, B. Militzer, V.V. Struzhkin, E. Gregoryanz, R.J. Hemley, H.-K. Mao, High pressure-temperature Raman measurements of H_2O melting to 22 GPa and 900 K, J. Chem. Phys. 121 (17) (2004) 8423–8427.
[27] M.R. Frank, Y. Fei, J. Hu, Constraining the equation of state of fluid H_2O to 80 GPa using the melting curve, bulk modulus, and thermal expansivity of ice VII, Geochim. Cosmochim. Acta 68 (13) (2004) 2781–2790.
[28] M.L. Huber, R.A. Perkins, A. Laesecke, D.G. Friend, J.V. Sengers, M.J. Assael, I.N. Metaxa, E. Vogel, R. Mares, K. Miyagawa, New international formulation for the viscosity of H_2O, J. Phys. Chem. Ref. Data 38 (2) (2009) 101–125.
[29] E.H. Abramson, Viscosity of water measured to pressure of 6 GPa and temperatures of 300 °C, Phys. Rev. E 76 (2007) 051203.
[30] C.P. Lee, T.G. Wang, The effects of pressure on the nucleation rate of an undercooled liquid, J. Appl. Phys. 71 (11) (1992) 5721–5723.
[31] H.R. Pruppacher, A new look at homogeneous ice nucleation in supercooled water drops, J. Atmos. Sci. 52 (1994) 1924–1933.

Journal of chemical & engineering data

Article

pubs.acs.org/jced

Determination of the Solid–Liquid Phase Diagram of the Binary System Propionic Acid/Water

Thouaïba Htira, Claudia Cogné, Emilie Gagnière, and Denis Mangin*

Laboratoire d'Automatique et de Génie des Procédés, UMR CNRS 5007, Université Lyon 1, Université de Lyon, CPE Lyon, 43 Boulevard du 11 Novembre 1918, F-69622 Villeurbanne, France

ABSTRACT: Solid–liquid phase diagram of the system water/propionic acid was achieved using two methods, the differential scanning calorimetry and a synthetic method. The liquidus curve is a simple eutectic diagram (89 wt % at 243 K) with an "S-shaped" form due to an inflection point (occurring at around 30% in weight of propionic acid), characteristic of a metastable liquid–liquid phase separation. The experimental data were modeled using experimental activity coefficients of the same system reported in the literature. The results are coherent, although the working temperature domains are different. The obtained phase diagram shows that ice is in equilibrium with the solution in a large composition domain; this is favorable for our further application of freeze wastewater treatment.

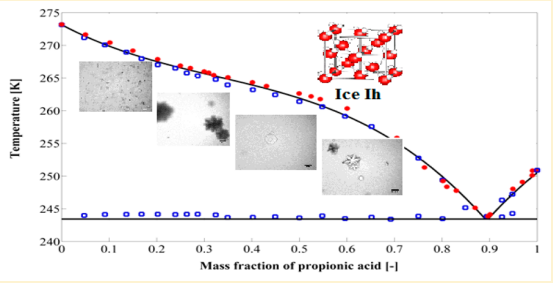

INTRODUCTION

Propionic acid, designation E280, is a food preservative commonly used in breads, cheeses, and dairy products. It is moderately harmless for humans in low quantity, but some recent scientific research studies have pointed out its potential role in some forms of autism in children.[1] This molecule is chemically close to the acrylic acid one. Acrylic acid, commonly used in paper and textile industries, generates polluted wastewater that requires treatment to satisfy the environmental norms. Several such wastewater treatment processes exist, such as chemical, biological, and physical processes. The most popular are the biological treatments using bacteria to discharge water from organic waste. However, bacteria are sensitive and could be destroyed by aggressive products. Moreover, these treatments do not allow recycling of the solvent. Recycling can be obtained through chemical or physical processes as distillation and membrane separation. However, both methods have high operating costs, high energy consumption for distillation, and heavy membrane maintaining due to fouling for membrane separation.

In this work, melt crystallization process is proposed as an alternative wastewater treatment process. This technology has some non-negligible advantages: a low energy consumption (the absolute value of the heat of vaporization of a product is higher than the absolute value of its heat of crystallization), and it is a green technology[2] since no additive substances are used to purify the water (unlike precipitation and flocculation processes). For aqueous solution containing a small amount of an organic substance, it allows production of clean water, and a concentrated solution that itself can be reused directly, or distilled at lower cost or at least easily oxidized or incinerated. Optimal design and scale-up of crystallizers need precise knowledge of solid–liquid phase behavior. Therefore, accurate phase diagrams are required to define the operational process conditions of crystallization and avoid the formation of undesired solid forms: the working zone is obviously limited by the nearest eutectic but can also be limited by the existence of defined compounds. Process limitations are encountered when a defined compound exists in the working zone, in spite of some studies demonstrating the possibility of eutectic separation using a specific device,[3] in which solids can be separated by density difference. Besides, the technique is effective in the presence of solid solution.

The binary system model chosen in this work is the water/propionic acid system, which was selected for its specific industrial interest. This work presents the solid–liquid phase diagram, which is the first step required to further develop the wastewater treatment process by freezing. To the best of our knowledge, the solid–liquid equilibrium of this system has not been reported in the literature. Many methods exist for building a solid–liquid phase diagram,[4,5] of which two have been chosen in this study, the calorimetric method[6,7] and the synthetic method.[8,9] The first method has been proven efficient in the determination of solid–liquid phase diagrams of several binary and ternary systems.[10−12] The second, older but well-known, was used to complete and confirm the calorimetric results. The material and these two methods are described in the first part of this work. The equilibrium diagram is then plotted experimentally and compared to predictive calculation based on thermodynamic properties and water activity coefficients found in the literature.

Received: July 22, 2015
Accepted: January 14, 2016
Published: January 28, 2016

DOI: 10.1021/acs.jced.5b00632
J. Chem. Eng. Data 2016, 61, 806–812

Journal of Chemical & Engineering Data Article

Table 1. Chemical Sample Table

chemical name	source	mole fraction purity	purification method	analysis
propionic acid	Acros Organics	0.99	none	gas chromatography
water	our laboratory		Millipore deionizer	

EXPERIMENTAL APPARATUS AND PROCEDURE

Materials. Propionic acid was purchase from Acros Organics with a reagent grade and was used without further purification. Table 1 summarizes the principal information on this product.

Calorimetric Method by Differential Scanning Calorimetry. The calorimeter used in this study is from Thermal Analysis Instruments (TA Q200) including a refrigerated cooling system allowing operation over the temperature range from 193 to 823 K. Samples (10−20 mg) of mixtures prepared at varying compositions were weighed with a METTLER balance with an accuracy of 0.01 mg and then placed in sealed aluminum pans. During the scanning operation, high-purity nitrogen gas was flushed throughout the differential scanning calorimetry (DSC) furnace to avoid condensation. To determine the phase change temperature, the experiments were performed according to the following program: (a) isotherm at 278 K, (b) cooling rate at 10 K·min^{-1}, (c) isotherm at 203 K during 5 min, (d) heating rate at 1 K·min^{-1}, (e) repeat steps a, b, and c, (f) heating rate at 5 K·min^{-1}, (g) repeat steps a, b, and c, and (h) heating rate at 10 K·min^{-1}. The results reported in this work correspond to data during the heating phase (steps d, f, and h). All DSC curves were normalized with respect to the sample mass.

In order to overcome the fact that DSC is a dynamic method while a phase diagram represents an equilibrium state, Kousksou et al.[13] proposed an original method to deduct more precisely the equilibrium temperature from the thermogram.

Figure 1 illustrates the application of this theory for an initial aqueous solution of 20% in weight of propionic acid. The graph shows the superposition of three thermograms at 1, 5, and 10 K·min^{-1}. For each thermogram, we note two endothermic peaks, characteristic of two solid fusions. The first equilibrium temperature is extrapolated at T_{eq1} = 267.03 K and the second one at T_{eq2} = 244.17 K.

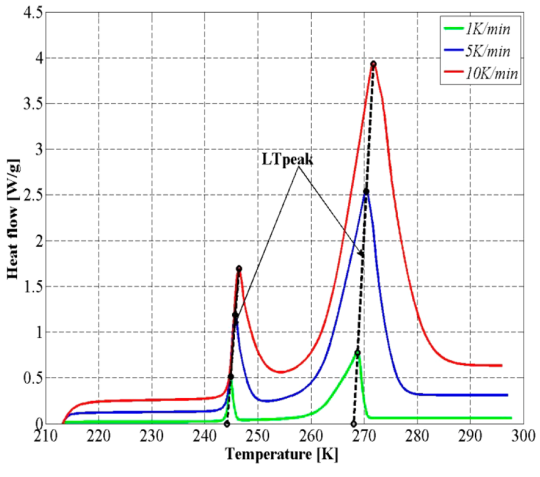

Figure 1. Thermogram example for 20% in weight of propionic acid (exo down).

The peak temperature, T_{peak}, corresponding to the maximum heat flow in the sample is used for the determination of the equilibrium temperature. The authors found a linear relationship between the peak temperatures at different heating rates; the solid−liquid equilibrium temperature, T_{eq}, of the initial solution is located at the intersection of this line and the abscissa (temperature).

Synthetic Method. The synthetic method[9,14] is classically a visual method; a solution is cooled until solidification and heated until crystal fusion; when the crystals disappear (visually), the solution is considered at the equilibrium temperature. Since the crystal detection was difficult because of their transparency, we have adapted this method by analyzing the evolution of the solution temperature.

Figure 2 shows the experimental apparatus, composed of a double jacketed vessel thermostated with a cryostat. Unlike the

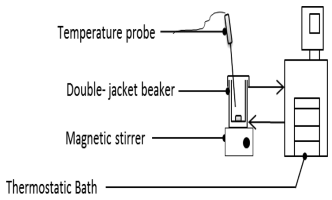

Figure 2. Experimental apparatus.

calorimetric method, which uses static solution, the solution in the vessel is homogenized with a magnetic stirrer in this method. Solid−liquid phase diagram was then determined by monitoring temperature using a calibrated Pt100 RTD.

A typical experiment is presented in Figure 3. The cooling and heating ramps have the same slope, 1 K·.h^{-1}. The solution temperature follows the bath temperature except during crystallization and melting of the crystals (between the point of crystallization and total dissolution on Figure 3) at which the suspension temperature is disturbed by the exothermal (crystallization) and endothermal (dissolution) phenomena. A

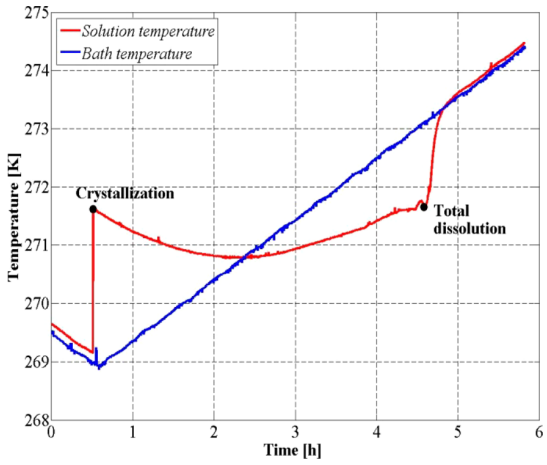

Figure 3. Typical temperature profile during an experiment.

DOI: 10.1021/acs.jced.5b00632
J. Chem. Eng. Data 2016, 61, 806−812

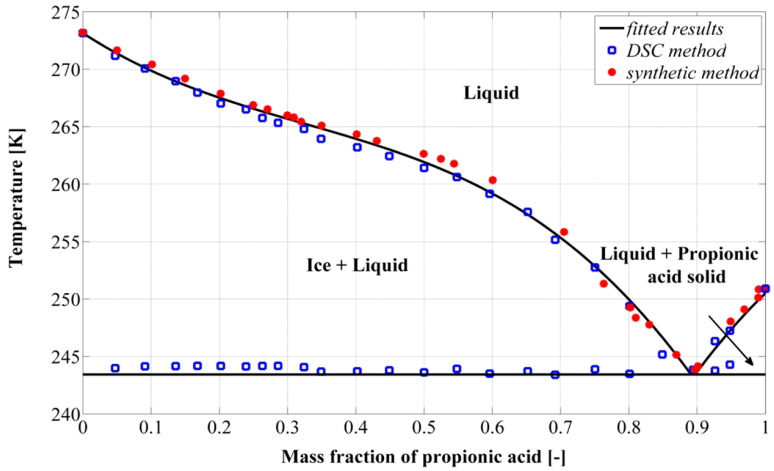

Figure 4. Solid−liquid diagram of water/propionic acid, experimental results.

supercooling of around 2.5 K is required to initiate nucleation. The crystallization rate is then rapid and induces a rapid temperature increase: the heat of crystallization cannot be compensated for by the heat transfer toward the double jacket. The crystallization rate slows when the suspension is close to equilibrium conditions. During this period, the suspension temperature decreases moderately. The dissolution process starts when the suspension temperature begins to increase. The equilibrium temperature of the solution at its initial composition (used for the construction of the phase diagram) corresponds to the point where the "last crystal" disappears. From that moment the solution temperature rapidly increases since the endothermal dissolution no longer occurs. After total dissolution, it might be surprising that the solution temperature curve is slightly over the bath temperature curve, while the temperature ramp is positive. This gap is due to heat transfer across the vessel cover and to a lesser extent, the mixing power.

RESULTS AND DISCUSSION

Experimental Solid−Liquid Diagram. The experimental phase diagram (Figure 4) was built from both the DSC and synthetic methods. The experimental results are resumed in Tables 2 and 3. In Table 2, T_{eq} is the equilibrium temperature and T_{eut} is the eutectic temperature. All studied compositions exhibited two endotherm peaks (Figure 1), except for samples with compositions close to the eutectic mixture. The temperature of the first peak varied with the composition; it was used to determine the experimental liquidus temperature. The second peak was always found at a fixed temperature, characteristic of an eutectic transition. The synthetic method (Table 3) was used to consolidate the liquidus temperatures measured by DSC. The two methods show good coherence, although the equilibrium temperatures given by the synthetic method tend to be slightly higher than the temperatures obtained by DSC. Based on differences in the results of the two methods, the standard uncertainty in the solid− liquid equilibrium temperatures determined by both methods is taken equal to $u(T_{eq}) = 1$ K (Tables 2 and 3). The polynomial fitting done with all of the experimental results gives the following liquidus equations:

Table 2. Experimental Results for the DSC Method at Pressure P = 1020 hPa[a]

w_{PA}[b]	T_{eq} [K]	T_{eut} [K]	solid phase
0.0473	271.17	243.98	ice
0.0910	270.07	244.14	
0.136	268.96	244.16	
0.168	267.97	244.18	
0.202	267.03	244.17	
0.239	266.51	244.13	
0.263	265.76	244.17	
0.286	265.33	244.18	
0.324	264.80	244.07	
0.349	263.95	243.68	
0.402	263.21	243.70	
0.449	262.44	243.79	
0.500	261.41	243.62	
0.548	260.62	243.92	
0.596	259.16	243.51	
0.652	257.58	243.71	
0.692	255.15	243.41	
0.750	252.75	243.88	
0.801	249.38	243.49	
0.849	245.17		
0.894	243.84		PA solid
0.926	246.33	243.76	
0.948	247.24	244.29	
1.00	250.89		

[a]Standard uncertainties (u) are $u_r(w_{PA}) = 0.001$, $u(T_{eq}) = u(T_{eut}) = 1$ K, and $u(P) = 10$ hPa. [b]w_{PA} = mass fraction of propionic acid.

$$\begin{cases} T_{eq} = -6.77 \times 10^{1} {w_{PA}}^{3} + 6.63 \times 10^{1} {w_{PA}}^{2} - 3.87 \times 10^{1} w_{PA} + 273.15, & 0 < w_{PA} < 0.89 \\ T_{eq} = -1.13 \times 10^{2} {w_{PA}}^{2} + 2.84 \times 10^{2} w_{PA} + 8.05 \times 10^{1}, & 0.89 < w_{PA} < 1 \end{cases} \quad (1)$$

DOI: 10.1021/acs.jced.5b00632
J. Chem. Eng. Data 2016, 61, 806−812

Table 3. Experimental Results for the Synthetic Method at Pressure P = 1020 hPa[a]

w_{PA}[b]	T_{eq} [K]	solid phase
0.0507	271.75	ice
0.101	270.42	
0.150	269.19	
0.202	267.88	
0.250	266.89	
0.271	266.53	
0.300	265.99	
0.309	265.82	
0.320	265.44	
0.350	265.1	
0.401	264.34	
0.431	263.77	
0.499	262.64	
0.525	262.2	
0.544	261.78	
0.600	260.35	
0.705	255.84	
0.763	251.33	
0.802	249.26	
0.810	248.37	
0.830	247.77	
0.901	244.15	PA solid
0.949	248.05	
0.969	249.1	
0.989	250.12	
0.990	250.84	

[a]Standard uncertainties (u) are $u_r(w_{PA})$ = 0.001, $u(T_{eq})$ = 1 K, and $u(P)$ = 10 hPa. [b]w_{PA} = mass fraction of propionic acid.

With an eutectic point at T_{eq} = 243.43 K, w_{PA} = 0.89 mass fraction of PA and a standard uncertainty of the fitting around 1 K.

From these results, it can be concluded that the phase diagram of the propionic acid/water system corresponds to a simple eutectic type. Nevertheless, a particular shape of the liquidus curve can be noted with an inflection point for a composition around 30% in weight of propionic acid. To ensure that this inflection is not due to the presence of a hydrate with a peritectic behavior, a complementary study was done, annealing using DSC.

Annealing Using Differential Scanning Calorimetry. When fast freezing rates are applied on samples, metastable solids may be formed. Certain operating conditions can be imposed to avoid the formation of metastable solids, such as lower cooling rate, repeating the freezing−thawing process,[15] or isothermal annealing. This last method was used in this study. Some samples were introduced in the DSC furnace and completely frozen to 203 K at the rate of 10 K·min^{-1}. The isothermal step was maintained at about 243 K; this temperature was determined beforehand with classical freezing−thawing of the sample by measuring the onset melt temperature of the supposed metastable compound. Then, the sample was refrozen to 203 K and finally melted with a heating rate of 5 K·min^{-1}. An example is represented in Figure 5, showing the results for 5% in weight of propionic acid with an isothermal step of 68 h, compared with the results obtained with the calorimetric method without isothermal annealing described earlier. The melt temperatures between the two experiments are quite similar, leading to the conclusion that the solid formed may be stable. Another possible interpretation is that the solid−solid transition from metastable to stable form is difficult from a completely solid state and at low temperature, because of narrow molecular mobility for such conditions.

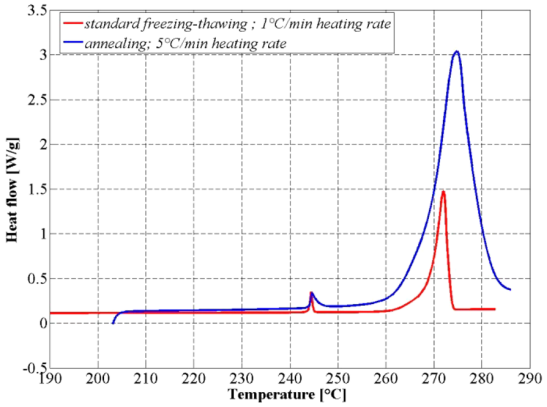

Figure 5. Thermogram comparison between standard method and annealing (exo down).

In conclusion, this complementary study does not point out the presence of a hydrate and leads to the conclusion of a simple eutectic diagram with an "S-shaped" characteristic of some alloy systems as Zn−Sn, Na−Rb, or Ag−Na.[16]

Comparison with Literature Data from Water Activities. We will focus on the left part of the liquidus, i.e., the ice/solution equilibrium. The solid−liquid phase equilibrium implies the equality between the chemical potential of the water in the solid and liquid phases. Since the solid is considered as pure ice, its chemical potential is that of pure solid (i.e., pure ice), μ_w^{S*}.

$$\mu_w^{S^*}(T) = \mu_w^{L}(T) \tag{2}$$

The chemical potential of the liquid water in the saturated solution is described by the following classical expression:

$$\mu_w^{L}(T) = \mu_w^{L^*}(T) + RT\ln(\gamma_w x_w) \tag{3}$$

where $\mu_w^{L*}(T)$ is the chemical potential of pure liquid water commonly used as the state of reference and γ_w and x_w are respectively the activity coefficient and the molar fraction of water in the saturated solution. Combining eqs 2 and 3 gives[17]

$$\mu_w^{L^*}(T) - \mu_w^{S^*}(T) = -RT\ln(\gamma_w x_w) \tag{4}$$

The chemical potential difference between the melt and the solid (water and ice) is given by

$$\frac{-\Delta H_w}{RT}\left(1 - \frac{T}{T_{f,w}}\right) - \frac{1}{RT}\int_{T_{f,w}}^{T} \Delta C_{p,w}\,dT + \frac{1}{R}\int_{T_{f,w}}^{T} \frac{\Delta C_{p,w}}{T}\,dT = \ln(\gamma_w x_w) \tag{5}$$

where ΔH_w = 6003 J·mol^{-1} is the molar enthalpy of ice fusion, R = 8.314 J·mol^{-1}·K^{-1}, $T_{f,w}$ = 273.15 K is the melting point of pure water at atmospheric pressure, and $\Delta C_{p,w}$ the heat capacity difference between liquid and solid water:

$$\Delta C_{p,w} = C_p^{L} - C_p^{S} \tag{6}$$

Although it is common to neglect the variation of this difference with the temperature and to simplify consequently expression eq 5,[18] the variation of heat capacities has been

DOI: 10.1021/acs.jced.5b00632
J. Chem. Eng. Data 2016, 61, 806−812

taken into account in this work. Thermodynamic data for ice and supercooled water are available in the literature from Choi and Okos' works;[19] the heat capacities as a function of the temperature can be represented by the following equations:

$$C_p^{L} = 1.79 \times 10^{-2} T^2 - 9.8813T + 1.4361 \times 10^{3} \quad (7)$$

$$C_p^{S} = 1.094 \times 10^{-1} T - 6.6994 \times 10^{1} \quad (8)$$

with T in K and C_p in J·mol^{-1}·K^{-1}).

In this section, we compare our experimental phase diagram with two literature results based primarily on water activity. The first work concerns the study of Hansen et al.[20] and focuses on activity coefficients of components in the water/propionic acid system at 298 K from experimental partial pressure measurements. The experimental data were represented by the following self-consistent activity coefficient function:

$$\log(\gamma_w) = x_{PA}^{2}\left[\frac{0.368}{x_{PA}^{2}} - 0.15 - 0.30x_{PA} + 0.90x_{PA}^{2} - e^{-2.8x_{PA}}\left(\frac{0.368}{x_{PA}^{2}} + \frac{1.030}{x_{PA}} - 1.03\right)\right] \quad (9)$$

where x_{PA} is the propionic acid mole fraction in the range [0,1] and γ_w the water activity coefficient. According to the authors, this equation is valid over the entire concentration range ($x_{PA} \in [0; 1]$).

The second work concerns the study of Pirouzi et al.[21] about experimental and correlation of osmotic coefficients for aqueous solutions of carboxylic acids, especially propionic acid. The experimental measurements are based on the isopiestic method at 298 K, which consists of the equilibrium between a sample container and a standard container (NaCl solutions in this study) by transferring water molecules from a container to the other. The measurements of samples' weight and acidity are required for the determination of the osmotic coefficient. The authors proposed a table of experimental values for different solute molalities (m_s) lower than 12.40 mol·kg^{-1} (corresponding to a maximum mole fraction of 0.18 or a maximum mass fraction of 0.48). Having the osmotic coefficient, the water activity is computed through the following equations:

$$\phi = \frac{-1000}{M_w m_s}\ln(a_w) \qquad \text{with } a_w = \gamma_w x_w \quad (10)$$

where ϕ is the osmotic coefficient, a_w the water activity, x_w the water mole fraction, M_w = 18 g·mol^{-1} the water molar mass, and m_s the solute molality. The activity coefficient has been fitted by the following polynomial function:

$$\log(\gamma_w) = -3.710x_{PA}^{3} + 2.082x_{PA}^{2} - 8.291 \times 10^{-3}x_{PA} - 2.927 \times 10^{-4} \quad (11)$$

for a mole fraction of propionic acid, $0 < x_{PA} < 0.18$

To calculate the freezing points of binary solutions with a composition lower than the eutectic point, an equilibrium between pure ice and the liquid mixture is assumed. The equilibrium temperature is calculated using eq 5 without any parametric adjustment. From this, our experimental results have been compared with the computational data from literature activity coefficients; the results are plotted in Figure 6.

From Figure 6, we can note the following:

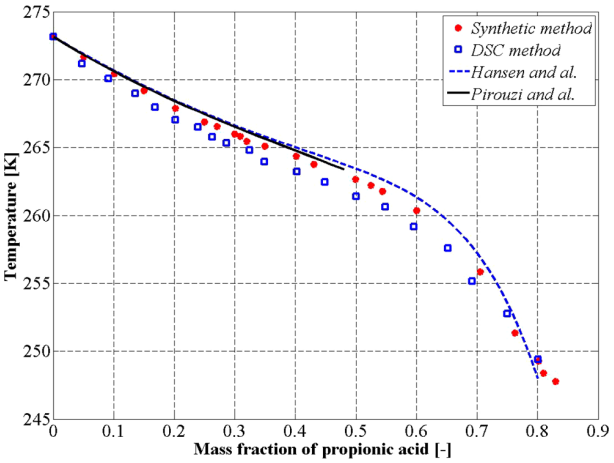

Figure 6. Comparison with literature data.

(a) For a mass fraction lower than 0.50, the literature data are in good agreement with the experimental results, although these data are only available at 298 K. It leads us to conclude a low influence of temperature on water activity in this range.

(b) For a mass fraction higher than 0.50, the prediction is difficult due to high concentration of solutions (up to 6.5 mol·L^{-1}). Further studies are required to model the liquidus curve by taking into account the electrostatic interactions that dominate in dilute systems, and also short-range interactions that cannot be neglected in concentrated electrolyte solutions.

(c) The diagram's shape is not affected by the ionic dissociation of weak acid. Indeed, the experimental ionization constant (pK_a) of propionic acid shows very low temperature dependency and remains almost constant at 4.9 over the temperature range 270−340 K.[22] pH measurements of the propionic acid solutions have also been carried out; the value varies from pH 2.54 (w_{PA} = 0.05) to pH 1.52 (w_{PA} = 0.70). This leads to the conclusion that the acids exists mainly in undissociated form for solution concentration higher than 0.05 mass fraction.

LIQUIDUS CURVE SHAPE

According to Ricci[16] and Levin,[23] an S-shape liquidus is characteristic of a metastable miscibility gap under the inflection point of the liquidus, as represented in Figure 7. It seems that the position of this oiling out (i.e., miscibility gap) depends on the flatness of the curve. The distance, Δ, between

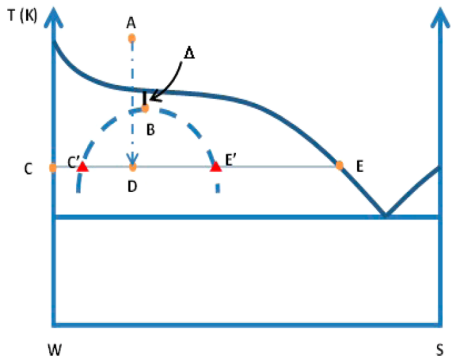

Figure 7. Schematic illustration of a phase diagram with submerged metastable miscibility gap (W = solvent; S = solute).

DOI: 10.1021/acs.jced.5b00632
J. Chem. Eng. Data 2016, 61, 806−812

the critical solution temperature (point B on Figure 7) and the liquidus decreases with the flatness of the curve. In our case, the inflection point is not so noticeable, suggesting that the phase separation tendency is weak or nonexistent. Nevertheless, the evolution of the Gibbs free energy change on mixing versus the mole fraction can be a good indicator to demonstrate the demixion tendency of the system. The equation of molar Gibbs free energy change on mixing, ΔG_m, is expressed as

$$\Delta G_m = RT \sum_{i=1}^{n} x_i \ln(\gamma_i x_i) = \Delta G_m^{id} + G^{ex} \quad (12)$$

where $\Delta G_m^{id} = RT \Sigma_{i=1}^{n} x_i \ln(x_i)$ represents the molar Gibbs free energy change on the formation of an ideal mixture from its pure components (with i being the number of species, 2 for a binary system) and $G^{ex} = RT \Sigma_{i=1}^{n} x_i \ln(\gamma_i)$ is the molar excess Gibbs free energy.

The excess Gibbs free energy has to respect the Gibbs–Duhem equation for all of the composition range, especially G^{ex} is zero for the pure components. The simplest equation satisfying this condition is the one-constant Margules equation:

$$G^{ex} = A x_{PA} x_w \quad (13)$$

where A is an adjustable parameter characteristic of the species interactions. As first approximation, this parameter was assumed to be independent of the temperature and the composition. With the support of experimental activities found in the literature[20] for the propionic acid/water binary system, the parameter A was fitted at T = 298 K according to

$$A x_{PA} x_w = RT[x_{PA} \ln(\gamma_{PA}) + x_w \ln(\gamma_w)] \quad (14)$$

where the water activity coefficient (γ_w) is determined with eq 9 and the propionic acid activity coefficient with[20]

$$\log(\gamma_{PA}) = (1 - x_{PA})^2 [0.30 x_{PA} + 0.90 x_{PA}^2 + 1.030 e^{-2.8 x_{PA}}] \quad (15)$$

In this condition, the optimized value of the interaction coefficient is A = 4330 J·mol^{-1}.

This quite simple model of excess Gibbs free energy has been extrapolated to predict the molar Gibbs free energy change on mixing of the solution at low temperature according to

$$\frac{\Delta G_m}{RT} = [x_{PA} \ln(x_{PA}) + x_w \ln(x_w)] + \frac{A x_{PA} x_w}{RT} \quad (16)$$

In Figure 8, the molar Gibbs free energy change on mixing was plotted versus the molar fraction of propionic acid, at two temperatures (T = 260 K and T = 240 K). For low temperatures, the molar Gibbs free energy has two minima, corresponding to the mixture separation into two phases. In the case of the one-constant Margules model, we can easily demonstrate[19] that the highest temperature at which phase separation is possible occurs at $x_{PA} = x_w = 0.5$, which gives the critical temperature $T_c = \frac{A}{2R}$ = 260 K.

Experimentally, to observe the liquid–liquid phase separation, the solution has to be cooled from point A, for example, to point D (Figure 7) without a crystallization event. In this case, the equilibrium is represented by the points C′ and E′. Since low cooling rate was applied in our case, crystallization occurred during cooling and the liquid–liquid phase separation was not observed.[24] The equilibrium is represented by the points C for solid and E for solution.[25,26] Such S-shaped systems with an undercooled metastable miscibility gap can be found in the literature, for example, the water/salicylic acid system[27] or carbon dioxide/n-hexane system.[28]

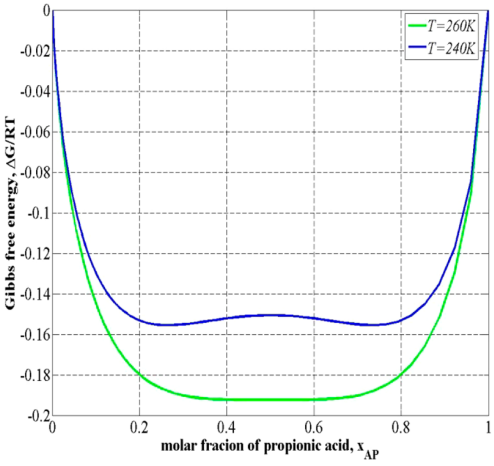

Figure 8. Molar Gibbs free energy of mixing for the water/propionic acid system.

CONCLUSIONS

The solid–liquid phase diagram of water and propionic acid has been determined experimentally by two methods, differential scanning calorimetry and synthetic method. The diagram is a simple eutectic with a wide range of ice existence. The liquidus curve lets us assume the presence of a submerged metastable miscibility gap around 30% in weight of propionic acid, which is also confirmed by the Gibbs free energy calculation. The experimental results were compared with thermodynamic data in the literature, and good agreement was found for low concentrations.

AUTHOR INFORMATION

Corresponding Author

*E-mail: denis.mangin@univ-lyon1.fr.

Funding

The project was funded by MENRT Institution (France).

Notes

The authors declare no competing financial interest.

REFERENCES

(1) Shultz, S. R.; Aziz, N. A. B.; Yang, L.; Sun, M.; MacFabe, D. F.; O'Brien, T. J. Intracerebroventricular Injection of Propionic Acid, an Enteric Metabolite Implicated in Autism, Induces Social Abnormalities That Do Not Differ between Seizure-Prone (FAST) and Seizure-Resistant (SLOW) Rats. *Behav. Brain Res.* **2015**, *278*, 542–548.

(2) Ulrich, J. Is Melt Crystallization a Green Technology? *Cryst. Growth Des.* **2004**, *4*, 879–880.

(3) van der Ham, F.; Witkamp, G. J.; de Graauw, J.; van Rosmalen, G. M. Eutectic Freeze Crystallization Simultaneous Formation and Separation of Two Solid Phases. *J. Cryst. Growth* **1999**, *198–199*, 744–748.

(4) Chen, M.; Ma, P. Solid–Liquid Equilibria of Several Systems Containing Acetic Acid. *J. Chem. Eng. Data* **2004**, *49*, 756–759.

(5) Cohen-Adad, R.; Cohen-Adad, M.-T. Solubility of Solids in Liquids. In *The Experimental Determination of Solubilities*;Hefter, G. T., Tomkins, R. P. T., Eds.; Wiley Series in Solution Chemistry; John Wiley & Sons: Chichester, West Sussex, England; Hoboken, NJ, USA, 2003; Chapter 4.1.

DOI: 10.1021/acs.jced.5b00632
J. Chem. Eng. Data 2016, 61, 806–812

(6) Shibuya, H.; Suzuki, Y.; Yamaguchi, K.; Arai, K.; Saito, S. Measurement and Prediction of Solid-Liquid Phase Equilibria of Organic Compound Mixtures. *Fluid Phase Equilib.* **1993**, *82*, 397−405.
(7) Coutinho, J. a. P.; Ruffier-Meray, V. A New Method for Measuring Solid-Liquid Equilibrium Phase Diagrams Using Calorimetry. *Fluid Phase Equilib.* **1998**, *148*, 147−160.
(8) Fiege, C.; Joh, R.; Petri, M.; Gmehling, J. Solid−Liquid Equilibria for Different Heptanones with Benzene, Cyclohexane, and Ethanol. *J. Chem. Eng. Data* **1996**, *41*, 1431−1433.
(9) Jakob, A.; Joh, R.; Rose, C.; Gmehling, J. Solid-Liquid Equilibria in Binary Mixtures of Organic Compounds. *Fluid Phase Equilib.* **1995**, *113*, 117−126.
(10) Benziane, M.; Khimeche, K.; Dahmani, A.; Nezar, S.; Trache, D. Experimental Determination and Prediction of (solid + Liquid) Phase Equilibria for Binary Mixtures of Heavy Alkanes and Fatty Acids Methyl Esters. *J. Therm. Anal. Calorim.* **2013**, *112*, 229−235.
(11) Lorenz, H.; Seidel-Morgenstern, A. Binary and Ternary Phase Diagrams of Two Enantiomers in Solvent Systems. *Thermochim. Acta* **2002**, *382*, 129−142.
(12) Li, N.; Machui, F.; Waller, D.; Koppe, M.; Brabec, C. J. Determination of Phase Diagrams of Binary and Ternary Organic Semiconductor Blends for Organic Photovoltaic Devices. *Sol. Energy Mater. Sol. Cells* **2011**, *95*, 3465−3471.
(13) Kousksou, T.; Jamil, A.; Zeraouli, Y.; Dumas, J.-P. Equilibrium Liquidus Temperatures of Binary Mixtures from Differential Scanning Calorimetry. *Chem. Eng. Sci.* **2007**, *62*, 6516−6523.
(14) Le Page Mostefa, M.; Muhr, H.; Plasari, E.; Fauconet, M. Determination of the Solid−Liquid Phase Diagram of the Binary System Acrylic Acid + Propionic Acid. *J. Chem. Eng. Data* **2012**, *57*, 1209−1212.
(15) Takaizumi, K. A Curious Phenomenon in the Freezing-Thawing Process of Aqueous Ethanol Solution. *J. Solution Chem.* **2005**, *34*, 597−612.
(16) Ricci, J. E. *The Phase Rule and Heterogeneous Equilibrium*; Van Nostrand: New York, 1951.
(17) Sandler, S. I. *Chemical and Engineering Thermodynamics*, 3rd ed.; John Wiley & Sons: Hoboken, NJ, USA, 1999.
(18) Prausnitz, J. M.; Lichtenthaler, R. N.; de Azevedo, E. G. *Molecular Thermodynamics of Fluid-Phase Equilibria*, 3rd ed.; Prentice-Hall International Series in the Physical and Chemical Engineering Sciences; Prentice Hall PTR: Upper Saddle River, NJ, USA, 1999.
(19) Choi, Y.; Okos, M. R. Effects of the Temperature and Composition on the Thermal Properties of Foods. *Food Engineering and Process Applications: Transport Phenomena*, Vol. *1*; Elsevier: Amsterdam, 1986; pp 93−101.
(20) Hansen, R. S.; Miller, F. A.; Christian, S. D. Activity Coefficients of Components in the Systems Water−Acetic Acid, Water−Propionic Acid and Water−n-Butyric Acid at 25°C. *J. Phys. Chem.* **1955**, *59*, 391−395.
(21) Pirouzi, A.; Nosrati, M.; Haghtalab, A.; Vasheghani-Farahani, E. Experiment and Correlation of Osmotic Coefficient for Aqueous Solution of Carboxylic Acids Using NRTL Nonrandom Factor Model. *Fluid Phase Equilib.* **2012**, *327*, 38−44.
(22) Gupta, R. B.; Heidemann, R. A. Solubility Models for Amino Acids and Antibiotics. *AIChE J.* **1990**, *36*, 333−341.
(23) Levin, E. Liquid Immiscibility in Oxide Systems. In *Phase Diagrams*, Vol. 3; Alper, A.; Academic Press; New York, 1970; Chapter V, DOI: 10.1016/B978-0-12-053203-2.50013-2.
(24) Brandel, C.; Gbabode, G.; Cartigny, Y.; Martin, C.; Gouhier, G.; Petit, S.; Coquerel, G. Crystal Growth, Structure, and Polymorphic Behavior of an Ionic Liquid: Phthalate Derivative of N-Butyl,N-Methylimidazolium Hexafluorophosphate. *Chem. Mater.* **2014**, *26*, 4151−4162.
(25) Coquerel, G. Crystallization of Molecular Systems from Solution: Phase Diagrams, Supersaturation and Other Basic Concepts. *Chem. Soc. Rev.* **2014**, *43*, 2286−2300.
(26) Davey, R. J.; Schroeder, S. L. M.; ter Horst, J. H. Nucleation of Organic Crystals–A Molecular Perspective. *Angew. Chem., Int. Ed.* **2013**, *52*, 2166−2179.
(27) Sidgwick, N. V.; Ewbank, E. K. CVII. The Influence of Position on the Solubilities of the Substituted Benzoic Acids. *J. Chem. Soc., Trans.* **1921**, *119*, 979−1001.
(28) Im, U. K.; Kurata, F. Heterogeneous Phase Behavior of Carbon Dioxide in N-Hexane and N-Heptane at Low Temperatures. *J. Chem. Eng. Data* **1971**, *16*, 412−415.

DOI: 10.1021/acs.jced.5b00632
J. Chem. Eng. Data 2016, 61, 806−812